

## Abstract

Title of Dissertation: Swashplateless Helicopter  
Experimental Investigation:  
Primary Control with  
Trailing Edge Flaps  
Actuated with Piezobenders

Peter Copp, Doctor of Philosophy, 2013

Dissertation directed by: Dr. Inderjit Chopra  
Department of Aerospace Engineering

Helicopter rotor primary control is conventionally carried out using a swashplate with pitch links. Eliminating the swashplate promises to reduce the helicopter's parasitic power in high speed forward flight, as well as may lead to a hydraulic-less vehicle. A Mach-scale swashplateless rotor is designed with integrated piezobender-actuated trailing edge flaps and systematically tested on the benchtop, in the vacuum chamber and on the hoverstand. The blade is nominally based on the UH-60 rotor with a hover tip Mach number of 0.64. The blade diameter is 66 inches requiring 2400 RPM for Mach scale simulation. The rotor hub is modified to reduce the blade fundamental torsional frequency to less than 2.0/rev by replacing the rigid pitch links with linear springs, which results in an increase of the blade pitching response to the trailing edge flaps. Piezoelectric multilayer benders provide the necessary bandwidth, stroke and stiffness to drive the flaps for primary control while fitting inside the blade profile and withstanding the high centrifugal forces.

This work focuses on several key issues. A piezobender designed from a soft piezoelectric material, PZT-5K4, is constructed. The new material is used to construct multi-layer benders with increased stroke for the same stiffness relative to hard materials such as PZT-5H2. Each layer has a thickness of 10 mils. The soft material with gold electrodes requires a different bonding method than hard

material with nickel electrodes. With this new bonding method, the measured stiffness matches precisely the predicted stiffness for a 12 layer bender with 1.26 inch length and 1.0 inch width with a stiffness of 1.04 lb/mil. The final in-blade bender has a length of 1.38 inches and 1.0 inch width with a stiffness of 0.325 lb/mil and stroke of 20.2 mils for an energy output of 66.3 lb-mil. The behavior of piezobenders under very high electric fields is investigated. High field means +18.9 kV/cm (limited by arcing in air) and -3.54kV/cm (limited by depoling). An undocumented phenomenon is found called bender relaxation where the benders lose over half of their initial DC stroke over time. While the bender stiffness is shown not to change with electric field, the DC stroke is significantly less than AC stroke.

A two-bladed Mach-scale rotor is constructed with each blade containing 2 flaps each actuated by a single piezobender. Each flap is 26.5% chord and 14% span for a total of 28% span centered at 75% of the blade radius. Flap motion of greater than 10 degrees half peak-peak is obtained for all 4 flaps at 900 RPM on the hoverstand. So, the flaps show promise for the Mach-scale rotor speed of 2400 RPM. A PID loop is implemented for closed loop control of flap amplitude and mean position.

On the hoverstand at 900 RPM, the swashplateless concept is demonstrated. The linear springs used to lower the torsional frequency are shown to have minimum friction during rotation. 1/rev blade pitching of  $\pm 1$  degree is achieved at a torsional frequency of 1.5/rev for each blade. At resonance, the blade pitching for each blade is greater than  $\pm 4$  degrees. Primary control is demonstrated by measuring hub forces and moments. At resonance state, the flaps in conjunction with the blade pitching provide  $\pm 15$  lbs of normal force at a mean lift of 15 lbs yielding  $\pm 100\%$  lift authority. Significant hub forces and moments are produced as well.

For a production swashplateless helicopter, it may be prudent to eliminate the pitch links by reducing the blade structural stiffness. A novel wire sensor system network is proposed in order to measure blade elastic flap bending, lead-lag bending and torsion. The theory for measuring blade twist is rigorously derived. A blade is constructed with the wire sensor network and validated on the benchtop for blade elastic bending and twist.

This work is a step forward in achieving a swashplateless rotor system. Not only would this reduce drag in high speed forward flight, but it would lead to a hydraulicless rotorcraft. This would be a major step in vertical flight aviation.

**Swashplateless Helicopter  
Experimental Investigation:  
Primary Control with  
Trailing Edge Flaps  
Actuated with Piezobenders**

by

Peter Copp

Dissertation submitted to the Faculty of the Graduate School of the  
University of Maryland at College Park in partial fulfillment  
of the requirements for the degree of  
Doctor of Philosophy  
2013

Advisory Committee:

Dr. Inderjit Chopra, Chairman/Advisor  
Dr. James Baeder  
Dr. Norman Wereley  
Dr. Sung Lee  
Dr. Amr Baz, Dean's Representative

© Copyright by  
Peter Copp  
2013

# Dedication

To the One who takes great delight in me  
and rejoices over me with singing,  
Who makes my hands able to bend a bow of PZT  
and gives man work that satisfies him  
and prepares him for eternity with His Son

# Acknowledgements

Acknowledgements are a space to remember how my accomplishments are more an amalgam of others' efforts on my behalf than my own. This PhD is no different.

My project was quite simple in definition - to make flaps move up and down. It either worked or it did not and they did not for what some might call a long time. Many attempts were made - it was a puzzle that refused to be solved. Growing up, I would have math or physics homework problems to solve before the night was over. After being out of the house for 13 hours for work, my tired father would joyfully help me solve these late into the night. He refused to quit (or let me quit) until the problems were solved. I doubt I have as much satisfaction in wrestling a problem as him, but surely, some of the tenacity rubbed off on me. My mom has encouraged me in many ways, but her prayers to the Father of Jesus Christ on my behalf, these, I have treasured. Both of my parents have lived as if doing something you love is of great value, which has led me to stick with this project. My brother, Chip, has been a constant source of friendship and fellow commiserator in trying to make a go of things while doing something you are called to do. Melissa is the apple of my eye and my satisfaction in finishing is made more complete with her.

One does not make it through this program without significant help from the other students and I miss those that have moved on to other places. Jaye and Shaju showed me the ropes. It was just a lot of fun to work with Nitin and get his car from the towlot. I miss playing basketball with Brandon. Anubhav set a high standard for excellence in research and publishing and also was concerned with my well-being.

My time working with and discussing each other's work with Anand and Vikram, I especially enjoyed. The highlight of my day was often talking through different research ideas. I wish them the very best going on.

Vikram graciously gave helpful revisions for the entire thesis.

Finally, I thank my committee, especially my advisor, Dr. Chopra: not only for his support, but also for his concern with how his students are faring beyond just school.

# Table of Contents

<b>List of Tables</b>	<b>viii</b>
<b>List of Figures</b>	<b>ix</b>
<b>Nomenclature</b>	<b>xiv</b>
<b>1 Introduction</b>	<b>1</b>
1.1 Background and Motivation . . . . .	1
1.1.1 Background . . . . .	1
1.1.2 Conventional Primary Control . . . . .	2
1.1.3 Swashplateless Concept . . . . .	6
1.2 Trailing Edge Flaps for Primary Control Analysis . . . . .	9
1.2.1 Simple Aeroelastic Model . . . . .	9
1.2.2 Refined Models . . . . .	10
1.2.3 Analysis Summary . . . . .	17
1.3 Kaman helicopters . . . . .	19
1.4 Mach Scale . . . . .	22
1.5 Trailing Edge Flap Actuators . . . . .	24
1.5.1 Introduction to Piezo Actuators . . . . .	24
1.5.2 Piezostacks . . . . .	25
1.5.3 Piezobenders . . . . .	30
1.5.4 Flap driven by tab . . . . .	34
1.5.5 Electric motors . . . . .	37
1.5.6 PAM . . . . .	42
1.6 Limitations of Previous Work . . . . .	48
1.7 Scope of Current Research . . . . .	49
1.8 Overview of Dissertation . . . . .	50

<b>2</b>	<b>Piezobenders</b>	<b>52</b>
2.1	Overview . . . . .	52
2.2	Piezobender Dimensions . . . . .	55
2.2.1	Piezobender Finite Element Code . . . . .	56
2.2.1.1	Constraints . . . . .	57
2.2.1.2	Bender Length . . . . .	58
2.2.1.3	Model refinements . . . . .	60
2.2.2	Model Results . . . . .	62
2.2.3	Final Bender . . . . .	64
2.3	Material Choice . . . . .	67
2.3.1	Hard vs. Soft . . . . .	67
2.3.2	Material Survey . . . . .	67
2.3.3	Curie Temperature . . . . .	69
2.3.4	Material Comparison . . . . .	71
2.3.5	Soft Material Bender Construction . . . . .	71
2.3.5.1	Stiffness measurement . . . . .	72
2.3.5.2	Materials with nickel-based electrodes (PZT-5H2) . . . . .	74
2.3.5.3	Materials with gold-based electrodes (PZT-5K4) . . . . .	75
2.3.5.4	Determining poling direction . . . . .	77
2.3.5.5	PZT-5K4 Bender Construction Conclusions . . . . .	78
2.4	Transferring Bender Force to Flap . . . . .	80
2.4.1	Slotted Rod . . . . .	80
2.4.2	Good Cantilever . . . . .	82
2.5	High Electric Fields . . . . .	82
2.5.1	Different Bias Voltages for PZT-5K4 Bender . . . . .	84
2.5.2	Bender Stiffness at High Electric Fields . . . . .	86
2.5.2.1	Bender Compliance . . . . .	87
2.5.2.2	Single Plate with Drift Removed . . . . .	89
2.5.2.3	Dead Cantilever Hypothesis . . . . .	89
2.5.2.4	Stiffness of Bimorph with Dead Cantilever . . . . .	91
2.5.2.5	Stiffness of 4-Layer Bender with Dead Cantilever . . . . .	95
2.5.2.6	4-Layer Bender Relaxation . . . . .	98
2.5.2.7	4-Layer Bender Constrained by Spring . . . . .	99
2.5.3	PZT-5K4 maximum strain . . . . .	101
2.5.4	High Electric Field Conclusions . . . . .	101
2.6	Conclusions . . . . .	102
<b>3</b>	<b>Mach Scale Rotor</b>	<b>104</b>
3.1	Overview . . . . .	104
3.2	Comparison to Previous Trailing Edge Flap Scaled Work . . . . .	106
3.3	Blade Assembly . . . . .	108
3.4	Flap Assembly . . . . .	109

3.4.1	TE Flap . . . . .	111
3.4.2	Flap Mount . . . . .	114
3.4.2.1	Low Friction Rotation . . . . .	115
3.4.2.2	Mass Balancing . . . . .	118
3.4.2.3	Complex Part . . . . .	118
3.4.2.4	Mass Balancing Position . . . . .	120
3.4.2.5	Final Flap . . . . .	121
3.4.3	Flap Anchor . . . . .	123
3.5	Vacuum Chamber Result . . . . .	125
3.6	Hoverstand Setup . . . . .	127
3.6.1	Flap Authority . . . . .	129
3.6.2	Soft Pitch Link . . . . .	131
3.7	Summary . . . . .	135
<b>4</b>	<b>Hoverstand Results</b>	<b>137</b>
4.1	Overview . . . . .	137
4.2	Closed Loop Flap Control . . . . .	137
4.3	Flap Effectiveness . . . . .	140
4.4	Primary Control Demonstration . . . . .	143
4.5	Conclusion . . . . .	145
<b>5</b>	<b>Blade Elastic Deformation Wire Sensor</b>	<b>147</b>
5.1	Proposal . . . . .	147
5.2	Introduction . . . . .	147
5.3	Blade Deformation Measurement Techniques . . . . .	149
5.3.1	PMI . . . . .	149
5.3.2	Photogrammetry . . . . .	151
5.3.3	Digital Image Correlation . . . . .	151
5.3.4	Optical Measurement Pros and Cons . . . . .	153
5.4	Introduction to Wire Sensor . . . . .	154
5.4.1	Basic Theory . . . . .	155
5.5	Beam Bending . . . . .	158
5.5.1	Theory Overview . . . . .	158
5.5.2	Wire Sensor Advantages . . . . .	160
5.5.3	Baz Proof-of-Concept . . . . .	160
5.6	Theory applied to Rotorcraft Blade . . . . .	161
5.6.1	Introduction . . . . .	163
5.6.2	Bending with Rotation . . . . .	163
5.6.3	Blade Strain . . . . .	166
5.6.4	Conclusion . . . . .	169
5.7	Model of Rotorcraft Blade Wire Sensor . . . . .	170
5.7.1	Bending . . . . .	172

5.7.2	Twist . . . . .	172
5.7.3	Blade Wire Sensor Network . . . . .	175
5.7.4	Wire Material . . . . .	177
5.7.5	Conclusion . . . . .	178
5.8	Validation of Rotorcraft Blade Wire Sensor . . . . .	178
5.8.1	Test Description . . . . .	179
5.8.2	Computational Model . . . . .	180
5.8.2.1	Model Description . . . . .	180
5.8.2.2	Model Results . . . . .	181
5.8.2.3	Model Conclusions . . . . .	184
5.8.3	Single Point Validation . . . . .	186
5.8.4	Motion Capture Camera Validation . . . . .	188
5.9	Conclusions and Future Work . . . . .	189
<b>6</b>	<b>Conclusions and Recommendations for Future Work</b>	<b>191</b>
6.1	Summary . . . . .	191
6.2	Full-scale Application . . . . .	193
6.3	Key Conclusions . . . . .	194
6.3.1	Piezobenders . . . . .	194
6.3.2	Mach Scale Swashplateless Rotor with Trailing Edge Flaps	196
6.3.3	Blade Wire Sensor Network . . . . .	197
6.4	Recommendations for Future Work . . . . .	198
6.4.1	$d_{33}$ Piezobender . . . . .	198
6.4.2	Present Setup Improvements . . . . .	201
	<b>Bibliography</b>	<b>204</b>

# List of Tables

1.1	UH-60 Rotor Properties . . . . .	11
1.2	Fulton Rotor Properties [51] . . . . .	32
1.3	Roget Mach-Scale Rotor Properties . . . . .	33
1.4	Optimized Flap-Tab System for UH-60A Rotor . . . . .	35
1.5	Maximum Flap Amplitude Versus Frequency . . . . .	38
2.1	Final Bender Properties . . . . .	66
2.2	Survey of Piezoceramic Materials . . . . .	68
2.3	Material Curie Temperatures . . . . .	70
2.4	Material Properties . . . . .	71
2.5	Effect of increasing bias on PZT-5K4 Bender Stroke . . . . .	85
2.6	PZT-5K4 'Dead' Bimorph Stiffness . . . . .	92
2.7	PZT-5K4 'Dead' Bimorph Stiffness by Frequency . . . . .	95
2.8	PZT-5K4 4-Layer Bender Stiffness with Various Cantilever Elec- trical Fields . . . . .	97
2.9	PZT-5K4 4-Layer Bender Stiffness, 'Dead' Cantilever, Maximum Electric Field . . . . .	98
2.10	Constrained Bender Stroke with Various Cantilever Electrical Con- ditions . . . . .	101
3.1	Mach Scale Rotor . . . . .	106
3.2	Flap Comparison: Roget Flap vs. Primary Control Outboard Flap	107
3.3	Flap Comparison: Roget Flap vs. Primary Control Outboard Flap per degree of flap HPP . . . . .	107
3.4	Mach Scale Rotor Weight Breakdown . . . . .	110
3.5	Flap Inertial Properties . . . . .	123
4.1	Predicted Flap Effectiveness at 900 RPM . . . . .	141
4.2	Predicted Flap Effectiveness at 900 RPM . . . . .	142
5.1	Steel vs. Constantan as Wire Sensor . . . . .	177

# List of Figures

1.1 Swashplate Diagram . . . . .	3
1.2 CH-53 Rotor Swashplate . . . . .	4
1.3 UH-60 IBC . . . . .	5
1.4 Multiple Swashplate (SP) Mechanism . . . . .	7
1.5 META mechanism diagram including actuators . . . . .	7
1.6 Effect of Index Angle on flap control angles, actuation power and moment, Flap overhang of $0.05c$ and $\mu = 0.32$ [26] . . . . .	12
1.7 Predicted and Measured Power for UH-60A in Forward Flight, $C_W/\sigma=0.0783$ (FW: free wake, Uniform: uniform inflow) [25] . . .	13
1.8 Effect on blade elastic twist angle of lowering torsional frequency [25]	14
1.9 Effect on non-rotating blade collective (Index angle) of torsional frequency and rotor thrust [25] . . . . .	14
1.10 Predicted Power for UH-60A in Forward Flight, TEF with trailed vortices, free wake [25] . . . . .	15
1.11 Blade Pitching Comparison . . . . .	16
1.12 Blade Pitching Comparison . . . . .	17
1.13 KMAX Servo Flap Side View [28] . . . . .	20
1.14 KMAX Servo Flap Exploded View [28] . . . . .	20
1.15 Comparison of trailing edge flap deflection for vibration reduction at $\mu = 0.40$ [32] . . . . .	23
1.16 Left: Piezoelectric Crystal Molecule, Right: Piezoplate . . . . .	24
1.17 L-L mechanism for stack actuator stroke amplification [37] . . . . .	26
1.18 Hall and Prechtl Flap Mechanism . . . . .	27
1.19 SMART rotor flap schematic and 2X-Frame . . . . .	28
1.20 SMART rotor hoverstand testing . . . . .	29
1.21 Piezobender with Flexure for Benchtop [50] . . . . .	31
1.22 Fulton's Blade schematic and exploded view picture . . . . .	32
1.23 Roget's Piezobender Flap Schematic . . . . .	33
1.24 Roget's Mach-scale Blade [53] . . . . .	34
1.25 Airfoil Schematic of Flap+Tab System . . . . .	34
1.26 Airfoil Schematic of Flap+Tab System . . . . .	37

1.27	Top:EMA Schematic, Middle: Stand-alone EMA, Bottom: EMA flap assembly in blade [56]	39
1.28	Secondary Cuff mounted between primary cuff and blade root	40
1.29	Brushless DC motor-flap schematic and picture [58]	41
1.30	Motor-flap system Hoverstand results, Mach scale is 2400 RPM [58]	42
1.31	Flap Control Scheme using motor [58]	43
1.32	PAM at no pressure and contracted	44
1.33	a) PAM Cartridge schematic and b.) Blade Flap Schematic [59]	45
1.34	PAM flap system for vacuum chamber	46
2.1	Multilayer piezobender exploded view	53
2.2	Top: Single layer, Bottom: Piezobender Bimorph	53
2.3	Rod-Cusp Concept	54
2.4	Piezoceramic plate, PZT-5H2, Free Strain-Electric Field Loops [35]	55
2.5	Mach Scale Blade Profile	57
2.6	Effect of Length Conceptualization	58
2.7	Required Bender Stiffness vs. Bender Length for range of Flap Aerodynamic Stiffnesses	59
2.8	Flap Driven by Piezobender Schematic	60
2.9	Effect of Hinge Distance on Flap Amplitude	62
2.10	Bender Energy vs. Total Mass including LE Weight Required	63
2.11	Bender Specific Energy vs. Total Mass including LE Weight Required	63
2.12	Flap Angle vs. Total Mass including LE Weight Required	64
2.13	Wiring for 6 layer bender where exposed layers at cantilever are both live	65
2.14	Bender Optimization: 8 vs. 12 Layers, Flap Angle vs. Total Mass	66
2.15	Final Bender, 8-layer	66
2.16	Curie Temperature Measurement	70
2.17	Measuring Bender Stiffness with Parallel Beam	73
2.18	Aluminum beam in jig used to determine cantilever stiffness	73
2.19	Best Case Cantilever Stiffness	74
2.20	Bender Stiffness: Effect of electrical boundary conditions	74
2.21	8-Layer PZT-5H2 Bender	75
2.22	12-Layer PZT-5K4 Bender Stiffness - Poor Bond	76
2.23	12-Layer PZT-5K4 Bender	77
2.24	12-Layer PZT-5K4 Bender Stiffness - Good Bond	78
2.25	Schematic for Charge Amplifier Circuit	79
2.26	Slotted Rod	81
2.27	Manufactured Slotted Rods	81
2.28	Free Strain of a PZT-5H2 10 mil thick plate [66]	83
2.29	Effect of increasing bias on PZT-5K4 Bender Stroke	85

2.30	Bender Relaxation . . . . .	87
2.31	12-Layer PZT-5K4 Bender Compliance for 2Hz Field . . . . .	88
2.32	Commercial PZT-5H2 Bimorph Compliance, No voltage vs. $\pm 3.94kV/cm$ . . . . .	88
2.33	Measuring Single Piezo Plate Stiffness with Electric Field . . . . .	89
2.34	Single Cantilevered PZT-5K4 Plate Stiffness with High DC Electric Field . . . . .	90
2.35	PZT-5K4 Bimorph with No Piezoceramic in Cantilever ('Dead') . . . . .	91
2.36	PZT-5K4 'Dead' Bimorph Stiffness . . . . .	92
2.37	Squarewave Output from 'Dead' Bimorph . . . . .	93
2.38	Close-up of Squarewave Output from 'Dead' Bimorph . . . . .	94
2.39	4-Layer Bender Stiffness with Electrically Separate Cantilever . . . . .	96
2.40	4-Layer Bender Stiffness with Various Cantilever Electrical Fields . . . . .	97
2.41	Bender Relaxation Sequence . . . . .	99
2.42	4-Layer Bender with Dead Cantilever Response to $-3.54kV/cm/+10.63kV/cm$ 0.005Hz Squarewave . . . . .	100
2.43	4-Layer Bender Constrained by Spring . . . . .	100
3.1	Spar in Blade Foam . . . . .	108
3.2	Main Blade Components . . . . .	109
3.3	Flap Assembly Exploded View . . . . .	110
3.4	Flap Assembly Exploded View . . . . .	111
3.5	Flap Free Body Diagram . . . . .	112
3.6	Flap with Overhang Schematic . . . . .	113
3.7	Effect of Overhang: Left: Flap Hinge Moment, Right: Drag [82] . . . . .	113
3.8	Flap Effectiveness vs. Flap Chord . . . . .	115
3.9	Roget TE Flap Setup . . . . .	116
3.10	Radial Bearing (SMR681x) and Thrust Bearing (F2-6c) . . . . .	117
3.11	Flap Mount Drawing . . . . .	119
3.12	Flap Mount . . . . .	119
3.13	Flap Mount Assembly . . . . .	120
3.14	Mass Balancing Positioning . . . . .	121
3.15	Flap Aerodynamic Stiffness . . . . .	122
3.16	Flap Forces . . . . .	122
3.17	Rod-Cusp Schematic . . . . .	124
3.18	Anchor Design . . . . .	124
3.19	University of Maryland Vacuum Chamber . . . . .	125
3.20	Single OB Flap with Overhang, Thrust+Radial Bearings in Vacuum, 38.3 Hz Flap Amplitude driven at $-50V/+150V$ . . . . .	126
3.21	Hoverstand with 2 blades . . . . .	127
3.22	2 Blades . . . . .	128
3.23	Flap Assembly in Blade Close-Up . . . . .	128
3.24	Maximum Bender Strokes at 2 Hz . . . . .	129

3.25	Blade 1 OB Flap Amplitude at 900 RPM . . . . .	130
3.26	Blade 1 Flap Freq Sweep at 900RPM - Fixed Driving Voltage Normalized at 2Hz . . . . .	131
3.27	Initial Soft Pitch Link . . . . .	132
3.28	Blade Pitch Frequency Response to TE Flaps, 900 RPM . . . . .	133
3.29	Left: Steel Radial Ball Bearings, Right: Replaced by all Ceramic Bearings . . . . .	134
3.30	Hall Sensor for Measuring Blade Root Pitching . . . . .	134
3.31	Blade Pitch Frequency Response to TE Flaps with Ceramic Bear- ings, 900 RPM . . . . .	135
4.1	Outboard Flap Amplitude Closed-Loop Control at 900 RPM . . .	138
4.2	Outboard Flap Mean Closed-Loop Control at 900RPM, Constant Amplitude . . . . .	139
4.3	All 4 Flaps on Two Blades Amplitude Closed-Loop Control at 900 RPM . . . . .	139
4.4	All Flaps Mean Closed-Loop Control at 900 RPM . . . . .	140
4.5	Blade 1 Flap Effectiveness . . . . .	141
4.6	Flap Effectiveness for Different Index Angles . . . . .	142
4.7	Blade Pitching at 900 RPM due to TE Flaps . . . . .	144
4.8	Lift Oscillation at 900 RPM due to TE Flaps . . . . .	145
4.9	Hub Force and Moment at 900 RPM due to TE Flaps . . . . .	145
5.1	PMI Test Data during Wind Tunnel Testing . . . . .	150
5.2	Spanwise Distribution of Blade Elastic Twist in Wind Tunnel . .	152
5.3	Basic Concept . . . . .	157
5.4	Beam Finite Element . . . . .	159
5.5	Distributed Wire Sensor in Cantilever Beam . . . . .	161
5.6	Distributed Wire Sensor Validation . . . . .	162
5.7	Rotating Beam Setup . . . . .	164
5.8	Distributed Wire Sensor in Rotating Cantilever Beam . . . . .	166
5.9	Splitting Blade: Beam in Bending + Rod in Torsion . . . . .	171
5.10	Blade Profile Split into Quadrants for Measuring Twist . . . . .	176
5.11	Sawtooth Pattern Required for Sufficiently Large Sensor $\theta$ . . . .	176
5.12	Twist Sensors in Mach Scale Blade Skin . . . . .	179
5.13	Laying Up Sawtooth Pattern - Skin Softness Causes Loss of Wire Tautness . . . . .	180
5.14	Blade Section Twist and Bending With Arbitrary Loading . . . .	182
5.15	Blade Section Bending: Actual vs. Sensor With Arbitrary Loading	182
5.16	Blade Section Twist: Actual vs. Sensor With Arbitrary Loading .	183
5.17	Blade Section Twist and Bending With Arbitrary Loading, Noise, Local Discontinuities . . . . .	183

5.18	Blade Section Bending: Actual vs. Sensor With Arbitrary Loading, Noise, Local Discontinuities . . . . .	184
5.19	Blade Section Twist: Actual vs. Sensor With Arbitrary Loading, Noise, Local Discontinuities . . . . .	185
5.20	Single Point Experimental Setup . . . . .	186
5.21	Calibration Curve for Single Twist Sensor . . . . .	187
5.22	Comparison of Single Twist Sensor to Actual . . . . .	187
5.23	Comparison of Single Twist Sensor to Actual for Small Angles . .	188
5.24	Single Twist Sensor for Small Angles with Motion Capture System	189
6.1	a) Top view of piezoplate with interdigitated electrodes b) Electric field lines between IDEs . . . . .	199
6.2	Electrical field zones in piezoceramic layer with IDEs . . . . .	200
6.3	Modification to allow for flap mean and hinge adjustment for primary control implementation . . . . .	202

# Nomenclature

$c$	Blade chord
$C_d$	Sectional Drag Coefficient
$C_m$	Sectional Moment Coefficient
$C_l$	Sectional Lift Coefficient
$C_{h_f}$	Sectional Flap Hinge Moment Coefficient
$C_{m_{\frac{1}{4}c}}$	Sectional Moment Coefficient about the blade $1\frac{1}{4}c$
AOA	Angle of Attack
CF	Centrifugal Force
CFD	Computational Fluid Dynamics
CG	Center of Gravity
E	Young's Modulus
E-B	Euler-Bernoulli
FM	Flap Mount
HPP	Half peak to peak
IB	Inboard
IBC	Individual Blade Control
ID	Inner Diameter
IDE	Interdigitated Electrodes
LE	Leading Edge
M	Mach number
OB	Outboard
OD	Outer Diameter
OH	Overhang
PID	Proportional Integral Derivative
PMI	Projection Moire Interferometry
psi	pounds per square inch
R	Blade radius
RPM	Revolution Per Minute
SISO	Single Input Single Output
SNR	Signal-to-Noise Ratio
SPL	Soft Pitch Link
TE	Trailing Edge
TEF	Trailing Edge Flap
UMARC	University of Maryland Advanced Rotorcraft Code
$\delta$	Flap angle

$\nu_\theta$	Blade Rotating Torsional Frequency
$\theta$	Blade Root Pitch Angle
$\omega$	Flap Angular Velocity
$\omega_\theta$	Blade Non-Rotating Torsional Frequency

# Chapter 1

## Introduction

### 1.1 Background and Motivation

#### 1.1.1 Background

For a typical helicopter, rotor primary control is achieved by changing the blade root pitch with a swashplate and pitch links. Eliminating the swashplate may lead to a reduction in mechanical complexity and in turn, the parasite drag associated with the swashplate's exposed pushrods and linkages. It would also be beneficial to develop an alternate system that can eliminate the hydraulic system associated with the swashplate. The multiple on-board actuators needed to carry out swashplateless control may also offer redundancy compared to control of a blade through a single pitch link. Elimination of this single point failure mode is a significant driver in the effort to develop a swashplateless rotor [1].

Also, in a swashplateless rotor, an individual blade control (IBC) is achieved, which would have other advantages. The traditional swashplate controlled blade is limited to 1/rev inputs. The rotor blade airflow is highly complex in forward flight, leading to dissimilar loading over the rotor disk. Therefore, the rotor

could benefit greatly from compensatory desired control inputs that minimize dissimilarity. With IBC, the rotor could be actuated at any arbitrary frequency and phasing. This can lead to lower vibration levels, lower noise levels and increased performance in forward flight. Significant work has shown this both analytically and experimentally [2], [3], [4]. An overview of this work more focused on European efforts can be found in Kessler's reviews [5], [6]. From a design perspective, IBC is beneficial because of noise and vibration control regardless of whether any gain in performance is obtained.

Trailing edge flaps offer a way to achieve IBC for primary control as well as lower noise, lower vibration and increase performance. The required actuation power is relatively low as the flaps take advantage of the high dynamic pressure near the blade tips. Thus, only part of the blade needs to be moved instead of the entire blade as for active pitch links and active twist concepts. The purpose of the current work is to demonstrate primary control of a Mach-scale rotor system using trailing edge flaps actuated with piezobenders. The flaps produce a torsional moment, which in turn twists the blade changing the airloads along the blade span. Due to the prohibitive costs of a full scale test, a Mach-scale rotor is constructed that can fit inside the Glenn L. Martin wind tunnel. The work will focus on both the piezobenders used to achieve the required flap deflection and the control authority of the trailing edge flaps in terms of blade response and hub forces and moments generated.

### **1.1.2 Conventional Primary Control**

With one major exception, all helicopters use a swashplate for control. As early as 1788, a swashplate was used to transfer sliding motion between a fixed and

rotating frame in the Watt flyball governor [7]. The swashplate transfers the pilots commands in the fixed (non-rotating frame) to the rotating frame of the blade through bearings (Fig. 1.1). Thrust magnitude depends on the collective pitch of the blades and corresponds to the mean of the blade pitch changing by the swashplate moving vertically. Cyclic input, where the blade pitch changes sinusoidally once per rotor revolution, changes the direction of thrust as well as producing pitch and roll moments. This corresponds to the swashplate tilting.

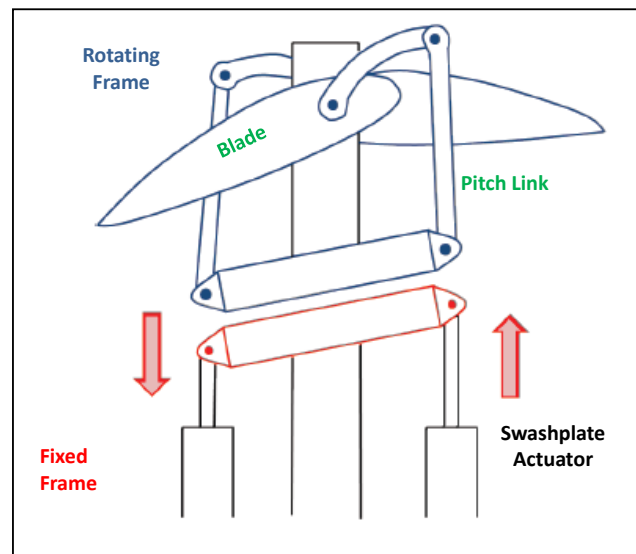


Figure 1.1: Swashplate Diagram

The swashplate must handle the loads produced by the blades necessitating large hydraulic actuators for all but the lightest helicopters. The hydraulic actuators add weight and increase maintenance costs. The swashplate mechanism was invented in the 1920's by Hafner [8] and became the preferred approach for cyclic pitch control in the 1930's [9] and has remained in use since then. In high forward flight, the swashplate is empirically found to cause 17% of the parasitic drag [10], [11]. If an alternative to the swashplate can be used for primary control, then much of this drag penalty and the hydraulic actuators could be

eliminated. The size and complexity of the swashplate is better appreciated by looking at the CH-53 rotor hub both in a close-up and from a distance (Fig. 1.2).



Figure 1.2: CH-53 Rotor Swashplate

A quantitative feel for the savings that could be found in the elimination of the swashplate and especially the hydraulics needed for actuation can be seen in the IBC experimental work done on the UH-60 [12]. Servo-hydraulic IBC actuators were installed in the rotating frame between the swashplate and blade pitch horn in order to provide  $\pm 6^\circ$  at 2/rev decreasing to  $\pm 1.6^\circ$  at 7/rev. To handle the pitch link loads in level flight, the actuators were designed for -4,000 lbf to +2,000 lbf. The actuator was designed for a stroke of 19.5 mm and peak load of 17,800 N. This approach (Fig. 1.3) requires a hydraulic slipring to carry oil at 3000 psi from the fixed frame to the rotating frame at 3.7 Liters/second. Each actuator weights 13.8 kg. Although the whole system is constructed, no weight breakdown for the hydraulics and electronics is given. The system was tested in the NASA Ames 40x80 foot Wind Tunnel. Power reduction of up to 5% for 2/rev IBC inputs at an advance ration  $\mu=0.40$  was observed. Noise reduction was accomplished and rotor imbalance could be eliminated. Actuator performance was not discussed [13]. Primary control for maneuvering flight requires

larger actuator strokes and higher actuator load ratings though everything can be in the fixed frame. However, it adds significant complexity and weight. It requires not only the hydraulic slipring but also an electronic slipring for sending control signals to the rotating frame and receiving blade pitch and actuator data from the rotating frame. The pitch link is also a single point failure and so the actuator, as it is also the pitch link, must be oversized in order to avoid any chance of failure.

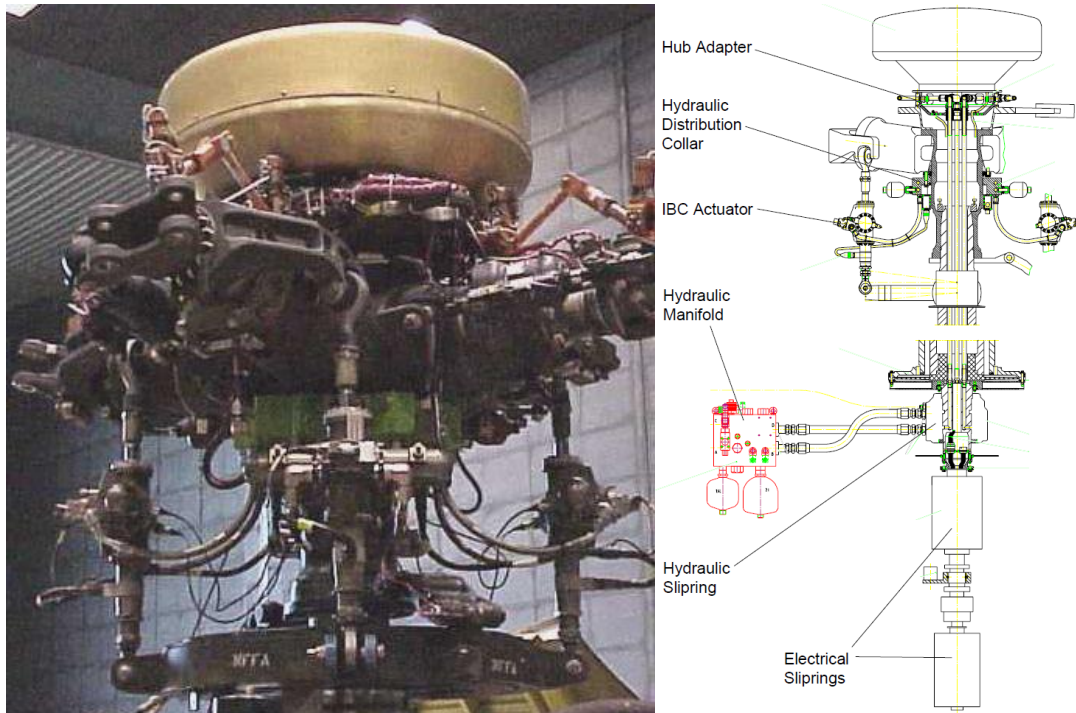


Figure 1.3: UH-60 IBC

Higher harmonic control (HHC) is not an individual blade control (IBC). The issue of actuation in the rotating frame can be avoided. DLR, the German Aerospace Center, has developed a multiple swashplate control system, META (Fig. 1.4). 3-bladed rotors can have HHC with a single swashplate as long as sufficient power is available to actuate the swashplate at the desired frequency.

This is because the swashplate has three degree-of-freedom opposed to three blade pitch angles. For more than 3 blades, more degrees-of-freedom are required and hence more swashplates which is what DLR has examined. A control methodology is developed in order to determine the swashplate motions needed to produce arbitrary blade motions. Electrohydraulic actuators are used to drive the swashplates. The system can provide  $19^\circ$  of collective,  $12^\circ$  of blade cyclic pitch at 1/rev and an additional  $4^\circ$  of higher frequency motion. This system is very complex and requires large fixed frame actuators (Fig. 1.5). Instead a move towards the elimination of the swashplate system, this is an addition to the swashplate system. Its main advantage is that electrohydraulic actuators have been proven and do not suffer from the increased rotor blade complexity of on blade actuators and hydraulic sliprings nor the durability issues of on blade actuators such as piezoelectrics [14]. So, like the blade root actuators, this system adds complexity, weight and requires high power. For all these reasons, much work has been done with on-blade actuators near the blade tip where the actuation force is low due the high dynamic pressure.

### **1.1.3 Swashplateless Concept**

On blade actuators can change the airfoil shape (discretely or continuously) producing aerodynamic torsional moments that in turn change the blade elastic twist distribution in order to control the helicopter. The general trend for rotorcraft is to place actuators on the blade to change the airloads to reduce noise and vibration at their source and increase performance of the rotor system in forward flight. To affect these, the blade needs to generate forces at multiple rotor harmonics. For example, for a 4-bladed rotor, the blades need to be excited

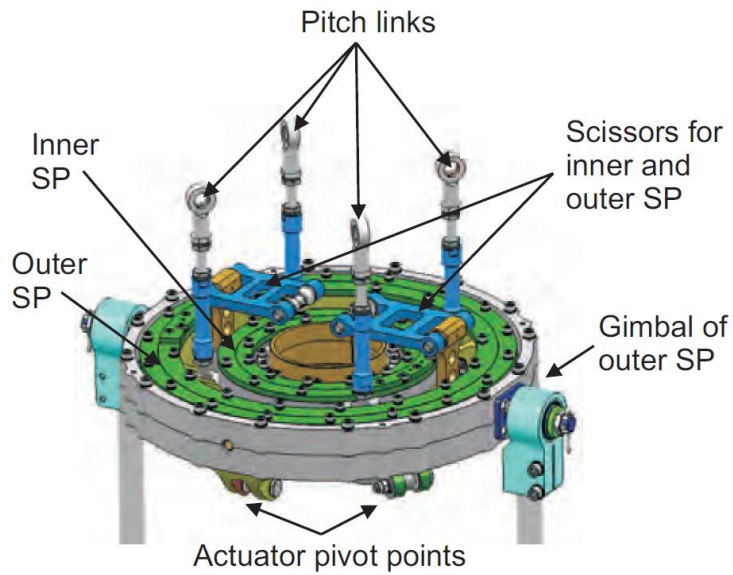


Figure 1.4: Multiple Swashplate (SP) Mechanism

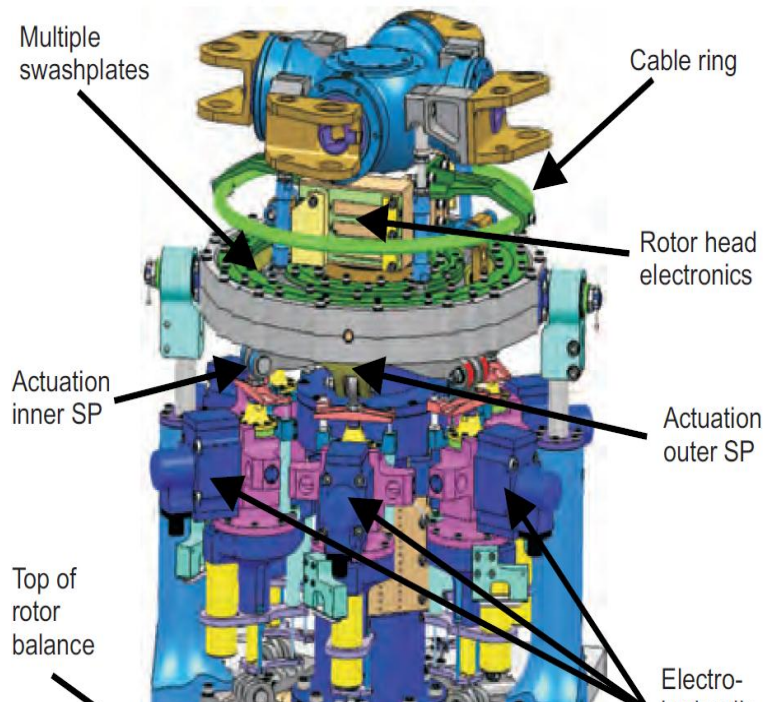


Figure 1.5: META mechanism diagram including actuators

at 2/rev for performance enhancement, 3, 4, and 5/rev for vibration minimization and at high frequencies for noise suppression. If the actuators' bandwidth is extended to 1/rev and DC, this would allow for primary control of the rotor system as well, thus allowing for the elimination of the swashplate. One approach can be to incorporate smart material actuators. These actuators are compact, lightweight and do not require a hydraulic slipring compared to actuators at the blade root.

On blade actuators have been tested experimentally that could be used for primary control. Chen [15] tested a Froude scale rotor with embedded piezoceramic elements placed at  $\pm 45^\circ$  respectively at the top and bottom surfaces with respect to the blade elastic axis. The blade twisted  $0.5^\circ$  at the tip which is found adequate for vibration control. A collaborative NASA/Army/MIT concept with embedded active composite fibers (ACF) and active twist implemented on a four-bladed rotor was built and tested in the NASA Langley Transonic Dynamics Tunnel. Active fiber composites actuators were embedded in the D-spar for torsional control. Blade tip twist of  $1.5^\circ$  was achieved. The actuators demonstrated robustness over 40 hours of testing [16], [17], [18]. Primary control requires significantly more blade twisting and this was outside the scope of this investigation.

## 1.2 Trailing Edge Flaps for Primary Control Analysis

### 1.2.1 Simple Aeroelastic Model

Significant analytical work has shown how to achieve primary control through integrated trailing edge flaps on the rotor blades. Integrated trailing edge flaps do not extend beyond the blade chord. When the flaps are deflected, an aerodynamic pitching moment is produced. This moment twists the blade changing the forces on the blade. Ormiston [19] used a simple aeroelastic model to examine the concept. His model used rigid blades, quasi-steady thin airfoil aerodynamics and uniform inflow. There were two main conclusions from the study. First, the blade stiffness should be reduced so that the fundamental torsion frequency should be between 1.5/rev and 2.5/rev. The lower torsional stiffness decreases the elevator reversal speed where the lift due to the flap becomes less than the lift change due to the blade twisting. Secondly, the blade index angle, or pre-collective, needs to be properly chosen to reduce the flap collective angle needed to trim the rotor. This reduces the actuation power and ensures that the flap operates in its drag bucket limiting the profile penalty of the flaps.

Ormiston kept the blade structural torsional stiffness unchanged and replaced the rigid pitch link with a soft pitch link to lower torsional stiffness. This is the chosen experimental method for this project. Making a blade that is soft in torsion adds an unnecessary level of complexity for initial analysis and experimentation. However, for a production helicopter, this would be unacceptable as the hub would still have exposed pitch links and so the drag penalty in forward flight would remain.

### 1.2.2 Refined Models

Several people have developed more refined analytical models than Ormiston for using trailing edge flaps for primary control. They all take a conventional rotor and replace the rigid pitch link with a soft pitch link to reduce the torsional stiffness. Shen carried out an in-depth numerical investigation of trailing edge flaps for swashplateless primary control using the University of Maryland Advanced Rotorcraft Code, UMARC [20]. Shen looked at eliminating the swashplate for a variety of helicopters: an ultralight teetering rotor, the bearingless McDonnell-Douglas Advance Rotor Technology (MDART) rotor and a heavy utility rotor. The aerodynamic model used thin airfoil theory with an unsteady model for flaps without aerodynamic balance. Flap drag was derived from the unsteady model. For the ultralight helicopter, the torsional frequency remained unchanged from the swashplate to the swashplateless design at 2.2/rev. For a blade index angle of  $18^\circ$ , the flap collective plus cyclic deflections were less than  $\pm 5^\circ$  in order to trim over a range of flight speeds to  $\mu = 0.18$ . The blade pitch angles for the swashplateless and conventional rotor were found to be the same [21].

For the MDART rotor, the model without trailing edge flaps was validated with wind-tunnel test data. A multicyclic controller for the flaps provided vibration and primary control simultaneously for a rotor with a torsional frequency of 2.1/rev. With a blade index angle of  $16^\circ$ , the half peak-to-peak values of flap deflections were below  $6^\circ$  and the mean values were below  $5^\circ$ . Flap aerodynamic balance is used to minimize flap actuation power. Overhang means that the flap hinge is behind its leading edge. At  $\mu = 0.2$ , the rotor was trimmed and vibratory hub loads reduced by 83% with flap deflections between just  $2^\circ$  to  $6^\circ$  [22].

Table 1.1: UH-60 Rotor Properties

<b>Property</b>	<b>Value</b>
Rotor Radius	26.8 ft.
Chord	20.76/20.965 in.
Thickness, %chord	9.5.4
Rotor Speed	258 RPM
Tip Speed	725ft/sec
Solidity	0.0826
Lock Number	8
Gross Weight	19,000 lbs
Root Cutout	14%
Twist Angle	-18°
Torsional Frequency	4.0/rev

Shen also looked at the UH-60 articulated 4-blade rotor system. The UH-60 helicopter rotor properties are shown in Table 1.5 [23], [24]. The present work is based upon this rotor system as Falls [25] also looked at UH-60 swashplateless rotor performance. Thus, a complete body of analytical work on a swashplateless rotor exists for the UH-60A.

For Shen’s UH-60 swashplateless work, the torsional frequency was reduced to 1.9/rev. The flaps were optimized for minimum actuation moment and power. The optimized flap resulted in a length of 28%R, chord ratio of 15%c centered at 80%R with an overhang of 5%c. Overhang is found to greatly reduce actuation power and hinge moment because the hinge arm of the flap lift is reduced. It is found that if flap overhang is increased beyond a certain amount, the actuation moment and power begin to increase again. The flap control angles are insensitive to flap chord but decrease with flap span. Actuation power and moment increase with increasing flap chord and decrease significantly with increasing flap span. The dramatic effect of index angle is clearly seen in Fig. 1.6. The flap half peak-peak flap requirement was 7.1° for primary control and 4.7° for vibration

control for a total of  $11.8^\circ$ . Actuation power for the 4-bladed rotor for primary control was 0.8 HP with no power given for the addition of vibration control [26].

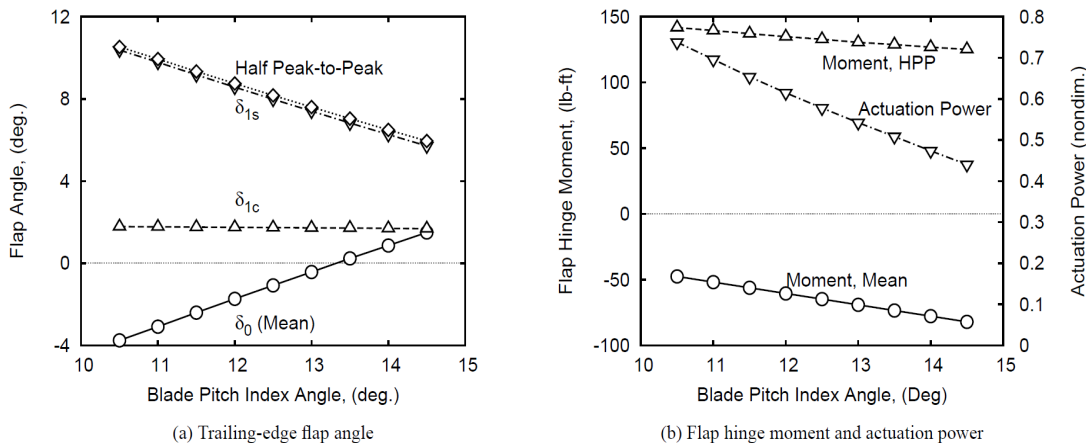


Figure 1.6: Effect of Index Angle on flap control angles, actuation power and moment, Flap overhang of  $0.05c$  and  $\mu = 0.32$  [26]

Falls also looked at the UH-60A rotor system for primary control with trailing edge flaps [25]. The basic rotor system is unchanged except for the addition of a trailing edge flaps and the reduction of the pitch link stiffness. The flaps were optimized for minimum actuator power and moment requirements. Two different aerodynamic models were used in the analysis, a quasi-steady thin airfoil theory and unsteady lifting line model with airfoil table lookup. The table lookup was based on wind tunnel test data and CFD. This allows for an accurate assessment of swashplateless rotor power. The conventionally controlled UH-60A rotor model was validated with data from the UH-60A Flight Test Program with excellent correlation for rotor power in hover and forward flight (Fig. 1.7). A free wake model was used with trailed vortices added at the inboard and outboard edges of the trailing edge flaps.

The full vehicle can be trimmed with the swashplateless rotor over the range of forward flight speed to  $\mu=0.30$  with a torsional frequency of  $2.0/\text{rev}$ . Beyond

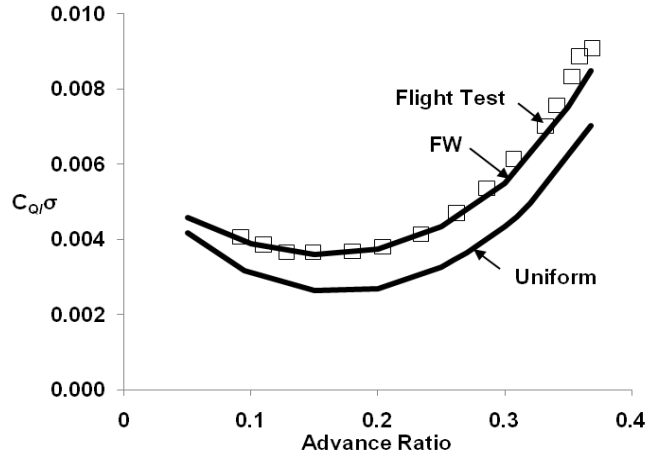


Figure 1.7: Predicted and Measured Power for UH-60A in Forward Flight,  $C_W/\sigma=0.0783$  (FW: free wake, Uniform: uniform inflow) [25]

this advance ratio, trim solutions are difficult to obtain. The index angle is the non-rotating collective pitch of the blade. The required index angle increases over the range of thrust and advance ratios as the torsional frequency is reduced while the rotor shaft angles are unchanged. The analysis visualizes a swashplate changing the blade collective and cyclic pitch with a soft pitch link in between the blade pitch horn and swashplate. When the blade is rotating, it twists downward both at the pitch link and in the blade structurally in response to inertial and aerodynamic loads. The downward twist increases as torsion frequency decreases thus requiring higher index angles. This is seen in the difference in the blade elastic tip twist angle (Fig. 1.8).

The index angle to trim the rotor rapidly increases as the torsional frequency reduces to 2.0/rev or as the thrust increases (Fig. 1.9). If the index angle is properly set, then trailing edge flaps do not have to change the blade collective but only provide cyclic pitching. For this study, the blade index angle is set by looking at a high advance ratio and thrust condition and then leaving it at the same angle for other flight conditions so the index angle is optimal for only one

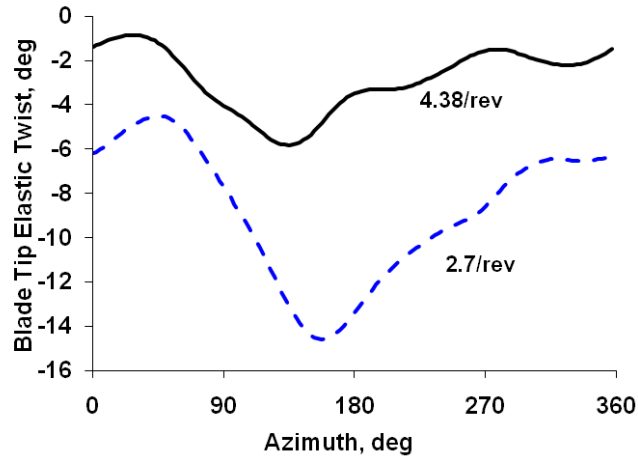


Figure 1.8: Effect on blade elastic twist angle of lowering torsional frequency [25]

flight condition.

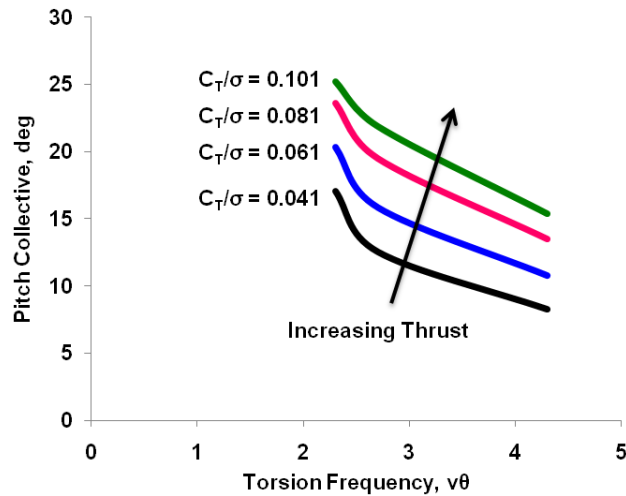


Figure 1.9: Effect on non-rotating blade collective (Index angle) of torsional frequency and rotor thrust [25]

The trailing edge flap chosen for performance studies on each blade is  $0.15c$  without aerodynamic balance and spans  $0.40R$ . The mean trailing edge flap deflections are  $-3^\circ$  to  $-9^\circ$  and the half peak-to-peak (HPP) flap deflections range from  $4^\circ$  to  $11^\circ$ . Until  $\mu=0.25$ , the swashplateless rotor requires less power than

the conventional rotor (Fig. 1.10). The change in power relative to the conventional rotor is because the trailing edge flaps in combination with blade twisting at a low torsional frequency redistribute lift and drag about the rotor disk. An index angle of  $15^\circ$  minimized the required TEF deflections. This is the highest index angle for which the rotor could be trimmed over a range of advance ratios. Blade divergence limited the maximum index angle and it was unclear if this was due to a numerical or physical issue. In hover, the swashplateless rotor requires less power than the conventional for a limited range of thrust. However, beyond the thrust where maximum figure of merit is reached for the swashplateless, the swashplateless rotor power increases rapidly compared to the conventional rotor. All of this analyses assumes no reduction in flat plate area for the helicopter. If the elimination of the swashplate leads to lower profile drag, then the swashplateless system would compare better to the conventional rotor system [25].

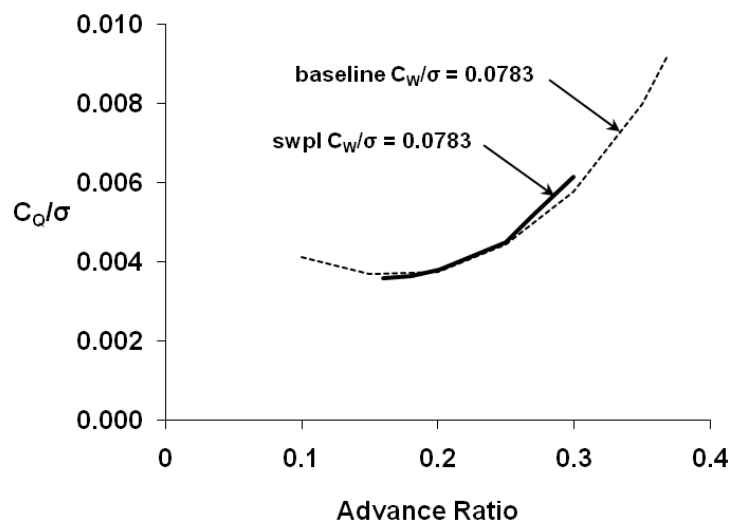


Figure 1.10: Predicted Power for UH-60A in Forward Flight, TEF with trailed vortices, free wake [25]

Falls also provided angle of attack components for the trimmed rotor (conventional and swashplateless with  $15^\circ$  index angle) in two flight conditions: transition and high speed forward flight, both of which are demanding for the rotor. An experimental confirmation would demonstrate blade root pitching with this analysis providing an idea of the blade root pitching required. So, the blade pitch angle at  $0.75R$  was condensed (Fig. 1.11). The blade pitch angle consists of the swashplate input, the tip twist of the blade (same for conventional and swashplateless) and the pitch angle due to deformation of the blade pitch link. The blade has no elastic twist beyond the pitch link.

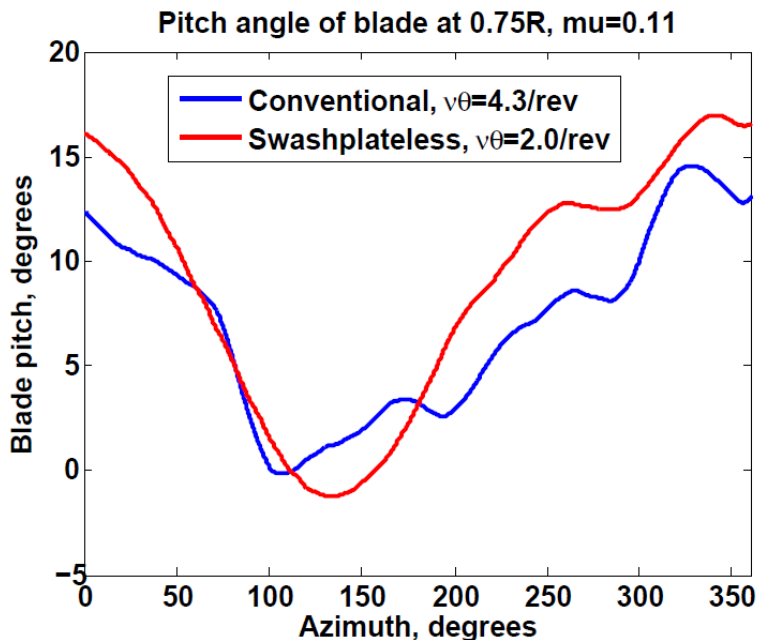


Figure 1.11: Blade Pitching Comparison

For  $\mu = 0.11$ , the swashplateless rotor pitches cyclically more than the conventional rotor. However, for a higher advance ratio of  $\mu = 0.30$  (Fig. 1.12), the conventional rotor pitches cyclically less than the swashplateless rotor. Half peak-to-peak blade pitching of  $9.12^\circ$  with a mean of  $8.79^\circ$  is sufficient for rotor trim at both advance ratios. The swashplateless rotor has a large 2/rev pitching

due to its torsional frequency. If just the required 1/rev is examined, HPP blade pitching of  $8.07^\circ$  is sufficient for rotor trim at both advance ratios.

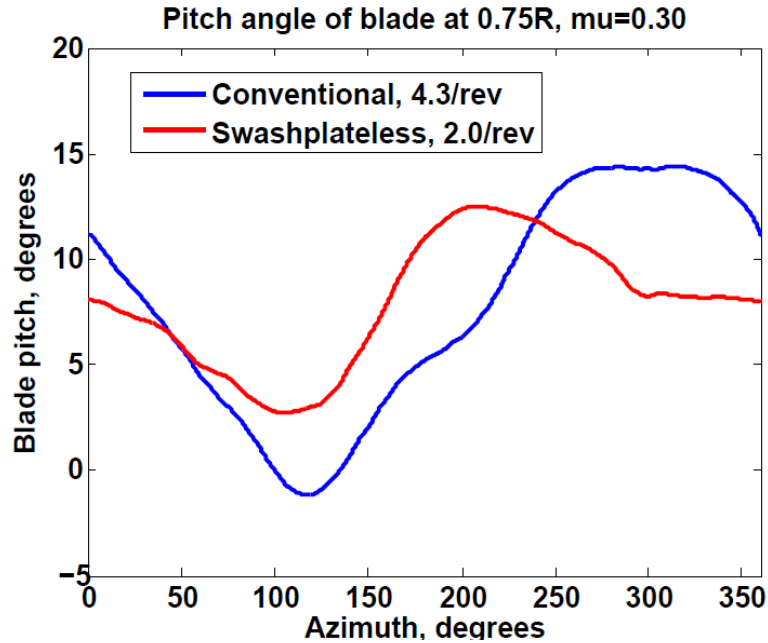


Figure 1.12: Blade Pitching Comparison

### 1.2.3 Analysis Summary

First, the torsional frequency of the blade must be reduced to about 2.0/rev to achieve with the flaps enough blade twist control authority. Secondly, flap sizing optimization greatly reduces actuation power. Third, a high index angle of greater than  $15^\circ$  is required. The above works showed that the actuation power reduced with higher index angle until an optimum value is reached. Fourth, the promise of the swashplateless system is seen in that up to moderate advance ratios, the swashplateless rotor draws less power than the conventional and the power penalty beyond that is small. So, the profile drag reduction due to the elimination of the swashplate will result in a significant reduction in profile drag.

Also, the flaps can simultaneously provide both primary and vibration control with moderate flap angles.

Several issues need to be pointed out about the analysis. First, the fundamental torsional frequency of the blade is

$$\nu_{\theta} = \sqrt{\frac{K_{\theta}}{I_b}} \quad (1.1)$$

The analytical work did not attempt to determine the change in blade torsional inertia due to adding a TE flap actuation system. However, the blade inertia will increase significantly because the flap actuator and flap with its support will add weight close to the trailing edge of the blade, which will also require leading edge weight to keep the blade CG at the quarter-chord. This will lower the torsional frequency even if the torsional stiffness is unchanged. All the analysis looks at lowering the torsional frequency to 1.9/rev to 2.1/rev for the rotor blade and does so by replacing the rigid pitch link with a linear spring while assuming the blade inertia remains unchanged. If the torsional frequency is reduced from 4.0/rev to 2.0/rev, this implies a reduction in stiffness by a factor of 4 while the inertia remains unchanged. If instead, the blade inertia is doubled, then the torsional frequency will be 1.41/rev.

Replacing the rigid pitch link with a linear spring or soft pitch link will require some kind of disc in the rotating frame to support this. Thus, the swashplate still remains and the soft pitch link will most likely be larger than the rigid pitch link in order to provide stiffness without friction in the rotating frame. A solution is to reduce the blade GJ or structural torsional stiffness. This leads to the TE flaps causing a change in twist distribution over the blade span instead of the entire blade pitch changing. This is a different analytical problem than

that discussed previously.

Third, although index angle has been shown to be very important, more analytical work is needed on variable index angle. Often, the most extreme trimmed flight condition is examined for system optimization. This is the highest advance ratio for the rotor system and from this the index angle is chosen. This is the first problem to solve but after this, what is the penalty in other flight conditions for choosing this fixed index angle. If the penalty is large enough, it may warrant an investigation into a different index angle.

### **1.3 Kaman helicopters**

It is important to look at the only operational helicopter using flaps for primary control. Kaman Aerospace Corporation has built servo-flap rotors since 1948 [27]. A servo-flap is an airfoil behind the blade trailing edge, which when deflected produces lift, in turn causing a large moment arm to twist the blade. Pilot commands are mechanically transferred through the swashplate outboard through the blade to the flap. The high aerodynamic pressure at the flap and large moment arm mean that no hydraulic actuation is needed. The KMAX helicopter has a gross weight with external load of 11,100 lbs. with two 48'2" diameter intermeshing main rotor blades. The servo flap is centered at 75%R with length 16%R. The flap chord is 53.9% of blade chord, but there is a 9.1% blade chord gap between the blade trailing edge and flap leading edge (Fig. 1.13). So, the total flap including the gap is 63.1% of blade chord providing a very large moment arm to induce blade twisting. The flap is driven by a push-pull rod at an offset from the flap hinge. The exploded view (Fig. 1.14) shows the mechanism and all the parts protruding into the flow.

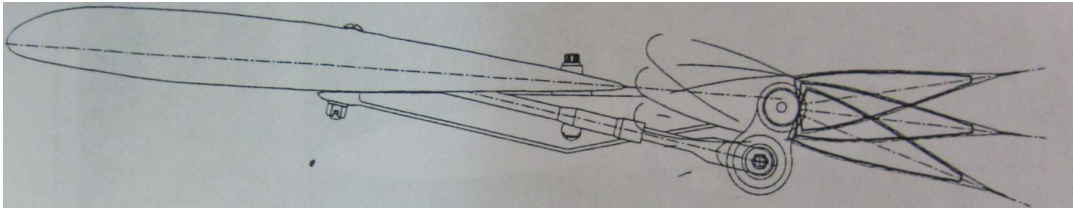


Figure 1.13: KMAX Servo Flap Side View [28]

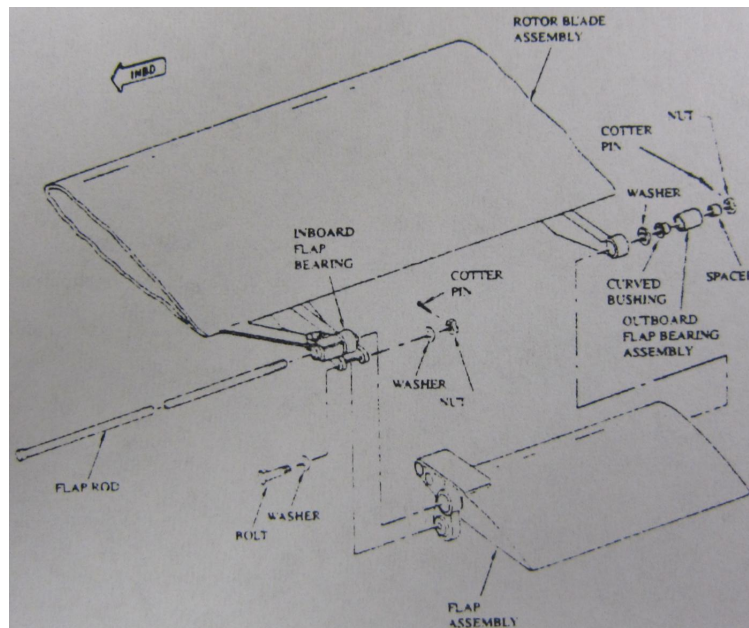


Figure 1.14: KMAX Servo Flap Exploded View [28]

This design leads to a large drag penalty, which Kaman has looked into reducing by integrating the servoflap section into the blade profile. This was done by increasing the blade chord and thickness and keeping the flap mechanism and dimensions the same. Wind tunnel testing for a 1/3 model scale looked at the performance of the new blade section but no further work was done [28]. Kaman looked at reducing the torsional frequency to 1.2/rev to limit the flap size or flap angles required for the integrated flap due to its small moment arm. This low torsional frequency can lead to many stability problems arising from cross coupling between flapping, lead-lagging and feathering motions. The integrated flap leads to a lighter blade as less leading edge weight is required to keep the blade chordwise center of gravity ahead of the  $\frac{1}{4}c$ . Kaman has no immediate plans to continue with this work for a commercial helicopter as a complete redesign of the blade would be required [29]. Wei also looked at blade indexing that could be changed in-flight allowing the blade to operate closer to its optimum index angle at all times though how exactly this could be done was not discussed. Performance improvements in hover and reduced vibration in high speed forward flight are possible due to the required flap collective being reduced [30].

Therefore, to eliminate the swashplate, trailing edge flaps appear appropriate. Taking advantage of the high dynamic pressure at the blade tip leads to small, low-power actuators when compared to actuation in the fixed frame or at the root of the blade. Significant analytical work has shown that the performance of the swashplateless rotor with TE flaps to be similar to the conventional rotor. The flap actuation power is minimized by properly choosing the flap dimensions, lowering the torsional stiffness and choosing the proper index angle. Also, Kaman successfully used helicopters with servoflaps for primary control for many years. The next step should be to demonstrate primary rotor control through integrated

TE flaps.

## 1.4 Mach Scale

In order to demonstrate a swashplateless rotor, a Mach scale rotor is chosen, because the cost in time and money of a full scale rotor test is prohibitive. The high cost leads to a limited test where the initial design is not easily changed so that lessons learned during initial testing cannot be expanded. When a scaled test is chosen, Mach scaling is selected so that the experiment has the same aerodynamics as the full-scale as the advance ratio is the same and the local rotor flow going beyond the critical Mach number is not a problem [31]. Friedmann looked specifically at the scaling issues for an offset hinged, spring restrained model of a helicopter blade and found 17 parameters that need to be matched. For vibration control, the TE flap motion required for vibration control is different for Froude and Mach scale rotors (Fig. 1.15). Results from vibration reduction tests with active rotor blades demonstrate that Mach scale rotors give the correct actuation requirements for actively controlled flaps for full-scale rotors [32]. The rotor diameter for our project is limited by the dimensions of the the test section of the Glenn L. Martin Wind Tunnel. To match the tip speed of the UH-60, this represents an approximately 1/10th scale rotor requiring an RPM of 2400.

There are issues related to Mach scale rotors too. Whereas a normal helicopter blade sees up to 700 g's, a Mach scale rotor will see greater than 4500 g's. This means that a flap weighing 5 grams near the blade tip sees a centrifugal force of 48 lbs. While this force scales down with  $R$ , the area available to handle forces scales down by  $R^2$ . This means friction at flap hinges is a major

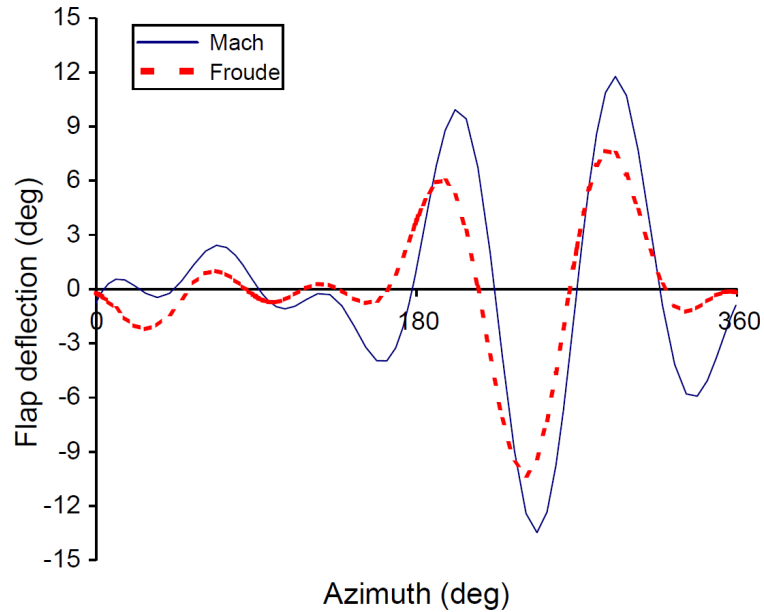


Figure 1.15: Comparison of trailing edge flap deflection for vibration reduction at  $\mu = 0.40$  [32]

problem in Mach scale rotors. In addition, there is not enough space to secure the flap assembly to the blade with screws. So, blade parts must be bonded together. The strength of bonds is determined by the bond surface area. The surface area available to create strong bonds scales down by  $1/R$ , thus causing many problems in making Mach scale blades. For handling the large loads, it is also useful to think in terms of volume available. More volume means more stiffness and as such, more material is available to handle the loads. The ratio of volume and stiffness to loads scales down by  $1/R$ . Also, for the same absolute machining tolerances, the relative tolerance will be larger as the scale decreases. For example, a gap between the flap and blade may be 50 mils for both the full scale and Mach scale but this is a 1.6% gap for the Mach scale and 0.24% gap for the full scale. So, Mach scale rotors have problems with friction, securing the blade together, making stiff enough parts and having sufficiently small gaps between moving parts such as the TE flap.

## 1.5 Trailing Edge Flap Actuators

Work abounds with trailing edge flaps used to alter the blade aerodynamics both at full scale and model scale for control of vibration, noise and performance. A flap actuator must meet several requirements. It must have sufficient bandwidth, low power requirements, light weight and compact size in order to fit inside the blade profile. Three main actuation methods for trailing edge flaps have been studied that meet these requirements: piezoelectric actuators and more recently, electric motors and pneumatic artificial muscles (PAM).

### 1.5.1 Introduction to Piezo Actuators

Piezoelectrics undergo deformation when an electric field is applied and conversely generate an electric field when a stress is applied. Their high stiffness and strain make them attractive for actuators. Fig. 1.16 shows a typical piezoelectric crystal as well as the direction labels for a piezo plate element. The plate 3 direction is the poling direction.

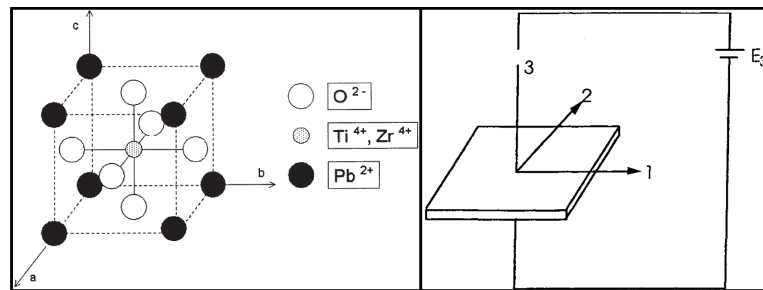


Figure 1.16: Left: Piezoelectric Crystal Molecule, Right: Piezoplate

Many surveys deal specifically with the application of piezo material actuators in rotorcraft applications. Chopra's review of smart structures is appropriately used as the starting point in applying piezoelectrics to rotorcraft problems [33]. Giurgiutiu also looks at smart material applications to rotorcraft

problems [34]. Distributed induced-strain actuation has come at odds with the high inherent stiffness of rotor blades and so experimental results with induced strain blade twisting have been less impressive. A multidisciplinary optimization approach that accounts for reducing the blade stiffness could yield a more successful design. Discrete actuation (usually trailing edge flaps) have been more successful in part because the blade design need not be considered, but instead the blade can be retrofitted. Both reviews consider the development of compact on-board power amplifiers designed specifically for the large reactive power requirement of piezoelectric systems as crucial. Chopra provides a basic circuit theory [33]. Sirohi [35] introduces the fundamental behavior of piezoceramic individual plates for a range of load environments. Using 10 mil thick sheets of PZT-5H2, a formulation was developed for electrical power consumption. The strain properties were not effected by tensile in plane stresses up to 2500 psi, thus showing promise for the CF environment of the rotating helicopter blade. Two types of actuators have been developed from piezoceramic plates: piezostacks and piezobenders.

### **1.5.2 Piezostacks**

Piezostacks consist of many piezolayers bonded together utilizing the  $d_{33}$  effect. This is the most energetic piezoelectric mode - the other direction strain effects are less than half of  $d_{33}$ . Many commercial piezostacks are available. These have been used for full scale blade sections for benchtop testing and 2-D wind tunnel testing. These have also been the choice to actuate TE flaps tested in full-size helicopters both in the wind-tunnel and in-flight. All experimental tests use commercial piezostacks. Lee examined 12 different piezostacks for their perfor-

mance with both external preload and static/dynamic excitation [36]. External preload can improve strain performance.

Lee and Chopra built a model of a blade section with length 12 in. and chord 12 in. with a TE flap of span 4 in. and 25% chord. The flap was actuated with piezostacks in conjunction with a double-lever (L-L) amplification mechanism. Figure 1.17 shows the mechanism. Multistage amplification is used to increase the very small stack stroke. The mechanism needed to use the stack actuator is significantly larger than the actuator itself. The mechanism must be heavy in order to have lever arms with large enough stiffnesses to limit losses due to elastic deflection of the lever arms [37].

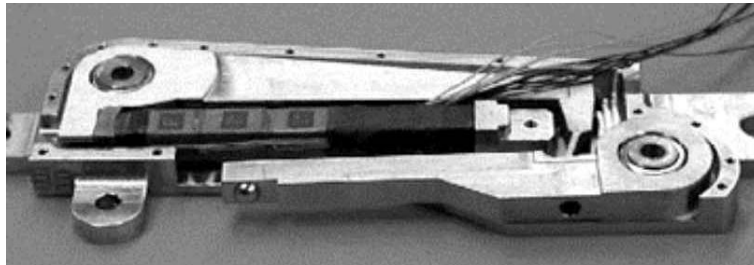


Figure 1.17: L-L mechanism for stack actuator stroke amplification [37]

This model was tested in a vacuum chamber to simulate full-scale CF (600g) and provided the desired amplification of 20x stroke. In an open-jet wind tunnel test,  $\pm 10^\circ$  at 120 ft/s was obtained.

Hall and Prechtl built a 1/6th Mach-scale CH-47D rotor with trailing edge flaps actuated by X-frame actuators (Fig. 1.18) [38]. Flap deflections of  $\pm 2.4^\circ$  were achieved on the hoverstand. A pair of commercial piezoceramic stacks (for bidirectional flap control capability), each with 140 layers (layer thickness of 22.1 mils) were utilized. This 3.1 in. long actuator had a stroke of 81 mils up to 200 Hz and a blocked force of 35.8 lb. A control rod and reaction tube are used with a flap horn to convert the X-frame output to flap motion. Hover tests showed

4° HPP deflection.

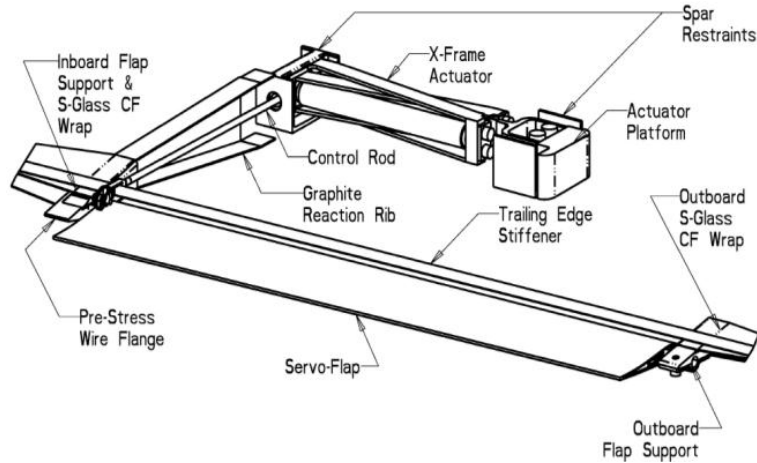


Figure 1.18: Hall and Prechtl Flap Mechanism

Under the DARPA sponsored Smart Material Actuated Rotor Technology (SMART) program, a Boeing MD900 rotor system was fitted with TE flaps for vibration and noise control. Straub, et. al carefully justified the use of TE flaps actuated by piezoelectrics [39], [40], [41]. The 5-bladed rotor is composite and bearingless with a 34 ft. diameter with one flap per blade and torsional frequency of 5.8/rev. Each flap has 0.24% $c$  chord, 18% $R$  span with 40% flap chord overhang. The flap parameters were chosen to minimize flap actuation requirements. The flap had both aerodynamic and mass balancing to lower the actuation force required. A key constraint to the project was to use the production blade tooling with only minor modifications. So, the actuator was carried inside the spar cavity with a short link connecting the actuator and flap. This reduces the amount of weight added behind the blade  $\frac{1}{4}c$  and so limits the LE weight required to balance the flap system.

Piezoelectric stack actuators were chosen with stroke amplification by 2 X-frame mechanisms actuated 180 deg out of phase in a push-pull mode (Fig. 1.19). The final 2X-frame actuator mechanism (after stroke amplification), had

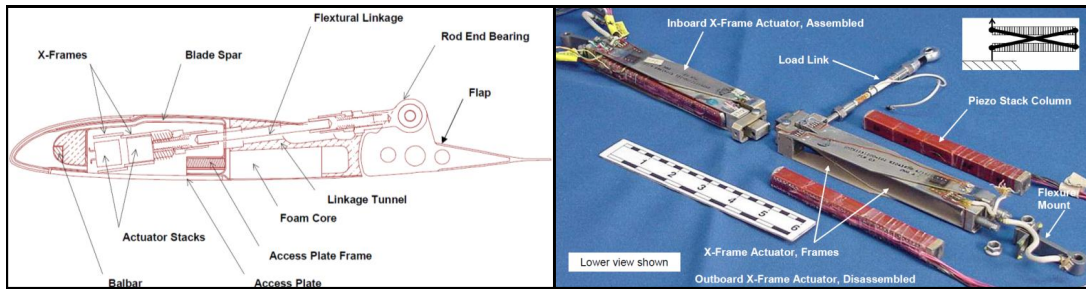


Figure 1.19: SMART rotor flap schematic and 2X-Frame

a blocked force of 113 lb, stroke of 0.081 in. and weighed 2.16 lb. A switching power amplifier was designed to drive the stack which used IGBT (Insulated Gate Bipolar Transistor) switching at 20 kHz and capacitive energy storage for efficient actuation. 66 million cycles were accumulated on the benchtop corresponding to 560 hours of operation at 4/rev demonstrating the maturity of piezoelectric actuators. At full RPM (Fig. 1.20), flap deflection amplitudes of  $2.8^\circ$  at 1/rev (6.35Hz) was obtained at  $\pm 450\text{V}$ , but the actuator is rated for  $\pm 725\text{V}$ . This provided lift authority of 10% of total lift so the system is sufficient for vibration and noise control [42]. However, the required flap deflection is higher for primary control. Wind tunnel testing has also been carried out up to at least 155 knots with large noise and vibration reduction demonstrated due to the flaps. The reliability of the actuation system was successfully proven in more than 60 hours of wind tunnel testing [43], [44].

Eurocopter has also implemented TE flaps on the BK117 rotor system in-flight with piezostack actuation. The blade torsional frequency was reduced from 4.3/rev to 3.5/rev in order to increase the servo-effect of the flap. Vibration reduction was shown over the entire speed range [5], [45].

JAXA (Japan) and NASA have the Novel Intelligent JAXA Active Rotor. The NINJA rotor has four articulated blades with a 19 ft. radius and 1.3 ft.

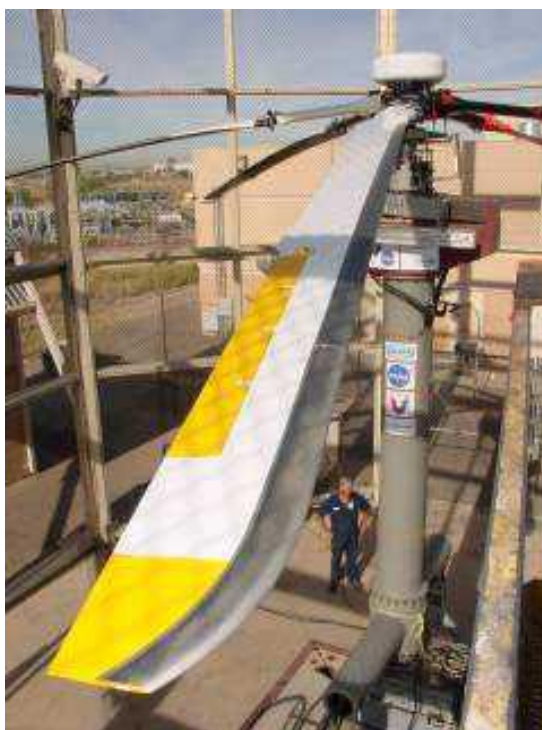


Figure 1.20: SMART rotor hoverstand testing

chord. The flap is 10%R centered at 75%R with a chord of 10%c and is sized for vibration and noise control. Hoverstand testing is planned for 2013 and wind tunnel testing is planned in the NFAC 40x80Ft wind tunnel at Ames Research Center in 2015 with the goal of acquiring a high fidelity data set of blade pressures. The flap system appears to be similar to the SMART rotor with 2 stack actuators operating a push-pull mechanism with a single lever for stroke amplification attached to a linkage extending to the TE flap [46].

All of the full scale testing with piezoelectrics driving trailing edge flaps have used piezostacks. This allows the  $d_{33}$  effect to be used and actuators with very large force and very small stroke are implemented. They have been successfully used to reduce vibration and noise on the benchtop, wind tunnel and even in-flight. The high piezostack bandwidth allows the design of TE flap system that

could carry out primary control, noise reduction, performance enhancement and vibration control. The difficulty in piezostacks is not the actuator but design of an efficient mechanism to amplify the small actuator stroke into sufficient flap stroke. This motivates the use of piezobenders in an effort to improve actuator stroke without needing significant lever amplification.

### 1.5.3 Piezobenders

A piezobender consists of piezoelectric plates bonded together. The actuator plates above and below the neutral axis have opposing strains that produces a bending moment that causes the bender tip to move. Strain is produced via the  $d_{31}$  effect which is less than  $\frac{1}{2}$  of the  $d_{33}$  effect. This leads to less than  $\frac{1}{4}$  the energy density of the  $d_{33}$  piezostacks. However, their relatively large stroke means that only one hinge is required to convert the piezo output to flap angular deflection. This is in comparison to a stack actuator that requires a complex heavy inefficient mechanism to increase the piezo stroke.

Spangler and Hall first proposed a piezoelectric bender (bimorph) to fit inside a blade profile (4.45 inch chord for Froude scale rotor, RC410 airfoil with 10% thickness) to drive a trailing edge flap [47], [48]. The bimorph was cantilevered at the spar and drove the flap with a mechanical linkage. Testing was carried out in the wind tunnel on a fixed wing section and significant flap deflection and force authority were demonstrated. However, effectiveness was limited by hinge friction and backlash in the flap linkage. So, Hall and Prechtl [49] improved the design with a multilayer bender instead of a bimorph and a flexure instead of a hinge to convert the bender motion to flap rotation. An 8-layer tapered bender of length 2.5 inches and width 1.5 inches was assembled from PZT-5A

wafers consisting of 7.5 mil thick piezoceramic sandwiched between 1 mil nickel electrodes. Arcing limited the maximum electric field to 40V/mil and a bias voltage was used so that the piezo was driven to its arcing limit in one direction and to its depoling limit in the other direction. Figure 1.21 shows the flexure mechanism. The flexure's additional stiffness was limited by design to less than 10% of the flap aerodynamic stiffness. The effective hinge from the flexure was chosen in order to match the flap external impedance to maximize the amount of energy from the bender converted into flap motion. The efficiency of the bender by itself is defined as,

$$\eta = \frac{\frac{1}{2}kw^2}{V}$$

where  $k$  is the bender tip stiffness,  $w$  the bender tip deflection and  $V$  the strain energy of the bender. Prechtl [49] proves that for a uniform thickness bender, the efficiency is 75%, but it can be increased to 100% if the bender has a square root taper pattern. There was difficulty in measuring the bender stiffness. The goal was not a rotating test and so the flexure did not need to handle the CF of the flap. The setup showed promise on the benchtop with 11.5° HPP without load at 10Hz. However, the final conclusion was that piezostacks were more promising because the  $d_{33}$  effect could be utilized (Section 1.5.2).

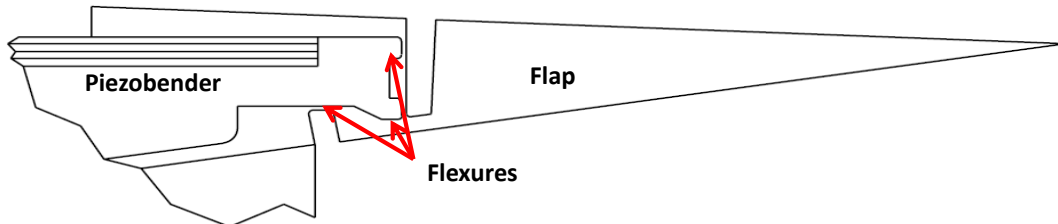


Figure 1.21: Piezobender with Flexure for Benchtop [50]

Fulton [51] built and tested a Froude scaled 2-bladed rotor (Table 1.2) with a

Table 1.2: Fulton Rotor Properties [51]

Property	Value
Rotor Radius	3.75 ft.
Airfoil	NACA0012
Chord	3.4 in.
Rotor Speed	760 RPM
Tip Speed	298ft/sec
Elevon Chord	10%c
Elevon span	12%R
Elevon Center	75%R

TE flap actuated by a piezobender (Fig. 1.22). At 760 RPM (298 ft/s,  $M=0.247$ ), flap deflection of  $6.5^\circ$  HPP was obtained at 5Hz. The flap was driven by 2 PZT-5A bimorphs with 20 mil thickness, 1.5 inch width and 1.8 inch length. A rod-cusp arrangement converted the bimorph motion into flap motion.

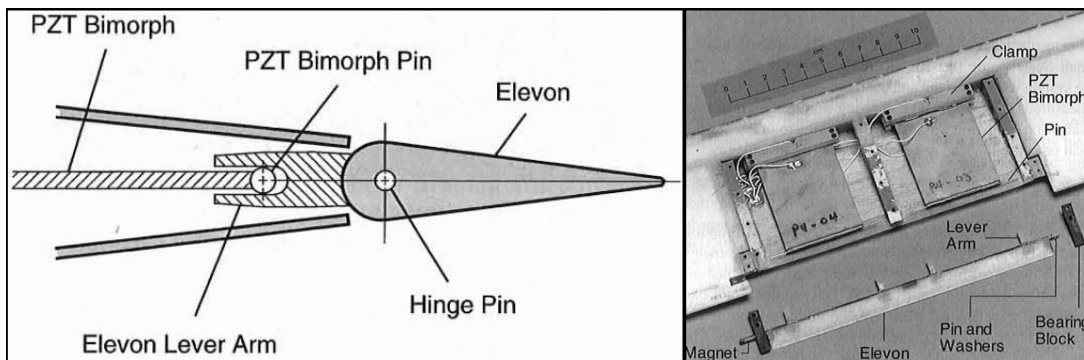


Figure 1.22: Fulton's Blade schematic and exploded view picture

Roget used TE flaps to demonstrate vibration control in a Mach scale rotor (Table 1.3) with a hingeless hub in forward flight [52]. The results were very impressive. The 1 and 4/rev fixed frame loads are reduced by 43% at 1500 RPM and  $\mu=0.25$  with rotor thrust of 12 lbs. A control algorithm is developed that allows the rotor blade to have dissimilarities resulting in non- $kN_b$ /rev harmonics in the fixed frame by having unique control inputs for each blade.

A piezoelectric 8-layer bender (PZT-5H2) is used to actuate the flap with a

Table 1.3: Roget Mach-Scale Rotor Properties

Property	Value
Rotor Radius	2.5 ft.
Airfoil	NACA0012
Chord	3 in.
Rotor Speed	1800 RPM
Tip Speed	472ft/sec
Flap span	2.4 in. (8%R)
Flap chord	0.6 in. (20%c)
Flap Center	75%R

rod-cusp to convert the actuator tip motion to flap motion. A flexure is used to support the flap and allow rotation (Fig. 1.23). Unlike designs with bearings, this setup with flexures fits completely inside the blade profile.

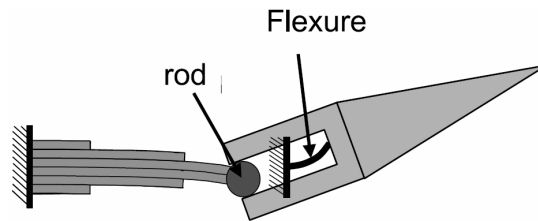


Figure 1.23: Roget's Piezobender Flap Schematic

The piezobender has a stroke of 15.75 mils and stiffness of 0.25 lb/mil at the tip. At 1800 RPM,  $190V_{RMS}$  (maximum electric field) yielded  $4^\circ$  HPP flap deflection at 1/rev (30Hz) increasing to a maximum of  $4.2^\circ$  at 5/rev (150Hz). The flap obtained  $6.5^\circ$  HPP in the vacuum chamber at 1800 RPM ( $9.8^\circ$  HPP at 0RPM) indicating that the main obstacle is the rotating environment and not the aerodynamic loads [53]. While sufficient for vibration control, an actuator with large stroke and/or stiffness would need to be developed to increase the flap deflection towards  $10^\circ$  HPP for the larger span flap required for primary control.

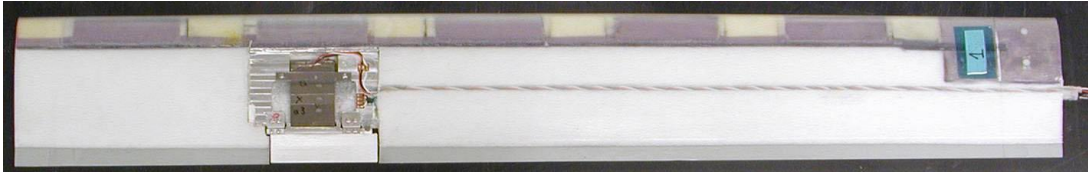


Figure 1.24: Roget’s Mach-scale Blade [53]

### 1.5.4 Flap driven by tab

In order to solve the problem of low actuator authority for piezobenders driving TE flaps for primary control, Falls looked at using a servotab to drive a TE flap (Fig. 1.25) [54], [55]. In this configuration, the tab is deflected using the piezobender, which in turn causes the flap to deflect and induces blade twist. Although the limited stroke of the piezobender is often cited as the issue; however, the tab too needs significant deflection. The tab angles are similar to the flap angles, but being smaller in chord and span, the force required to drive the tab is less. Through the hinge to convert bender tip translational motion to flap rotational motion, a very small stroke can create any flap angle as long as the actuator has sufficient force. The tab requires less force than the flap, because the force generated by the bender is amplified by the tab aerodynamic forces to drive the flap.

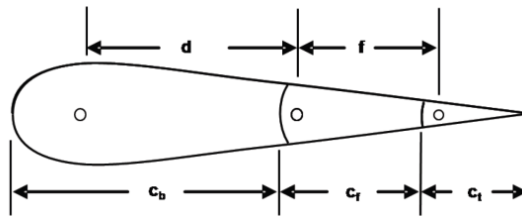


Figure 1.25: Airfoil Schematic of Flap+Tab System

Falls developed a comprehensive analysis with inertial and aerodynamic contributions of the flap and tab, blade flexibility, unsteady flow and free wake for the UH-60A helicopter to optimize the flap and tab parameters. The rotor (Table

Table 1.4: Optimized Flap-Tab System for UH-60A Rotor

Parameter	Value
TEF chord	22% <i>c</i>
Tab Chord	13% <i>c</i>
Flap/Tab Span	39% Radius
Blade Index Angle	18°
TEF Overhang	30% <i>c<sub>flap</sub></i>
Tab Overhang	33% <i>c<sub>flap</sub></i>

1.4) could be trimmed from hover to  $\mu=0.368$ . At  $\mu=0.368$  and  $C_T/\sigma = 0.084$  and torsional frequency of 1.99/rev, 5° HPP and 5 ft-lb of hinge moment HPP is required to trim the helicopter. The flap stiffness needs to be low enough to allow flap movement independent of the blade, but not so soft that extreme flap deflections can occur. The model did not include the drag penalty from the gaps in the flap and tab or the wakes arising from the discontinuities present in the flap and tab. As with the flap alone, blade index angle has a large effect on the tab and flap angles required.

Falls also built a full size fixed wing test setup for testing in an open jet wind tunnel. The tab was driven by an 8-layer piezobender made from PZT-5H2. At 100 ft/s wind tunnel speed, the flap to tab gain was 0.95 at 6.5Hz (1/rev for MD900 SMART rotor) and decreased to 0.2 at 19.5Hz (3/rev). This was close to the predicted response.

Two issues remain for the flap-tab setup.

1. For the UH-60A design, both the flap and tab have large aerodynamic overhang, which can reduce the hinge moments. The rotor power for this flap-tab setup is not examined. The tab is helpful because it reduces the required hinge moment from the flap. This can also be accomplished by increasing the aerodynamic overhang of a flap without a tab. With

enough overhang, the hinge moment can be reduced to zero or even become unstable. The trade-off with overhang is the LE now protrudes into the airflow increasing drag. So, the question for the flap-tab system is whether this produces less drag than just a flap with enough overhang that the actuation requirements are similar to the flap-tab system.

2. No demonstration of a rotor system with a flap-tab system has been conducted. The tab requires the actuator to be in the flap. The Mach scale flap setup (Fig. 1.26) has a piezobender to actuate the tab through a rod-cusp mechanism. The flap weighs over 10g due to the bender and the aluminum support for the tab. Aluminum is required in order to have sufficient stiffness in the tab support arms under the CF. The CF of the flap would be greater than 100 lbs. This compares to 3-4g for just a flap ( $\leq 40$  lbs CF). It is difficult to have a thrust bearing that can allow for the flap rotation with low friction with this high load. Also, the small dimensions (maximum thickness of 0.16 inch) lead to manufacturing tolerance issues as well as protrusions into the airflow over 15% of the flap span. It may also be difficult to keep the blade CG properly placed due to the flap weight at the trailing edge.

However, if the drag calculations showed the tab superior to just the flap, the large weight and small size of the tab would not be as difficult to deal with at the full scale. In this case, the piezobender would fit inside the flap profile nicely whereas a piezostack with stroke amplification might not fit inside the flap profile.

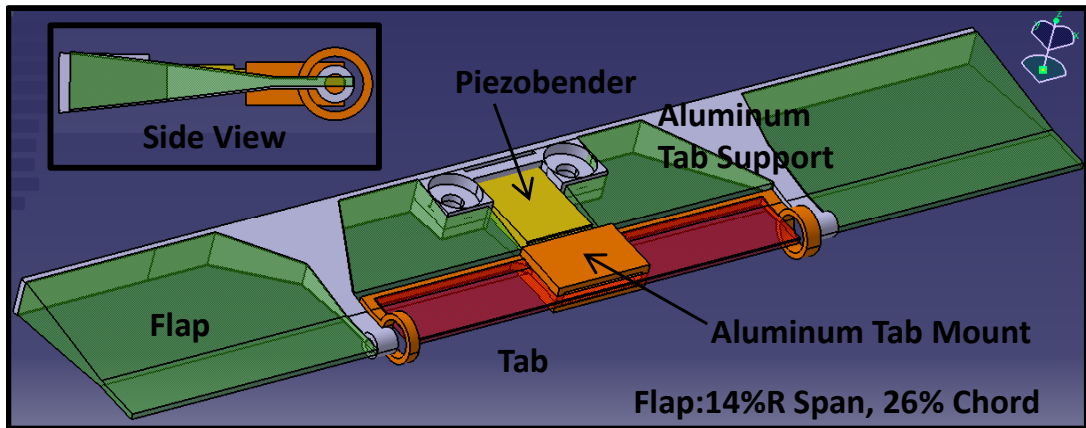


Figure 1.26: Airfoil Schematic of Flap+Tab System

### 1.5.5 Electric motors

DC motors have been used in both the full scale and Mach scale for actuating TE flaps. The key to these efforts has been to add control of not just the motor rotational speed but also the motor direction of rotation. This must allow for any desired flap motion with arbitrary frequency and phase. Since 2005, Sikorsky has been developing a high authority actuator for primary and secondary control for the S-434 28 ft. diameter rotor system [56]. They settled on an electro-mechanical actuator (EMA) which uses an electric motor. The EMA drives a TE flap of size 24%*c* and 12%*R* centered at 72%*R* that is limited by flap stops to  $\pm 12^\circ$ .

The EMA (Fig. 1.27) consists of a planetary roller screw and a permanent magnet brushless motor. The actuator lies behind the blade 1/4*c* and has a linear output. The linear output is converted to flap rotational motion using a bell crank with a counterweight on the crank to reduce the inertial loads on the actuator. The actuator was thoroughly benchtop tested for endurance and performance under load. A loaded spin test in a high-g (700g) spin-test facility with simulated torsion loading was also conducted. The actuators performed

Table 1.5: Maximum Flap Amplitude Versus Frequency

<b>Flap Freq, per rev</b>	<b>Flap Freq (Hz)</b>	<b>Flap HPP</b>
Steady	DC	10.0°
1	7	9.0°
2	14	7.3°
3	21	4.2°
4	28	2.7°
5	35	1.8°

well and were shown to have good performance from DC to 5/rev or 21.5Hz. The actuator is shown in Fig. 1.27.

The blade system (Table 1.5) was then tested on the hoverstand with the flaps actuated safely for 15 hours. The EMA provided significant flap motion at operating RPM over a range of frequencies as seen in the table below.

A secondary pitch cuff (Fig. 1.28) was placed inbetween the blade root and the lead-lag and flap hinges. The cuff allowed  $\pm 10^\circ$  pitching with low friction though the cuff torsional frequency was not provided. For 2/rev flap actuation at full rotor rotational speed, the cuff allowed  $0.8^\circ$  of blade pitching up to  $\pm 3.25^\circ$  HPP of flap deflection. This was close to the predicted pitch to flap sensitivity value of  $1.0^\circ$ . Very little results with the blade pitching are provided. A  $60^\circ$  phase delay is observed between the flap and blade pitch and the cuff at 2/rev indicating either high friction in the cuff or that the cuff torsional frequency is close to 2/rev. 1/rev and steady flap inputs were used to demonstrate thrust control and moment control. The thrust varied by  $0.01 CT/\sigma$  per degree of flap input. The rotor system was tested in the 40x80 foot wind tunnel for 55 hours but only preliminary results with vibration and noise reduction are provided. This may be a demonstration of primary control through trailing edge flaps. However, so little detail is given in the published work, it is difficult to draw

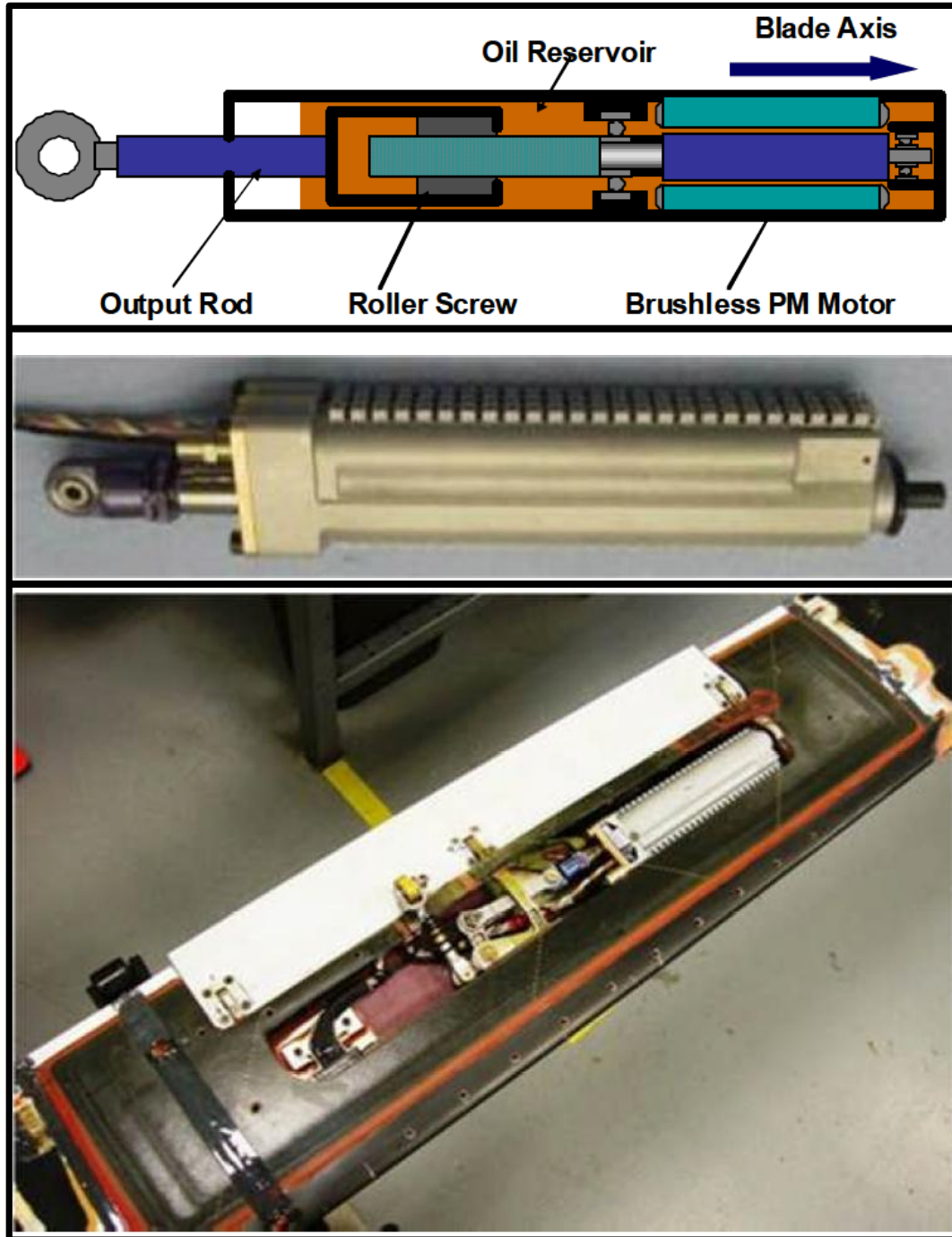


Figure 1.27: Top:EMA Schematic, Middle: Stand-alone EMA, Bottom: EMA flap assembly in blade [56]

significant conclusions.



Figure 1.28: Secondary Cuff mounted between primary cuff and blade root

At the Mach scale, Saxena [57], [58] has developed and tested a TE flap actuated by a compact brushless DC motor (Fig. 1.29) in order to achieve primary control. The rotor blade has a diameter of 66 inches and chord of 3.15 inches and must rotate at 2400 RPM to achieve Mach scale. The flap has dimensions of  $15\%c$  by  $14\%R$  centered at  $82\%R$  and is sized for primary control using UMARC. A Maxon EC-10 Motor with a 4:1 planetary gearhead was chosen. The motor weighs 15 g (6.7 g more for the gearhead), with a diameter of 0.4 inches, 1 inch length and rated power output of 8W. The NACA0012 airfoil has a maximum thickness of 0.378 inches and so the motor profile protrudes from the blade. The motor was evaluated on the benchtop with a torsion spring of 45 lb-mil per degree to simulate the aerodynamic flap load. The expected aerodynamic load is 11.85 mil-lb per degree. At 40 Hz, (1/rev on Mach scale rotor), the motor could produce  $15^\circ$  HPP rotational amplitude at an 8V input. However, the input voltage can be increased to greater than 40V demonstrating the large actuation authority available. A four-bar based mechanism that fits inside the blade profile transfers the motor gearhead motion to the flap via a flap rod. The flap system is shown below.

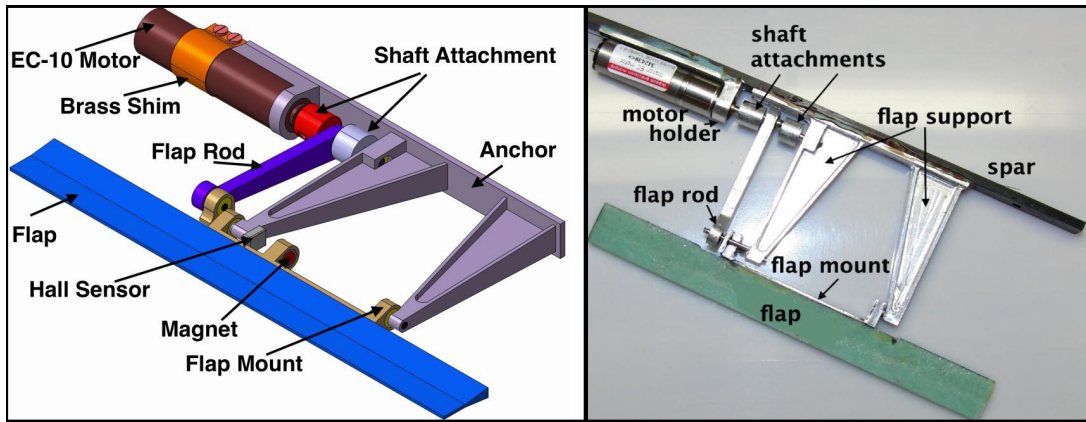


Figure 1.29: Brushless DC motor-flap schematic and picture [58]

The motor flap setup was tested in vacuum chamber up to 1400 RPM (1600 g's on the motor) with a simulated aerodynamic stiffness and it performed satisfactorily. The flap mechanism has a 3:1 gear reduction. A lack of air cooling in the vacuum chamber limited the testing RPM and motor voltage. This is not a problem on the hoverstand. At 1600 RPM on the hoverstand (Fig. 1.30), the flap achieved  $11.5^\circ$  half peak to peak at 40 Hz. The motor temperature reached  $55^\circ\text{C}$  indicating that the motor could be driven to higher flap angles because the temperature limit of the motor is due to the motor windings being damaged ( $\geq 100^\circ\text{C}$ ). So, the motor demonstrates enough flap deflection and bandwidth for rotor primary control.

Closed-loop amplitude control of the flaps was demonstrated by using 3 input variables. The motor input voltage determines the motor torque and speed. The frequency of direction change determines the flap frequency. The motor was also turned off for part of the flap cycle. The input voltage and the motor time on/off per cycle (duty cycle) control amplitude. The duty cycle is needed for small angles because the motor has a stall voltage. Figure 1.31 shows the control scheme. The motor can be disabled for part of the flap cycle while

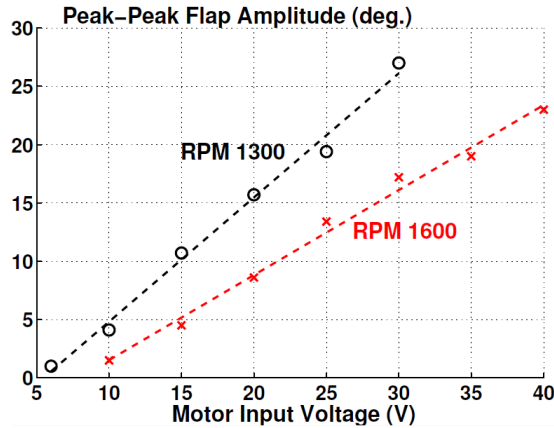


Figure 1.30: Motor-flap system Hoverstand results, Mach scale is 2400 RPM [58]

the flap restoring moment brings the flap back to its neutral position. So, a higher voltage and shorter duty cycle may be a more efficient method of driving the flap than a longer duty cycle and lower voltage. Presumably, mean control of the motor could be accomplished by making the enable/disable duty cycle non-symmetric. This would cause the motor to be driven further in one flap direction than another, though this has yet to be demonstrated. Continued testing at higher RPM is planned until primary control is demonstrated in the wind tunnel.

### 1.5.6 PAM

Pneumatic Artificial Muscles (PAMs) have been examined for actuating a TE flap system with bandwidth sufficient for primary control and vibration control. PAMs are attractive due to their high specific work and power output and an expendable operating fluid (air). Pneumatic cylinders are not attractive due to the effects of CF and off axis loading on the piston rods and seals. Also, large blade deformations lead to alignment issues with the piston components. PAMs

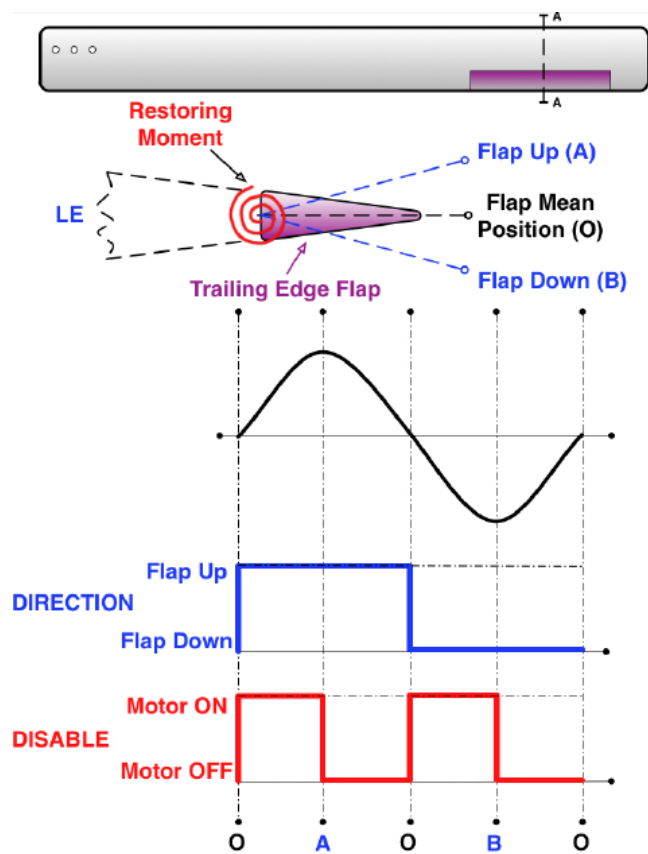


Figure 1.31: Flap Control Scheme using motor [58]

lack a piston rod or dynamic seals and are naturally compliant. Also, unlike hydraulics, PAMs use pressurized air instead of oil eliminating the need for a return circuit, the risk of fire or explosion. Low pressure air can be distributed to the PAMs with flexible tubing. Woods [59] developed this concept for a full size active rotor system for a Bell 407 size helicopter.

PAMs consist of an inner elastomeric bladder surrounded by a helically braided sleeve. When the inner bladder is inflated, the braided sleeve is forced to expand radially (Fig. 1.32), but due to the fixed length of the stiff sleeve fibers, the fibers generate a contractile force and displacement along the PAM main axis. This is a unidirectional actuator. For bidirectional control, which is needed for a trailing edge flap system, two PAMs need to operate as a pair of agonist/antagonist muscles as in the human body.

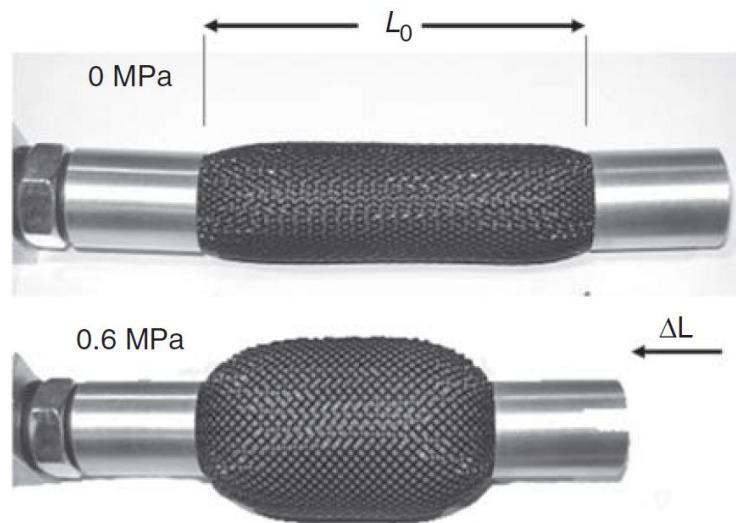


Figure 1.32: PAM at no pressure and contracted

An experimental setup with a Bell 407 blade tip section was modified for testing in the Glenn L. Martin Wind Tunnel. A TE flap with 16% span, 15% centered at 83%R according to the full rotor radius of 17.6 ft, was added. The

flap is driven by a pair of PAMS mounted in an actuator cartridge at the root of the blade (Fig. 1.33). A bell crank converts the PAMs forces to moments about a hinge with lever arms to provide proper gearing. The output torque and motion are transferred by a pair of linkages out to the flap where a second bell crank rotates the spanwise linkage motion into chordwise motion of a flap control rod which drives the flap.

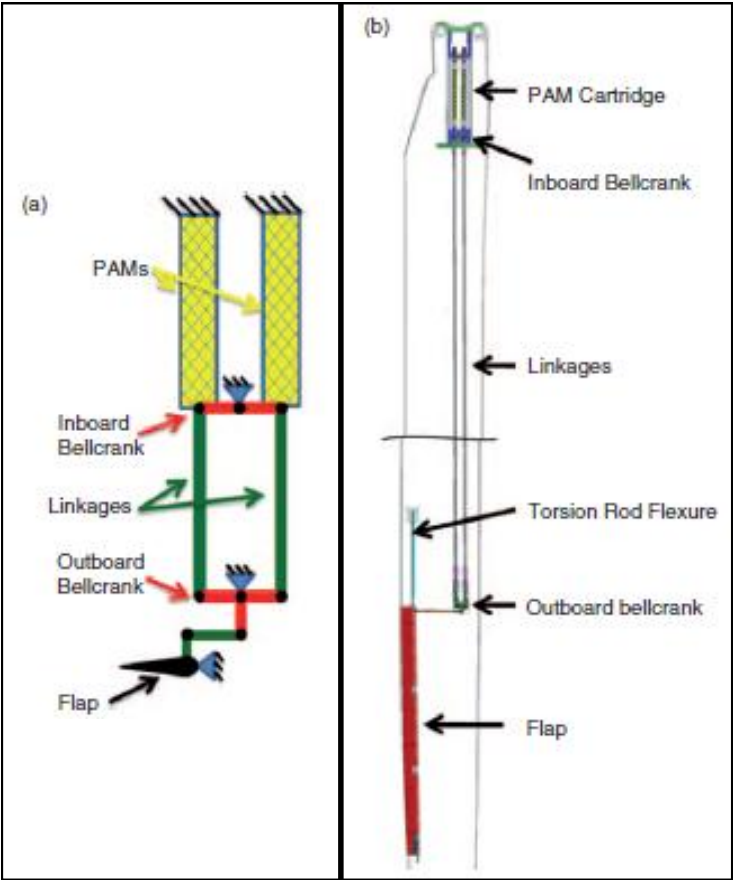


Figure 1.33: a) PAM Cartridge schematic and b.) Blade Flap Schematic [59]

Also, the flap setup with PAMs was tested under CF in the vacuum chamber. Linear springs simulated the flap aerodynamic load. Pressurized air was supplied from the fixed frame to the PAMs via a rotating frame air supply system that used a commercially available pneumatic rotary union. The objective was to

prove the concept under full scale CF and not to look at the flap aerodynamics, so the radial locations of the flap and PAM actuator were set such that the  $\Omega^2 R$  term matches the Bell407 full scale value. This means at a vacuum chamber rotational speed of 792 RPM, the flap center sees 843 g's, the blade tip 1017 g's and PAM sees 163 g's. In the schematic and picture of the setup (Fig. 1.34), the torsion rod for supporting the flap CF while allowing rotation is shown. It is unclear why the PAM is placed at the blade root instead of at the flap.

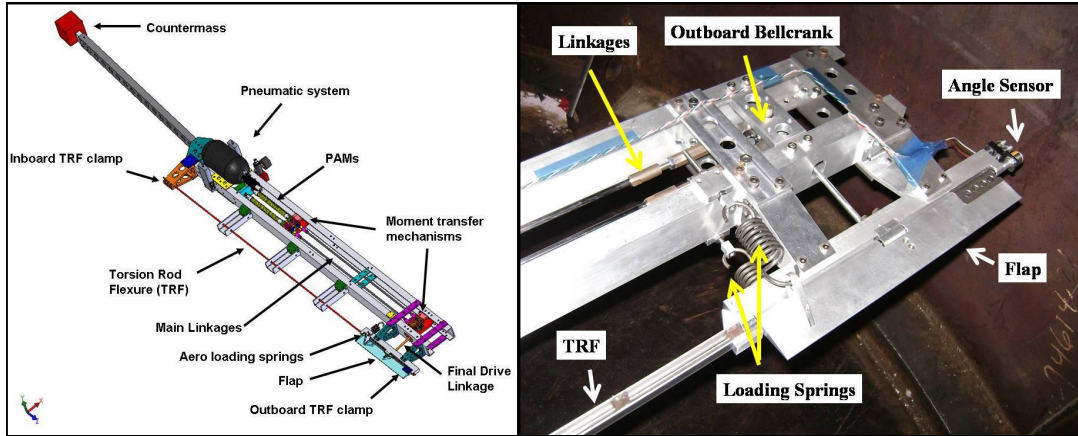


Figure 1.34: PAM flap system for vacuum chamber

It should be noted that this is not the same design space as the previous TE flap actuation methods where the flap actuator was located at the flap. By placing the PAM cartridge at the root, it no longer needs to fit inside the blade profile, handle large blade deformations, or have low weight. Previous work on piezos with L-frame actuators and various other setups have found serious losses in just 2 lever arms and this setup has 2 sets of lever arms (inboard and outboard bellcrank) and linkages. These linkages must be designed for the blade deformations as well as be well supported. This likely leads to significant losses. The TE flap is no longer an addition to a previous blade but the entire blade must be redesigned to handle all the linkages. Also, the design is no longer

modular as in the piezo and electric motor designs. If a flap fails, repair or replacement may be difficult.

Two simple experiments will show the difference placing the actuator at the root can make from the actuator perspective. For the piezostack, for the same CF, a heavier actuator could be placed at the root as compared to a much lighter actuator located out at the flap. The heavier actuator at the blade root would have significantly more force capability that can be traded for stroke. This actuator could have more piezo material and so require lower electric fields which would increase the actuator life. Also, at lower electric fields, the hysteresis in the piezoelectric material is generally less, leading to more simple control and much lower energy losses.

For an electric motor placed at the blade root, the motor diameter could be increased as protrusion into the airflow is not a concern. Saxena showed that motor torque scales by the cubic of diameter [57] so motor authority would greatly increase. It is not clear with the advantages talked of for the PAM why it should need to be placed at the root. So, although specific work clearly shows the advantage of PAMs over piezoelectrics (200x more) [60], it is difficult to compare the previously discussed flap actuation methods with PAMs. Future work for all methods should look at the power required for flap actuation. The power required to provide the pressurized air to the PAMs is not discussed.

Nevertheless, the setup showed significant promise in both the wind tunnel non-rotating and the vacuum chamber rotating tests. In the wind tunnel at 30% of full scale loading, the system provided 1/rev (7Hz) HPP of  $18.8^\circ$  and the performance was maintained to 5/rev (35Hz) with  $17^\circ$  HPP. The vacuum chamber results were limited to 80% of full scale but showed HPP deflections of  $17^\circ$  at 1/rev and  $8^\circ$  at 5/rev [61].

Finally, the PAMs have been modified to have a fatigue life sufficient for aerospace applications. Literature reported a short fatigue life of 18,000 cycles but by employing a swagging process to provide smooth and distributed clamping of the bladder and braided sleeve components onto the end fittings, the stress concentrations are minimized. Long term fatigue testing showed an increase in actuator life to 120 million cycles which should be sufficient for helicopters. [62]

## **1.6 Limitations of Previous Work**

Much work has been carried out on the development and demonstration of full size actuators for trailing edge flaps. These include electric motors, piezostacks and PAMs. All these can work in the blade rotating environment. The analytical work has shown the feasibility of eliminating the swashplate with TE flaps and lowering the blade torsional frequency. Scaled rotors with TE flaps have been used for vibration control. The missing step is to put all of this together into a scaled rotorcraft set of blades with TE flaps while lowering the blade torsional frequency. Only the piezoelectric bender can fit easily inside the Mach scale blade profile making it ideal for testing the aerodynamics of rotor primary control through TE flaps. Other actuators may protrude out of the airfoil. The piezobender has the added advantage of high bandwidth so adding performance improvement, noise reduction and vibration control to primary control through the TE flaps is not difficult.

## 1.7 Scope of Current Research

This work focuses on the development and demonstration of a Mach scale swash-plateless rotor system with trailing edge flaps. Piezobenders are chosen to actuate the TE flaps due to the ease of placing them inside a Mach-scale blade profile. All the necessary theoretical groundwork has been laid down for this project. The goal is to demonstrate primary control of the rotor system using the TE flaps specifically driven by piezobenders. This work is the culmination of work done at the University of Maryland for many years, starting with investigations into piezoelectric plate elements under high in-plane loads such as in a high CF environment.

The high centrifugal environment poses many problems as does the small scale of parts for the experimental setup. All composite blades and parts are designed and built in-house. All piezoelectric benders are assembled in-house from commercial piezoelectric plates. The work is divided into three parts. First, the piezobender is examined thoroughly. New, soft piezoelectric materials, PZT-5K4 and M1876, are examined for the bender. Significant effort is put towards finding the best piezoelectric material and learning how to implement it. The piezobender performance at high electric fields will be examined closely and any undocumented phenomenon of bender relaxation will be carefully investigated. The method of converting the bender tip linear motion into flap rotational motion with minimal losses in the Mach scale rotor will be developed.

The Mach scale blade with flaps is shown first to work in the rotating environment by testing it in a 10 ft. diameter vacuum chamber. Then, the blades will be tested on the University of Maryland hoverstand to show flap authority. Then, the rigid pitch links will be replaced with a linear spring setup that allows

for the index angle and torsional frequency to be changed and the blade pitching to be measured during rotation. Adjustments will be made to this setup to eliminate any torsional friction in the blade pitch system. Primary control will be demonstrated at 900 RPM, which is less than the Mach scale goal of 2400 RPM. Although the flaps should work at this high RPM, it has not been proven.

## 1.8 Overview of Dissertation

Chapter 1 examines at the idea of eliminating the swashplate. Various ways of twisting the blade either at the root or structurally distributed for primary control are examined. The large amount of analytical and experimental work with TE flaps on blades is examined. Finally, the development of the piezobender as the means of actuation is examined. Chapter 2 is devoted to the experimental piezobender development. The bender is optimized for the experiment and a new soft piezoelectric material is explored. The bender's behavior under very high electric fields is examined systematically. Chapter 3 examines closely the Mach scale experimental blades with TE flaps development. Mach scale rotors pose their own problems that must be overcome to have a working flap system. Hoverstand results show the success of the setup. Chapter 4 investigates a demonstration of primary control of a 2-bladed rotor system using TE flaps. Closed-loop control of the flaps is proven. The blade pitch links are replaced with linear springs and the blade pitches at the root in response to the flaps deflecting. Primary control is demonstrated by the flaps causing large blade pitching and large changes in hub moments and forces. Chapter 5 examines a wire network sensor that measures blade elastic deflections in-flight including blade flapping, lead-lagging and twisting. This is outside the main focus of the

project, but nevertheless quite relevant for the swashplateless rotor concept if the blade structure is made torsionally soft. The theory for the wire sensor is developed. An experimental setup with this network inside a Mach scale blade is constructed. The wire sensor network is calibrated and tested under driven and impulse conditions. The deflections measured by the wire sensor network are compared to the deflections recorded by a motion camera system. Chapter 6 discusses the key contributions of this work and offers recommendations for future work.

## Chapter 2

# Piezobenders

### 2.1 Overview

This chapter will discuss a piezobender that can drive a TE flap sized for primary control of a Mach scale rotor. The rotor design will be discussed in detail in the following chapter. The Mach scale rotor has a chord of 3.15 in. and a maximum thickness of 0.33 in. This small size requires the piezobender design to be carefully optimized to fit inside this blade profile. Then, new piezoceramic materials are examined in order to increase bender authority. Finally, the bender behavior under very high electric fields is examined, as for primary control, the bender must be driven to its maximum capability.

Piezoceramics have high bandwidth, high stiffness and moderate strain making them useful for actuating a trailing edge flap. A piezobender can fit inside the Mach scale blade profile, which has a maximum thickness of 0.33 in., while also handling more than 4500 g's of centrifugal force. A piezobender is made of piezoceramic layers bonded together as seen in Fig. 2.1 with a shim at the center. The concept is shown in Fig. 2.2, where an applied voltage across the piezoceramic layer's thickness leads to an increase or decrease in its length via

the  $d_{31}$  effect. When opposing strains are produced across the bender neutral axis, a bending actuation is produced causing the bender tip to deflect. The main tradeoff with additional layers is increased stiffness and decreased stroke. Against the direction of polarization, the applied voltage is limited by the depolarization of the material. In the direction of polarization, however, the applied voltage can be much higher, limited only by dielectric breakdown and arcing. So, a bias circuit is used to divide the voltage signal. Voltages in the poled direction are scaled up by a factor of 2-4 relative to voltages against the poling direction. This allows larger fields to be applied without depoling. This significantly increases bender stroke. The shim handles the large strain differential from the actuator top half to bottom half. With a cantilevered arrangement, the tip displacement can be used for actuation of a TEF.

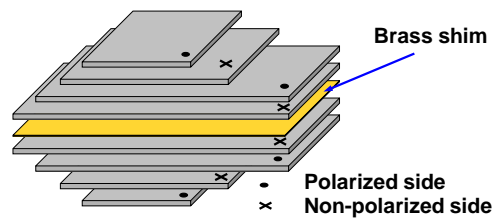


Figure 2.1: Multilayer piezobender exploded view

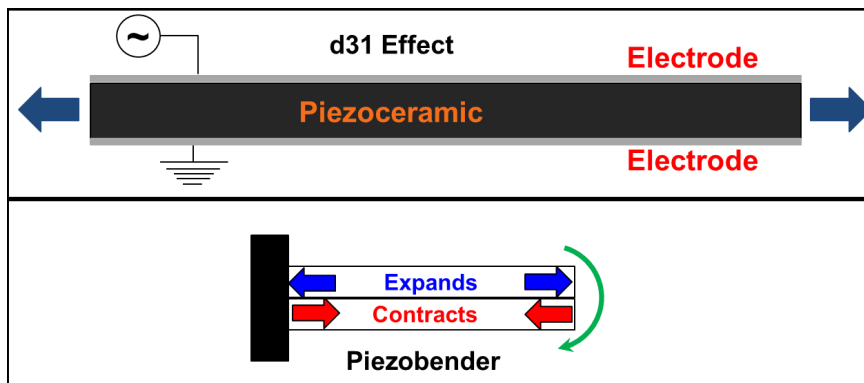


Figure 2.2: Top: Single layer, Bottom: Piezobender Bimorph

In order to obtain flap angles from the piezobender tip translational motion,

a rod-cusp mechanism is used (Fig. 2.3). This has been developed for TEF on Mach scale rotors at the University of Maryland [63], [64], [65]. The rod-cusp is used, because it does not constrain the bender motion lengthwise (beam shortening effect from tip vertical motion). The mechanism will be discussed in greater detail in Chapter 3.

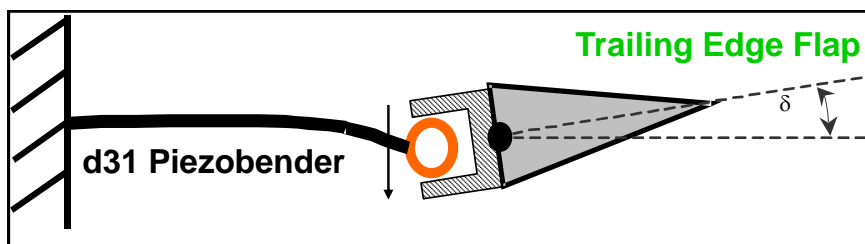


Figure 2.3: Rod-Cusp Concept

Sirohi [66] looked at the fundamental behavior of piezoceramic plate elements. It was found that a small increase (10%) in free strain due to large external tensile stress (2500psi) such as is found in the high centrifugal force environment of the Mach scale rotor. The depoling field decreases with increasing excitation frequency. Depoling is commonly incorrectly referred to as a loss of the material's piezoelectric properties. Depoling means that the piezoceramic has increased dielectric losses and lower efficiency and the strain-field hysteresis loop transforms from an ellipse to a butterfly loop. As seen in the two loops (Fig. 2.4), the peak to peak strain is reduced by just 7%. Increased area inside the curve indicates the losses. So, if a piezoactuator is depoled, it can function as long as enough excess electrical power is available and the controller can handle the butterfly loop. An individual plate can be depoled and then repoled by application of an AC field with a large positive DC bias. The material can also depole due to exceeding its Curie temperature or if a large enough stress is applied.

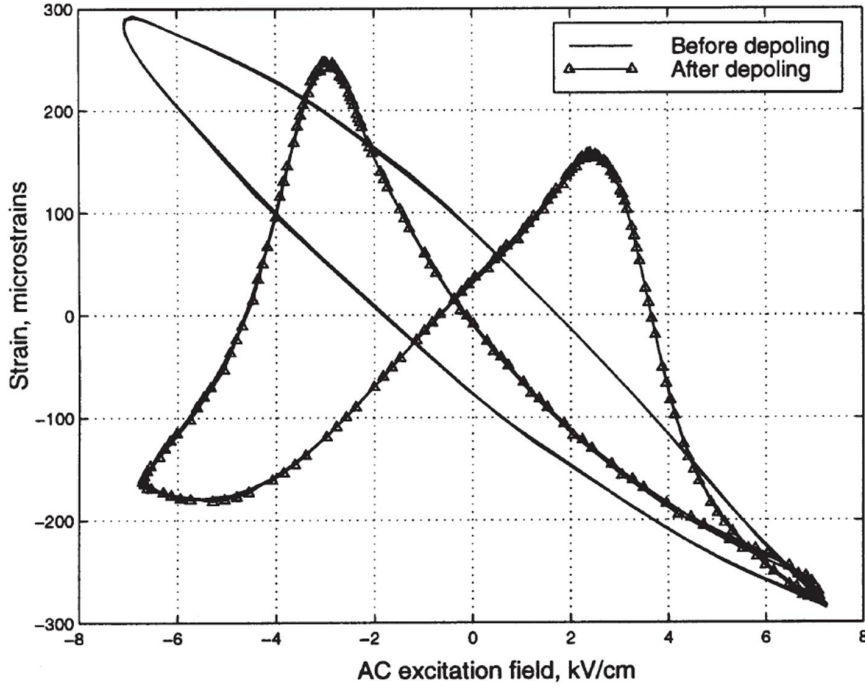


Figure 2.4: Piezoceramic plate, PZT-5H2, Free Strain-Electric Field Loops [35]

## 2.2 Piezobender Dimensions

With the space (blade profile) and weight (high CF) constraints of the Mach scale blade, the piezobender dimensions (length, number of layers, taper pattern) need to be carefully chosen. The actuator taper pattern needs to be optimized. Tapering the bender also lets it fit better inside the airfoil's tapering thickness, as well as moves the actuator CG close to the airfoil leading edge. Prechtl [50] explains the effect of taper on efficiency. Efficiency is defined as the ratio of useful tip deflection energy to strain energy and so, this neglects the efficiency of moving from electrical energy to strain energy.

$$\eta = \frac{\frac{1}{2}kw^2}{\frac{1}{2}E\Lambda^2} \quad (2.1)$$

where  $k$  is the bender tip stiffness,  $w$  is the tip stroke,  $E$  is the material Young's modulus and  $\Lambda$  is the material free strain. A bender with constant lengthwise thickness is shown to have an efficiency of 75%. It can be increased to 100% with a taper pattern such that the bender thickness has a square root decrease from cantilever to tip. This keeps the strain at the bender surface constant along its length.

To optimize the taper, the bender stroke and stiffness need to be estimated. Chopra [33] reviewed various methods of determining piezobender stroke and stiffness and recommends a finite element model. The choice of piezoelectric material does not matter for the optimization, but will be discussed later. This is acceptable because the stiffness for different piezoelectric materials is similar and though the maximum strain is different, this changes only the bender stroke. The material choice will not affect the optimum bender, but instead change the flap angle that the optimum bender can obtain.

### 2.2.1 Piezobender Finite Element Code

A finite element model of the bender is created using an Euler-Bernoulli beam model with induced strain actuation. The model treats the shim and piezoceramic sheets as a continuous structure with a linear distribution of strain within the piezoceramic layers. While many models are concerned with modeling of the bond between layers due to imperfect bonds, this will be shown to be unnecessary (Sec. 2.3.5). A 'perfect' bond can be obtained and so, this model neglects the bond layer. Flap deflection,  $\delta$ , and flap hinge moment,  $M_h$ , can be directly related to the bender tip displacement,  $w$ , and actuation force,  $F$  as a function of hinge offset,  $d$ , with small angle assumption:

$$F = \frac{M_h}{d} = \frac{M_h \delta}{w} \quad (2.2)$$

The FE code is used to determine the bender length, taper pattern and number of layers in order to maximize the flap deflection for an acceptable weight. The flap stiffness to be overcome by the bender,  $\frac{M_h}{\delta}$ , is derived from UMARC (Chapter 3) as 12 mil-lb/° of flap deflection.

### 2.2.1.1 Constraints

The bender must fit inside the blade profile (Fig. 2.5). The bender width is 1.00 in. because this is the standard commercial piezo plate width. For the thickness, the bender and the clamps sandwiching the bender to form the bender cantilever must fit behind the spar. This leaves about 0.13 in. for the bender thickness near the spar. Thinner piezo plates lower the driving voltage required for the same electric field strength. 10 mil thickness is a good compromise between required voltage and fragility. With this plate thickness, the number of layers is limited to 12 to fit inside the available space. For the bender length, the bender, its cantilever and the flap hinge must fit in the space available. So, the bender length is limited to 1.38 in.

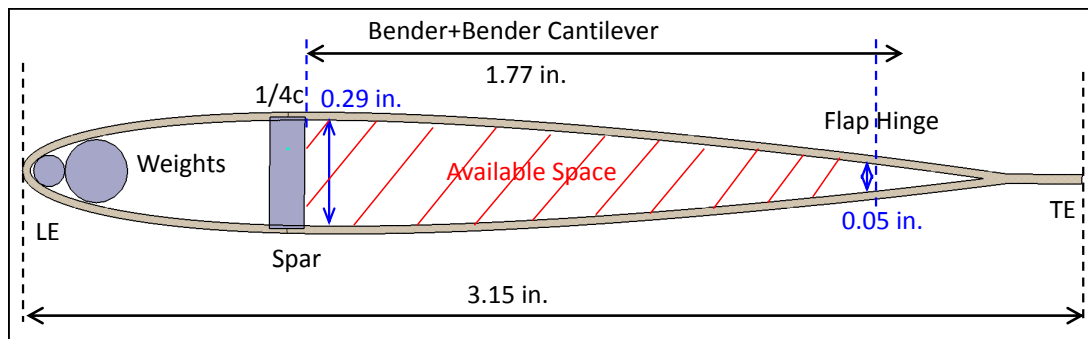


Figure 2.5: Mach Scale Blade Profile

### 2.2.1.2 Bender Length

There is an inverse relationship between the length of the bender and the bender stiffness required to drive the TE flap. This is because for the same stiffness as a shorter bender, a longer bender can have a higher stroke (Fig. 2.6). The bender must produce a moment to drive the flap. The moment required by the bender is directly proportional to the product of bender tip stiffness and stroke. So, if the bender stroke is increased, the stiffness required to produce the required moment decreases. A lower bender stiffness means that the stiffness of the cantilever holding the bender and the flap hinge support will be relatively higher, thus increasing system efficiency. For example, if the cantilever stiffness relative to the bender tip stiffness is not large, then the bender moment will deflect the cantilever support instead of the flap. It is advantageous therefore, to use a longer bender, as the bender stiffness can be lower. This will be explained more in Chapter 3.

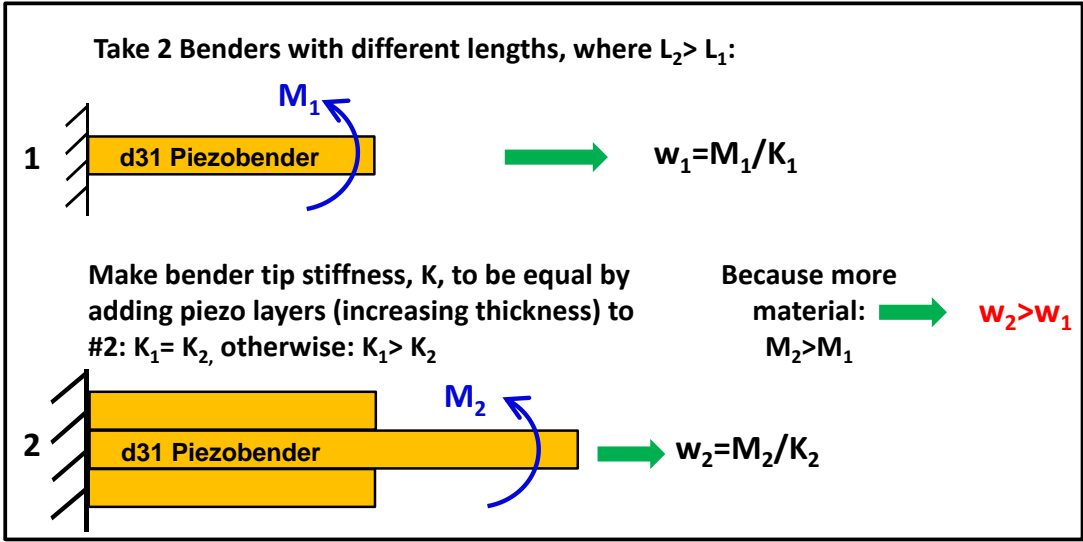


Figure 2.6: Effect of Length Conceptualization

The effect of length on the required bender stiffness is large (Fig. 2.7). For

this study, the desired HPP flap angle is  $5.5^\circ$  (sufficient for primary control according to UMARC study, see Chapter 3 [67]). So, each line in Fig. 2.7 shows the required bender tip stiffness to reach  $5.5^\circ$  for various length benders. The material is PZT-5K4 with an assumed maximum strain of  $1023 \mu\epsilon$ . Each bender has 10 layers. Several lines indicating a range of aerodynamic flap stiffness requirements (aerodynamic moment on flap per unit flap deflection) in mil-lb are shown, as this has not been measured experimentally.

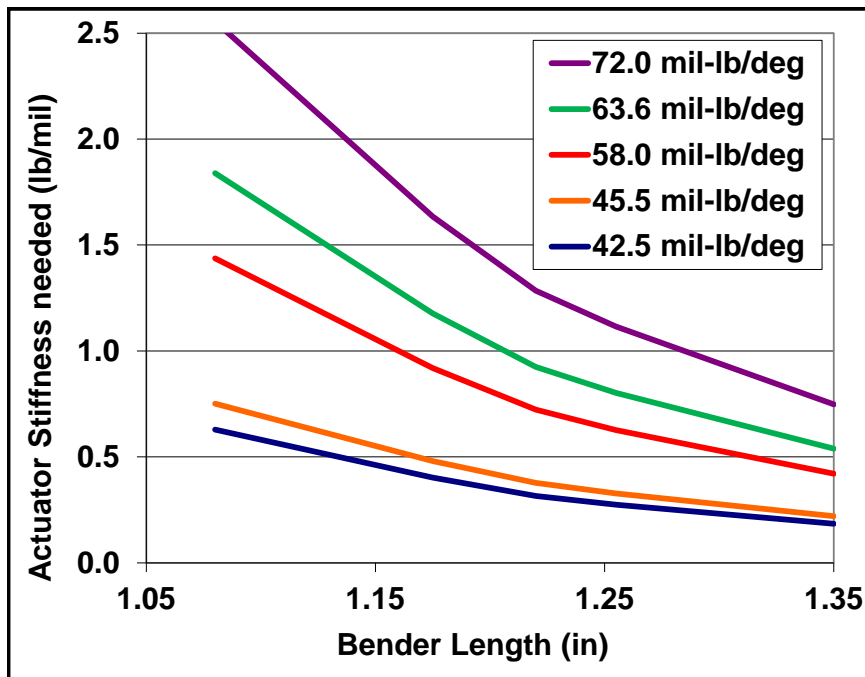


Figure 2.7: Required Bender Stiffness vs. Bender Length for range of Flap Aerodynamic Stiffnesses

The effect is large as the flap aerodynamic stiffness increases. For the mid-range stiffness of  $319 \text{ mil-lb}/5.5^\circ$ , if the bender length is increased by 25% from 1.08 in. to 1.35 in., the required bender tip stiffness falls by 71% from 1.44 lb/mil to 0.42 lb/mil. So, the piezobender should be as long as possible. For the present blade chord with the bender behind the spar at the  $\frac{1}{4}c$ , the maximum possible length is 1.38 in.

**2.2.1.3 Model refinements**

With the length fixed, the number of layers and the taper pattern need to be determined. With the length of the bender similar to its width, it is closer to being a plate than a beam. Falls [55] showed for an 8-layer bender with both length and width equal to 1.00 in., that the bender theoretical stroke differed by less than 1% between the plate and beam theories. So, beam theory is acceptable for the present length and width. The cantilever stiffness is not infinite and so this was measured and added to the code. The bender weight and CG were calculated in order to determine the leading edge weight required to bring the blade CG to 24.5%c. The bender must have 4 layers at its tip. Two layers (bimorph) is too fragile to handle the flap loads. Finally, for all benders, the optimum hinge distance was chosen. The optimum hinge distance corresponds to impedance matching between the bender and flap.

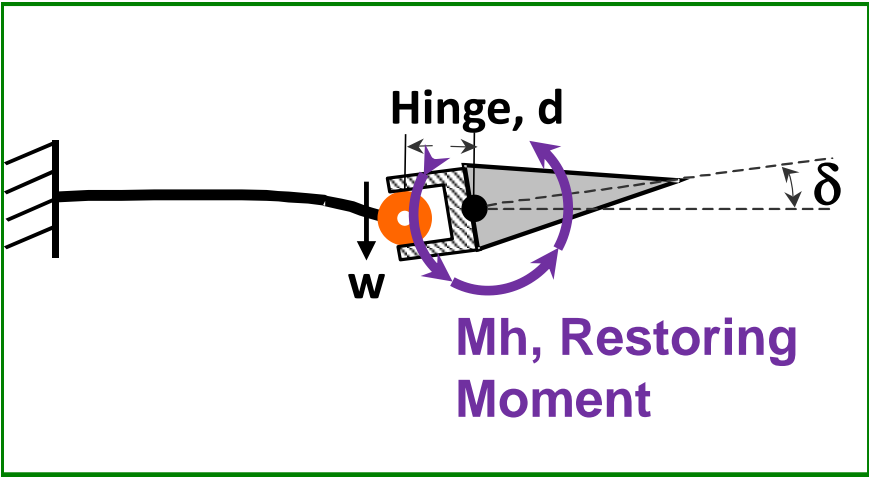


Figure 2.8: Flap Driven by Piezobender Schematic

The basic equation for this setup is:

$$\sin\delta = \frac{w}{d} \tag{2.3}$$

where  $w$  is the bender stroke and  $d$  the hinge distance. In Fig. 2.8, the bender tip has an orange rod sliding inside a cusp. For a real rod-cusp, a gap exists (the cusp is larger than the rod diameter). If there is no gap, the mechanism can jam. The bender must travel through the gap before it can move the flap, making part of the bender stroke ineffective. The code assumes a 4 mil gap in the rod-cusp (2 mils HPP loss). A larger hinge reduces the flap angle for a given stroke but it reduces the load on the bender tip for the same flap angle. This is reflected in the equation below (small angle approximation):

$$\delta = \frac{\frac{w}{d}}{1 + \frac{M_{H\delta}}{Kd^2}} \quad (2.4)$$

where  $M_{H\delta}$  is the linear flap stiffness and  $K$  is the bender tip stiffness. The tradeoff is seen in Figure 2.9 with each line representing a different flap aerodynamic stiffness, (200% UMARC is two times the stiffness predicted by UMARC for a flap suitable for primary control).

The hinge was limited to between 20 mils (assembly tolerance limits) and 200 mils (space constraints). Taking the derivative of Eq. 2.4 yields that the maximum flap angle is achieved when:

$$d = \sqrt{\frac{M_{H\delta}}{K}} \quad (2.5)$$

As flap stiffness increases, the optimum hinge distance increases. It makes sense to choose a hinge to the right of the peak hinge as the slope is more gradual to the right of the peak. This means that the inability to manufacture the hinge exactly will have a smaller penalty.

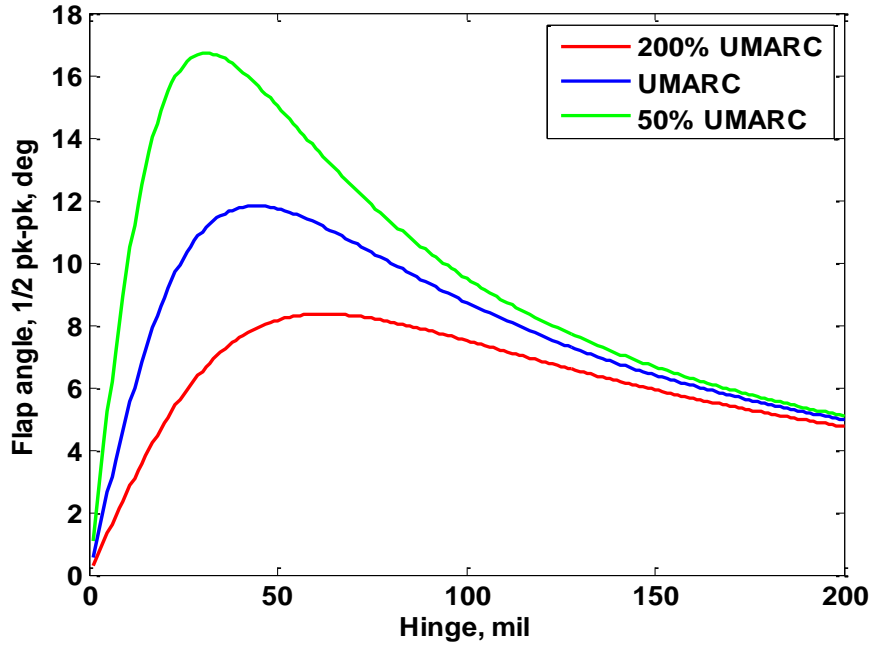


Figure 2.9: Effect of Hinge Distance on Flap Amplitude

## 2.2.2 Model Results

A brute force method was used for optimization where all taper patterns within 0.1 in. of each other from 4 layers to 12 layers were calculated. Bender energy is calculated as  $\frac{1}{2}kw^2$ . Fig. 2.10 shows that for the same total weight, more layers means more energy.

The next plot (Fig. 2.11 shows specific bender energy or energy per total mass (including LE weight). Specific energy is not affected by the number of layers.

Then, the flap angle versus total mass is shown in Fig. 2.12.

Several conclusions are drawn from the study:

1. More layers means increased flap angle for the same total mass (Bender energy and flap angle are not the same thing).
2. Maximum bender specific energy does not change with number of piezoce-

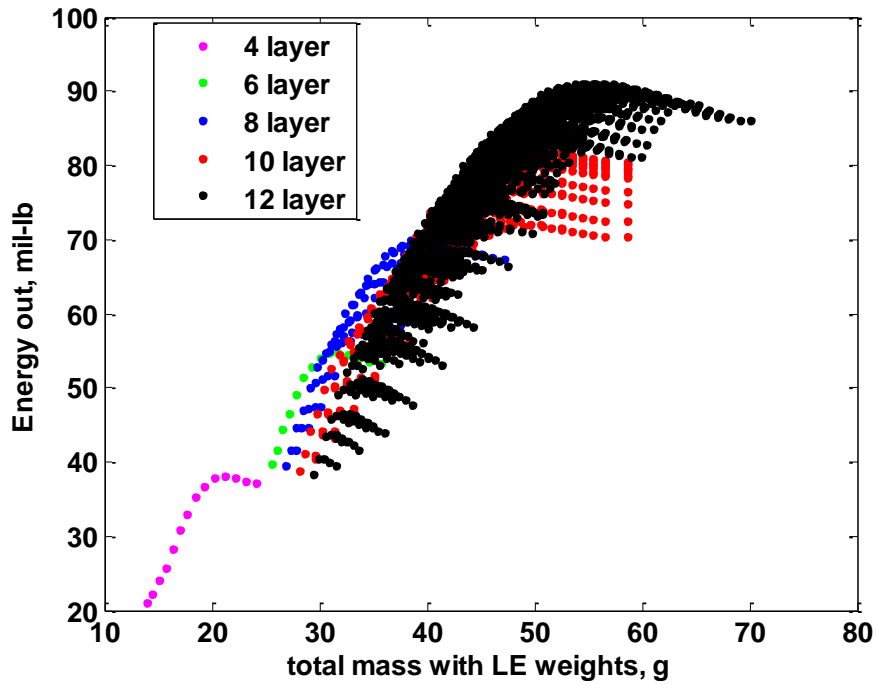


Figure 2.10: Bender Energy vs. Total Mass including LE Weight Required

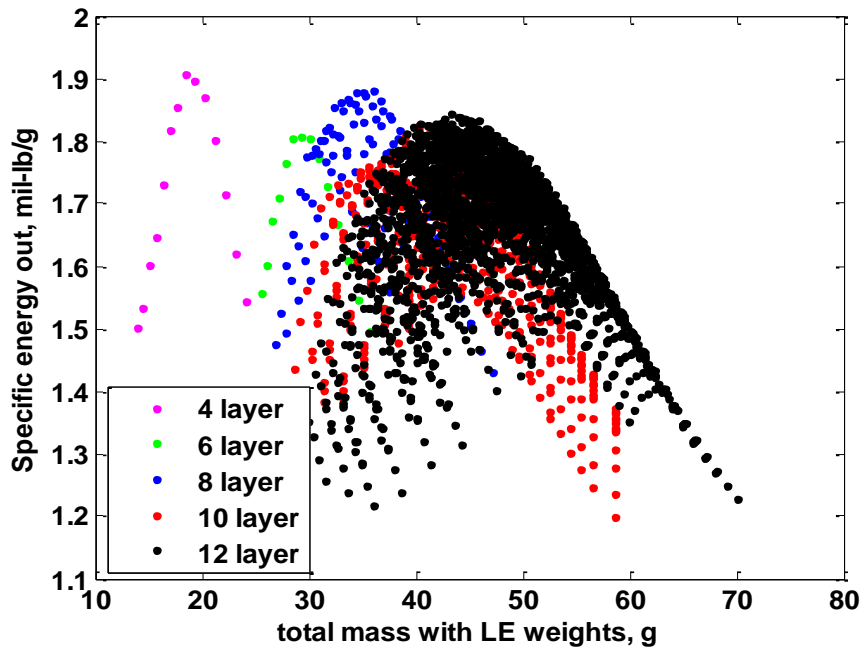


Figure 2.11: Bender Specific Energy vs. Total Mass including LE Weight Required

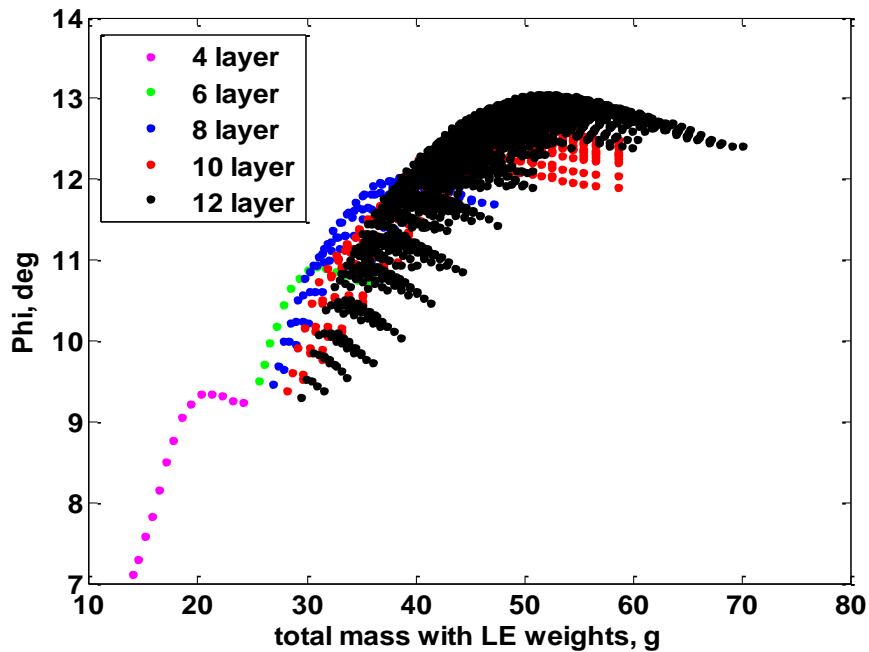


Figure 2.12: Flap Angle vs. Total Mass including LE Weight Required

ramic layers.

3. For the same total mass, the specific energy can vary by over 50% depending on the taper pattern.
4. A 4 layer bender provides significantly less flap deflection than 6,8,10 and 12 layers.

### 2.2.3 Final Bender

To choose the bender, several constraints are added. First, the 4 layer options are too compliant and offered 33% less flap angle than more layers. Second, all benders need to have 4 layers at the tip to handle the flap loads. Two layers at the tip could be too fragile. Third, either end (cantilever and tip) of the bender needs to be electrically grounded. These layers touch other parts of the blade. If they are live electrically, then great care has to be taken to insure these layers

are insulated from the rest of the blade and this is difficult. If the piezoceramic layers in contact with other parts of the blade are grounded, then the possibility of shorting is eliminated. This eliminates 6 and 10 layer benders. A 6 layer bender is seen in Fig. 2.13 with the wiring shown. G is for ground and P+ and M- are the driving voltage for each half of the bender.



Figure 2.13: Wiring for 6 layer bender where exposed layers at cantilever are both live

Then, the total mass is limited to avoid the total CF on the hub being too large and to prevent the bond holding the bender to the spar from failing. Fig. 2.14 shows all the possible actuators that fit the constraints of 8 or 12 layers and low enough total mass (including required LE weight). It is seen that with these constraints, both 8 and 12 layers give the same performance in terms of flap angle. So, an 8 layer bender is chosen because less layers mean less manufacturing time and a smaller possibility of failure due to less bonds and less chance of a crack in a layer during manufacturing.

The final bender taper pattern is shown in Fig. 2.15 and Table 2.1 shows the properties calculated by the model. The model will be shown to be valid later in the chapter. The piezoceramic material is PZT-5K4, but the material properties will not be discussed until the following section on material choice. The stroke is the stroke at low frequencies (Less than 5Hz).

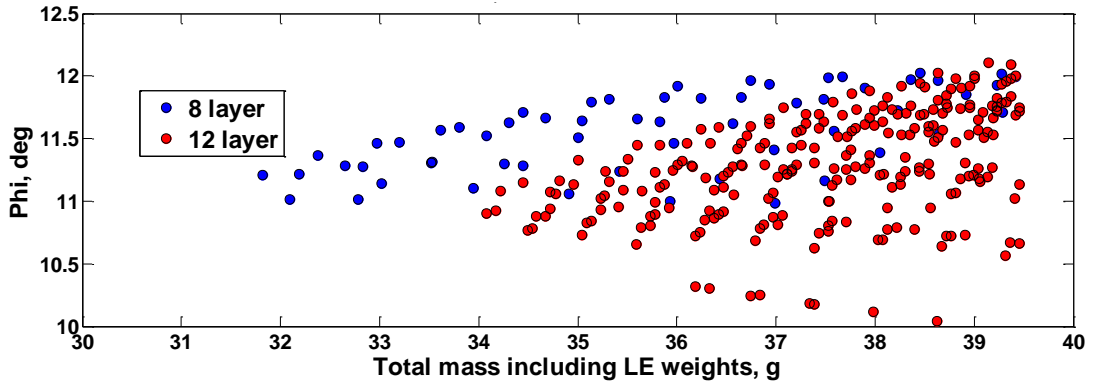


Figure 2.14: Bender Optimization: 8 vs. 12 Layers, Flap Angle vs. Total Mass

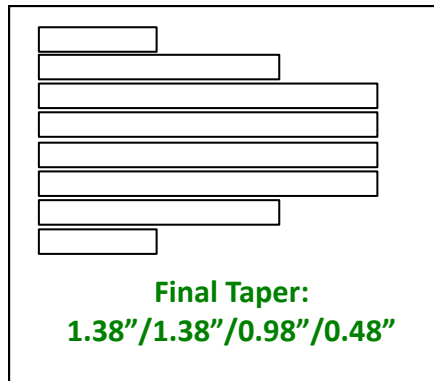


Figure 2.15: Final Bender, 8-layer

Table 2.1: Final Bender Properties

Property	Value
Mass	15.11 g.
Tip Stiffness	0.325 lb/mil
Tip Stroke	20.2 mils
Energy Output	66.3 mil-lb
Specific Energy	5.34 lb-ft/slug

## 2.3 Material Choice

### 2.3.1 Hard vs. Soft

In order to maximize bender authority, an extensive survey of material characteristics was conducted to find a material with greater strain energy than PZT-5H2. PZT-5H2 is a standard material often used for piezobenders. Greater strain energy implies a higher piezoelectric coefficient and higher stiffness (Young's modulus,  $E$ ). Piezoelectric materials are loosely classified as hard or soft. It is expected that softer materials have higher free strains but lower depoling field strengths and Curie temperatures. Softness does not imply a less stiff material. Instead it indicates they are relatively easy to polarize (and hence easier to depole) [68]. Hard materials have lower dielectric and mechanical losses than soft materials. A higher relative permittivity indicates the material is easier to pole.

### 2.3.2 Material Survey

To choose possible materials, an estimate of spring strain energy, in terms of  $d_{31}^2 E$  relative to PZT-5H2 strain energy, was used. The details of this survey are shown in Table 2.2. Manufacturer given values are used. Stiffness refers to the closed-circuit condition (electrodes are shorted to ground and hence no electric field). Blue indicates a property higher than PZT-5H2 and green indicates a material with higher strain energy.

PZT-5K4 HD and VIBRIT1876 (or M1876) have over two times the strain energy of PZT-5H2 for the same stiffness and so these materials are investigated carefully.

Company	Material	d31 x10 <sup>-12</sup> (m/V)	E1 (GPa)	Relative Permittivity	Curie Temp (°C)	Density (kg/m <sup>3</sup> )	Estimated Relative Energy
Morgan Electroceramics	PZT5H2	-274	61.0	3400	195	7450	1.000
	PZT507	-280	62.5	3300	165	7800	1.070
	PZT508	-315	61.0	3900 (33)	220	7900	1.322
	PZT407	-150	83.3	1225	315	7900	0.410
	PZT-5K2 HD	-401	63.0	6200 (33)	150	8200	2.213
	PZT-5K4 HD	-410	63.0	7100 (33)	137	8200	2.313
Argillon	VIBRIT420	-160	64.9	1600	320	7600	0.363
	VIBRIT524.5	-230	67.1	2400	290	7900	0.776
	VIBRIT1100	-315	70.4	4500	177	8100	1.526
	VIBRIT202	-90	84.7	1000	330	7700	0.150
	VIBRIT455	-120	78.7	1450	300	7700	0.248
	VIBRIT1334	-230	64.5	3500	200	7900	0.746
	VIBRIT1876	-385	63.3	7000	121	8000	2.049
TRS Technologies	610 HD	-340	60.6	3900	210	7950	1.530
	600FG HD	-310	67.6	3650	190	7900	1.418
	200 HD	-190	67.6	2000	340	7950	0.533
	HK1 HD	-360	64.9	6000	150	7950	1.838
	PMN-32%PT	-1050	16.8	8000	166	8000	4.034
Piezo Systems Inc.	PSI-5A4E	-190	66.0	1800	350	7800	0.520
	PSI-5H4E	-320	62.0	3800	230	7800	1.387
Marco	FPM231	-300	68.5	4000	205	7820	1.347
	FPM240	-275	70.4	3600	185	7820	1.163
Piezo Kinetics	556	-310	58.0	3900	180	7800	1.218
	406	-150	72.0	1500	300	7700	0.354
	502	-175	71.0	1800	150	7700	0.475
	802	-100	73.0	1000	350	7700	0.159
	804	-100	72.0	1050	320	7600	0.157
CTS Corp	3195STD	-175	69.0	1800	350	7700	0.462
	3195HD	-190	67.0	1900	350	7800	0.528
	3221HD	-300	62.0	3450	242	7870	1.219
	3203STD	-275	63.0	3250	235	7700	1.041
	3203HD	-320	62.0	3800	225	7870	1.387
	3252HD	-345	69.0	5000	160	8200	1.794
	3257HD	-364	68.0	5700	155	8200	1.968
	3265HD	-367	69.0	6500	135	8200	2.030
Channel Industries	C-5400	-135	82.0	1475	300	7550	0.326
	C-5500	-185	64.0	1775	350	7600	0.478
	C-5700	-250	62.0	2950	190	7400	0.846
	C-5804	-105	86.0	1340	300	7550	0.207

Table 2.2: Survey of Piezoceramic Materials

### 2.3.3 Curie Temperature

Analogous to a ferromagnetic material, a piezoceramic material has a temperature where depolarization occurs. It can also occur due to high mechanical or electrical stresses. The Curie temperature needs to be known precisely. The bender layers are bonded together under heat and the entire bender is bonded to its support with elevated temperature curing. If the Curie temperature is below these curing temperatures, the piezoceramic material cannot be used. A fall in the piezoelectricity of a material indicates that depoling has occurred. This can be observed by measuring capacitance which is directly proportional to  $d_{31}$ . So, an oven with precise temperature control is used to measure the Curie temperature. Samples of three piezoelectric materials were placed in an oven (holds to  $1^\circ\text{C}$  of set temperature) and the capacitance measured. The results are shown in Fig. 2.16.

The PZT-5H2 has a Curie temperature of  $195^\circ\text{C}$  according to the manufacturer. So, during tests well below this temperature, only slight variations in capacitance of up to 4% were observed. The measured Curie temperature for PZT-5K4 lies between  $125^\circ\text{C}$  and  $127^\circ\text{C}$ . So, another set of samples of PZT-5K4 was exposed to  $125^\circ\text{C}$  for 4 hours. The capacitance fell by only 4%. So,  $125^\circ\text{C}$  is a safe temperature for this material. Table 2.3 shows the measured Curie temperature. The measurements also show that temperature depoling occurs suddenly and not gradually with rising temperature and leads to a 35-40% loss in measured capacitance.

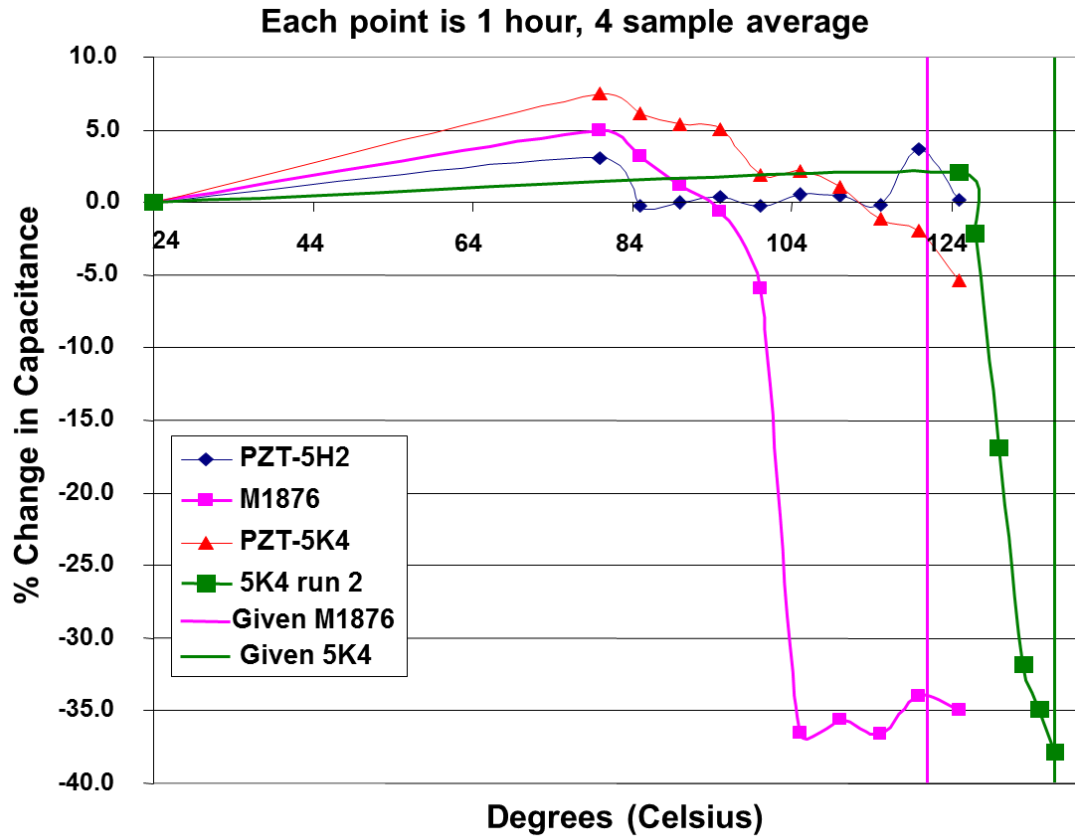


Figure 2.16: Curie Temperature Measurement

Table 2.3: Material Curie Temperatures

Material	Given Curie Temp.	Measured Curie Temp.
M1876	121°C	95-100°C
PZT-5K4	137°C	126°C

Table 2.4: Material Properties

<b>Property</b>	<b>5H2</b>	<b>M1876</b>	<b>5K4</b>
$d_{31}$ ( $\times 10^{-12} m/V$ )	-274	-385	-410
Density ( $kg/m^3$ )	7450	8000	8200
Stiffness (GPa)	61	63.3	63.0
Curie Temp ( $^{\circ}C$ )	195	95	125
40Hz Depoling Field (kV/cm)	6.69	5.12	3.74

### 2.3.4 Material Comparison

Manufacturers do not provide depoling fields so this must be measured experimentally by bonding strain gages to individual plates and seeing at what electric field the butterfly strain to voltage loop develops. The plates are 10 mils thick for PZT-5K4 of size 2 in. by 1 in. The M1876 plates are of the same size except for a thickness of 9.8 mils. The maximum strain range was not measured due to difficulty getting consistent strain gage results between different samples. So, it is assumed that a higher  $d_{31}$  means a higher maximum strain range, but this has not been proven.

A comparison between these two new materials and PZT-5H2 are shown in Table 2.4 using measured properties. PZT-5K4 is chosen due to its higher measured Curie temperature.

### 2.3.5 Soft Material Bender Construction

For an unknown reason, PZT-5H2 and many other harder materials have nickel-based electrodes, but softer materials such as PZT-5K4 and M1876 have gold-based electrodes. This necessitated a new manufacturing method for the piezobenders made from these materials leading to a perfect bond between layers. A perfect bond means that the stiffness predicted by the finite element code matches

the measured stiffness because the bond is not modeled in the code. Many others have stated in literature that their piezobender models need to be refined by accounting for the bond layer. This will be shown to be unnecessary because a perfect bond is achieved by the new bonding method for materials with gold-based electrodes.

### 2.3.5.1 Stiffness measurement

The bender stiffness is measured by clamping one end of the bender between aluminum clamps 0.24 in. wide. The bender is bonded to the clamps using FM196, a film adhesive that requires a 1 hour cure at 100°C (or 1.25 hours at 93°C). The clamps are held in a vise. Loads are attached to the bender tip and the deflection is measured using a laser height sensor with 0.01 mil resolution. For the piezobenders of interest, the stiffness at the tip is  $\geq 0.25 \frac{lb}{mil}$ . At this stiffness, it becomes difficult to measure, because the surface on which the laser gage and vise are mounted can have a similar stiffness. A parallel beam is placed in the vise to remove any motion not due to the piezobender (Fig. 2.17).

One other uncertainty remains, the bender's cantilever stiffness. To eliminate this, an aluminum beam was bonded inbetween clamps in the same way that a piezobender would be (Fig. 2.18). FM196 film adhesive is used between the aluminum clamps in the same way as for a piezoceramic bender. The film adhesive flows when first heated and so in the oven during curing, screws were used to tighten the clamps to the bender for a good bond. The beam's stiffness is assumed known and so, the difference between the measured and predicted stiffness is due to the cantilever. A parallel beam is again used to eliminate any motion not due to the aluminum beam or its cantilever deflecting. The cantilever slope stiffness is measured to be  $9.70 \frac{lb-in}{mil}$  (Fig. 2.19). This cantilever

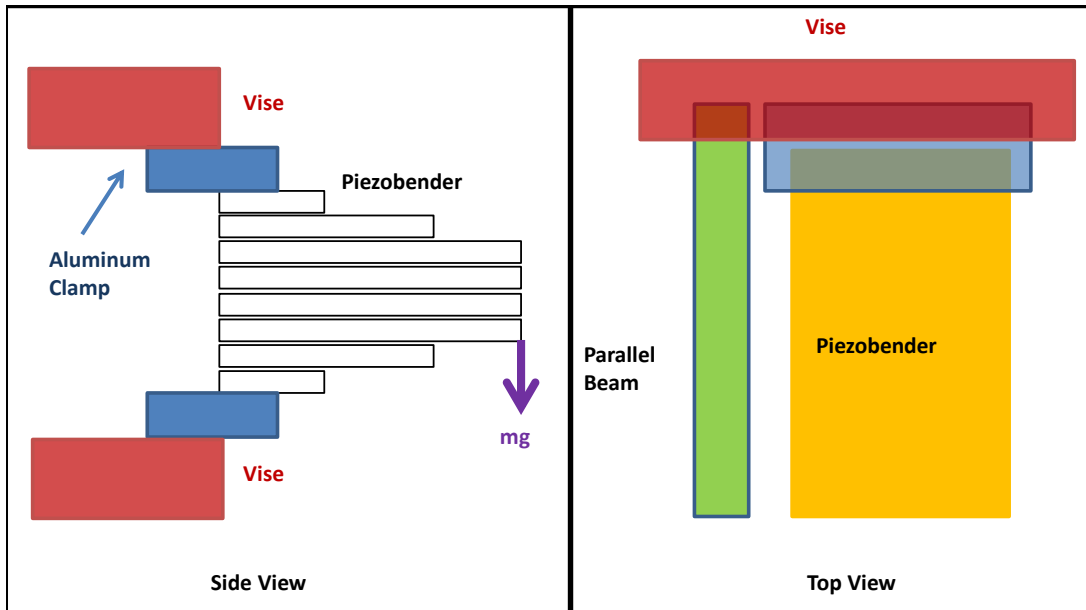


Figure 2.17: Measuring Bender Stiffness with Parallel Beam

arrangement can fit inside the Mach scale blade.

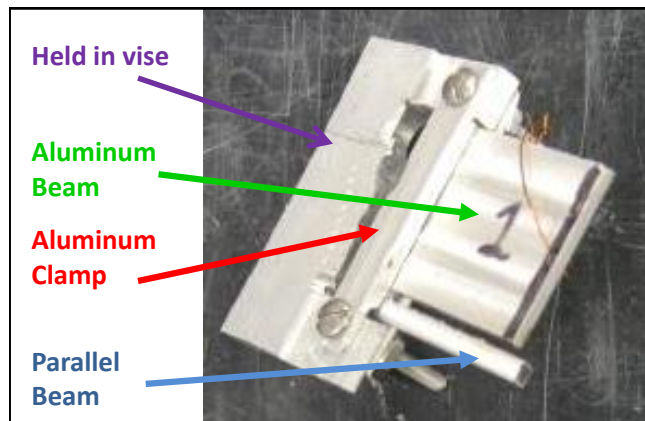


Figure 2.18: Aluminum beam in jig used to determine cantilever stiffness

All stiffness measurements are made with the bender electrodes shorted together and grounded. After a weight is added and before the deflection is measured, any charge that develops due to stress is allowed to discharge to ground. Fig. 2.20 shows a stiffness test for a PZT-5H2 bender with the electrodes shorted and open [69]. The open case has a stiffness that is double the closed case be-

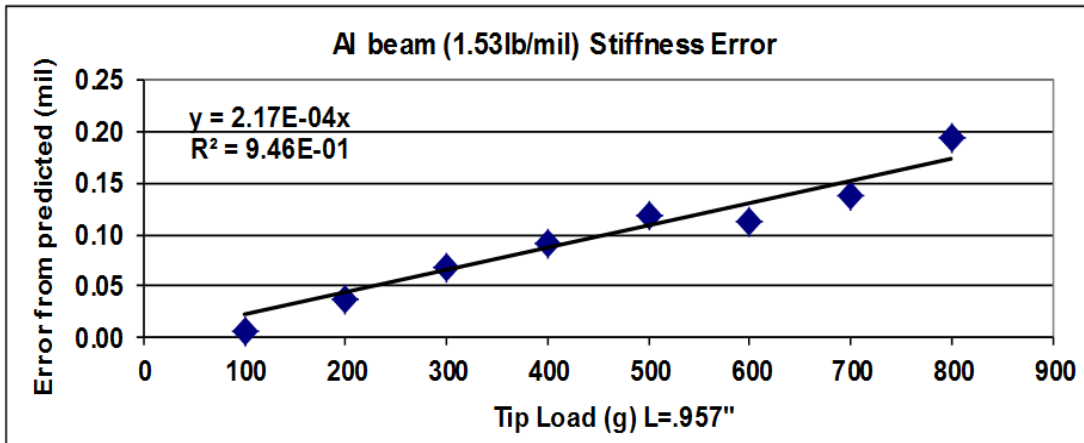


Figure 2.19: Best Case Cantilever Stiffness

cause the electric field that develops due to the applied load causes an opposing moment.

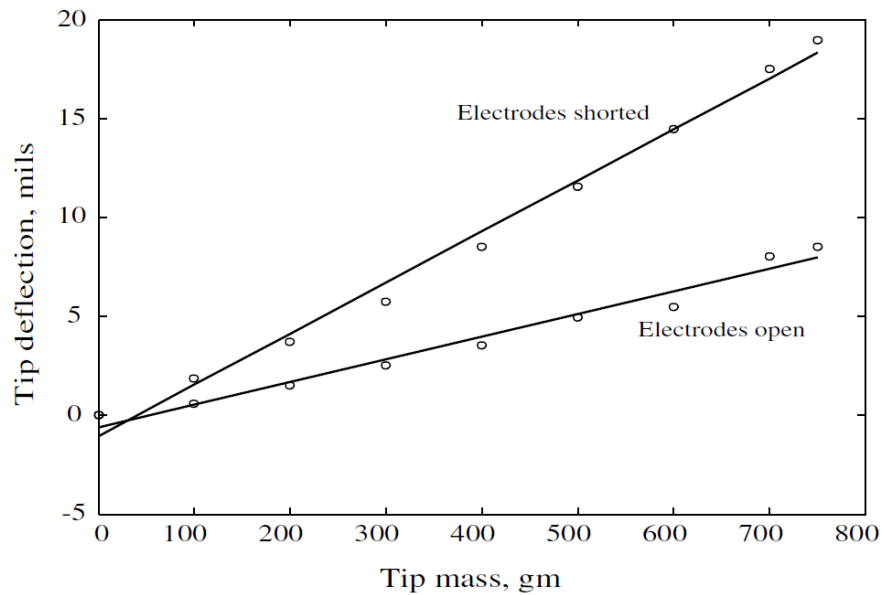


Figure 2.20: Bender Stiffness: Effect of electrical boundary conditions

### 2.3.5.2 Materials with nickel-based electrodes (PZT-5H2)

Before discussing the new bonding method, it is worth looking at the method for making PZT-5H2 benders. The piezoceramic layers are bonded together under

pressure in the oven with M-Bond610 which requires a cure of 1.25 hours at 177°C. MBond610 is a two component, solvent-thinned, epoxy-phenolic adhesive often used for attaching strain gages to a surface [70]. Electrical connections are made between sheets of matching polarity. This method has been validated by Falls [55]. For an 8 layer bender (1 in. x 1 in. x .08 in.) (Fig. 2.21), the Euler-Bernoulli method accurately predicts the measured bender stiffness of  $0.28 \frac{lb}{mil}$ .

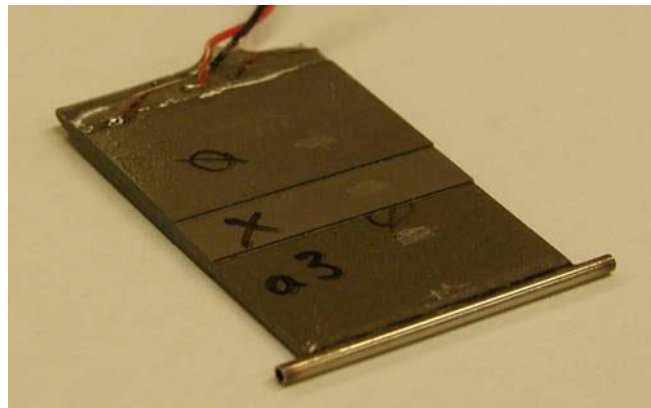


Figure 2.21: 8-Layer PZT-5H2 Bender

### 2.3.5.3 Materials with gold-based electrodes (PZT-5K4)

Many PZT-5K4 benders were made in the same fashion as PZT-5H2, but their stiffnesses did not come close to the predicted stiffnesses. As a side note, MBond600 was used instead of MBond610. MBond600 has a lower curing temperature making it acceptable for the low Curie temperature of 5K4, but once cured, should have the same properties as MBond610. If the bond between layers is a problem, then making an actuator with more layers should accentuate the problem. So, a 12 layer actuator was made with PZT-5K4 10 mil thick layers. The bender is 1.00 in. wide with a taper pattern of

1.08/1.08/0.90/0.80/0.50/0.35 in. with each layer extending 0.25 in. into the aluminum clamps forming the cantilever. The stiffness is seen in Fig.2.22 and the measured stiffness is just 50% of the expected ( $1.64 \frac{lb}{mil}$  vs.  $3.31 \frac{lb}{mil}$ ). The cantilever stiffness is accounted for.

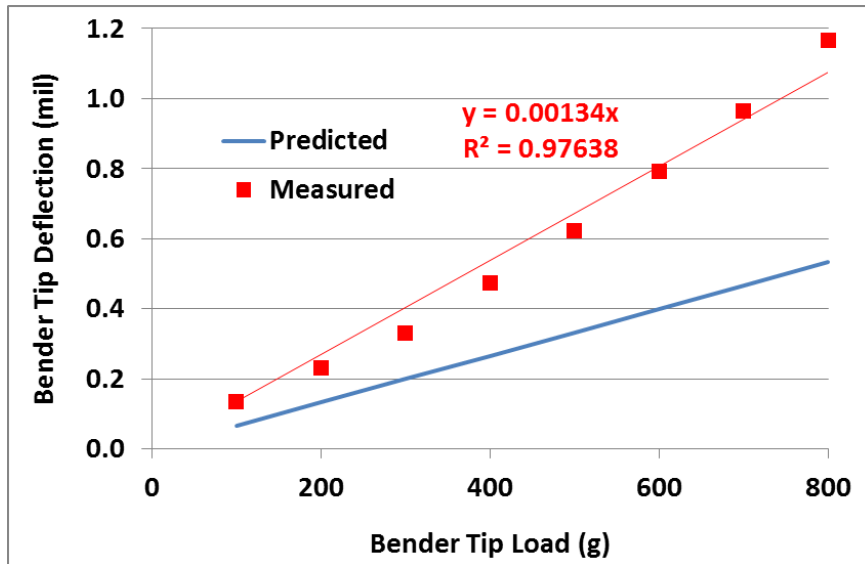


Figure 2.22: 12-Layer PZT-5K4 Bender Stiffness - Poor Bond

It makes sense that a gold-based electrode would require a different bonding method than a nickel-based electrode when the standard reactivity series is examined. Nickel is near the middle of the chart and reacts with acids whereas gold is the second least reactive metal (platinum is the least), and gold reacts only with strongly oxidizing acids. Another 12 layer PT-5K4 bender is made with a new bonding method. The layers are added to each other one at a time with each layer cured with Loctite680 [71] at 93°C for 1 hour at 2 psi. This is well below the Curie temperature of both M1876 and PZT-5K4. Loctite680 is a methacrylate ester that cures anaerobically. A 5 mil brass shim is used at the bender centerline. Any shim thickness less than this leads to a shim with wrinkles that lead to a very poor bond to the piezoceramic. The bender dimensions are 1 in.

wide, 0.125 in. thick and a taper pattern of 1.14/1.14/0.82/0.62/0.36/0.25 in. with 0.25 in. for each layer extending into the cantilever (Fig. 2.23).

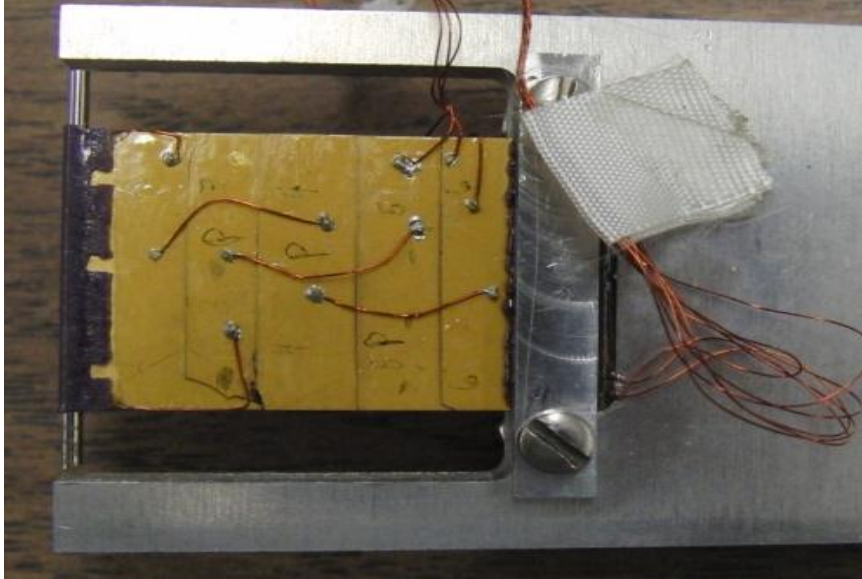


Figure 2.23: 12-Layer PZT-5K4 Bender

The expected stiffness is  $1.04 \frac{lb}{mil}$  and the measured is  $0.98 \frac{lb}{mil}$  with less than 6% deviation (Fig. 2.24). If the cantilever effect is taken out, the measured stiffness is  $1.11 \frac{lb}{mil}$  or 7% more than expected. So, with this new bonding method, the stiffness for a multilayered PZT-5K4 (soft piezoceramic with gold electrodes) matches the value predicted by the Euler-Bernoulli beam theory using finite elements. PZT-5H2 benders made with the MBond600 method also had the stiffness match predicted because PZT-5H2 has nickel electrodes which react with the MBond600.

#### 2.3.5.4 Determining poling direction

Sometimes the piezoceramic layers are available from the manufacturer without the plate poling direction marked. This must be known to properly wire and assemble the bender. A quick way to determine the poling direction that will not

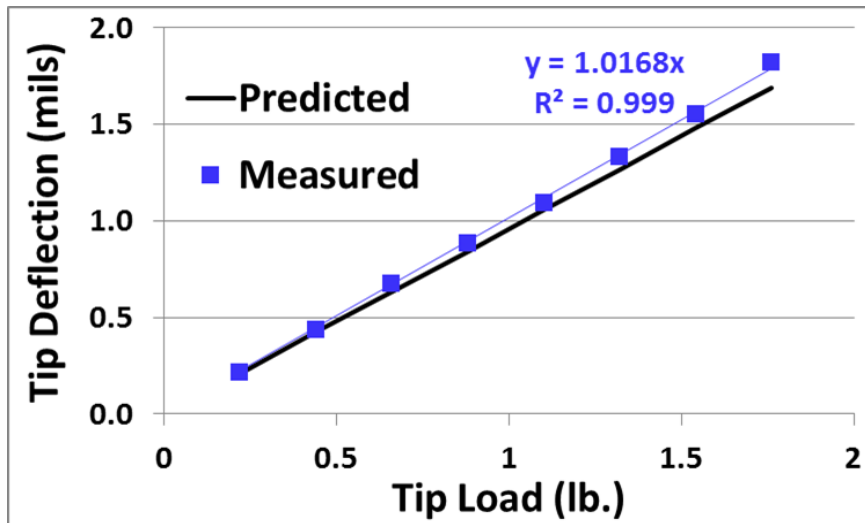


Figure 2.24: 12-Layer PZT-5K4 Bender Stiffness - Good Bond

damage the piezo is needed. A non-destructive, quick method for determining the poling direction uses the charge amplifier circuit shown in Fig. 2.25. The piezoplate is laid on a conductive surface that is grounded to an oscilloscope measuring voltage difference. Then, the positive scope lead is pressed lightly into the exposed plate, so any charge can dissipate through the scope impedance. Then, the positive probe is pressed slightly more into the plate. This causes a compressive stress in the 3 direction (thickness). An initial voltage drop indicates the positive lead is touching the poled side whereas a voltage increase indicates the side touching the conductive surface is the poled side. It is only the initial voltage change that matters. This is the  $d_{33}$  effect.

### 2.3.5.5 PZT-5K4 Bender Construction Conclusions

1. A stiffer bender (more layers) is affected more by a poor bond than a softer (less layers) bender.
2. The stiffness of a best-case cantilever is measured so that the bender stiff-

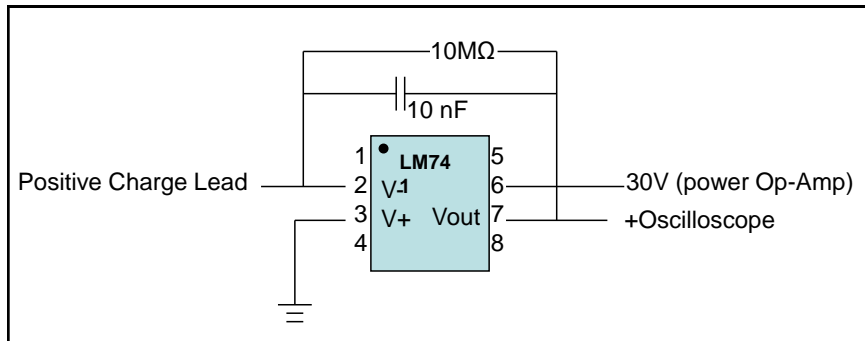


Figure 2.25: Schematic for Charge Amplifier Circuit

ness values have the imperfect cantilever effect removed.

3. Gold-based electrodes require a different adhesive layer between piezoceramic layers than nickel-based electrodes. A methacrylate adhesive where each layer is added one at a time and cured for 1 hour at 93°C with 2 psi applied to the layers during the cure forms a perfect bond for PZT-5K4. The low temperature is crucial due to the low Curie temperature of soft piezoceramics.
4. Much of the literature suggests the need of a conductive adhesive layer. This is only true if the bond layer is thick. A thin bond layer will allow direct contact between the plate faces so the bond does not need to be conductive. In fact, bender manufacturing is easier if the glue is an insulator as there is no concern with shorting between layers due to excess glue.
5. A 12 layer PZT-5K4 bender is constructed with this new method and the predicted stiffness matches the measured, demonstrating several things:
  - (a) A perfect bond can be achieved, so even for a stiff, many layer bender which is like a plate (1 in. width and 1.14 in. length), the stiffness can be predicted by a finite element model of an Euler-Bernoulli beam

where the bond layer is neglected.

- (b) Again, it is unnecessary to model the bond layer - the effort is better spent perfecting the bonding method.
- (c) If the bender stroke is measured and the model can predict stiffness, then the free strain of the piezoceramic can be deduced. This will be discussed in the section on bender stroke.

## 2.4 Transferring Bender Force to Flap

With the bender dimensions and material chosen and the construction method proven, the next step is to efficiently convert the bender tip motion into flap motion.

### 2.4.1 Slotted Rod

Fig. 2.26 shows the bender-flap schematic. In order to ensure that the rod at the end cannot move relative to the bender, a slotted steel rod is used. The rod moves inside the cusp of the flap. Previous work has just bonded a steel rod to the end of the bender [67], [53], but this leads to the rod moving relative to the bender, effectively lowering the bender stiffness. No damage to the bender tip was observed over many actuation cycles from the high local strain and force where the bender tip meets the slotted steel rod. The slotted rod is made by milling a 50 mil wide groove into an 85 mil diameter steel rod (Fig. 2.27). The bender tip thickness is 45 mils and is bonded into the slotted rod.



Figure 2.26: Slotted Rod

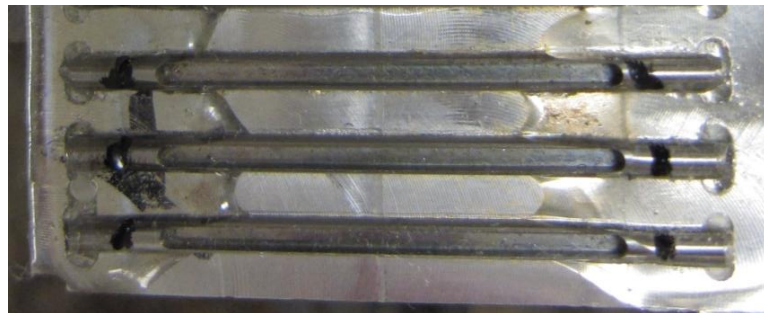


Figure 2.27: Manufactured Slotted Rods

## 2.4.2 Good Cantilever

A good cantilever has a stiffness much higher than the flap stiffness. Otherwise, the bender moment will move the cantilever instead of the flap. The previously described method for cantilevering the bender (see Sec. 2.3.5.1) requires a compressive stress on the bender. It is worth noting that this did not damage the bender. No loss of capacitance due to micro cracks was measured and no arcing was observed with a high voltage applied to the bender.

## 2.5 High Electric Fields

For primary control of the rotor, the bender needs to be driven to its maximum stroke at 40Hz (1/rev for primary control at Mach scale RPM). This means that the highest possible electric fields are applied to the bender piezoceramic plates and so, the bender behavior at high electric field must be understood. The maximum electric field is limited by the depoling field in one direction and dielectric breakdown or arcing in the other direction. A negative field means voltage against the poling direction. High electric field means at least  $-3.54/+10.63kV/cm$  which is  $-90/+270V$  for 10 mil thick piezolayers.

For just piezoceramic plates, Sirohi looked at even higher fields for PZT-5H2 from  $-6kV/cm$  to  $+27kV/cm$ . The strain is linear up to even  $+10kV/cm$  (Fig. 2.28, [66]).

Chapyla looked at PZT-5H plates under compressive stress at up to  $\pm 20kV/cm$  at the molecular level using volume fraction of non-180° domains to explain differences in behavior [72]. Uchino took PZNT to  $\pm 40kV/cm$  and a PZT unimorph bender to  $\pm 7.5kV/cm$  and reported nothing unexpected [73]. For benders made of one or more piezoelectric layers offset from the beam neutral axis, there is

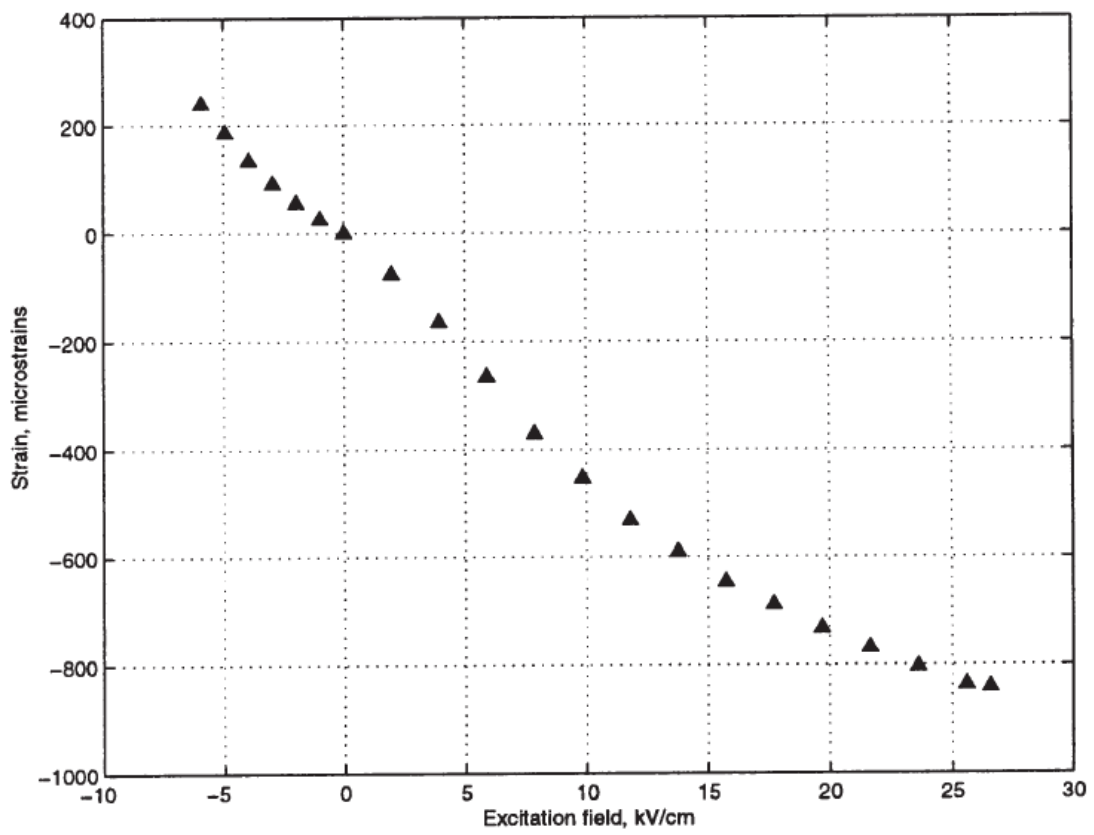


Figure 2.28: Free Strain of a PZT-5H2 10 mil thick plate [66]

a tremendous amount of literature devoted to complex modeling of piezobenders, but very little, if any, experimental validation of these models. The models are often concerned with modeling power draw but this is before even stroke and stiffness of the bender have been validated. Presumably, if the strain and stiffness properties of individual plates are properly modeled, then superposition can be used for modeling more than one plate put together, as in a piezoelectric bender. This section will examine the behavior of piezoelectric benders at these high fields, looking at the basic properties of stroke and stiffness.

### **2.5.1 Different Bias Voltages for PZT-5K4 Bender**

The depoling electric field is already determined as  $-3.54$  kV/cm at 40Hz. Instead of having this limit the electric field in the direction of poling, a non-symmetric driving voltage is used, such that in the poling (positive) direction, a much higher electric field (a multiple of the depoling electric field) can be applied. Arcing and dielectric breakdown limit this maximum field. However, instantaneous dielectric breakdown is not the concern. Instead, there is a tradeoff between increasing the bender stroke at higher voltages and lowering the bender's life. At higher electric fields, the bender will not instantly breakdown dielectrically, but over time, it may.

To examine this positive field limit on the benchtop, a 10-layer PZT-5K4 actuator with 10 mil thick layers was constructed. The layer length dimensions for each half were

0.28\0.40\0.51\0.64\0.64 in. with 0.78 in. width. The actuator tip HPP deflection at 2 Hz driving voltage was measured with a laser height sensor. The driving voltage was increased until the depoling limit of  $-90$ V was reached. The

Table 2.5: Effect of increasing bias on PZT-5K4 Bender Stroke

Bias Change	Change in Voltage Range	Stroke Improvement
3:1 to 4:1	25%	7.0%
4:1 to 5:1	20%	6.0%
3:1 to 5:1	50%	13.4%
5:1 to 5.33:1	5.5%	0.0%

bias (the ratio of voltage in poled direction to depoled direction) was increased from 3:1 (-90V/+270V,  $-3.54kV/cm/+10.63kV/cm$ ) to 5.33:1 (-90V to +480V,  $-3.54kV/cm/+18.89kV/cm$ ). The results are shown in Figure 2.29 and tabulated in Table 2.5. In the plot, the maximum actuator stroke is the focus. As the bias increases, the negative applied voltage is lower at the same RMS voltage. Moving from -80V to -90V has a larger effect on stroke than moving from +200V to +220V. This is why the lines shift right as the bias is increased.

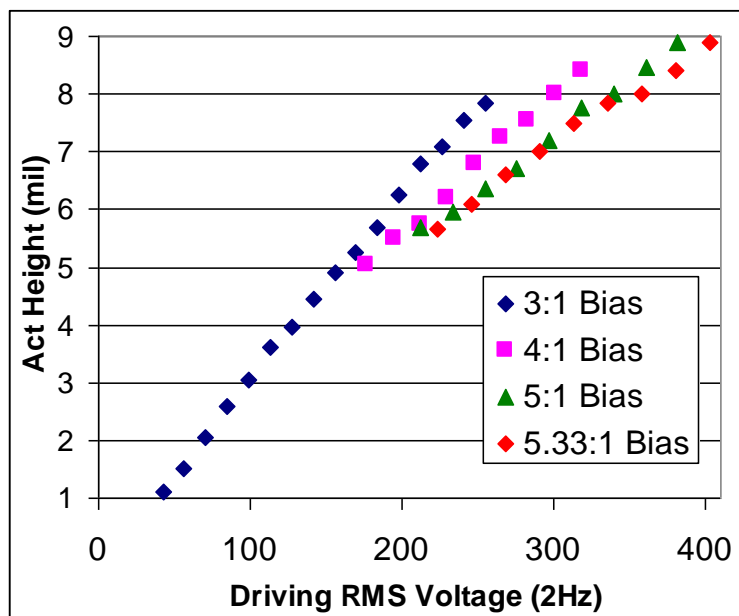


Figure 2.29: Effect of increasing bias on PZT-5K4 Bender Stroke

So, by changing to a 3:1 bias (-90V/+270V) from 4:1 bias, the actuator loses

7% of its stroke capability. This actuator was then tested for fatigue. The actuator was run from -90V to +360V at 33Hz for 247500 cycles (125 minutes) before dielectric breakdown took place. Running at -90V/+270V should lengthen the actuator life beyond this. It is clear that the 5K4 material is approaching a saturation in strain as a 50% increase in voltage range (3:1 to 5:1) causes only a 13% increase in stroke. If the bender stiffness remains constant with increasing voltage, then the increase in stroke seen here, is due to a directly proportional increase in material strain. This will be proven to be the case shortly.

## **2.5.2 Bender Stiffness at High Electric Fields**

Contrary to the vast amount of literature on piezoelectric benders, the benders relax with time in the direction of an applied load. In literature, it is clear that a bender should hold its position over time with an applied load. This relaxation will be proven to be not related to creep or the softening of the bender stiffness. For low applied voltage, Jung, et. al developed a controller to deal with a piezo stack actuator creep of a few percent of initial step response by controlling the voltage step input down in amplitude with time [74]. Sirohi documented creep for fields varying from 0.4kV/cm to 5.5kV/cm for the strain in 5H2 plates. The percent of strain creep is observed to be independent of field strength and field direction. After 30 minutes, the strain had increased up to 18% over its original value [35]. The current relaxation observed is greater in amplitude than Sirohi found with creep, happened over a smaller timescale and was in the opposite direction of creep.

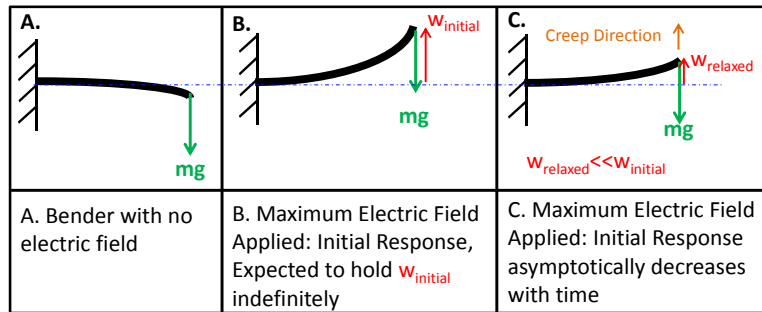


Figure 2.30: Bender Relaxation

### 2.5.2.1 Bender Compliance

Many different actuators have been built with varying number of layers (4, 6, 8, 10, 12 layers using both PZT-5K4 and PZT-5H2 materials) and these all exhibited this phenomenon of relaxation. Bender relaxation means that if a low frequency (2Hz) signal is used to drive the bender and a steady load is applied to the tip, the amplitude of the motion will remain unchanged with load, but the mean will change by around 100% more than would be expected from the measured stiffness with no electric field. The relaxation is dependent on the electric field strength.

For a 12 layer 5K4 actuator, Fig. 2.31 shows the stiffness under different electric fields, up to 10.63kV/cm (270V per 10 mil thick piezo plate). The actuator deflection is the change in the mean of the tip motion at 2Hz. The amplitude of motion is independent of the applied steady tip load, but the mean is not. Each measurement is taken after the actuator has had the electric field applied for 2 seconds with the weight suspended from the tip. The bender voltage is set by the driving amplifier, or in the no voltage case, the piezoceramic layers are discharged to ground (short-circuit condition).

As the electric field strength is increased, it appears that bender compliance has increased significantly (by about 60%). This was not expected, according

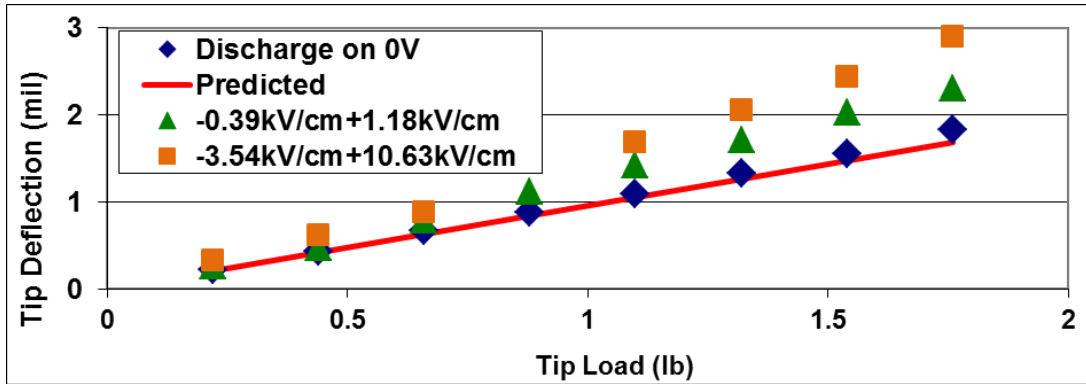


Figure 2.31: 12-Layer PZT-5K4 Bender Compliance for 2Hz Field

to the published literature. This behavior is seen to be the same for both 5K4 and 5H2 benders of 4, 6, 8, 10 and 12 layers. It is also true for a commercial PZT-5H2 bimorph( Fig. 2.32).

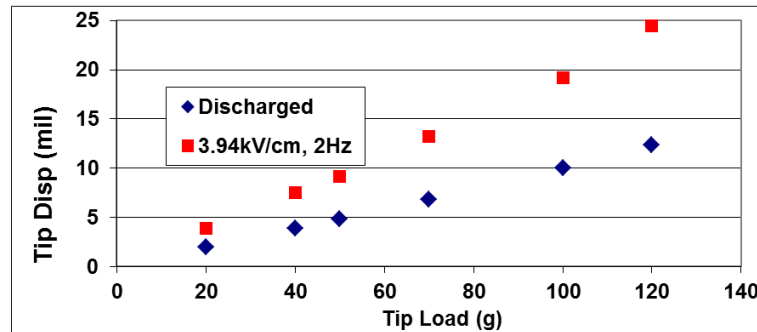


Figure 2.32: Commercial PZT-5H2 Bimorph Compliance, No voltage vs.  $\pm 3.94kV/cm$

Several tests will be discussed to prove that this phenomenon is not related to the bender compliance increasing with increasing electric field, but instead, it is a relaxation of the actuator tip in the direction of the applied constant tip load.

### 2.5.2.2 Single Plate with Drift Removed

The stiffness of a single PZT-5K4 plate both with and without an electric field was measured. A load is hung from the plate tip (cantilevered at one end) and the tip displacement is measured with a laser height sensor. A single plate is not expected to move vertically with an electric field as it is not a bender, but just a single layer undergoing contraction or expansion. In practice, after a DC voltage is applied, the plate tip drifts in an arbitrary direction in a free condition (when no load is present). With a load present, the plate drifts in the direction of the applied load. The rate of drift asymptotically decreases. Before measuring stiffness with an electric field, the plate is allowed to drift until it stops drifting (takes several minutes) before applying the loads and measuring deflection (Fig. 2.33). The results of this test are shown in Fig. 2.34.

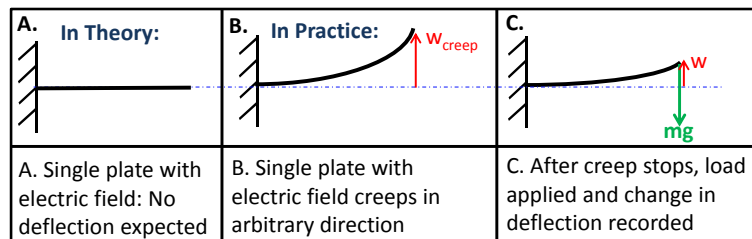


Figure 2.33: Measuring Single Piezo Plate Stiffness with Electric Field

So, after the drift is removed, the measured stiffness for no electric field and fields of 0.39kV/cm and 3.54kV/mm are seen to be the same. So, the stiffness of the material is not changing with electric field.

### 2.5.2.3 Dead Cantilever Hypothesis

It is possible that although the material stiffness does not change with increasing electric field, that the bender stiffness does. The bender stiffness could change for one of two reasons. First, the bond layer could weaken with high voltage,

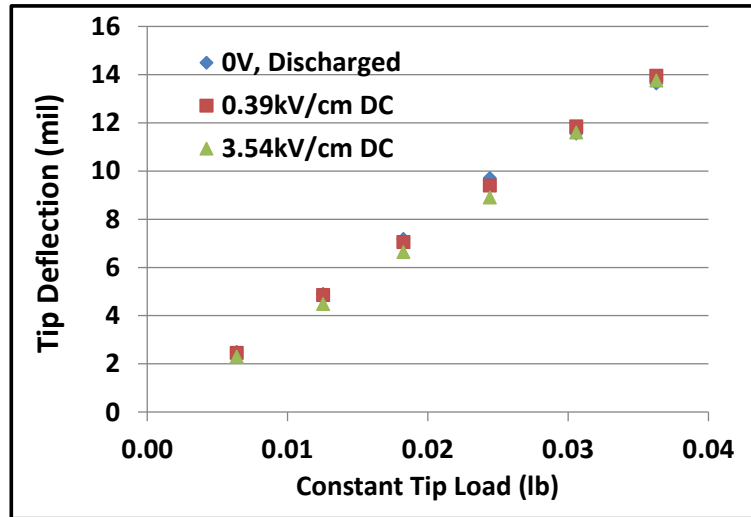


Figure 2.34: Single Cantilevered PZT-5K4 Plate Stiffness with High DC Electric Field

such that the individual piezoceramic layers slide relative to one another. This is highly unlikely as each bond layer has no electric field (no voltage drop across bond) and if the bond is slipping, then the bond should be damaged over time. However, this was not observed. The second option is the "dead cantilever" hypothesis. The bender extends into the cantilever. The bender top half and bottom half expand and contract ( $d_{31}$  effect) in the opposite direction. Inside the cantilever support, each half of the bender can be thought of as a  $d_{33}$  stack actuator. Each stack actuator has a large blocked force and a small stroke. Consider the 12-layer actuator in Sec. 2.3.5.3. Each 6-layer half has a theoretical stroke of 0.061 mils and a blocked force of 140.3 lb. Ideally, these cancel out, but local variations may cause the root slope of the beam to change (at the cantilever), which would relieve the large stress caused by not allowing the stack actuator to expand. So, if the cantilever support area of the actuator does not have an applied electric field ('dead cantilever'), then the relaxation may be eliminated. In order to verify this hypothesis, a couple of experiments were

conducted.

#### 2.5.2.4 Stiffness of Bimorph with Dead Cantilever

A bimorph was made from a 5 mil thick brass shim and a 10 mil thick 1.00 inch wide PZT-5K4 plate on both sides of the shim (Fig. 2.35). The shim extends beyond the piezo plates such that only the shim is cantilevered. The stiffness of the beam is measured by hanging weights from the tip and measuring the tip deflection for a few electrical conditions. The results are tabulated in Table 2.6, as well as graphed in Fig. 2.36 to show linearity of results. The bender with weight applied is allowed to settle for 30 seconds before measuring the tip displacement. The applied voltage is  $-3.543\text{kV}/\text{cm}/+10.630\text{kV}/\text{cm}$  ( $-90\text{V}/10\text{mil}/+270\text{V}/10\text{mil}$ ).



Figure 2.35: PZT-5K4 Bimorph with No Piezoceramic in Cantilever ('Dead')

For DC tests, the beam tip was allowed drift until it stopped before taking measurements. This helped eliminate drift from the measurement. The stiffness actually increased for DC down and was unchanged for DC up. The sinusoidal driving signal stiffness was expected to be inbetween DC up and DC down and

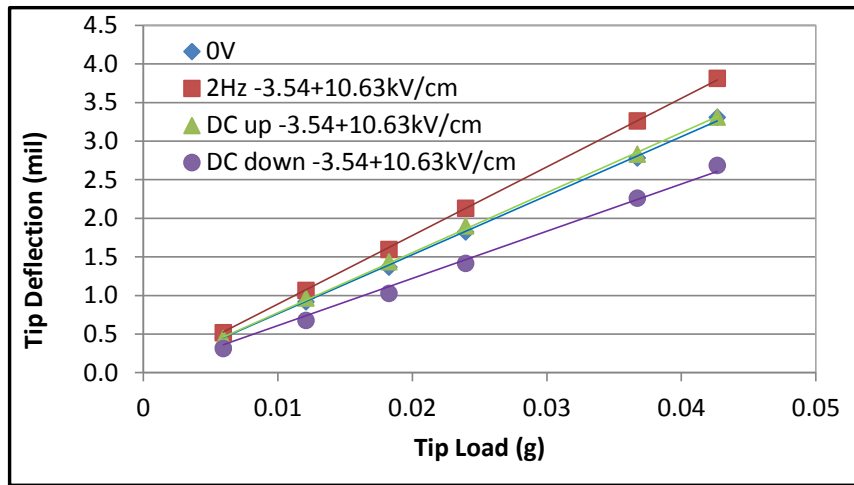


Figure 2.36: PZT-5K4 'Dead' Bimorph Stiffness

Table 2.6: PZT-5K4 'Dead' Bimorph Stiffness

Electrical Field	Stiffness (N/m)	Off from 0V Stiffness
None	2297	-
2 Hz Sine	1975	-14.0%
DC up	2256	-1.8%
DC down	2871	+25.0%

that is what is seen. This test suggests the relaxation phenomenon is possible in the piezo plates ( $d_{31}$  effect) and it is not the property of the plates in a  $d_{33}$  mode, such as in a stack actuator, as this test setup does not have any piezo plates clamped in the cantilever support. The 2Hz tests suggest that applying a load forces the actuator to relax in the direction of the applied load. In order to arrive at a better understanding, another method of measuring stiffness for the beam was carried out.

A square wave electrical field is applied to the beam causing it to oscillate at its natural frequency. Fig. 2.37 shows the square wave. Fig. 2.38 shows the oscillatory response. The beam is also struck with no electric field and a DC electric field.

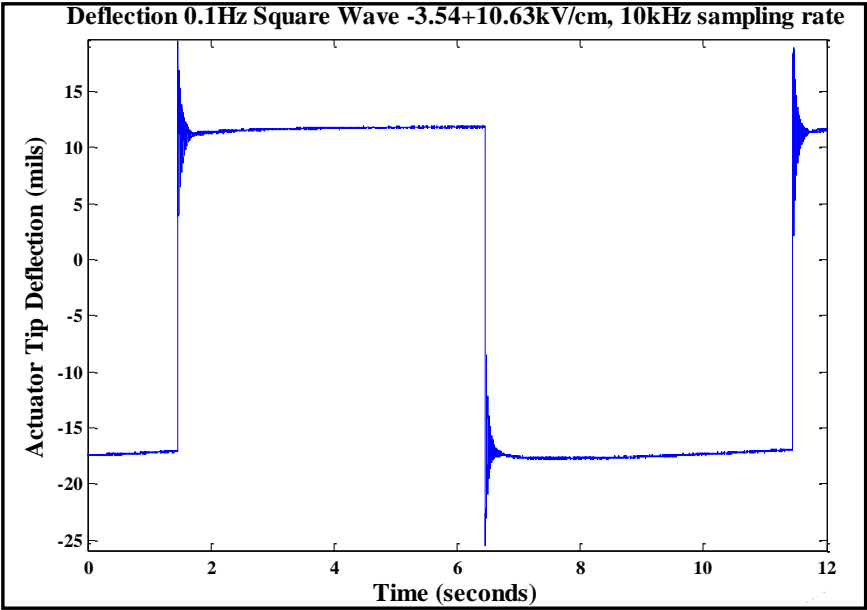


Figure 2.37: Squarewave Output from 'Dead' Bimorph

Fig. 2.38 shows actuator transient response. It can be seen that the actuator drifts slightly. From this impulse testing, the natural frequency was determined and the results tabulated below in Table 2.7. As before, the applied voltage

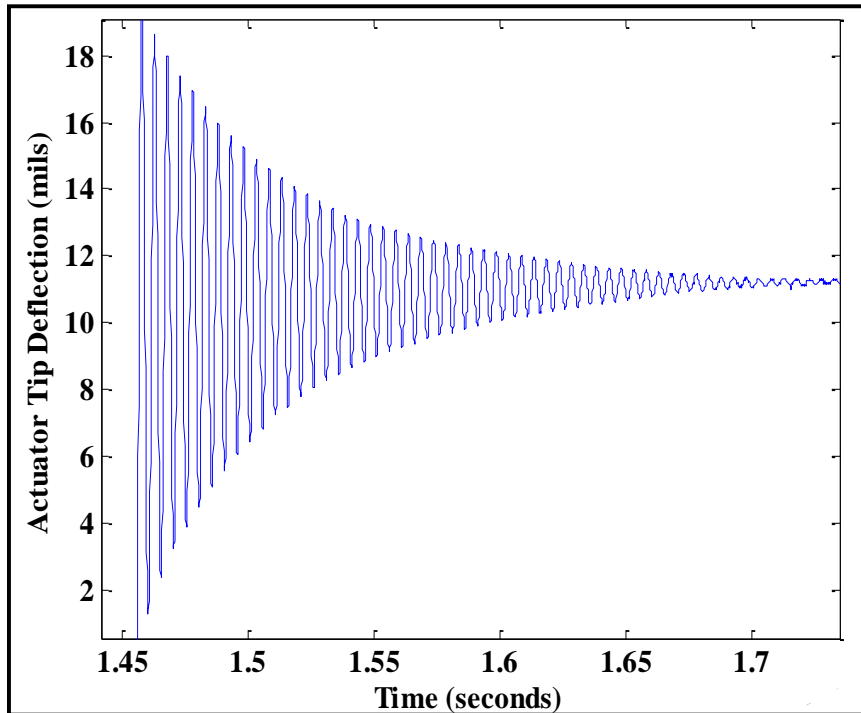


Figure 2.38: Close-up of Squarewave Output from 'Dead' Bimorph

is  $-3.54\text{kV/cm}/+10.63\text{kV/cm}$ . For each square wave, two natural frequencies were found: one for after the bender moved up and another for after the bender moved down. The uncertainty in frequency measured correlates to a less than 2.0% uncertainty in stiffness.

Several observations were made. First, the trends for the electrical impulses are the same as the weight tests. Secondly, the sinusoid has the lowest stiffness. Third, the stiffness for all the squarewaves is higher than the DC case. This is because for the DC tests, the drift has been removed by only actuating in one direction and letting the bender settle. It could be that when the beam field direction switches, the drift resets and so begins again making the stiffness appear lower. It does imply that the small change in stiffness for different electrical condition and the drift are connected. The drift is more pronounced right after the electric field changes. The cantilever is the same for up and down because

Table 2.7: PZT-5K4 'Dead' Bimorph Stiffness by Frequency

Electrical Field	Fundamental Freq. (Hz)	Normalized Stiffness	Off from No Field
No Field	214.6	1.000	-
DC down	225.2	1.101	10.1%
0.1 Hz Squarewave Down	221.2		
1 Hz Squarewave Down	221.1		
10 Hz Squarewave Down	221.6		
Average Squarewave Down	221.3	1.063	6.3%
DC down	209.3	0.951	-4.9%
0.1 Hz Squarewave Up	201.5		
1 Hz Squarewave Up	199.2		
10 Hz Squarewave Up	198.3		
Average Squarewave Up	199.7	0.865	-13.5%

no piezoelectric material is in the cantilever support. So, the small change in frequency from up to down could be due to a material property perhaps. The frequency would change because the plates may be slightly dissimilar. So, if the effect is dependent on field strength and the field applied to each plate is different - one plate is at  $-3.54\text{kV/cm}$  and the other plate is at  $+10.63\text{kV/cm}$ , then, the effect will different when the direction of the tip changes. The voltage on the plates is reversed, so that the one with  $-3.54\text{kV/cm}$ , then has  $+10.63\text{kV/cm}$ , and vice versa. With dissimilar plates, the effect will not be symmetric. The main point though, is that the stiffness does not change enough to explain the change in compliance seen in Fig. 2.32. Also, the stiffness change measured by frequency both increases and decreases depending on the DC direction, so further testing is needed for clarification.

#### 2.5.2.5 Stiffness of 4-Layer Bender with Dead Cantilever

A 4 layer bender could exaggerate the phenomenon observed in the dead cantilever bimorph in order to bring clarification. The bender has a width of 0.49

in. with 10 mil thick plates. The length of all 4 plates is 0.73 in. with a 0.24 in. cantilever. The cantilever is electrically isolated from the piezo plates beyond the cantilever.

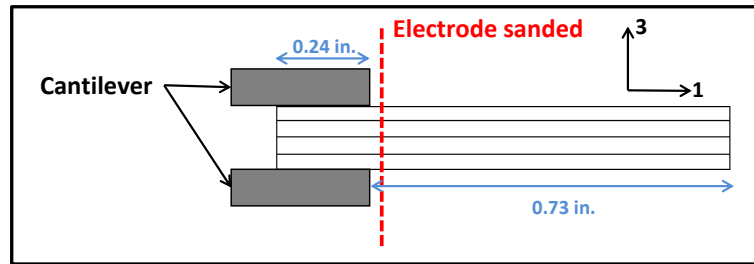


Figure 2.39: 4-Layer Bender Stiffness with Electrically Separate Cantilever

This is done by lightly sanding off just the electrodes from the plates up to where the cantilever support ends, separating it from the area beyond the cantilever begins. Thus, the cantilever can have a different electric field than the rest of the bender. Various electrical conditions can be tried such as the cantilever with no electric field (dead cantilever), a live cantilever with the same field as the rest of the bender, the cantilever contracted in the 3 direction or the cantilever expanded in the 3 direction from the  $d_{33}$  effect.

The stiffness was measured by hanging weights as before. The voltage applied to the bender beyond the cantilever is always  $-3.54\text{kV/cm}/+10.63\text{kV/cm}$ . For all DC cases, the voltage was applied and the bender was allowed to stop drifting (5-15 minutes) before the weights were applied and the tip deflection measured. The results are presented in Fig. 2.40 and tabulated in Table 2.8.

Live means that the cantilever has the same electric field as the active bender and free indicates that the cantilever part is electrically free-floating. The predicted value is from beam bending theory for a uniform beam. The error from predicted for no field is just 28% which indicates a good bond layer and root end support. The test suggests that the cantilever electrical condition does not affect

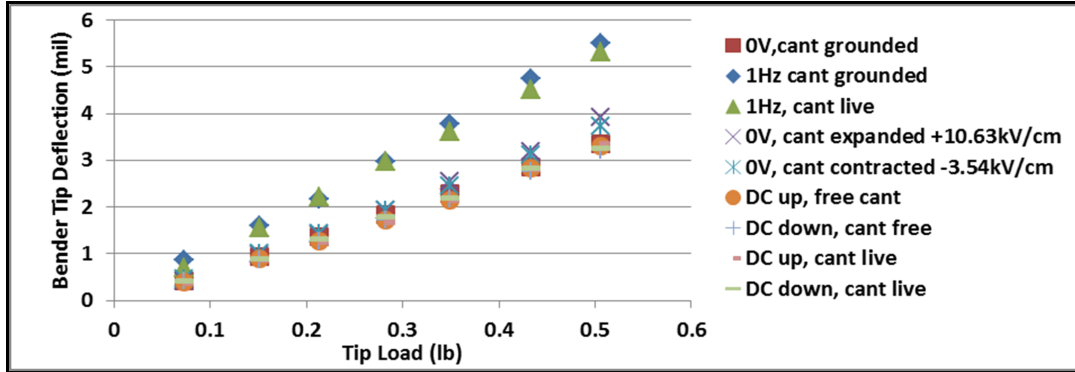


Figure 2.40: 4-Layer Bender Stiffness with Various Cantilever Electrical Fields

Table 2.8: PZT-5K4 4-Layer Bender Stiffness with Various Cantilever Electrical Fields

Bender Electrical Condition	Cantilever Electrical Condition	Stiffness, lb/mil	Compliance Error Over Predicted	Compliance Error Over No Field for Bender and Cantilever
Predicted, No Field	No Field	0.183	-	-
Measured, No Field	No Field	0.144	28%	-
1 Hz	No Field	0.092	98%	56%
1 Hz	Live	0.096	91%	50%
No Field	Expanded +270V	0.137	34%	5%
No Field	Contracted -90V	0.140	31%	3%
DC up	Free	0.165	11%	-13%
DC down	Free	0.168	9%	-14%
DC up	Live	0.165	11%	-13%
DC down	Live	0.164	12%	-12%

Table 2.9: PZT-5K4 4-Layer Bender Stiffness, 'Dead' Cantilever, Maximum Electric Field

	<b>Avg. Freq (Hz)</b>	<b>Stiffness Uncertainty</b>	<b>Stiffness Ratio</b>	<b>Stiffness Change from 0V</b>
0V	1042	6%	1.00	-
DC down	1013	4%	0.97	-3%
DC up	1089	5%	1.05	5%

the stiffness. However, it may still affect the drift, but for these measurements, the drift has been removed. Interestingly, the stiffness has increased by around 13% with field for all DC cases.

The stiffness was also measured using the frequency method for an electrically free floating cantilever. A square wave did not provide a large enough impulse for this stiff bender to get a good frequency reading before the oscillation was dampened out. So, just DC was applied in both directions and then the bender was struck 10 times and the average frequency recorded. This test showed that the stiffness does not change with electric field. The frequency test removes the effect of relaxation from the stiffness measurement. So, these results indicate that the bender relaxation (very large drift) explains the changes in measured stiffness. This is strong evidence that the bender stiffness (nor the material stiffness) does not change with high electric fields.

#### **2.5.2.6 4-Layer Bender Relaxation**

The time history of applying a very low frequency squarewave without load is shown in Fig. 2.42. Figure 2.41 shows the relaxation phenomenon in one direction.

The bender relaxes much more than expected from creep. Even after 100s,

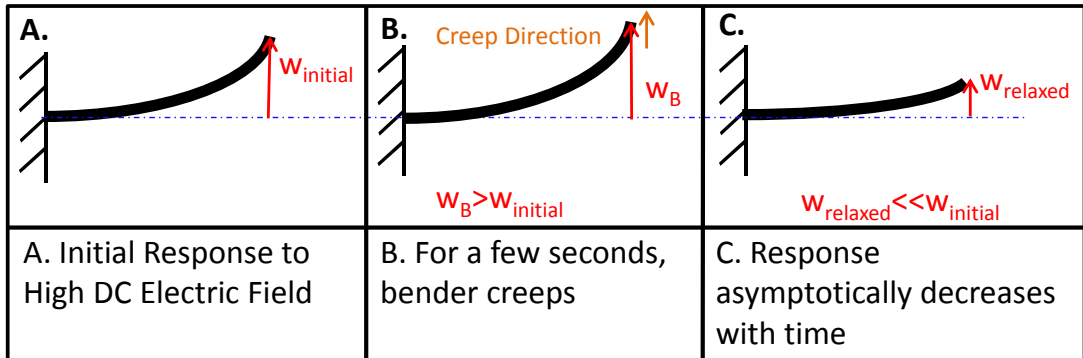


Figure 2.41: Bender Relaxation Sequence

the bender tip has not settled to a steady state, though it is relaxing at a slower rate than initially. Initially, the bender drifts in the initial direction of motion. This should be the creep often mentioned in literature. However, after this, the actuator starts to relax and moves against the initial direction of motion. The relaxation is not due to the cantilever support (as this test has a dead cantilever) and it is not due to the bender stiffness changing (as shown previously).

#### 2.5.2.7 4-Layer Bender Constrained by Spring

The tip of the 4 layer bender is constrained by a linear spring and driven by a sinusoidal voltage (Fig. 2.43). This allows a simple measurement of actuator energy. Without a tip spring, it is unclear if an increase in bender tip stroke is due to a softening of the actuator or an increase in the actuator moment produced.

From the previous discussion, it can be assumed that the actuator stiffness is not changing, but this test does not require this assumption. For  $\pm 3.54 kV/cm$ , several cantilever conditions were tried: dead cantilever, live cantilever and anti-live cantilever. Anti-live cantilever means the cantilever electric field is  $180^\circ$  out of phase with the bender electric field. The results of the spring motion in Table

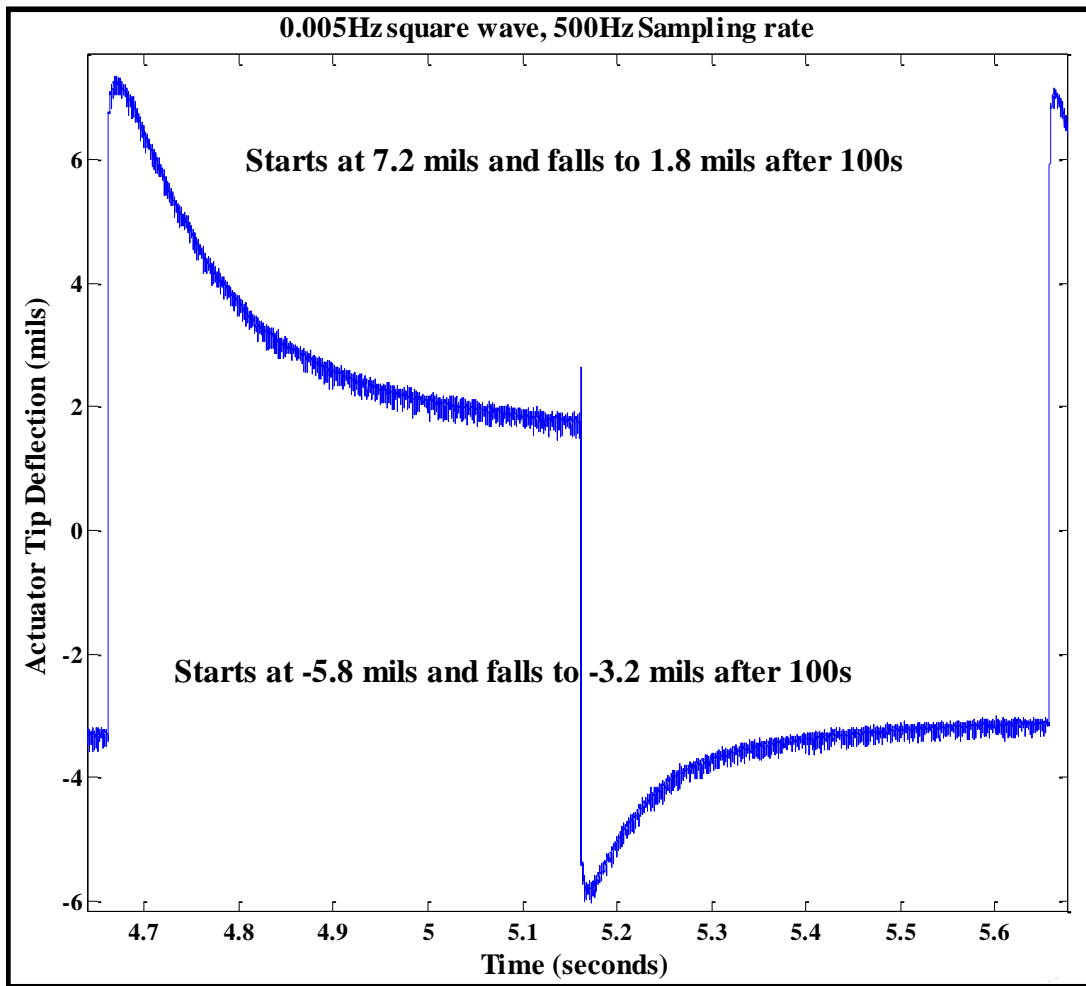


Figure 2.42: 4-Layer Bender with Dead Cantilever Response to  $-3.54\text{kV/cm}/+10.63\text{kV/cm}$  0.005Hz Squarewave

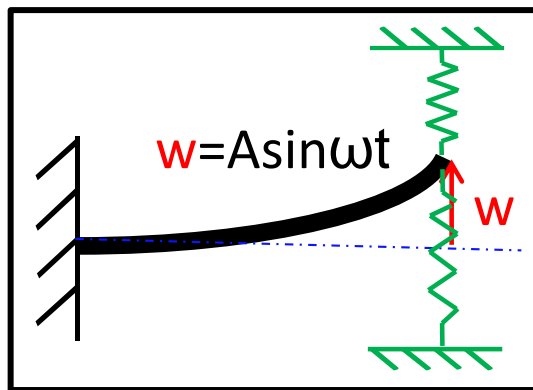


Figure 2.43: 4-Layer Bender Constrained by Spring

Table 2.10: Constrained Bender Stroke with Various Cantilever Electrical Conditions

Cantilever Electrical Condition	Stroke (mil)	Stroke Change	Energy Change
Dead	0.955	-	-
Live	1.065	+11.5%	+24.4%
Anti-Live	0.830	-13.1%	-24.5%

2.10. It shows that the live cantilever is best in terms of actuator output energy.

### 2.5.3 PZT-5K4 maximum strain

It has been proven that the stiffness of a multilayer bender does not change at high electric fields. So, if the stroke of the bender is measured, the material free strain can be extrapolated. Free strain and bender stroke are directly proportional. For the 12-layer PZT-5K4 bender whose stiffness matched predicted, the stroke at 2Hz,  $-3.54\text{kV/cm}/+10.63\text{kV/cm}$ , is 11.64 mil HPP. This means that the piezoceramic plates had a strain range of  $1022\mu\epsilon$ . PZT-5H2 has a strain range of  $790\mu\epsilon$  at  $-4.72\text{kV/cm}/+14.16\text{kV/cm}$  [35]. So, this is an increase of 29% over PZT-5H2 (66% increase in strain energy). If the electric field is extended to  $-3.54\text{kV/cm}/+17.72\text{kV/cm}$ , the strain range is increased to  $1159\mu\epsilon$ . This is an extrapolated conclusion. It would be better to have strain gage data for many piezoelectric materials at high electric fields.

### 2.5.4 High Electric Field Conclusions

The following conclusions are drawn:

1. PZT-5K4 offers a significant increase in strain range (29%,  $1022\mu\epsilon$ ) at a lower driving voltage for the same stiffness compared to PZT-5H2.

2. Increasing the electric field from  $-3.54\text{kV/cm}/+10.63\text{kV/cm}$  to  $-3.54\text{kV/cm}/+17.72\text{kV/cm}$  increases strain by 13%, but also shortens the bender life.
3. The cantilever electrical field does not affect stiffness but it does affect the bender stroke.
4. The bender (and piezoceramic material) stiffness is not a strong function of electric field strength. Evidence of a slight stiffness increase (about 10%) at high electric fields is observed.
5. Piezobenders relax with time. This is an undocumented phenomenon. It is much larger than creep. A 4-layer piezobender lost 60% of its maximum initial DC stroke in 100 seconds. It is not associated with any change in the material stiffness due to field or the bender layers slipping relative to one another.

## 2.6 Conclusions

The taper pattern of a piezobender for driving a trailing edge flap for primary control of a Mach-scale rotor has been optimized. After an extensive survey of commercially available piezoceramics, two new 'soft' materials, PZT-5K4 and M1876, were thoroughly examined for the piezobender. PZT-5K4 was chosen over M1876 due to its higher Curie temperature. In comparison to PZT-5H2, PZT-5K4 offers a large increase in strain energy ( $> 60\%$ ) at lower driving voltages for the same stiffness. A new bonding method for PZT-5K4 is developed that yields a perfect bond between piezoceramic layers. Perfect means that a simple Euler-Bernoulli beam method correctly predicts the bender stiffness without incorporating bond layer effects. A good cantilever support is developed for

the piezobender in a Mach scale blade. Then, the use of a slotted rod in the cusp for transferring the bender stroke and stiffness to a flap is demonstrated. The piezoceramic and bender stiffness are proven to not decrease with increasing electric field. However, a new phenomenon is observed, called relaxation, where the bender loses much of its initial maximum stroke with time. In order to examine this phenomenon, the cantilever supported part is electrically isolated from the rest of the bender. Then, different electrical fields were applied to the cantilever than the bender. The cantilever electric field does not decrease bender stiffness, but it does affect the bender stroke.

For continued improvement in piezobender design, it would be useful to have not just the piezoelectric coefficient ( $d_{31}$  and  $d_{33}$ ) for various materials, but their strain vs. electric field data up to the maximum electric field that can be applied. It would also be of value to have an understanding for what molecular phenomenon limit piezoceramic strain. Does the strain saturate (no longer increase with increasing electric field) because all the dipoles have rotated? Or are other phenomena involved? If this was known, then a key question could be answered: Does a higher piezoelectric coefficient mean a larger strain range, or just that for the same maximum strain range, a lower driving voltage is required? Also, this needs to be for reasonable electric field strengths. Park [75] and Randall [76] have looked at some of these questions and found materials with very high strain (single crystal materials). However, the material stiffness is not provided and the electric field strengths are in excess of 30kV/cm. Even though the materials have the dielectric strength to take these high electric fields, it would be very difficult to avoid arcing for a piezobender in a rotor blade at this very high field strength.

## Chapter 3

# Mach Scale Rotor

### 3.1 Overview

The goal of this research was to demonstrate primary control of a Mach scale rotor blade with trailing edge flaps driven by a piezoelectric actuator. The previous chapter focused on the development of a piezobender that could fit inside the blade profile of a Mach scale rotor blade. This chapter will focus on the development of the rotor blade. TE flaps actuated by piezoelectric actuators have been successfully employed for vibration control in both Froude scale [77] and Mach scale [53] wind tunnel tests. However, no experimental work has been carried out to demonstrate primary control with integrated flaps.

Compared to vibration control, primary control necessitates the use of larger flaps, more powerful actuators, larger actuation strokes and lowering the blade torsional frequency. Integration of these characteristics within the volumetric constraints of the blade, while maintaining low weight and sufficient structural integrity, imposes a major challenge in the development of a swashplateless rotor system. Sirohi [78], Allen [67] and Bao [79] demonstrated marginal swashplateless control in hover at 1200 RPM for a 66 in. diameter rotor with a soft

pitch link and integrated TE flaps. A multilayer, tapered PZT-5H2 bender was used. Beyond 1200 RPM, flap deflection degraded rapidly due to high centrifugal forces. Several pitch link stiffnesses (torsional frequencies) were tested at 900 RPM and 1200 RPM. With lower torsional frequencies (as low as 1.26/rev), the flap effectiveness (blade root pitching to flap deflection) increased. This was, of course, expected. At 1200 RPM and 15° index angle, the maximum flap deflection yielded  $\pm 8\%$  normal force authority. The present work builds on this previous work.

The objective of the present work is to systematically test in different flight conditions the primary control of the rotor system. Desired wind tunnel testing in the Glenn L. Martin wind tunnel imposes a constraint on the rotor diameter. An existing articulated rotor hub for the University of Maryland model rotor rig is used for convenience. The rotor blade has a length of 28 in. plus a 5 in. root cutout for a total diameter of 66 in. This requires the blade to spin at 2400 RPM (tip Mach number 0.65) to match the tip speed of the UH60-A rotor system. This means that for primary control, the flap must operate at 40Hz for 1/rev inputs. The blade in turn must survive the high CF environment, support the flaps and have a CG ahead of the  $\frac{1}{4}c$  in order to avoid blade divergence or flutter. As discussed in Chapter 1, Mach scale rotors are difficult, because the CF loading is much higher than the full scale. For example, a 1/5th scale model will experience five times the CF loading of a full scale blade. To simplify construction, the blade has a rectangular, untwisted planform with a uniform NACA0012 airfoil. We expect that these variations from full-scale rotor systems may have small effects on the concept worthiness for primary control. The flap sizing was guided by UMARC. The basic blade properties are shown in Table 3.1. The flap is divided into 2 equal span flaps.

Table 3.1: Mach Scale Rotor

<b>Rotor</b>	
No. of Blades	4
Diameter	66 in.
Blade Span	32.75 in.
Blade Chord	3.15 in.
Airfoil	NACA0012
Max. RPM	2400 (40Hz)
<b>TEF</b>	
Span	28%R
Chord	15%c
Radial Location	75%R

In this chapter, the blade assembly will be described in detail. The flap assembly is designed carefully in order to handle the high CF environment. It is easy to make a TE flap assembly that can handle the expected aerodynamic flap loads on the benchtop. However, it may be difficult for it to work well in the rotational environment. The flap is designed with both mass balancing and aerodynamic overhang in order to lower the loads on the flap. The entire blade assembly is made in-house. The blade with flap is tested in the vacuum chamber and on the hoverstand. Significant flap deflections are demonstrated for different flight environments.

## 3.2 Comparison to Previous Trailing Edge Flap Scaled Work

Roget [53] carried out the fabrication and testing of a Mach scale rotor with piezobender-actuated TE flaps and the present study attempts to compare its findings with this work. Roget’s flap will be compared to this project with a 15%c flap (initial size), and this project with the final flap chord of 26%. The

Table 3.2: Flap Comparison: Roget Flap vs. Primary Control Outboard Flap

	<b>Roget</b>	<b>Copp</b>
Hub	Hingeless	Articulated
Rotor Dia.	5.0 ft.	5.46 ft.
Testing Speed	1800RPM (30Hz)	2400RPM (40Hz)
Mach No.	0.42	0.61
Blade Chord	3.00 in.	3.15 in.
Flap Chord	20%	15% or 26.1%
Flap Span	8%	14%
Flap Center	75%R	82%R

Table 3.3: Flap Comparison: Roget Flap vs. Primary Control Outboard Flap per degree of flap HPP

	<b>Roget</b>	<b>15%c</b>	<b>26%c</b>
Compressibility, Glauert Effect Ratio	-	0.89	0.89
g's at flap center	2071	4921	4921
g Ratio	-	2.4	2.4
Flap Inertial Stiffness Ratio	-	2.5	4.3
Flap Aerodynamic Stiffness Ratio	-	3.5	6.1

reason for choosing 26% will be explained later in this section. The comparison will assume that  $C_{h_f}$  is the same for each of the 3 flaps (Table 3.2).

Roget achieved 4°HPP flap deflection at 1800 RPM for 1, 2, 3, 4, and 5/rev. Table 3.3 compares the flaps per degree of flap deflection HPP. For the comparison, the flap mass/area is assumed the same, where area is the flap span x flap chord. The ratios are to Roget's flap. The compressibility effects should be similar. The bender for primary control needs significantly more authority per degree of flap deflection. This is in addition to the required flap angle for primary control being larger than what is required for vibration control in Roget's study.

### 3.3 Blade Assembly

Each blade is made of a Rohacell 31 foam core wrapped in 2 layers of graphite epoxy 0/90 cloth that provides the blade shape and torsional stiffness. The second layer of cloth wraps around only the blade LE to keep the CG close to the LE, while increasing the torsional stiffness. A spar made with 16 layers of unidirectional graphite epoxy wrapped around an aluminum root insert provides axial strength and attachment points for the hub and flap sub-assemblies. The spar is seen in Fig. 3.1, dividing the foam into the leading edge and trailing edge. A tensile test of a finished spar using an MTS material test machine confirmed its structural integrity up to a spanwise load of 16,000 N, at which point the single supporting bolt pulled through the aluminum insert. With the added support of the skin and two additional mounting bolts, the finished blades support the maximum design load with an adequate safety factor.

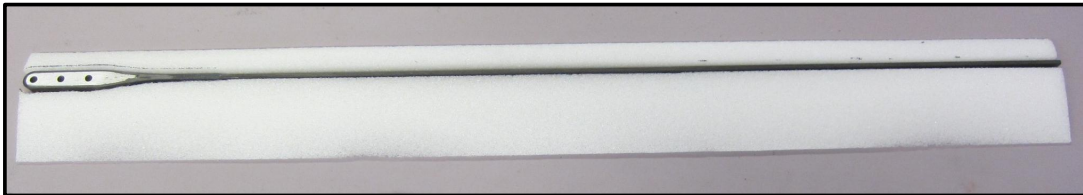


Figure 3.1: Spar in Blade Foam

Tungsten carbide rods are used as LE weights to bring the blade CG forward of the  $\frac{1}{4}c$  (Fig. 3.2) to avoid blade pitch-flap flutter. FM300 film adhesive [80], is used to secure the blade foam, LE weights, skin and spar together. This requires a 180°C cure.

The blade weight breakdown is given (Table 3.4). To bring the blade CG forward, LE weights are added. More than 40% of the spar load is due to the LE weights. Most of this is due to the two flap assemblies (inboard and outboard)

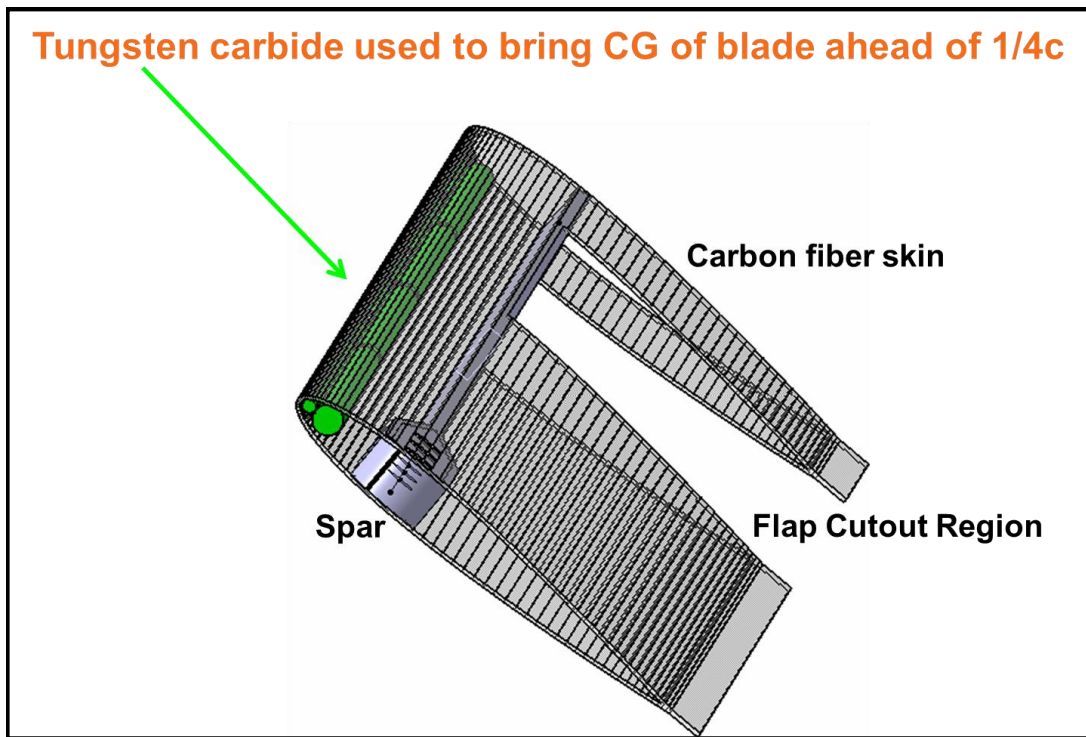


Figure 3.2: Main Blade Components

that are aft of the spar. The final blade weighs 392g and at 2400 RPM, the spar sees a load of 2569 lbs. and the hub, 2602 lbs. This is close to the hub limits. The spar is rated for 16,000N (3600 lbs.), so the spar expected load is 71% of the rated load. So, the piezobender cannot be made significantly heavier because of the hub limits.

### 3.4 Flap Assembly

Two flap assemblies are placed inside each blade. The flap assembly must be lightweight, while stiff enough to avoid inefficiency due to the rod-cusp arrangement. It must support the flap while allowing for frictionless flap rotation. It must also support the bender. The flap assembly is shown in Fig. 3.3 and in Fig. 3.4. The anchor is bonded to the flap spar and holds the piezobender and

Table 3.4: Mach Scale Rotor Weight Breakdown

Component	Chordwise %c	Weight g	% of total weight behind 1/4c	Spar Load, lb.	% of Hub Load
Skin+FM300	45.5%	61.7	36.3%	409.3	15.7%
LE skin	14.1%	13.2	N/A	89.6	3.4%
Foam	37.5%	10.5	3.8%	61.4	2.4%
IB Flap Assembly	51.6%	39.1	29.9%	311.3	12.0%
OB Flap Assembly	51.6%	39.1	29.9%	376.7	14.5%
LE weight	6.3%	185.6	N/A	1138.6	43.8%
Wires	29.5%	1.19	0.2%	5.8	0.2%
Spar	25.0%	26.1	N/A	176.0	6.8%
Root Insert	25.0%	15.1	N/A	33.6	1.3%

the steel rods about which the flap mount rotates. In this section, each part of the flap assembly will be examined with justification for every design decision.

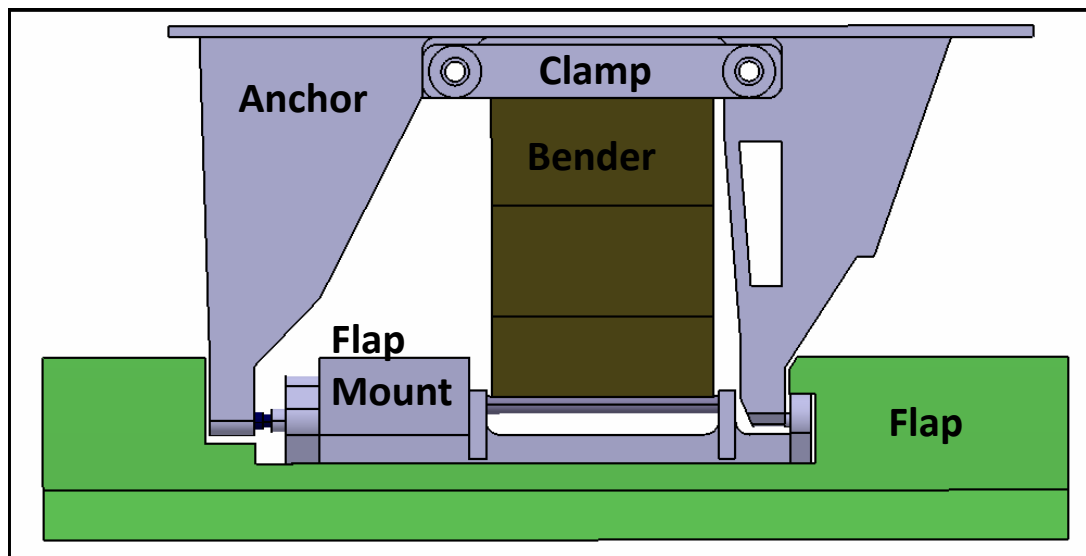


Figure 3.3: Flap Assembly Exploded View

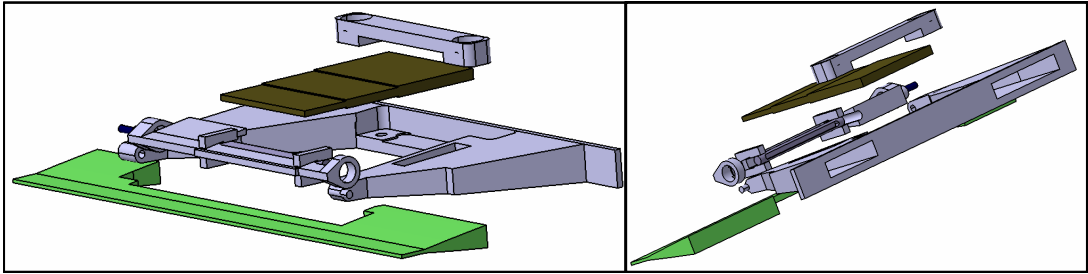


Figure 3.4: Flap Assembly Exploded View

### 3.4.1 TE Flap

The first step is to determine the flap sizing. The flap must be lightweight and minimize the required bender authority. The initial flap chord of 15% was based on UMARC sizing analysis where the goal was to minimize the actuator requirements. Initial hoverstand testing showed insufficient flap deflection. So, in order to increase flap deflection, the inertial and aerodynamic loads on the flap needed to be reduced. This can be done with mass balancing and aerodynamic overhang.

*Mass-Balancing* Reduces the flap inertial load. The free body diagram (Fig. 3.5) of the flap shows the moments acting on the flap: the well-known propeller moment,  $I_f \Omega^2 \delta$ , mass acceleration,  $I_f \omega^2 \delta$  and an additional moment due to the flap axis not being at the blade elastic axis,  $m_{flap} p h$ .  $I_f$  is the blade torsional inertia,  $\Omega$  the RPM,  $\omega$  the flap angular velocity,  $\delta$  the flap angle,  $h$  the distance from the blade elastic axis to the flap rotational axis and  $p$  the distance from the flap rotational axis to the flap CG. These are all stabilizing moments. It is worth noting that the propeller moment does not depend on the flap's radial location, but only the rotor rotational speed. So, it is not correct to call it a centrifugal force component. If mass is added ahead of the flap axis, then a destabilizing moment,  $M_b r h$ , is produced which lowers the flap inertial load, if

properly placed. The distance from the flap rotational axis and the CG of the added mass is  $r$ . If improperly placed, then the increase in  $I_f$  will be greater than  $M_b r h$ . Mass balancing has an added benefit of moving the flap CG forward which increases the flap flutter speed. The drawback is the flap weight increases leading to a larger CF on the flap setup.

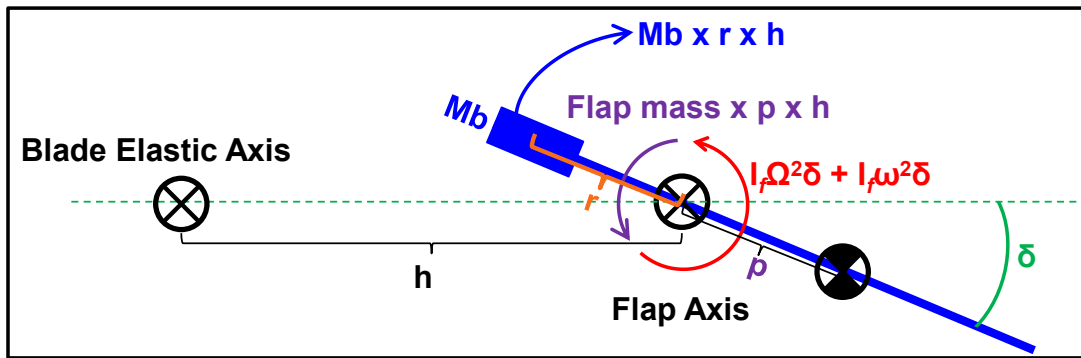


Figure 3.5: Flap Free Body Diagram

*Aerodynamic Overhang* Means the flap hinge is behind the flap LE. More overhang means lower (even negative) flap aerodynamic stiffness. Jose, et. al investigated the effect of flap overhang on  $C_l$ ,  $C_m$ ,  $C_d$  and  $C_{h_f}$  with CFD [81], [82]. Fig. 3.6 sketches a flap with overhang. They examined a NACA0006 airfoil at  $M=0.3$ , blade angle-of-attack =  $0^\circ$ ,  $\delta = 4^\circ$  and  $8^\circ$ , Reynolds number =  $6 \times 10^6$ ,  $x_{h_f} = 0.75$ .

Overhang was found to have a large effect on  $C_{h_f}$  with increased drag as a drawback (Fig. 3.7). Experimental HH-06 airfoil data with TE flap at  $M=0.45$  with overhang provided validation that overhang reduces the hinge moment significantly. For this work, drag is not a key concern at this time, but the flap authority is the major issue.

In order to apply this, a linear fit was made for  $C_{h_f}$  versus overhang. Thickness changes the values by less than 20% for an increase from 6% thickness to 15% thickness. So, this effect was neglected. The gap can cause a large in-

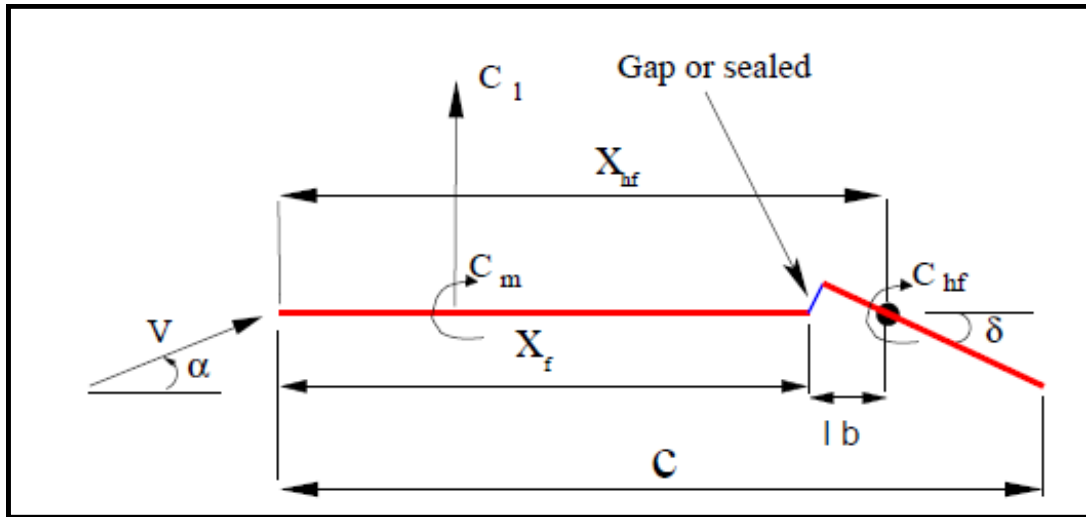


Figure 3.6: Flap with Overhang Schematic

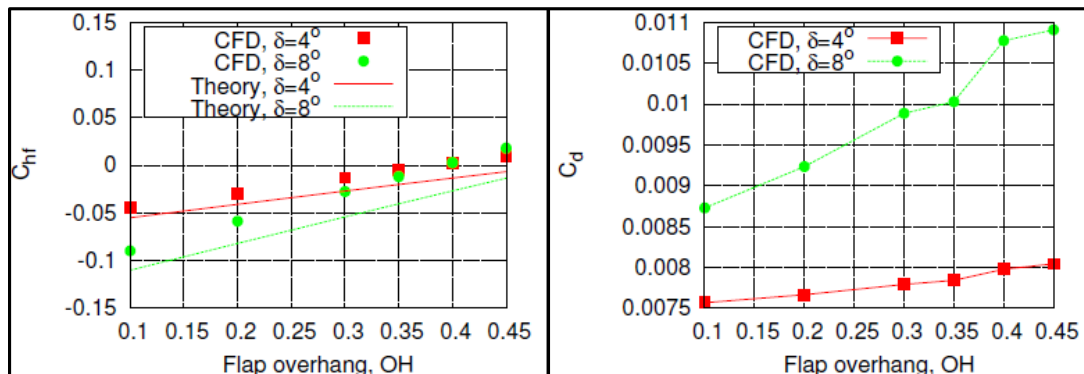


Figure 3.7: Effect of Overhang: Left: Flap Hinge Moment, Right: Drag [82]

crease (50%) in the hinge moment at  $0^\circ$  angle-of-attack, so the gap needs to be minimized. The gap effect is much less at a positive blade angle-of-attack. At the center of the flap, the Reynolds number is  $0.78 \times 10^6$ , which is similar to the CFD study. So, the only large difference is the Mach number. A linear fit makes sense, if the main effect of overhang is shifting the flap center of pressure distance from the flap hinge. Overhang is defined as the ratio of the flap chord before and aft of the hinge. An overhang of 60% is chosen in order to make the flap aerodynamically neutral. Final flap numbers will be provided in the next section. The initial flap from UMARC had a chord of 15%, so to add overhang, the flap was extended forward, keeping the hinge location unchanged. So, the final flap chord is 26.1% $c$ .

This flap chord value also maximizes the flap effectiveness. Fig. 3.8 shows flap effectiveness,  $\partial C_{m_{\frac{1}{4}c}} / \partial \delta$  versus flap chord ( $E$  is ratio of flap chord to total blade chord), as calculated by Glauert using thin airfoil theory [83]. This is also used to determine expected flap effectiveness for this setup. With the flap chord determined, the next step is to design the flap mount to support the flap in the rotating environment.

### 3.4.2 Flap Mount

The flap mount must perform several functions. It must hold the flap CF, allow for low friction flap rotation, incorporate the cusp, have sufficient torsional stiffness and have the mass-balancing.

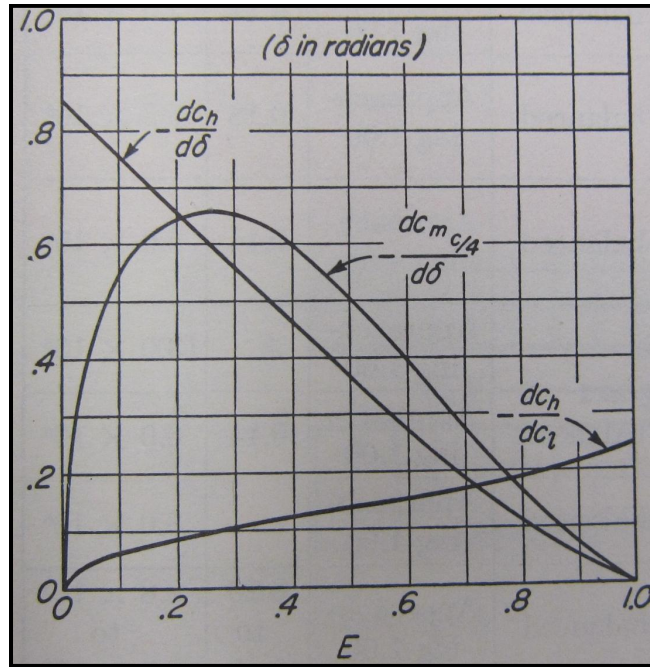


Figure 3.8: Flap Effectiveness vs. Flap Chord

### 3.4.2.1 Low Friction Rotation

This is the major problem with Mach scale TE flaps: to achieve frictionless hinges. The hinges should facilitate low friction flap rotation while supporting the very high CF on the flap and providing sufficient stiffness in the chordwise (radially) direction. For the present flap, at Mach scale, the outboard flap has a spanwise CF of 51 lbs. Several methods have been tried at the University of Maryland and are discussed by Allen [67], Roget [53] and Koratkar [84]. Roget used flexures (Fig. 3.9), that lowered friction and fit inside the blade profile. However, they required fine tuning (trial and error) in the material choice and thickness to develop a flexure with enough strength to support the flap without adding too much torsional stiffness to the flap system. They did not last too long under loading.

Radial bearings were attempted, but the large thrust load leads to large

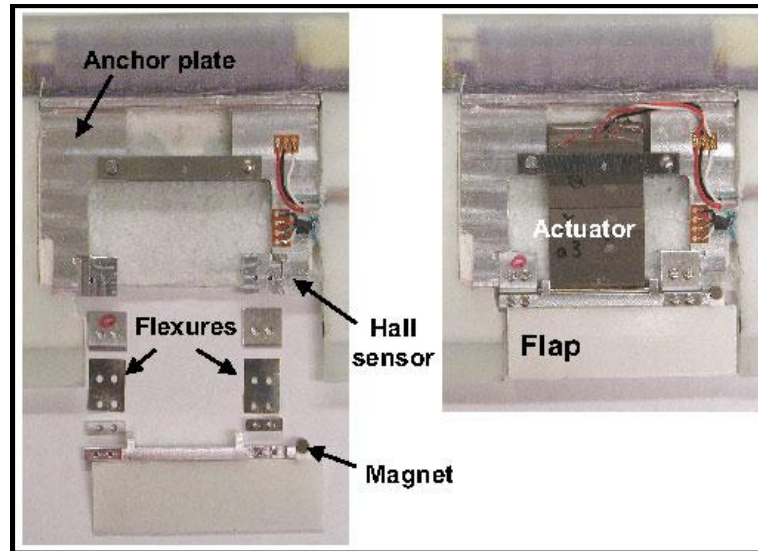


Figure 3.9: Roget TE Flap Setup

friction forces and failure of the radial bearings. Koratkar used a thrust bearing with the rod-in-tube hinge (teflon-coated metal sleeve sliding along a steel rod at the flap hinge) to support the flap radially. This method also had large friction forces.

So, the solution is to have radial bearings to support the flap radially which handle only radial loads and a thrust bearing to support the flap spanwise which handles only thrust loads. This necessitates a complex part that has both radial and thrust bearings. SMR681X radial bearings are chosen. These have a 4mm OD (Outer Diameter), 1.5mm ID (Inner Diameter) and 2mm width and are rated for 7.7 lb. It is recommended to limit the bearing load to 25% of its rated load or 1.93 lb. The flap is supported radially at two points by two bearings offset from the flap CG, so that the moment on the flap due to the flap CF is supported. Each support point has 2 bearings. The radial bearings' inner races are free to slide spanwise along the steel rods supporting them in the flap fixed frame.

F2-6c thrust bearings were chosen. These are 3mm wide, 6mm OD and 2mm ID. They consist of a steel cage with ceramic balls sandwiched inbetween 2 steel washers. One washer is in the fixed frame. They are rated for 150 lbs. and the ceramic balls offer lower friction than steel due to ceramic being harder than steel. So, at the point of contact, the ceramic ball has less deformation than a steel ball. All ceramic bearings are commercially available at this size, but the reduction in friction is not large enough over ceramic balls-steel cage bearings to justify the cost increase of about 400%. The bearings protrude from the airfoil, but these are the smallest bearings commercially available with a thrust rating near the flap CF. The bearings are shown in Fig. 3.10.

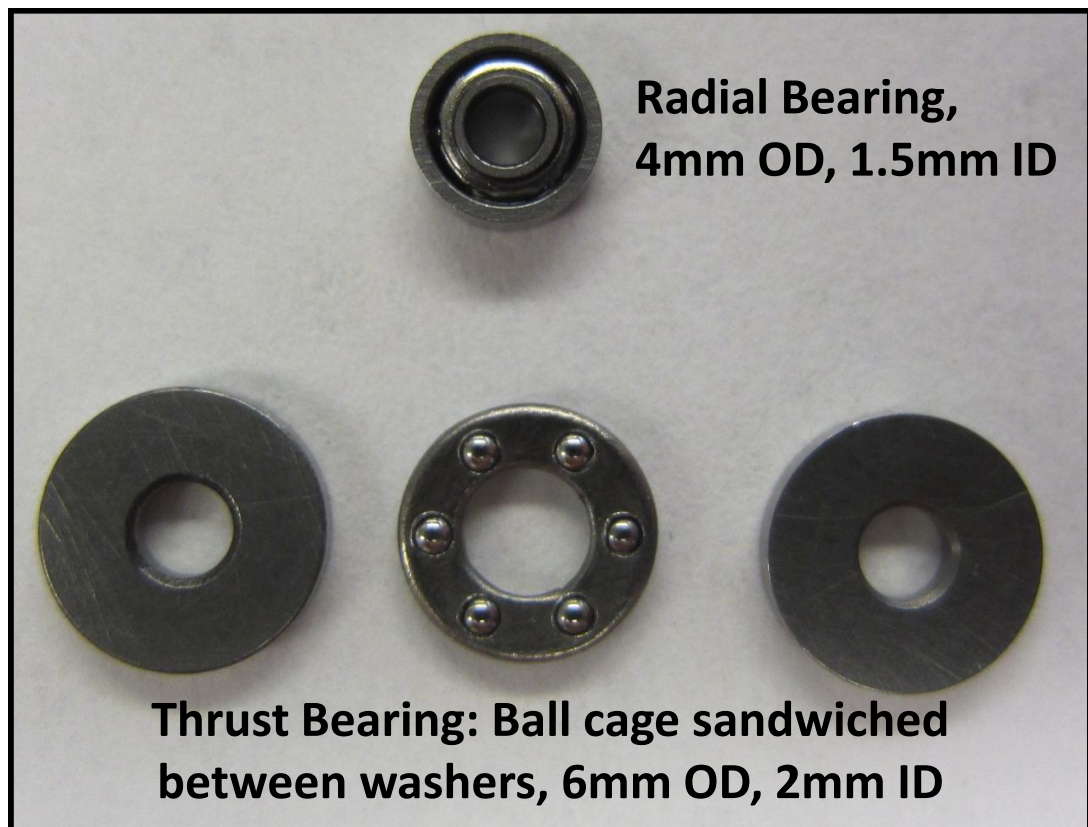


Figure 3.10: Radial Bearing (SMR681x) and Thrust Bearing (F2-6c)

The flap mount is free to slide spanwise outboard on the radial bearings' inner

race until stopped by the thrust bearing, so the thrust load must be held by the thrust bearing and not at all by the radial bearings. Also, the rod supporting the flap radial bearings' inner race does not make contact with the thrust bearing (larger diameter hole than the radial bearing rods). So, the thrust bearing cannot support the flap radially. This means that the radial bearings take only radial loads and the thrust bearing takes only the thrust load. So, the flap loads are properly supported for minimal friction while allowing easy flap rotation.

#### **3.4.2.2 Mass Balancing**

The flap mount also must incorporate the mass balancing to lower the flap inertial load. The flap mount is made from aluminum 6061, so the mass balancing is also aluminum and is smoothly integrated with the flap mount. This allows for both mass balancing and aerodynamic overhang to be obtained while maintaining the flap profile.

#### **3.4.2.3 Complex Part**

The flap mount is shown drawn in Fig. 3.11 and is fabricated in-house. It is made of milled aluminum and except for the cusp arms and bearing locations, it has the blade airfoil profile. The torsional stiffness is much higher than the expected flap aerodynamic stiffness in order to avoid the flap mount deforming in twist from the piezobender force instead of the flap rigidly rotating.

The manufactured flap mount is seen in Fig. 3.12 with the mass balancing section labeled. Two radial bearings are at each end of the flap mount for a total of 4 bearings. The flap mount is placed in the flap rotating frame. The radial bearings of the flap mount are free to slide along steel rods in the flap fixed frame (blade rotating frame).

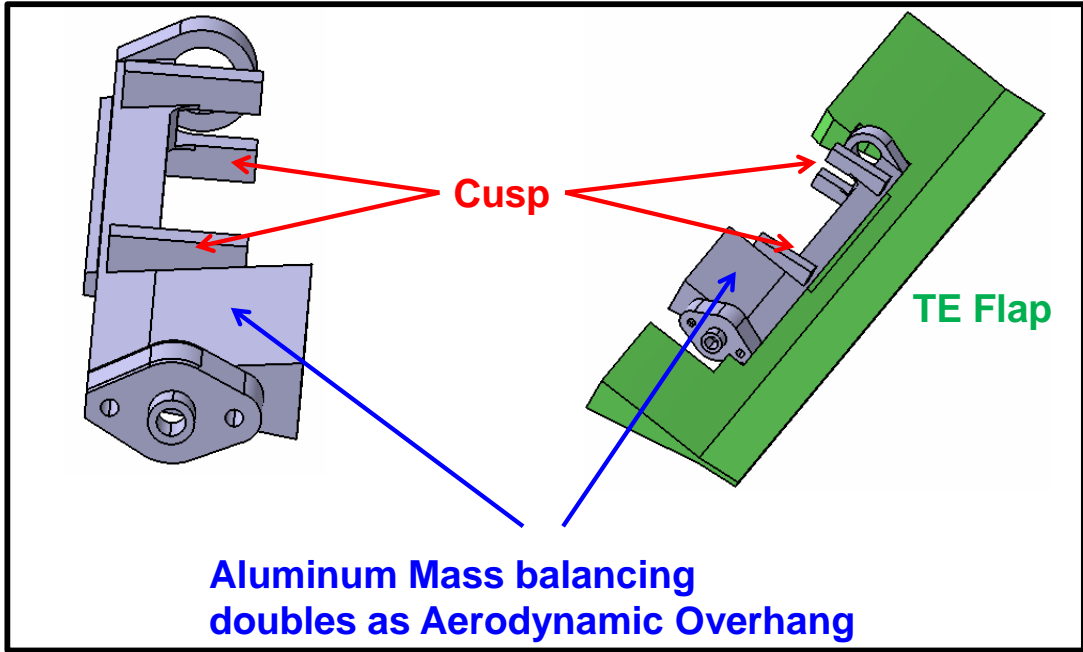


Figure 3.11: Flap Mount Drawing

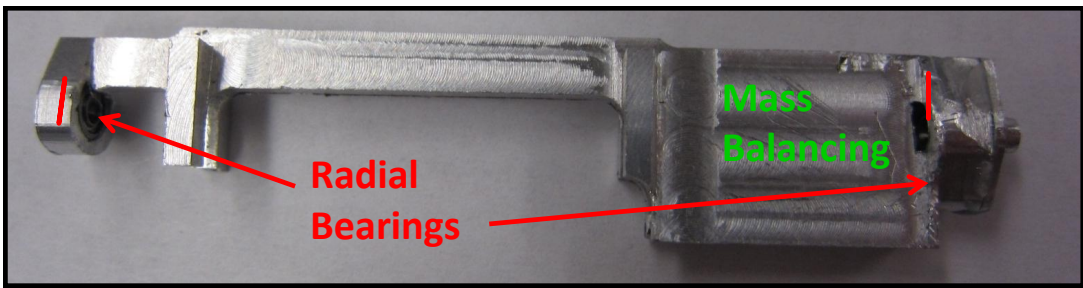


Figure 3.12: Flap Mount

The thrust bearing must be on the outside of the flap mount and so 2 of the radial bearings must be enclosed in the flap mount. This necessitates making the flap mount as 2 separate pieces and joining them together with copper rods and epoxy (Fig. 3.13. The assembled flap mount is seen in the inset. The 2 radial bearings are secured to the flap mount and then the separate piece is added. The thrust bearing goes on over the flap mount separate piece. The rod going through the radial bearings ID is smaller than the ID of the separate piece so no contact can be made. This is needed to force the flap CF to be supported by only the thrust bearing.

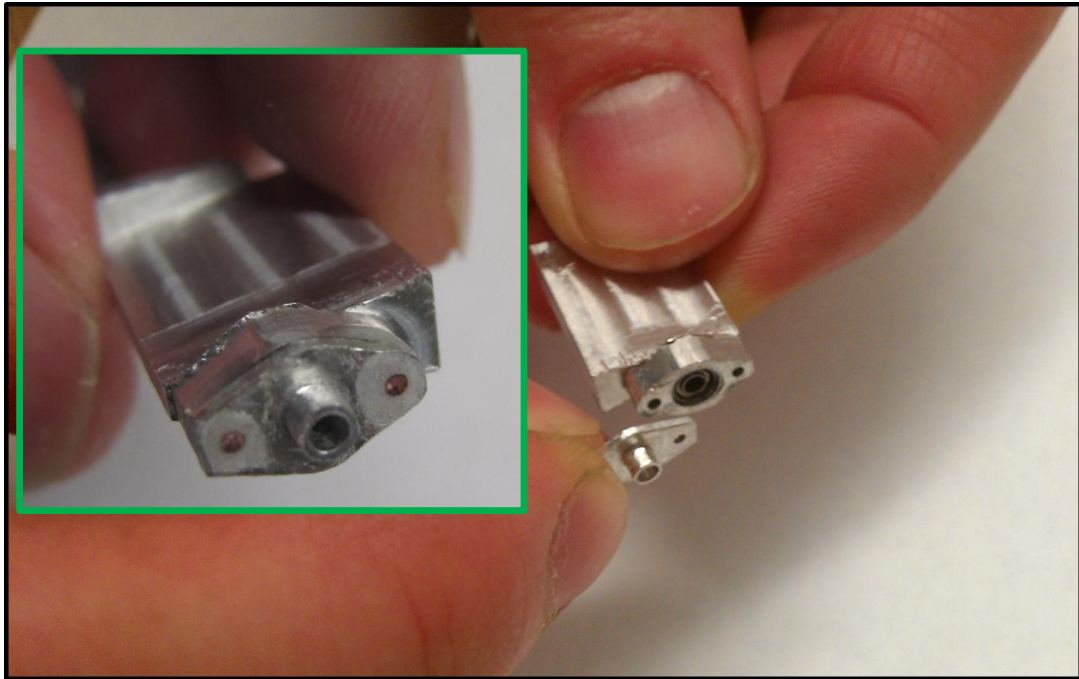


Figure 3.13: Flap Mount Assembly

#### 3.4.2.4 Mass Balancing Position

The mass balancing is positioned to minimize the radial loads on the radial bearings. Fig. 3.14 shows the force balance equations. The x direction is spanwise

and  $y$  is chordwise.  $R$  indicates reaction forces. The reaction forces,  $R_{IB}$  and  $R_{OB}$ , are minimal if they equally share the load (-0.85 lb. on each). However, there is not space to set  $l_1$  and  $l_2$  to obtain this. So,  $l_1$  and  $l_2$  are chosen such that  $R_{IB} = -1.15$  lb. and  $R_{OB} = -0.55$  lb. This is below the recommended rating for 2 radial bearings of 3.9 lbs., thus minimizing friction. The thrust bearing is also rated for 150 lbs.

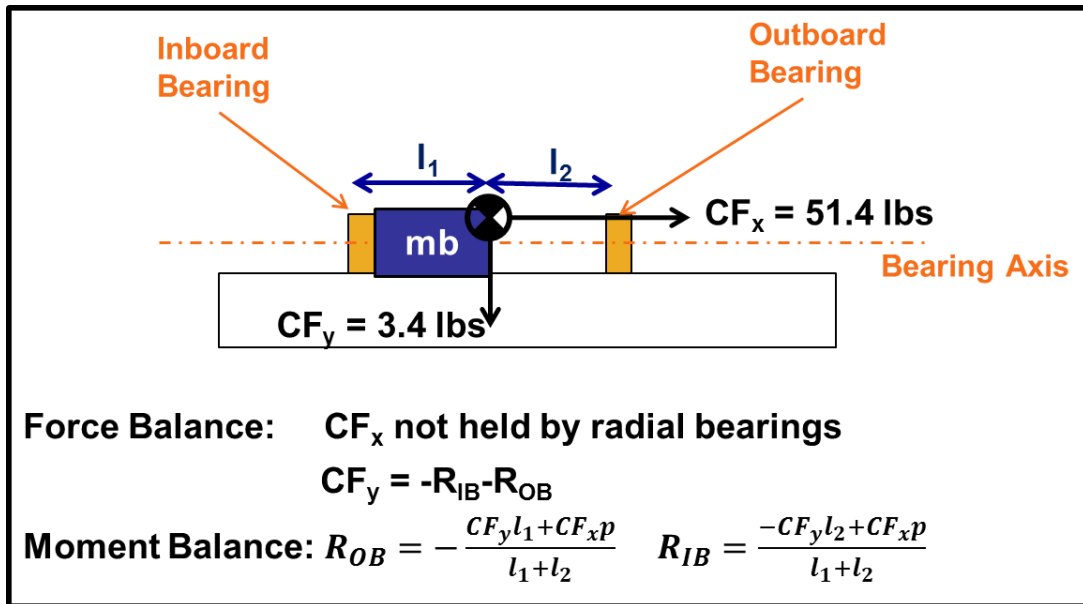


Figure 3.14: Mass Balancing Positioning

### 3.4.2.5 Final Flap

Some final numbers for the flap are now given. The flap aerodynamic stiffness with overhang is determined by breaking the flap into spanwise sections, because the flap mount has varying overhang (due to the bearings and cusp arms) and calculating  $M_h = C_{h_f} c^2 r^2$ , where  $r$  is the flap section span and  $c$  is the flap chord (Fig. 3.15). The aerodynamic stiffness is found to be slightly negative (unstable).

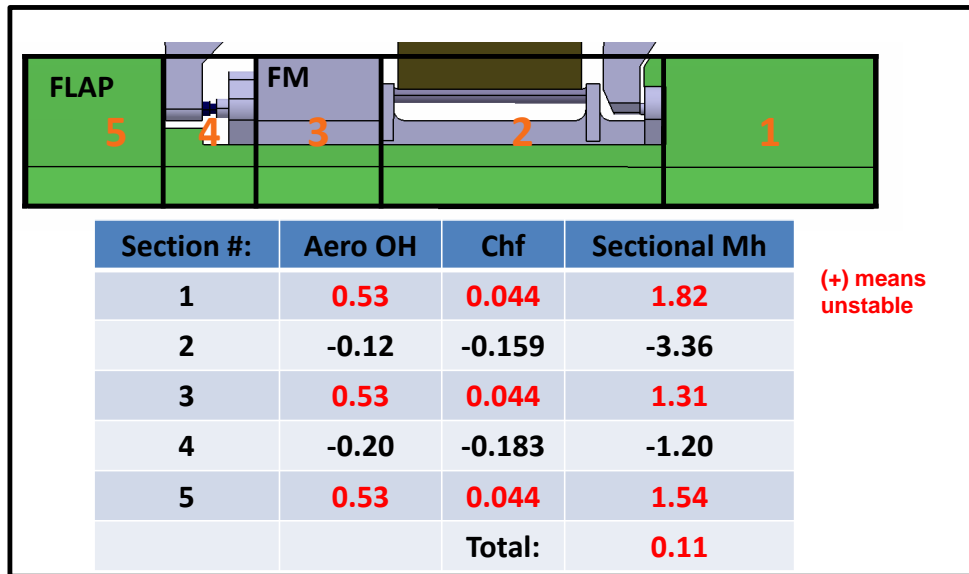


Figure 3.15: Flap Aerodynamic Stiffness

Fig. 3.16 shows the flap layout from the side in order to show the forces on the flap again. The distance from the blade elastic axis to the flap hinge is  $h$  and the distance of the flap+flap mount CG from the flap axis is  $p$ . There is the propeller moment,  $I_f \Omega^2 \delta$ , the acceleration term,  $I_f \omega^2 \delta$  and an additional moment due to the flap and flap mount CG not being at the blade elastic axis ( $\frac{1}{4}c$ ), Flap+FM mass  $\times p \times h$ .

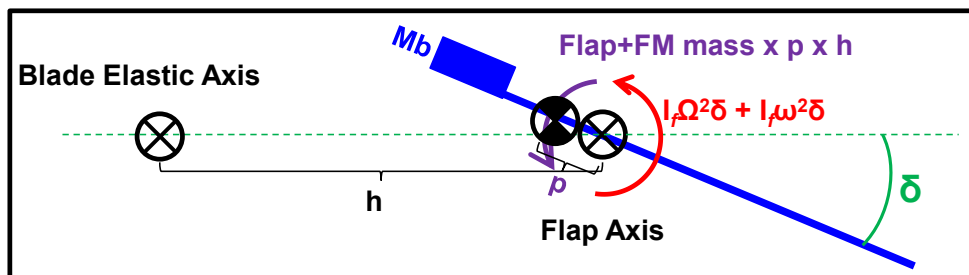


Figure 3.16: Flap Forces

Table 3.5 shows the flap numbers needed to determine the forces on either the inboard or outboard flap. The acceleration term is dependent on the flap frequency and it is 40 Hz (the requirement for primary control, 1/rev). The total

Table 3.5: Flap Inertial Properties

	<b>Flap</b>	<b>FM</b>	<b>Total</b>
Weight (g)	2.15	3.16	5.31
CG from spar (in)	1.832	1.765	1.792
CG from flap axis (in)	0.057	-0.009	0.018
Inertia (lbf-in <sup>2</sup> )	2.83e-4	1.53e-4	4.36e-4
Mass x p x h (lbf-in <sup>2</sup> )	4.18e-4	-1.15e04	3.66e-4
Acceleration (lbf-in <sup>2</sup> )	2.83e-4	1.53e-4	4.36e-4

torsional inertia is  $1.24 \times 10^{-3}$  lbf-in<sup>2</sup>. The flap CG is slightly behind its axis so flutter could be a concern.

The final flap has overhang and mass balancing. This has minimized the aerodynamic and inertial loads on the flap at the cost of higher flap weight (CF), which can be dealt with by the thrust bearing. Reducing loads on the flap is important for reducing actuator power requirements and increasing actuator life.

### 3.4.3 Flap Anchor

The anchor serves two purposes. First, it supports the piezobender and second, it supports the flap. The rod-cusp arrangement is shown again in Fig. 3.17 with the basic equation:  $\sin\delta = \frac{w}{d}$  where  $\delta$  is the flap angle,  $w$  is the bender tip deflection and  $d$  is the flap hinge. If the flap hinge support stiffness is small relative to the bender stiffness, then the rod-cusp arrangement will be inefficient.

So, a lightweight anchor with high stiffness is needed. This is obtained using a box beam design to minimize the anchor arms deflection under the high CF environment and the loads on the flap. Finite element analysis is used in anchor design to minimize the weight and deflection of the anchor arms under flap inertial and aerodynamic loads, bender loads (supporting weight and induced strain

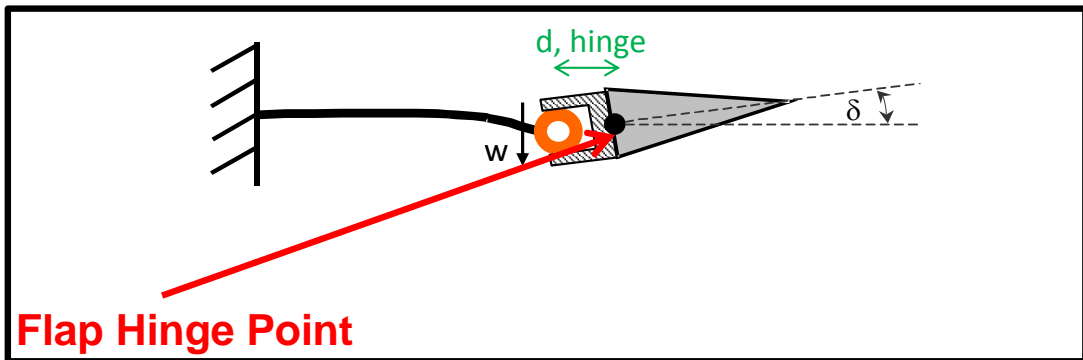


Figure 3.17: Rod-Cusp Schematic

moment) and centripetal accelerations. Fig. 3.18 shows the anchor drawing with the hollowed out anchor arms (box beams) and the analysis. The anchors are made in-house from aluminum 6061.

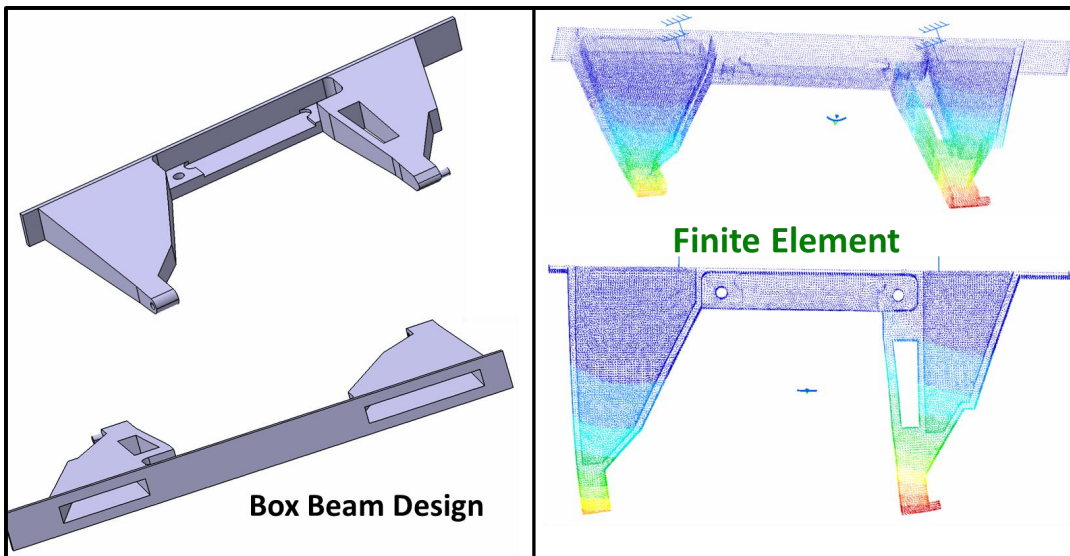


Figure 3.18: Anchor Design

The expected deflection for the anchor arms is less than 2.4 mils in the spanwise direction and less than 1.1 mils transverse to the blade chord. This translates into a loss in flap deflection of  $0.15^\circ/1^\circ$  flap deflection. This is just an estimate as the loads on the flap are not known. The anchor cannot be made

stiffer (heavier). This is the inefficiency in the rod-cusp mechanism - the hinge point for the cusp does not have infinite stiffness and so, its motion subtracts from the bender motion.

### 3.5 Vacuum Chamber Result

To prove this Mach-scale flap assembly, the flap is tested in vacuum at high RPM. A blade with a single outboard flap assembly is constructed and spun in the University of Maryland 10 foot diameter vacuum chamber (Fig.3.19). The vacuum chamber has a 1 HP electric motor rated for 1700 RPM with a slipring for passing power to the rotating frame and sending sensor data back to the fixed frame. Vibration issues limited the test to 1300 RPM and a vacuum chamber resonance around 1000 RPM needed to avoided.



Figure 3.19: University of Maryland Vacuum Chamber

The flap is driven at  $-50V/+150V$  or half its maximum voltage ( $-90V/+270V$ )

at 38.3 Hz (1/rev for 2300 RPM). The results are good, showing almost no flap angle degradation up to 1300 RPM. Results from two separate tests are shown. The angle at no RPM is not shown because it is misleading, due to the gap in the rod-cusp. This gap leads to larger angles than if the flap has even a small load that forces the flap cusp to always be in contact with the rod. From 600 RPM to 950 RPM, the flap deflection does not decrease smoothly due to the cusp being lightly loaded. Then, from 950 RPM to 1300 RPM, it falls by 1.4° HPP to 11.7° HPP. So, large flap authority for a 15%R (span), 26.5%c (chord) flap has been demonstrated. The setup has very large flap authority up to 1300 RPM when the target is 2400 RPM. More authority is available if the flap is driven at its maximum voltage. Friction is not significant. Thus, the radial+thrust bearing idea, where the thrust and radial loads are isolated, along with mass-balancing, works well.

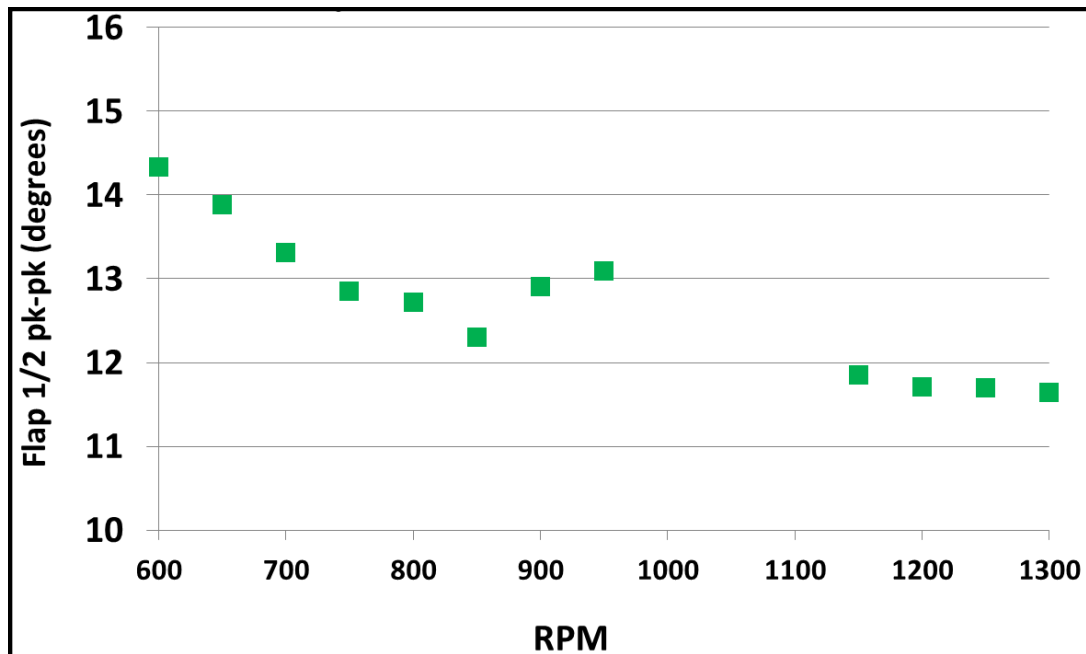


Figure 3.20: Single OB Flap with Overhang, Thrust+Radial Bearings in Vacuum, 38.3 Hz Flap Amplitude driven at -50V/+150V

### 3.6 Hoverstand Setup

Two blades each with an inboard and outboard flap assembly were constructed. Testing was carried out on the University of Maryland hoverstand. The hoverstand is driven by a 50 HP hydraulic motor. It has an articulated rotor hub. A fixed frame balance measures the 3 forces and 3 moments at the hub in the fixed frame. A 60 channel sensor slipring and a 32 channel power slipring allow electrical signals to move between the fixed and rotating frame. Several pictures below show the setup. The 2 blades on the hoverstand are seen in Fig. 3.21.

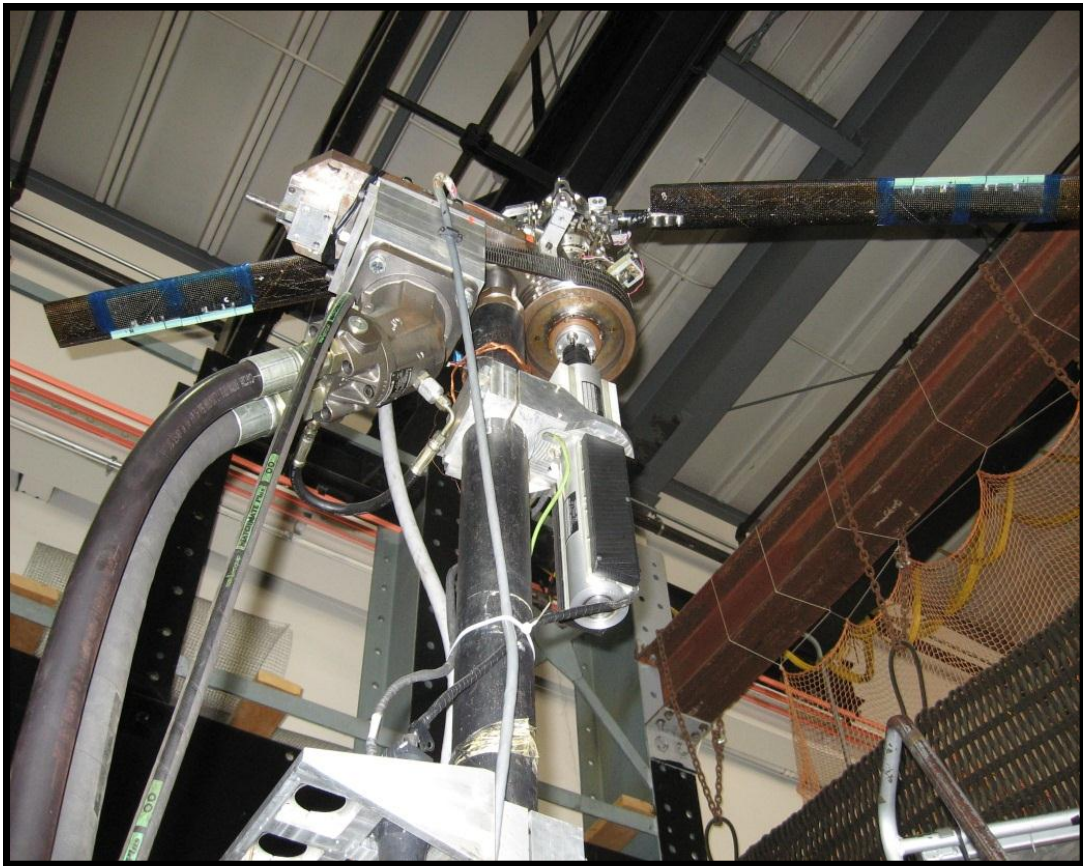


Figure 3.21: Hoverstand with 2 blades

The two blades with the flap covers removed are shown in Fig. 3.22. The blade is only cut out on the pressure side to insert the flap assembly.

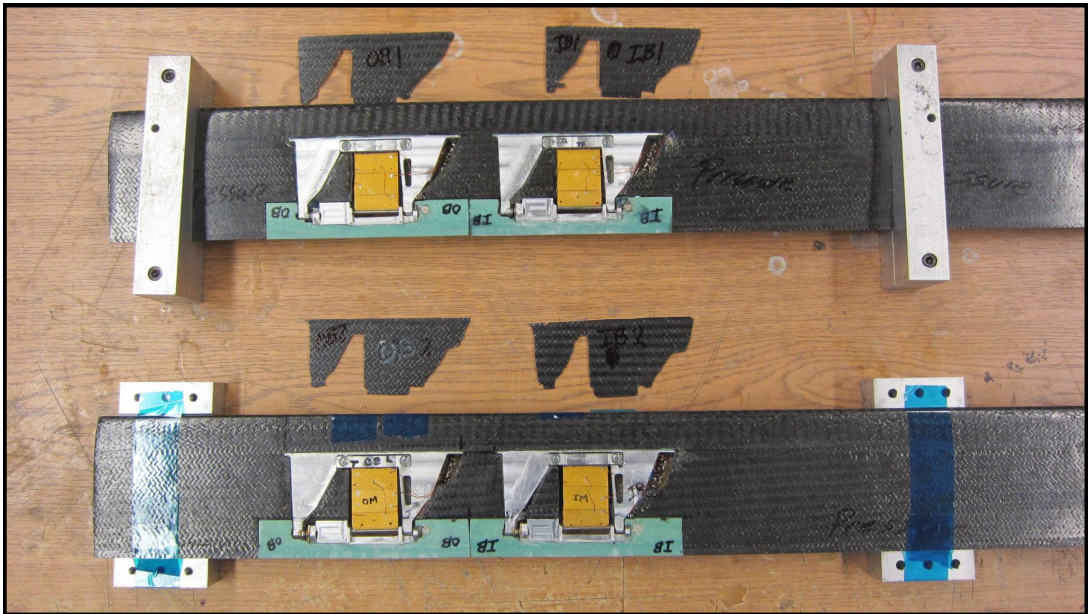


Figure 3.22: 2 Blades

Fig. 3.23 shows a closeup of a flap assembly in the blade showing how only the cusp arms, bearings and anchor arm tips protrude out of the airfoil profile.

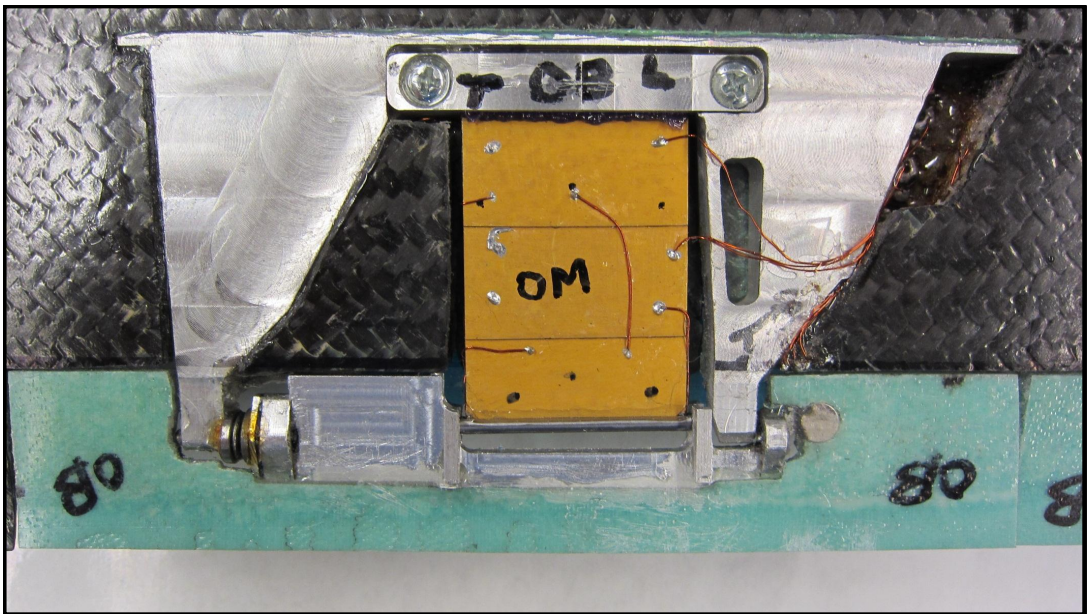


Figure 3.23: Flap Assembly in Blade Close-Up

First, the flap authority with rigid pitch links will be shown. Then, to use

the flaps for primary control, the blade torsional stiffness needs to be reduced by replacing the rigid pitch links with soft pitch links.

### 3.6.1 Flap Authority

First, the piezobender stroke for each flap on the benchtop is shown in Fig. 3.24. 1 and 2 represent respectively Blade 1 and Blade 2. The average stroke at maximum voltage (-90V/+270V) for all 4 benders is 19.57 mils HPP which is off from the predicted stroke of 20.2 mils half peak-to-peak by just 3%.

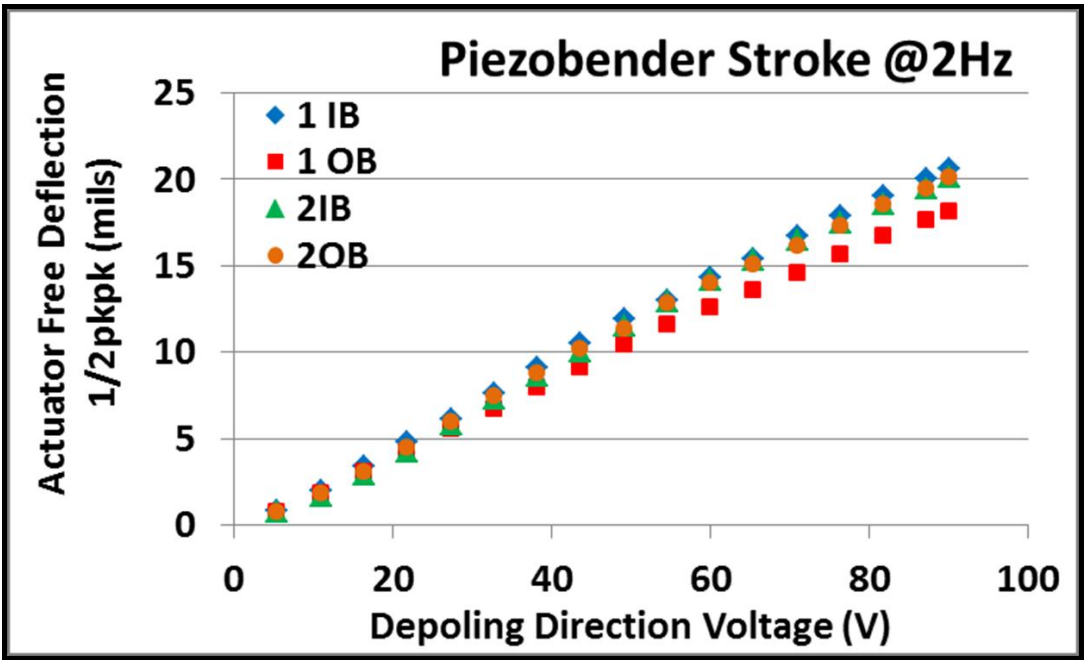


Figure 3.24: Maximum Bender Strokes at 2 Hz

Then, the blades are rotated at 900 RPM and the flaps actuated. The flaps do not all have the same deflection due to differences in the manufacture of the flap hinges. Flap angles are measured with a non-contact Hall sensor. Figure 3.25 shows the flap deflection for one of the OB flaps. On the benchtop, the maximum flap deflection was 15.1°HPP for this flap. The x-axis is the driving voltage in

the depoling direction. A 3:1 bias is present, so the maximum bender voltage is  $-90\text{V}/+270\text{V}$ . The flap is driven at  $15\text{Hz}$  or  $1/\text{rev}$  for  $900\text{ RPM}$ . The maximum flap deflection is  $12.7^\circ\text{HPP}$ . So, the flap angle has fallen by only  $2.4^\circ\text{HPP}$  from non-rotating to  $900\text{ RPM}$ . Some of this loss is due to the rod-cusp gap loss. As seen in the figure, at low voltage, the deflection is low because the rod is moving in the cusp gap and not transferring force to the flap. The OB flap sees  $45\%$  higher aerodynamic stiffness in theory than the IB flap, due to higher dynamic pressure, so the IB flaps will perform better than the OB. Even at  $900\text{ RPM}$ , the inertial load on this outboard flap at  $12.7^\circ\text{HPP}$  is estimated at  $2.1$  times Roget's flap at  $1800\text{ RPM}$  and  $4^\circ\text{HPP}$  and  $3.0$  times the aerodynamic load. So, this is a significant improvement over Roget's setup.

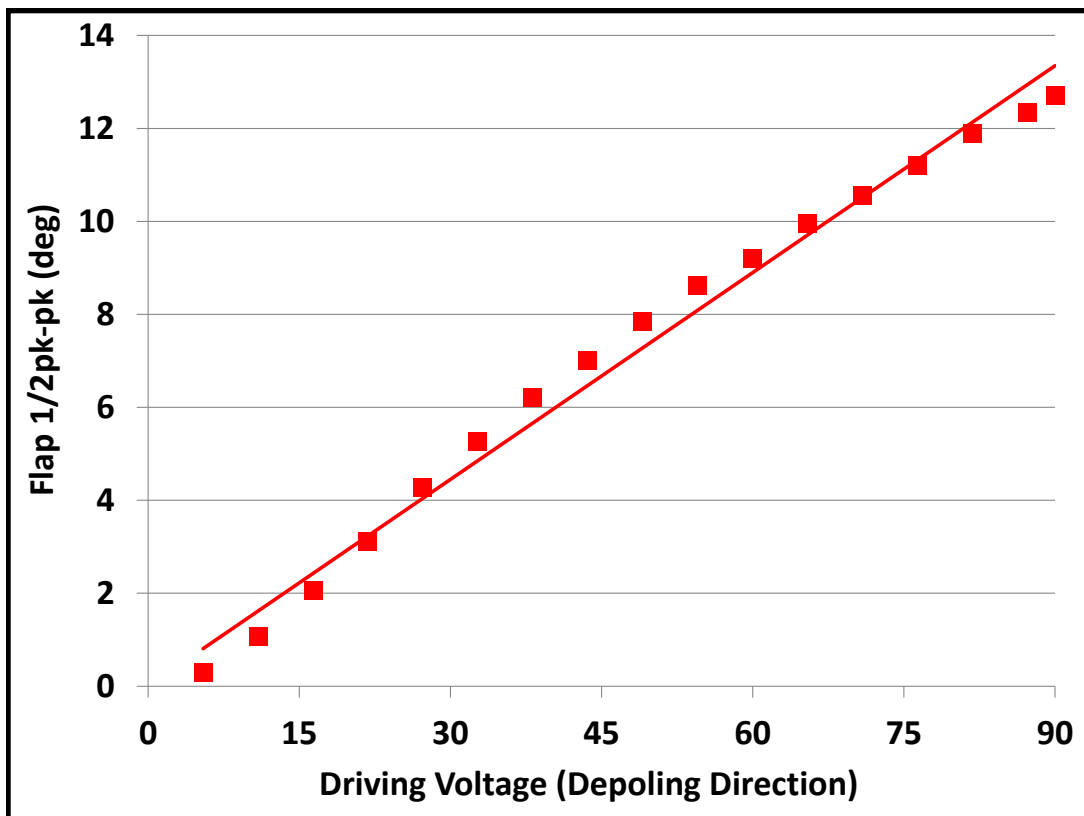


Figure 3.25: Blade 1 OB Flap Amplitude at 900 RPM

As a note, this is not a resonant system: the flap and piezobender fundamental frequency is not close to 15 Hz and is well above 40 Hz (Fig. 3.26). The OB flap has less of an increase than the IB, as its natural frequency is higher due to the higher dynamic pressure.

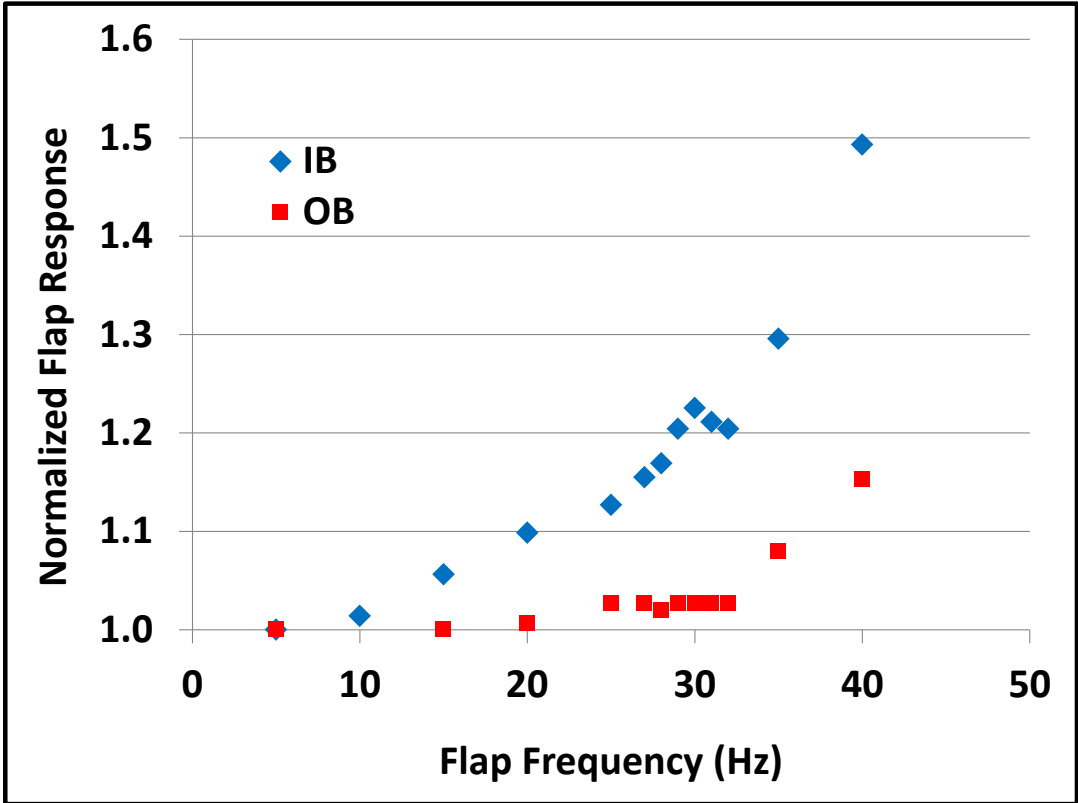


Figure 3.26: Blade 1 Flap Freq Sweep at 900RPM - Fixed Driving Voltage Normalized at 2Hz

### 3.6.2 Soft Pitch Link

Primary control through TE flaps requires not just significant deflections with a large flap, but also lowering the torsional stiffness of the blade. This is done by reducing the pitch link stiffness by replacing the rigid pitch link with a linear spring. This forms a torsional spring through the pitch horn. A soft pitch link

(SPL) must allow for blade pitching without friction and the blade pitching must be measured. For experimentation, the soft pitch link should allow for both the torsional stiffness and index angle to be easily changed.

The initial SPL is shown in Fig. 3.27 and it replaces the blade rigid pitch links on the hub. It has 4 linear springs that can be quickly swapped to change stiffness. The index angle is changed by changing the stiffness ratio of the upper and lower springs. A linear bearing is used to support the CF with low friction. A linear potentiometer is used to measure the blade angle. Steel ball bearings transfer the blade radial load to the hub while allowing blade root pitching and a tension-torsion strap transfers the blade CF to the hub while allowing blade root pitching. The torsional stiffness of the tension-torsion strap is negligible.

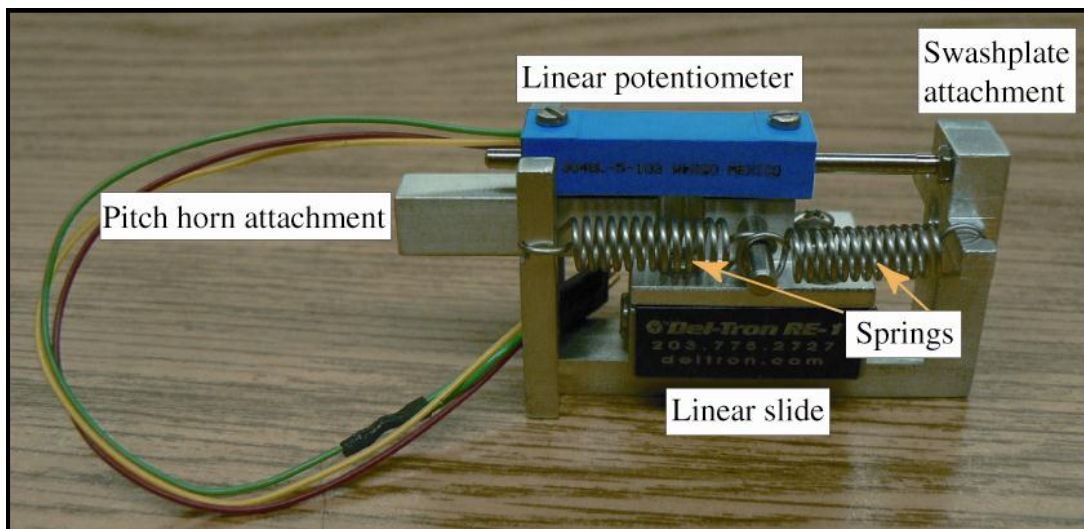


Figure 3.27: Initial Soft Pitch Link

The initial SPL had friction when the blades were rotated. The torsional stiffness is expected to be  $Ka^2$  using the small angle assumption, where  $K$  is the spring stiffness and  $a$  is the moment arm (pitch horn) equal to 5.84 in. Springs were chosen such that after measuring the non-rotating torsional stiffness,  $\nu_\theta$ ,

the rotating natural frequency, is expected to be 1.76/rev at 900 RPM. When the blade is rotated and the TE flaps deflected thus causing blade root pitching, then  $\nu_\theta$  is found to be 1.27/rev. This is seen in Fig. 3.28 which plots blade pitching versus flap deflection for a single blade with both flaps deflecting about 7.5°HPP. The blade inertia would need to be off predicted by 350% to explain this, or the damping ratio should be 0.69, implying very large friction.

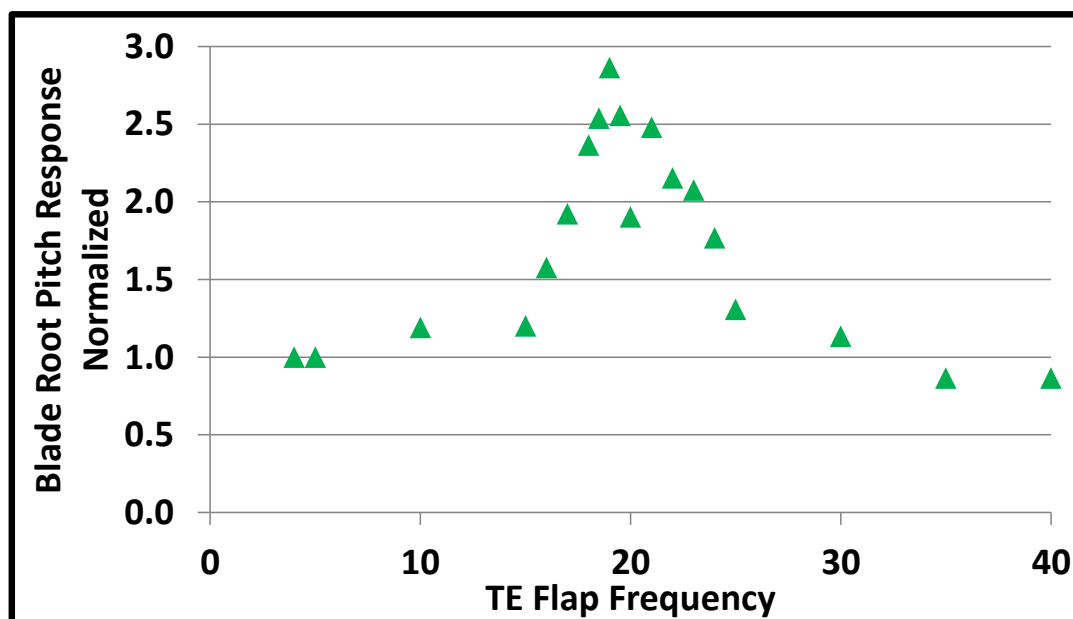


Figure 3.28: Blade Pitch Frequency Response to TE Flaps, 900 RPM

The solution to this is to replace the steel ball bearings with all ceramic ball bearings. Fig. 3.29 shows the original setup on the left with the bearings replaced on the right. The blade grip slides over the radial bearings on the hub grip. The blade grip is attached to the hub through the tension-torsion strap. The blade spar is held with 3 bolts to the blade grip. To fit inside this setup, the bearing must have an ID of 17 mm (over the hub grip) and OD of 23 mm (inside the blade grip).

Also, the linear potentiometer was found to have stiction on the benchtop.

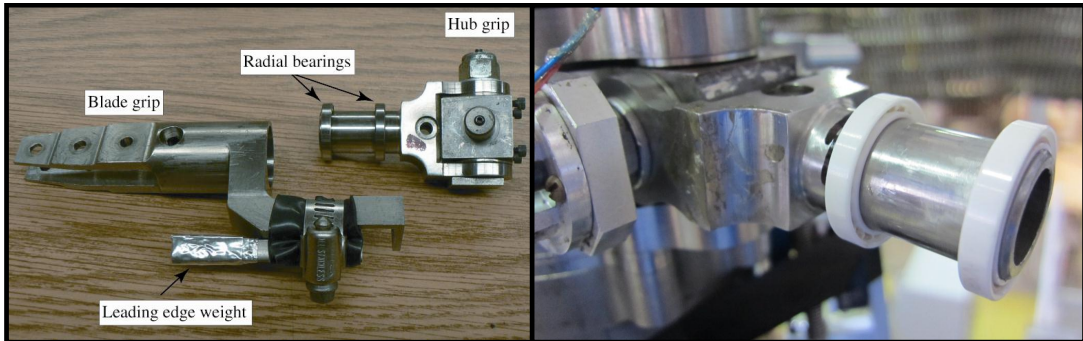


Figure 3.29: Left: Steel Radial Ball Bearings, Right: Replaced by all Ceramic Bearings

So, it was also replaced with a non-contact Hall sensor. The magnet is on the blade grip (blade pitching frame) and the sensor is mounted on the hub grip (Fig. 3.30). This eliminates stiction at the cost of a poor SNR (signal-to-noise ratio) relative to the linear potentiometer.

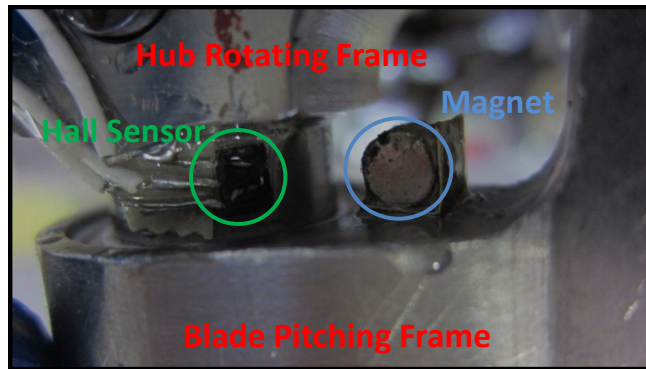


Figure 3.30: Hall Sensor for Measuring Blade Root Pitching

With these changes the blades were spun again to 900 RPM with stiffer springs such that the expected  $\nu_\theta$  is 1.91/rev. The flap driving voltage is held fixed, but the flap amplitude is not. So, the normalized flap response accounts for the flap amplitude changing with frequency. Both flaps have an amplitude of about  $7.5^\circ$  HPP at 5 Hz. The measured  $\nu_\theta$  is 29 Hz or 1.93/rev (Fig. 3.31). Thus, the soft pitch link setup, with ceramic ball bearings for pitching and a

non-contact Hall sensor to measure the pitching, is shown to have no friction up to 900 RPM.

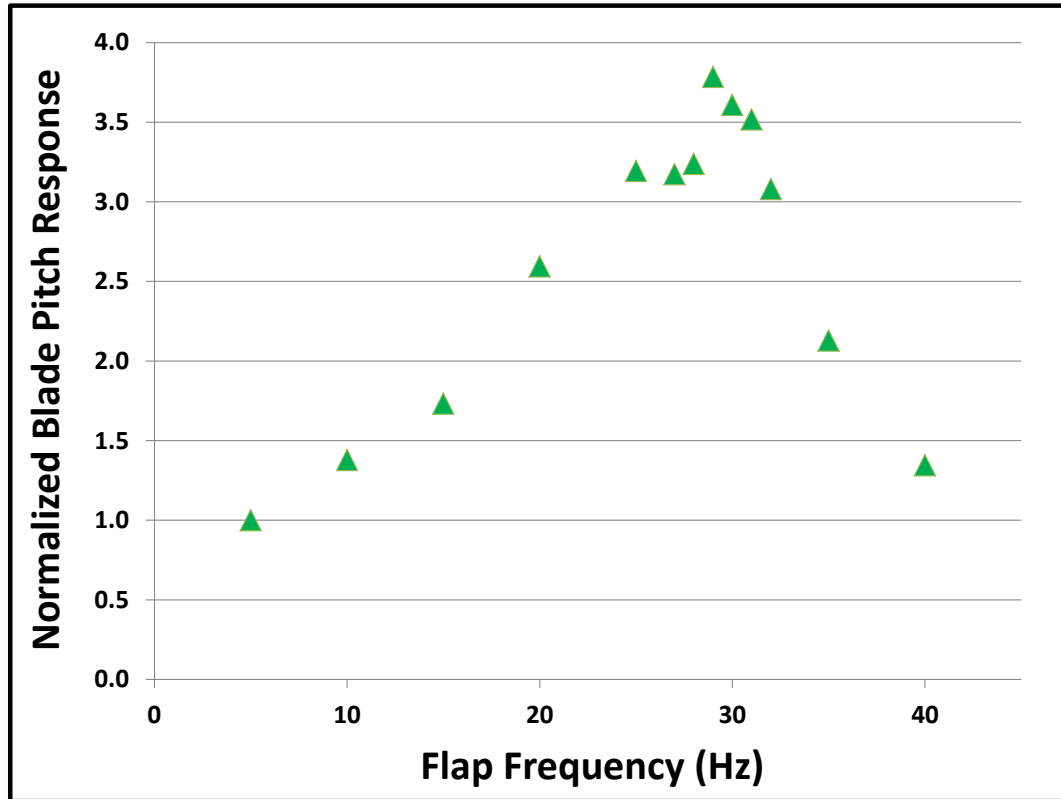


Figure 3.31: Blade Pitch Frequency Response to TE Flaps with Ceramic Bearings, 900 RPM

### 3.7 Summary

A Mach scale rotor with TE flaps sufficient for primary control has been designed, constructed and tested systematically. The work built upon the previous work at the University of Maryland with several significant changes. First, a flap system with minimal friction during rotation was developed. This required the use of micro radial bearings and thrust bearings in the flap mount. The flap mount holds the bearings such that the radial bearings cannot take any thrust

load and the thrust bearing cannot take any radial load. This is the key to low friction - each bearing takes only the loads it is designed for. Secondly, relative to previous work, the flap is larger and so the flap aerodynamic stiffness is higher. This means that the stiffness of each piece in the setup needs to be high. This requires a good cantilever support for the piezobender, a slotted rod to transfer bender motion to the flap cusp and a box beam anchor with high stiffness and low weight. Significant flap deflection of  $\geq 11^\circ$  HPP for an outboard flap at 1300 RPM was obtained at just half the maximum bender driving voltage in vacuum. On the hoverstand at 900 RPM, flap deflection of  $\geq 12^\circ$  HPP for an outboard flap was obtained. This is sufficient for primary control and perhaps even vibration control simultaneously. A soft pitch link mechanism that uses a non-contact Hall sensor, a linear slide and ceramic bearings, lowers the blade torsional stiffness without adding friction to blade pitching motion. There is no reason why the flap deflection should not be sufficient at higher RPM. Only, it has not been demonstrated yet.

## Chapter 4

# Hoverstand Results

### 4.1 Overview

In this chapter, the 2-bladed rotor with TE flaps and soft pitch links is tested on the hoverstand at 900 RPM. The rotor can safely be spun faster, but in order to ensure results, testing was carried out at this moderate RPM. Closed loop control of the flaps is demonstrated with rigid pitch links, followed on, with soft pitch links, TE flap deflection causes blade pitching and thus a change in hub forces and moments that is measured. Also, the flap effectiveness (blade pitching to flap deflection) is compared to a simple aerodynamic model. This is a demonstration of primary control through the TE flaps, i.e., a swashplateless rotor.

### 4.2 Closed Loop Flap Control

A PID controller is sufficient to control the flap mean and amplitude. The frequency and phase is determined by the bender driving voltage. The driving voltage is always sinusoidal for these tests. The flap output is always close to

sinusoidal. The flap phasing is such that the flap angles for the 2 blades are  $180^\circ$  out-of-phase. The flaps are not in phase with the blade azimuth. This requires closing the loop on phase between blade azimuth and flap angle. The hoverstand RPM is not constant, but varies by  $\pm 0.5\%$  or  $\pm 1.8^\circ$  per revolution. So, the phase difference between the blade and the flap is non-deterministic, since the flap driving frequency does not exactly match the hoverstand RPM.

For amplitude and mean value, 2 separate SISO PID loops run with gains tuned using the Ziegler-Nichols method at 900 RPM. Control is proven in several ways. First, a single outboard flap has its amplitude (HPP) changed in  $1^\circ$  increments from  $1^\circ$  to  $6^\circ$  and then back down to  $1^\circ$  (Fig. 4.1). The noise and overshoot are small. The elapsed time is about 80 seconds and the time to converge to a desired amplitude is about 2 seconds.

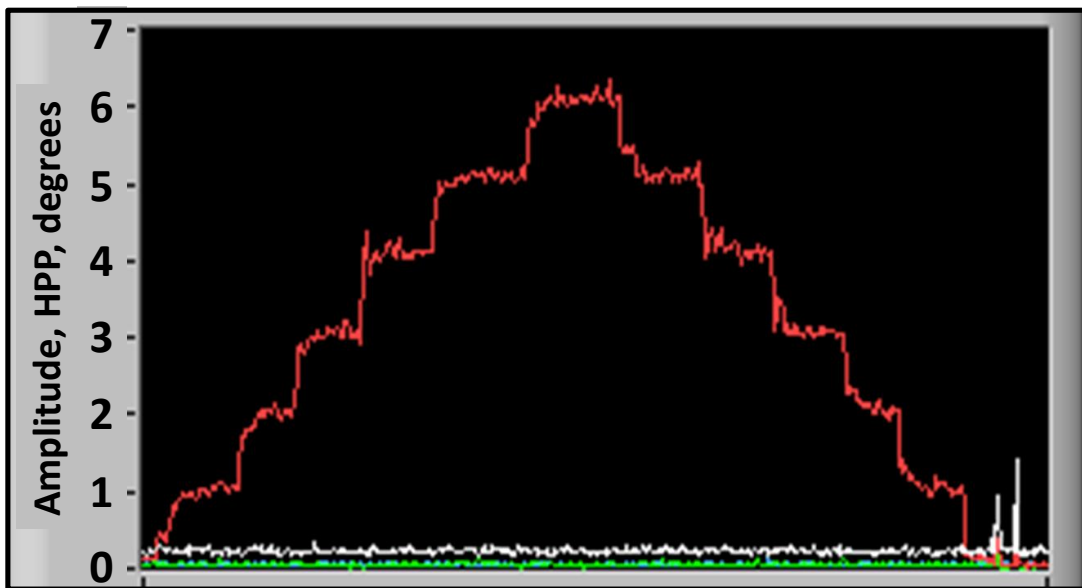


Figure 4.1: Outboard Flap Amplitude Closed-Loop Control at 900 RPM

Then, for the same flap, the mean was commanded to change in  $1^\circ$  increments from  $-12^\circ$  to  $-4^\circ$  (Fig. 4.2). The controller holds the amplitude to  $3^\circ$  for the entire

time (57 seconds).

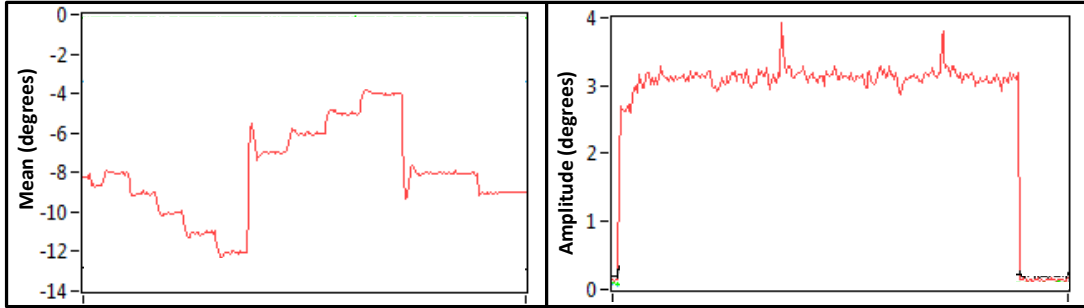


Figure 4.2: Outboard Flap Mean Closed-Loop Control at 900RPM, Constant Amplitude

Then, for both blades, the mean of all 4 flaps was commanded to go from  $2^\circ$  to  $4^\circ$  back to  $2^\circ$  over a total time of 41 seconds (Fig. 4.3). The 4 colors are for the flaps. The angle changes are not at the same time because the commanded angles are not changed simultaneously, but one at a time.

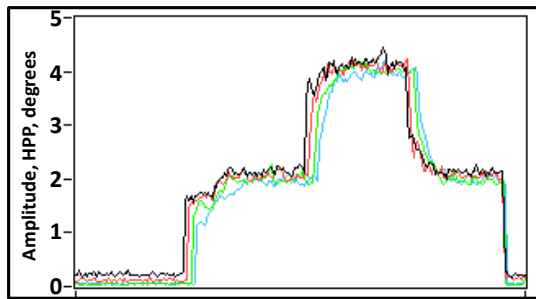


Figure 4.3: All 4 Flaps on Two Blades Amplitude Closed-Loop Control at 900 RPM

Then, for both blades, the amplitude of all 4 flaps was commanded to go from  $+4^\circ$  from neutral to  $-4^\circ$  from neutral and then back to neutral while the amplitude was held to  $3^\circ$  HPP over a total time of 41 seconds (Fig. 4.4). The flap angles do not have the same neutral angle due to machining and assembly tolerances where a small change in the bender height relative to the cusp ( $\leq 10$  mils) can cause the neutral angle to change by  $8^\circ$ .

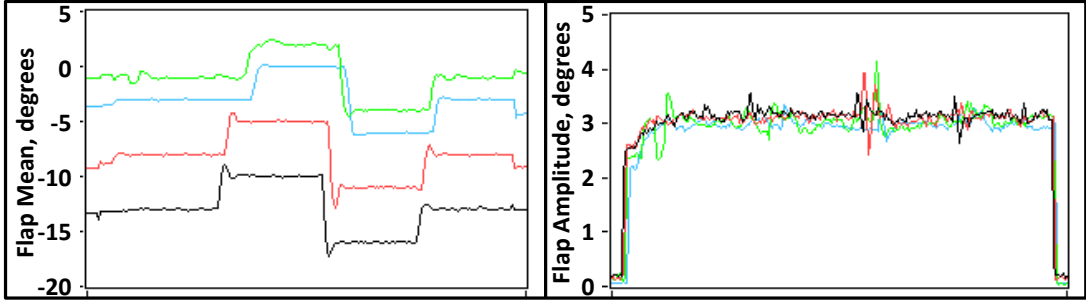


Figure 4.4: All Flaps Mean Closed-Loop Control at 900 RPM

So, the flap controller works well with 2 separate PID SISO loops for mean value and HPP amplitude. The controller is designed for primary control proof-of-concept (trimming the rotor and not maneuvers) and so bandwidth is not a concern.

### 4.3 Flap Effectiveness

Flap effectiveness,  $\frac{\theta}{\delta}$ , is defined as blade pitch change due to flap deflection. A static moment balance is used to predict  $\frac{\theta}{\delta}$ . From Abbot and von Doenhoffen [83], for plain flaps,  $\frac{\partial C_{m\frac{1}{4}c}}{\partial \delta} = -0.0115$ . Jose [82] looked at a  $1\%c$  gap between the blade and plain flap on its performance and found a small change in this value. So, for this setup, where the gap is less than  $1\%c$  ( $\leq 31$  mils), this effect is neglected. This leads to the expected flap effectivenesses shown in Table 4.1.

The values for the model are measured on the hoverstand. The TE flaps of both blades are deflected and the blade pitching measured. The IB and OB flaps are deflected one at a time as well as simultaneously. Fig. 4.5 shows the blade pitching for both flaps. The flaps, especially the inboard flaps, are ineffective for smaller flap angles. This is due to an unknown source of stiction in the soft pitch links and/or flow separation. To get around stiction and measure IB flap

Table 4.1: Predicted Flap Effectiveness at 900 RPM

Blade $I_f$	1.86e-4 slug-ft <sup>2</sup>
SPL Linear Spring Stiffness	336 lb/ft
Pitch Link Arm	0.0967 ft
SPL Torsional Stiffness	0.0414 lb-ft/ $^\circ\theta$
$\omega_\theta$ , Non-rotating Torsion	18.0 Hz
$\nu_\theta$ , Rotating Torsion	1.56/rev @900 RPM
IB Flap Sensitivity	$-0.268 \frac{^\circ\theta}{^\circ I_B \delta}$
OB Flap Sensitivity	$-0.389 \frac{^\circ\theta}{^\circ O_B \delta}$
Both Flaps Sensitivity	$-0.656 \frac{^\circ\theta}{^\circ both\ flaps\ \delta}$

effectiveness, the outboard flap was deflected at a constant amplitude and then the IB flap amplitude varied. This is the line labeled "outside stiction". The stiction region can be seen from 0° to 3° for the OB flap and both flap lines.

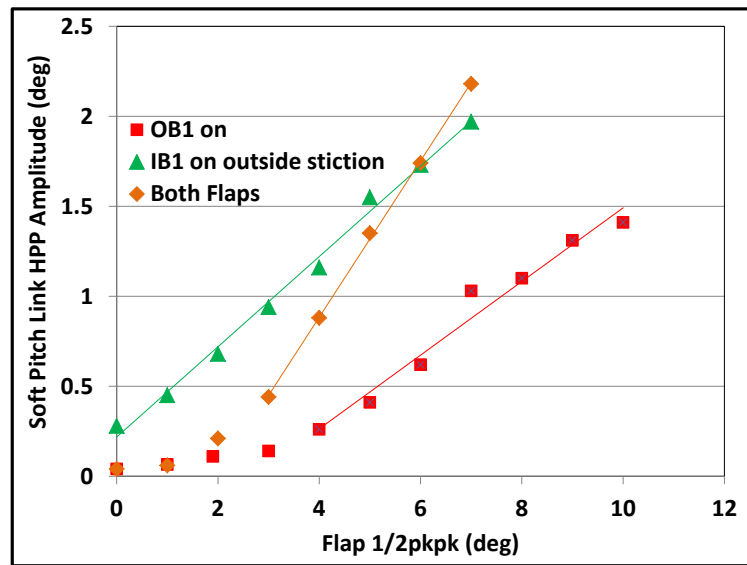


Figure 4.5: Blade 1 Flap Effectiveness

Table 4.2 summarizes the flap effectiveness measurements for all 4 flaps when they are outside the stiction. The mean blade root pitch angle of blade 1 is 7° and for blade 2, it is 5.4°. The expected values are slightly different for the 2 blades due to the blade torsional stiffnesses being different.

Table 4.2: Predicted Flap Effectiveness at 900 RPM

Flap	Expected	Actual	% of Expected
IB1	0.156	0.047	30%
IB2	0.171	0.251	147%
OB1	0.227	0.162	71%
OB2	0.248	0.205	83%
Both1	0.384	0.227	59%
Both2	0.419	0.434	104%

For blade 2, the model is close to the actual. The difference between the flaps is the mean angle and it is quite different due to the previously mentioned tolerance issues with bender rod and cusp (Section 4.2). If the flap angle relative to the blade is high, then flow separation over the flap could lower the flap effectiveness. The flow may separate especially over the inboard flap at this low RPM. To verify this, the flap effectiveness was measured at a 3° higher index angle for both blades (Table 4.6).

Flap	Higher Index			Initial Index			% of Initial Index
	Flap Mean	SPL Mean	Flap E (°/°)	Flap Mean	SPL Mean	Flap E (°/°)	
IB1	-15.0	10	.027	-14	6.9	.047	57%
IB2	-1.8	8.8	.148	-.9	5.3	.251	59%
OB1	-5.8	10	.126	-5.4	7	.162	78%
OB2	-3.9	9	.218	-3.4	5.4	.205	106%

Figure 4.6: Flap Effectiveness for Different Index Angles

The flap mean did not change but the flap effectiveness has dropped significantly at the higher index angle. The blade has not stalled as measured hub thrust has not plateaued. This is especially true for both inboard flaps where due to lower dynamic pressure, flow separation is more likely. So, the flap effec-

tiveness matches the predicted value when the flap mean angle is close to zero relative to the blade. At higher RPM (and flap with neutral angles of  $0^\circ$ ), it should match more closely the predicted for all flaps by eliminating the region of flow separation over the flaps.

## 4.4 Primary Control Demonstration

Primary control is demonstrated both by measuring significant blade pitching due to deflecting the TE flaps. Significant blade pitching causes a large change in hub forces. The maximum 1/rev blade pitching at 900 RPM was  $2.66^\circ$  HPP for a torsional frequency of 1.50/rev and deflection of  $7.2^\circ$  HPP for the IB flap and  $9.7^\circ$  HPP for the OB flap. At higher RPM, the blade pitching should increase at 1/rev as per the previous section, the flap should not operate in a stiction region. At 900 RPM, to demonstrate large blade pitching due to the flaps, a frequency sweep was conducted with the TE flaps. The flap controller was used to keep the TE flap HPP deflections constant over the frequency sweep (Fig. 4.7). Both blades have a torsional frequency of about 1.50/rev. Blade 1 has a mean pitch angle of  $10^\circ$  and blade 2 has a mean of  $9^\circ$ .

Large blade root pitching is observed. For this frequency sweep, the hub forces were recorded. Due to the flaps not being in phase with the blade azimuth, the resultant force and moment are taken where at every instant in time, the following equations are applied.

$$HubForce = \sqrt{Axial^2 + Side^2} \quad (4.1)$$

$$HubMoment = \sqrt{Pitch^2 + Roll^2} \quad (4.2)$$

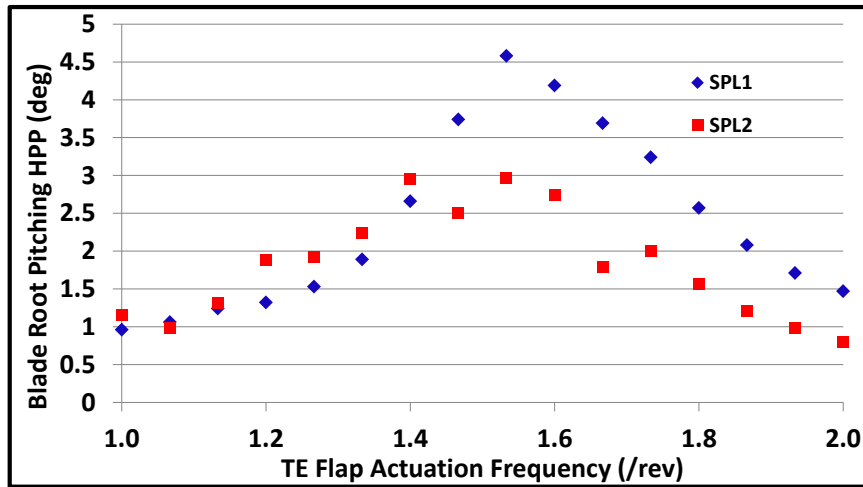


Figure 4.7: Blade Pitching at 900 RPM due to TE Flaps

High control authority for the flaps over the hub forces indicates primary control of the rotor system. It is common to refer to the control authority in terms of the lift. Blade 1 and 2 do not pitch by the same amount, so there is an oscillation in lift at the TE flap frequency (Fig. 4.8). The flaps are 180° out-of-phase. At 1.0/rev flap deflection, the blade TE flap deflection for each blade is set so that each blade is pitching  $\pm 1^\circ$  HPP by adjusting the TE flap amplitude. There is no lift oscillation because each blade is pitching the same amount. The mean lift is 15 lbs. As the flap frequency is increased, the blades do not have the same pitch amplitude leading to a lift oscillation. The oscillation reaches  $\pm 15$  lbs. at a torsion frequency of 1.73/rev so lift authority of the flaps is  $\pm 100\%$ .

The hub forces and moments are also affected during the flap frequency sweep. Again, large control authority is observed (Fig. 4.9). For the forces, at 1/rev, the blade pitching magnitude is the same and so the rotor is just thrusting upwards. At 1/rev, the hub moment is non-zero as the symmetric blade pitching is a cyclic so from flaps off to flaps on, there is a moment generated. As the flap

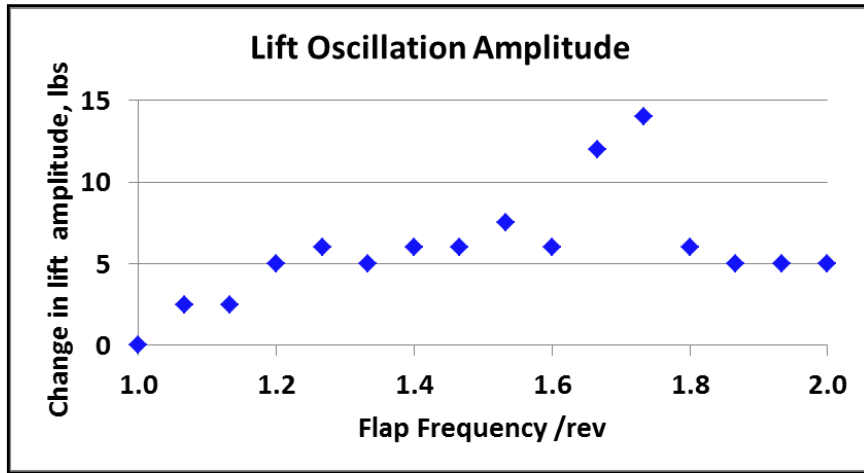


Figure 4.8: Lift Oscillation at 900 RPM due to TE Flaps

frequency increases, the blade cyclic pitching increases and generates up to 4.7 lbs. of hub force at 1.60/rev. The hub moment also increases from a baseline of 2 lb-in. at 1/rev to 10 lb-in. at 1.73/rev.

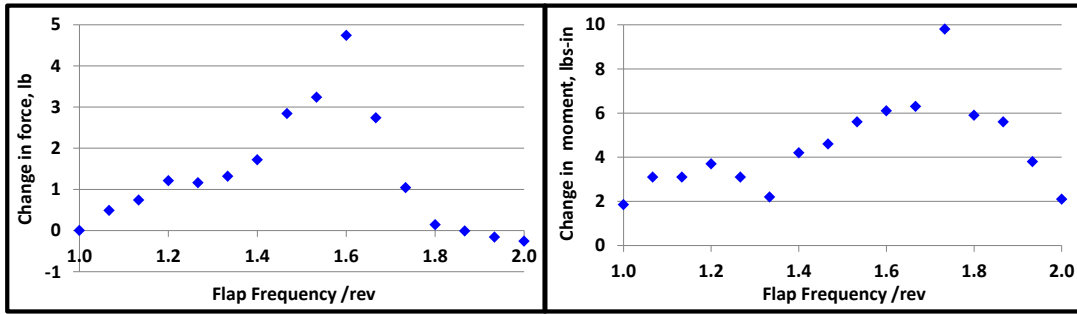


Figure 4.9: Hub Force and Moment at 900 RPM due to TE Flaps

## 4.5 Conclusion

Thus, primary control of a rotor blade through trailing edge flaps driven by piezobenders has been demonstrated. The flaps are driven at less than their maximum voltage and yet lift authority of  $\pm 100\%$  is obtained. These results have been obtained at a torsional frequency of 1.53/rev. If the blade inertia

is unchanged from a conventional blade to a blade with TE flaps as in Falls analytical work (where only the torsional stiffness changes), then the torsional frequency would be 1.90/rev. For  $8^\circ$  HPP TE flap deflection, up to  $6.9^\circ$  HPP of blade pitching was obtained at blade pitch resonance. As required for primary control, the hub forces and moments are significantly affected by the TE flaps. The main concern is that the present system needs to be tested at higher RPM and the TE flaps synchronized with the blade azimuth. The control authority of the flaps should not decrease with increasing RPM and the torsional stiffness is high enough to avoid aeroelastic instabilities according to the analytical work. With the flaps synchronized, wind tunnel testing could be conducted. These results, even at moderate RPM instead of Mach scale, are the state-of-the-art for the swashplateless rotor concept.

## Chapter 5

# Blade Elastic Deformation Wire Sensor

### 5.1 Proposal

A method for measuring rotorcraft blade elastic twist in-flight is proposed using an expansion of strain gage theory. The theory for the method is rigorously derived from first principles. Then, it is proven on the benchtop by embedding the system inside the Mach scale blade used in this project. The system requires little power, has negligible weight and does not disturb the blade airflow or structure and has no safety concerns. The method can also be used to measure blade elastic bending in both the flap and lead-lag directions.

### 5.2 Introduction

Designing and building a rotor with trailing edge flaps efficiently actuated on-blade and with enough authority for primary control is the main hurdle to a swashplateless rotor. This has been dealt with in the previous chapters. Primary control has been demonstrated with the blade torsional frequency reduced by replacing the rigid pitch link with a soft pitch link. However, this may not be

implemented in a full-scale helicopter, because this would result in a set of pitch links exposed to the forward air flow resulting in a drag penalty. To get around this problem and take full advantage of the swashplateless concept in terms of a reduction in parasitic drag, the pitch links must be eliminated. This can be done in two ways.

First, elastomeric bearings can be designed that give a low torsional stiffness with a torsionally stiff blade. Take for instance, the SMART rotor system, which has a bearingless hub. The elastomeric bearing provides flap, lead-lag and pitch degrees of freedom. In order to convert this into a swashplateless rotor, this bearing must be adjusted to provide the desired lower torsional stiffness without a pitch link. This adjustment may lead to significant torsional damping that could stabilize torsional motion, but also cause the required trailing edge flap angles to be high, thus leading to increased actuator power consumption.

As an alternate approach, the blade torsional stiffness itself can be reduced. This requires a complete redesign of the blade. It also poses a control problem. For the first method using an elastomeric bearing, the pitching motion at the blade root can be measured using a non-contact Hall sensor. However, if the pitch motion does not occur mostly at the root, but is distributed over the blade (elastic twist), then the blade pitch angle is unknown. Though the blade pitch does not need to be known to control the helicopter, measuring it would improve helicopter control as an inner loop controlling the blade pitch by TE flap deflection could be added to the control system. Also, if one of the blades is not twisting properly, this malfunction could be measured directly instead of being deduced from hub vibration measurements. A method for measuring the blade elastic twist in-flight is proposed.

Aside from elastic twist, the system can measure blade elastic flap bending

and lead-lag bending. This would be of benefit not just for a swashplateless system, but for any helicopter. If in-flight blade deformations could be measured, then analysis could be better verified. Higher fidelity blade dynamics modeling would lead to improved rotor performance, lighter weight blades (less overdesigning), lower noise and lower vibration either passively or with active methods that morph the blades or change their local AOA (such as TE flaps). Also, in-flight deformations would provide a tool for examining whether blade morphing concepts are working as expected in real time, thus improving system performance and realizing the start of system failure before a catastrophic event.

## **5.3 Blade Deformation Measurement Techniques**

Significant work has gone into measuring blade elastic deformation during wind tunnel and hoverstand testing. In this section, various methods will be summarized. Optical methods are good because they are non-contact and do not require a slipring to carry data from the rotating blade frame to the fixed frame.

### **5.3.1 PMI**

Projection Moiré Interferometry (PMI) has been used to obtain near instantaneous, quantitative blade deformation measurements of a generic rotorcraft model at different test conditions in the wind tunnel. PMI provides full azimuthal field blade deformation data. PMI is an optically simple, non-contacting measurement technique used since the 1970's for surface topology and shape characterization [85]. The fundamentals of PMI are documented in [86], [87]. Only in the last decade, has it been applied to rotor blades in the wind tunnel. For PMI, a grid of equispaced, parallel lines are projected onto the object of interest.

Structural deformation deforms the gridlines and subtraction of digitized undeformed and deformed gridlines yields an interferogram containing moiré fringes or deformation contours. So, the system can measure out-of-plane deformation yielding flap bending and twist, but cannot measure lag deformations.

A PMI system was tested in the Langley 14x22 ft. Wind Tunnel. A 15W, 800 nm broadband laser was used to project the gridlines. This laser was sufficient for a  $50^\circ$  of rotor azimuth with  $1.4^\circ$  frame increments at 2000 RPM. This implies a very high bandwidth. A sample of the results is shown in Fig. 5.1. Measurement accuracy was estimated to be 3% and 3 mils. However, this is only an estimate, as the absolute measurement was not available to compare [88]. PMI accuracy for twist was found to be  $0.05^\circ$  for the Active Twist Rotor [89] on the benchtop. Good measurements were also obtained in the wind tunnel [90].

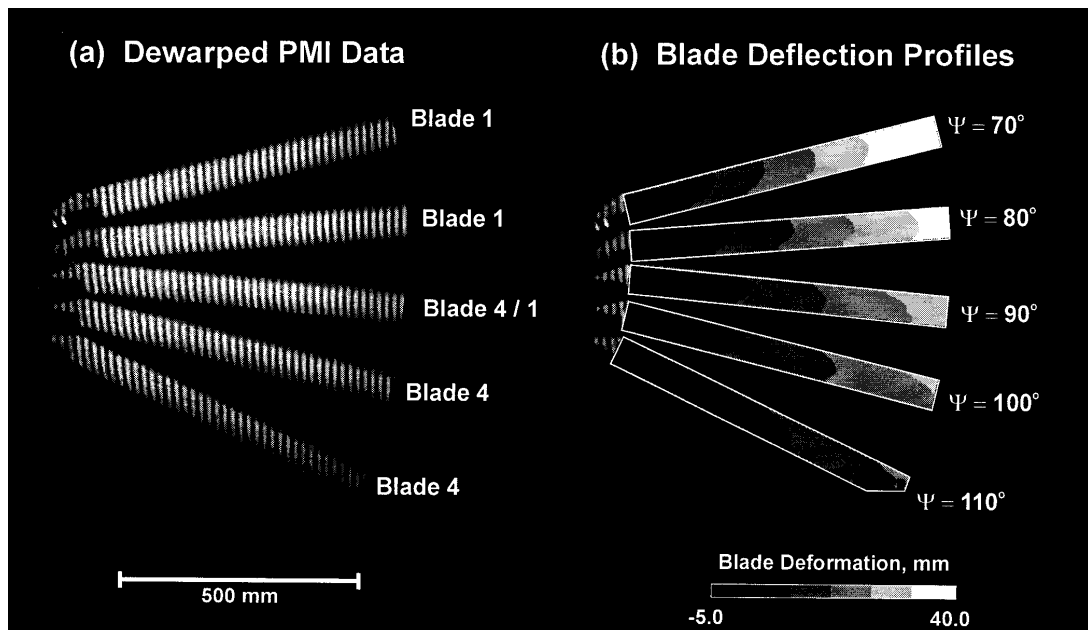


Figure 5.1: PMI Test Data during Wind Tunnel Testing

The drawback to this system is seen from basic optics. In order to capture dynamic motion and avoid blurring, the camera must have a fast shutter speed,

which reduces the light entering the camera. The shutter speed would need to be faster for this Mach-scale model rotor blade with a higher RPM. This necessitates the use of a device with high light intensity such as a laser. Also, a higher power laser would be needed to capture the full azimuth topology. Lasers with this power (frequency) are invisible to the human eye, yet can instantly cause severe damage, even burning the skin. So, extreme safety is needed when operating these and the test section must be enclosed. The enclosure requirement adds a large cost to Mach-scale testing at the University of Maryland hoverstand. Also, eliminating unwanted reflections in the test setup is quite difficult. Additionally, this system cannot be used in-flight.

### **5.3.2 Photogrammetry**

Another measurement techniques is stereo photogrammetry, which was demonstrated for a full-scale UH-60 helicopter in wind tunnel. Reflective, circular targets with 2 in. diameter are attached to the blade at specific locations. Illumination is provided by high-power xenon flash lamps. The blade target images can be compared to a known set of stationary targets to obtain target positions. At each spanwise location (5%R apart), three targets are attached chordwise. So, twist is obtained from the difference in the flap height of these three points. The system performed poorly for elastic twist (Fig. 5.2). The data is very scattered [91].

### **5.3.3 Digital Image Correlation**

Digital Image Correlation (DIC) has been applied to rotors of diameter 24 and 39 in. DIC relies on stereoscopic 3-D digital image correlation. DIC also provide

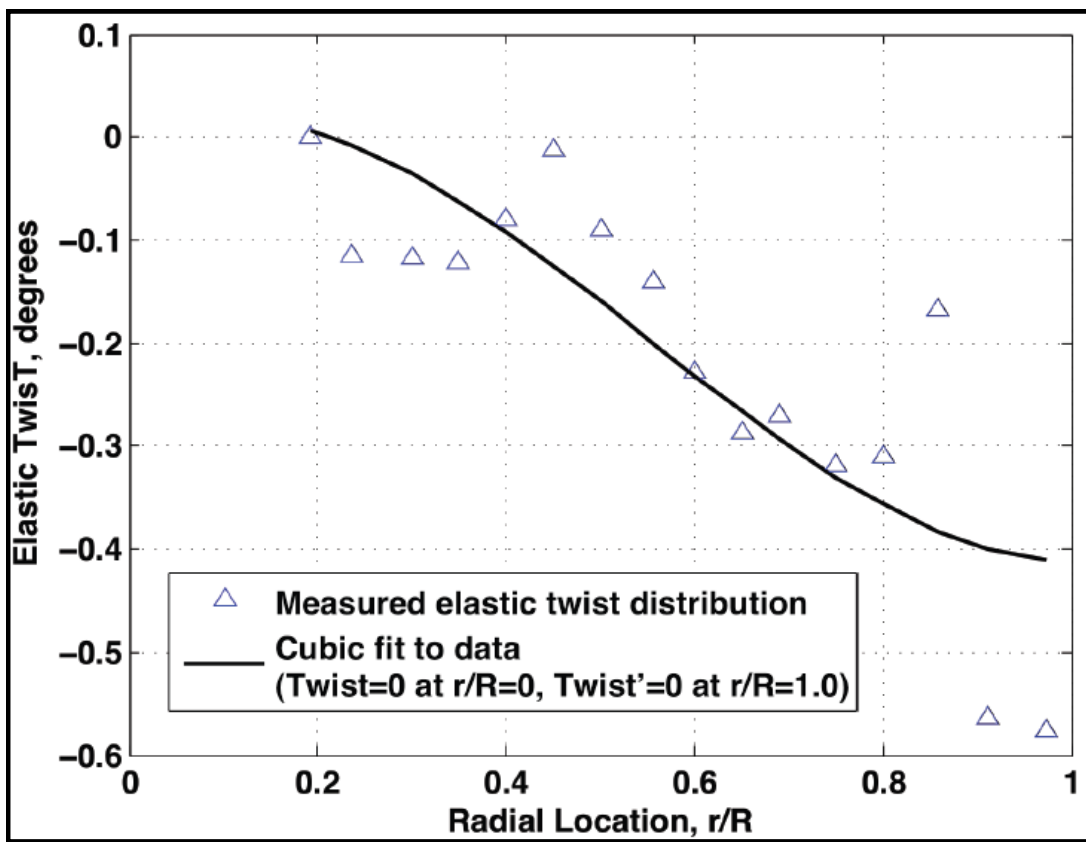


Figure 5.2: Spanwise Distribution of Blade Elastic Twist in Wind Tunnel

a spatial deformation map and has the accuracy needed to derive strain from the deformation map gradients. For DIC, the model surface is painted with a random dot pattern. A high-resolution camera captures images of the surface before and after deformation and cross-correlation yields a 2-D, in-plane deformation map. It can be extended to 3-D by photogrammetric principles using 2 cameras at different angles to the model. The technique is validated with a laser height sensor for a single point on a cantilevered beam and will be applied to a scaled rotor in hoverstand testing in the future [92].

### 5.3.4 Optical Measurement Pros and Cons

Various optical measurement techniques have been applied to measure elastic blade deformation while the blade is rotating in the wind tunnel, or on the hoverstand. All these methods require cameras and a calibration of those cameras to the test subject. The pros and cons are listed below.

Advantages:

1. Non-Contact: These measurements do not disturb the airflow over the blade or the internal structure of the blade.
2. No slipring required: No signals need to be sent from the rotating frame to the non-rotating frame.
3. Continuous Deformation: These measurement techniques yield close to a spatially continuous deformation field instead of only at discrete points.
4. Many of these offer resolution sufficient for taking derivatives of deformations in order to estimate force and moment spatial distributions.

Disadvantages:

1. Bandwidth: The bandwidth is limited by the shutter speed. A higher shutter speed is also needed to avoid blurring from blade rotation. A higher shutter speed requires higher light intensity eventually requiring powerful lasers. Lasers are difficult to use in a wind tunnel that is not dedicated to this system and also can be a safety concern. Strobed light avoids these problems but getting a powerful enough strobe can be difficult and it must be synchronized with the blade.
2. Non In-flight: These systems are only useful in the wind-tunnel. It is quite difficult to implement for in-flight measurements.

## 5.4 Introduction to Wire Sensor

An in-flight system for blade deformation measurements needs to meet several requirements. It must be lightweight, should not disturb the airflow, must not affect the blade structural integrity, draw little power, have high bandwidth, and work in a high CF environment. The bandwidth for a Mach scale rotor is at least 8/rev for higher vibratory loads, or for a rotor spinning at 2400 RPM, which means a bandwidth of 640 Hz is needed to satisfy the Nyquist condition. The wire sensor system first proposed by Baz [93] meets these requirements. This is an extension of strain gage theory. Strain gages can be used to obtain global displacements instead of local displacements with a single clever adjustment to the gage. Strain gages have negligible weight, can be embedded in the blade structure, draw little power, have very high bandwidth and can function well in the high CF environment of a rotor blade (full scale or Mach scale). The main drawback to strain gages is the poor SNR (signal-to-noise ratio), especially when the output is transmitted through an electric slipring. This new sensor has

a significantly better SNR ratio than a traditional strain gage. Baz's work for beam bending will be summarized. Then, his work will be extended to elastic twist. Finally, the theory will be applied to a rotor blade. Validation of the sensor embedded in a Mach scale rotor using a camera motion capture system will be discussed.

### 5.4.1 Basic Theory

Strain gages and finite elements are used to obtain continuous bending deformations of a beam. This was first proposed by Baz and Poh [93], [94], [95] and is classified as a distributed sensor as opposed to a discrete sensor. In terms of a beam, a distributed sensor gathers information over a spanwise portion of the beam in order to measure a global property of that spanwise section. On the other hand, a discrete sensor provides information at just one point on the beam and measures only local information. Local sensors can be affected by local phenomenon, such as manufacturing non-uniformities. Hence, it is difficult to extrapolate global phenomenon from local sensors.

The strain gage is a local sensor that measures strain at a point. In theory, a gage can be bonded to a beam to measure strain at a point. However, because the beam local behavior is difficult to predict due to non-uniformities in even a supposedly uniform beam and different quality bonds between the gage and beam, a calibration with either known loads or deflections is conducted before using the gage in testing. This locality also makes it difficult to obtain global information from the strain gage. In theory, beam local deflections can be extrapolated from local strain gages. Various authors have attempted to determine global deflections from local strain data. In practice, noise and local strain dis-

continuities lead to large errors. Double integration is needed to go from the second derivative of bending to deflection, so the noise and discontinuities are integrated twice, leading to a poor SNR ratio. More strain gages would help improve the accuracy of the deflection measurements. Many gages also avoids the issue of placing a gage on a node where little motion occurs. As the number of gages approaches infinite, the deflection measurement will become more accurate. The global deflections must be a summation of the local strains.

For Euler-Bernoulli beams with small deflections, a strain gage on the surface of a beam measures a local strain:

$$\epsilon = h \frac{\partial^2 w}{\partial x^2} \quad (5.1)$$

where  $w$  is the beam transverse deflection,  $x$  is along the beam span and  $h$  is the distance from the beam neutral axis. An infinite number of strain gages along  $x$  over a span of length,  $l$ , would result in a total strain of:

$$\int_0^l \epsilon \partial x = \int_0^l h \frac{\partial^2 w}{\partial x^2} \partial x \quad (5.2)$$

If  $h$  is a constant, then it can be moved outside the integral such that:

$$\int_0^l \epsilon \partial x = h \int_0^l \frac{\partial^2 w}{\partial x^2} \partial x = h(w'(x=l) - w'(x=0)) = h\Delta w' \quad (5.3)$$

So, if  $h$  is known, then the measurement is the change in the beam slope over the span. A strain gage unfolded over the span is an infinite number of strain gages (Fig. 5.3).

This means a wire laid along the span integrates all the local strains over the span. This simple concept of an integrated strain gage will be the basis

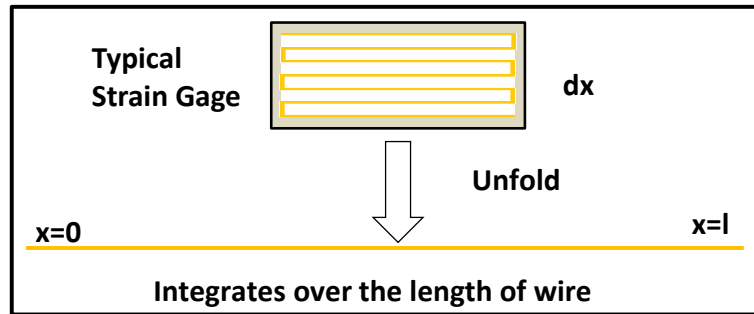


Figure 5.3: Basic Concept

for measuring rod elastic twist. Integration also has an advantage in that the integral of zero mean noise in theory is zero. So, the sensor will have a high signal to noise ratio. Nothing is known about the beam properties or the loading on the beam and yet the sensor will give the beam slope at its endpoint.

The integral is the change in length of the unfolded strain gage called  $\Delta L$ . A change in length of the wire (unfolded strain gage) will cause a change in resistance which can be measured using a Wheatstone bridge:

$$\Delta L = \Delta RA/\rho \quad (5.4)$$

where  $A$  is the cross-sectional area of the wire,  $R$  is the total resistance of the wire and  $\rho$  is the wire material electrical resistivity. This is a well established technique. Constantan is often used for strain gages, but this is not necessary. If circuit printing techniques are used, the cross-sectional area can be so small that even conducting materials can be used and the wire will have enough resistance to provide a good SNR.

Using finite element theory, the beam bending deflection,  $w$ , can be derived from several of these wire sensors. This does require the beam transverse bending deflection shape functions to be assumed. So, this is a kind of integration of the

blade slopes to get blade deflections. Baz, et. al examined beam bending, but his work will be extended to rod twisting. It will be shown that for rod twisting, no assumptions about the rod twist shape functions need to be made because no numerical integration is needed. Instead, the wire sensor directly measures elastic twist angle.

## 5.5 Beam Bending

In this section, the basic concept is explained for measuring beam bending in detail. This is a summary of Baz’s theory, along with some experimental validation. The finite element method is used to assemble the information from multiple wire segments along the beam. The focus here will be on a single beam finite element. For understanding the finite element method, Baz provides a clear, in-depth overview.

### 5.5.1 Theory Overview

The beam is split into spanwise elements (Fig. 5.4). The transverse deflection,  $w$ , within the  $i^{th}$  beam-sensor element is written in terms of the nodal deflection vector  $\{\sigma_i\}$  as follows:

$$w = [N(x)] \{\sigma_i\} = [N(x)] \left\{ \begin{array}{l} w'(x = 0) \\ w(x = 0) \\ w'(x = L) \\ w(x = L) \end{array} \right\} \quad (5.5)$$

where  $N$  is a vector of the shape functions which are chosen according to the expected deflection shapes of the element. The order,  $p$ , of the shape function polynomial determines the number of wire sensors needed within an element. The boundary conditions for continuity with the previous spatial element gives  $w$  and  $w'$  at  $x=0$ . This eliminates two degrees-of-freedom, so the number of wire sensors needed for each element is  $p-2$ . The shape function is the main assumption made for beam bending. Substitution of Eq. (5.5) into Eq. (5.1) yields:

$$\epsilon(x) = h \left\{ \frac{\partial^2 N}{\partial x^2} \right\} \{ \sigma_i \} \quad (5.6)$$

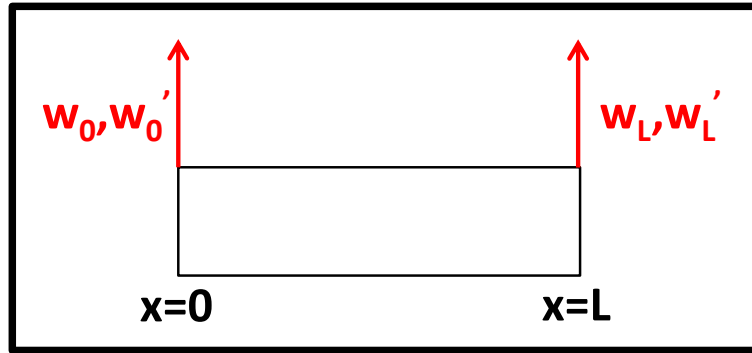


Figure 5.4: Beam Finite Element

A wire sensor,  $s$ , within the element, will have a change in length from bending of:

$$\Delta L_{s_i} = \int_0^{L_{s_i}} \epsilon dx = h \int_0^{L_{s_i}} \left\{ \frac{\partial^2 N}{\partial x^2} \right\} dx = [G_{s_i} \{ \sigma_i \}] \quad (5.7)$$

For many beam elements, a matrix equation can be assembled:

$$\{ \Delta L \} = [G] \{ \sigma \} \quad (5.8)$$

and inverted in order to get the nodal deflections:

$$\{\sigma\} = [G]^{-1} \{\Delta L\} \quad (5.9)$$

### 5.5.2 Wire Sensor Advantages

The beam transverse shape function within each element is assumed, so the wire sensors are really beam slope sensors with no assumptions made for pure bending. The wire sensors give the beam slope at their endpoints for any arbitrary beam deflection (arbitrary loading). Deflection is found through assuming the relationship between beam bending slope and deflection. This assumes the beam bending shape function and an integration is carried out. However, it is just a single integration and not double as would be needed for discrete point strain gages. With the shape function assumption, the deflection and strain distribution along the beam are given by:

$$w(x) = [N(x)] \{\sigma\} \quad (5.10)$$

$$\epsilon(x) = h \left\{ \frac{\partial^2 N(x)}{\partial x^2} \right\} \{\sigma\} \quad (5.11)$$

The wire lengths can be chosen such that the elemental G matrix has zeros diagonally, so matrix inversion can be avoided for real time computation.

### 5.5.3 Baz Proof-of-Concept

Baz carried out an experiment to validate the theory with a two-segment wire sensor embedded in a cantilever beam shown in Fig. 5.5.

The beam has ten strain gages and ten displacement sensors to compare

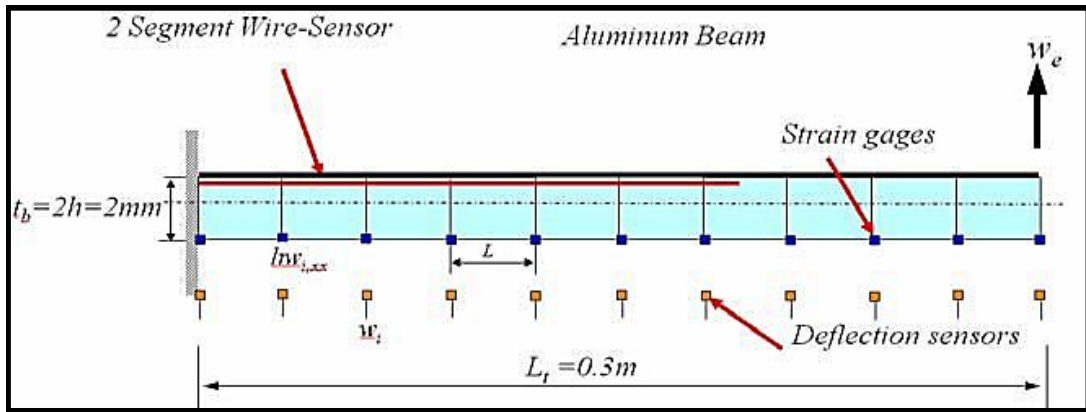


Figure 5.5: Distributed Wire Sensor in Cantilever Beam

with the wire sensor output. The comparison is shown in Fig. 5.6. The two wire sensors match the 20 strain gages and deflection sensors well. So, Baz has validated the wire sensor.

## 5.6 Theory applied to Rotorcraft Blade

The theory will be applied to a rotorcraft blade in order to determine the blade lead-lag bending, flap bending and elastic twist during flight. The blade elastic deflections are modeled in the same way as in UMARC (University of Maryland Advanced Rotorcraft Code). This code has been used in conjunction with CFD to predict blade deflections of the UH60A during high speed and high vibration level flight [96] as well as maneuvers [97]. The model was validated with flight test data. In order to apply Baz's wire sensor concept to a rotorcraft blade, two things need to be added. First, the rotorcraft blade has a large, constant centrifugal force and second, the theory for measuring elastic twist needs to be developed. This section will look at the full derivation of the blade strain due to elastic deformations. The following section will look to expand the wire sensor theory to these deformations.

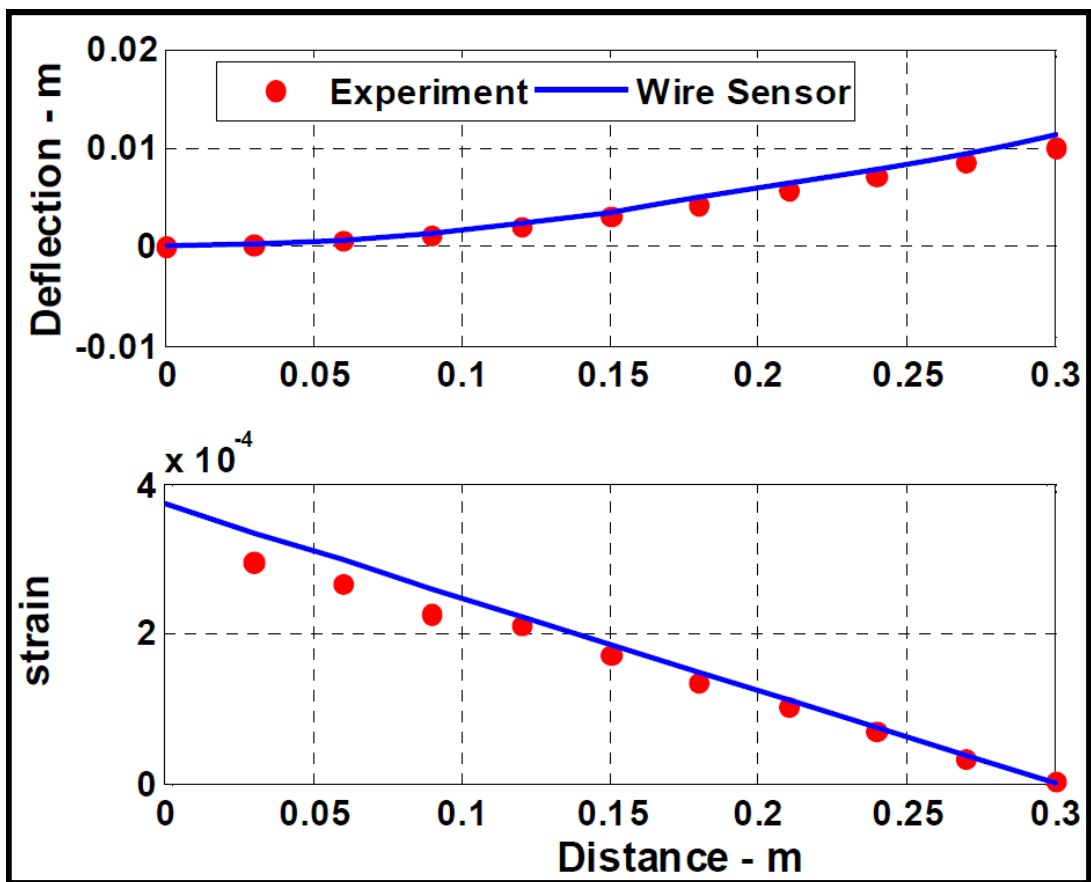


Figure 5.6: Distributed Wire Sensor Validation

### 5.6.1 Introduction

An appropriate model for the blade needs to be chosen in order to allow the wire sensor strain information to be converted to blade deformations. In the work by Abhishek, as well as Datta, with UMARC, the blade is modeled as a second order nonlinear Euler-Bernoulli beam with axial elongation from the CF and elastic twist modeled as quasi-coordinates [98], [99], [100]. The rotor blades are slender structures and hence can be idealized as beams. This means that out-of-plane warping and shear are neglected, so that the cross section remains rigid and perpendicular to the elastic axis after deformation. This implies that the angle of elastic twist is the only rotational variable. This approximation is acceptable up to moderate deformations, which are up to 15% deflection. This derivation will be limited to a straight blade, but could easily be extended to incorporate structural sweep and droop [101]. The goal is to look at only the blade elastic deformations, whereas for UMARC, the goal is to relate the blade deformations to the helicopter body motion in order to trim the rotor. So, unlike UMARC, the blade motion does not need to be translated to the hub fixed frame.

### 5.6.2 Bending with Rotation

Baz showed that beam bending can be measured in a rotating beam [102]. It is worth looking at this experiment because of the quality of the results. The experimental setup is seen in Fig. 5.7.

The beam strain measured by the wire is:

$$\epsilon(x) = -h \frac{\partial^2 w}{\partial x^2} \quad (5.12)$$

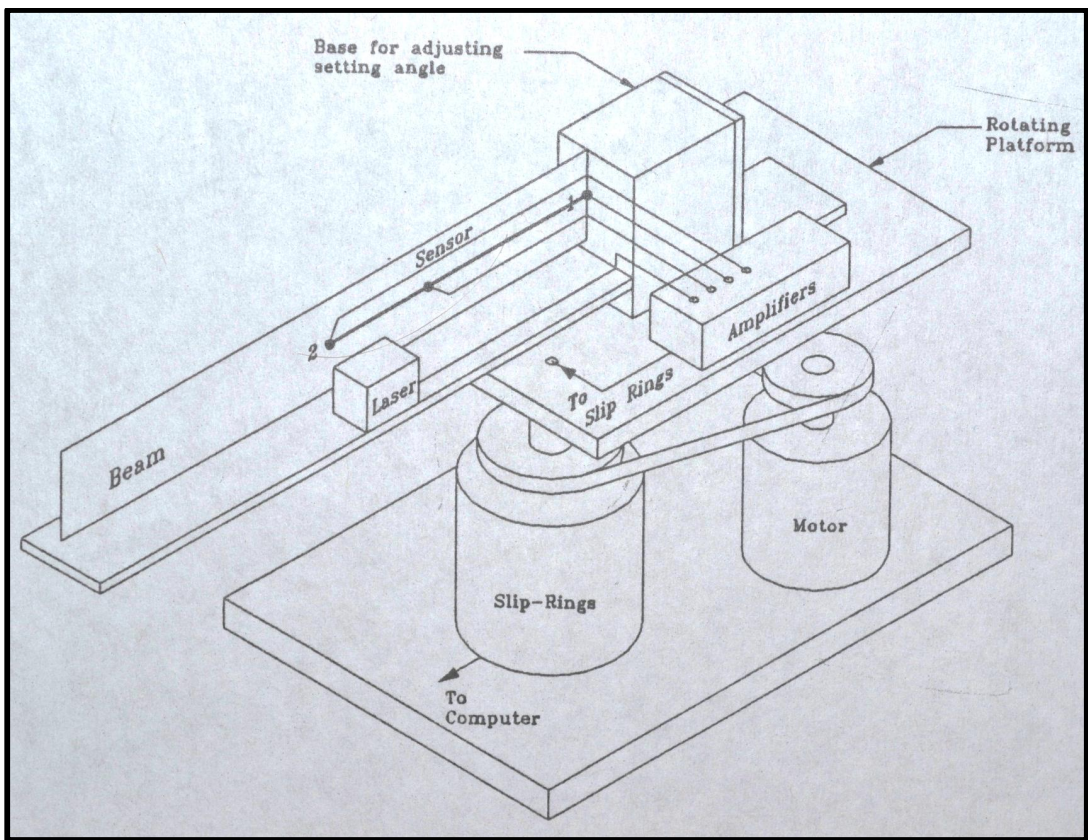


Figure 5.7: Rotating Beam Setup

where  $x$  is along the beam span,  $h$  is the distance from the neutral axis and  $w$  is the transverse deflection. The beam lengthening due to CF is neglected. Within the finite element, a third order polynomial is assumed for the beam bending shape function. As seen in the figure, the wire sensor consists of just one finite element extending from the beam root to its mid-span. The element has 2 wire lengths as the elements has two unknowns: the transverse displacement and slope at the end of the element. The beam is cantilevered, so the slope and displacement at the other end of the element are zero. The wire sensor lengths are chosen as  $L$  (element length) and  $\frac{2}{3}L$ . Integrating the strain over both wire lengths yields the matrix equation:

$$\begin{bmatrix} \Delta L_1 \\ \Delta L_2 \end{bmatrix} = -h \begin{bmatrix} 0 & 1 & 0 & -1 \\ 4/3L_1 & 4/3 & -4/3L_1 & 0 \end{bmatrix} \begin{bmatrix} w_1 \\ w'_1 \\ w_2 \\ w'_2 \end{bmatrix} \quad (5.13)$$

where  $\Delta L$  is the change in the length of the wire section. 1 and 2 are the element endpoints. So, due to the chosen shape function and wire length, the displacement depends on just  $L_2$ :

$$w_2 = (3L_1/4h)\Delta L_2 \quad (5.14)$$

The beam has a length of 16 inches. While the beam is rotating at 65RPM, the beam deflection is recorded using a laser height sensor. Fig. 5.8 shows the comparison of the wire sensor displacement value and the laser sensor. For these small deflections ( $\pm 0.12$  in.), the sensor exactly matches the laser for a sinusoidal motion and random motion. So, a wire sensor with just two wires

is shown to give the displacement exactly for a rotating beam for very small deflections ( $w/L \leq 1.5\%$ ).

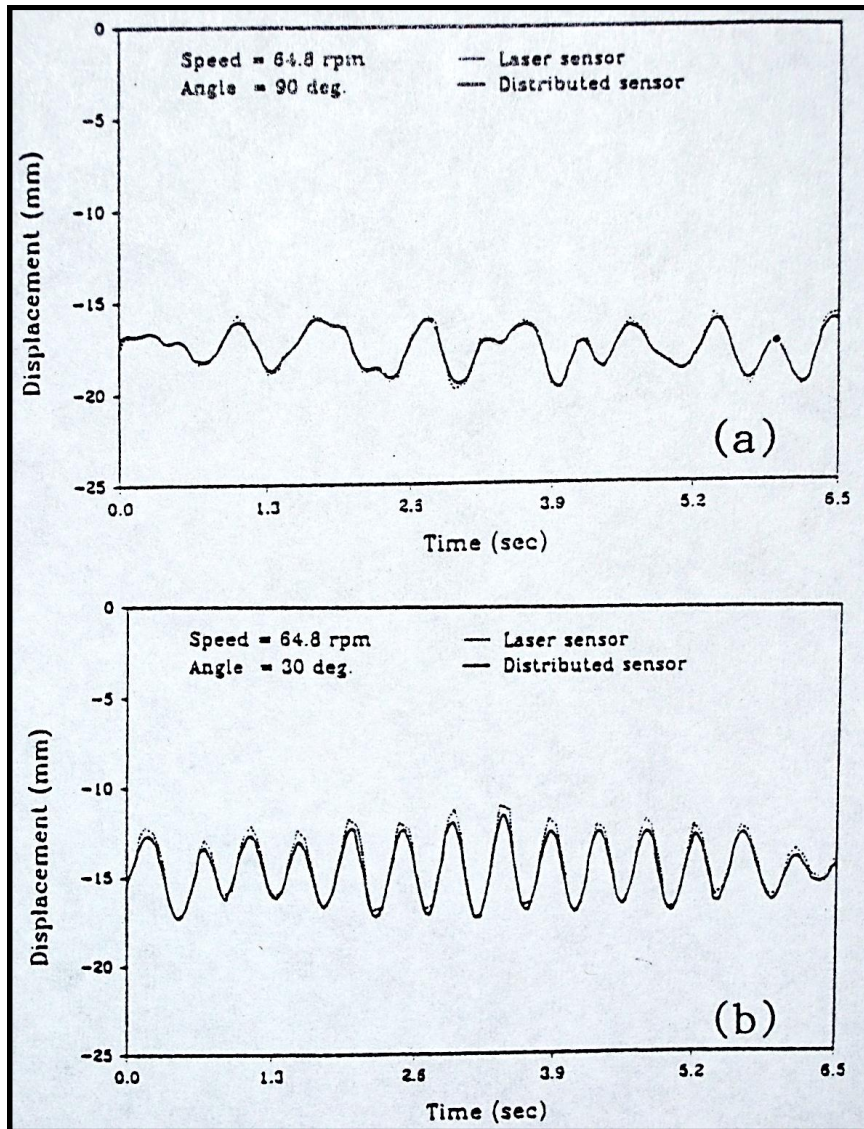


Figure 5.8: Distributed Wire Sensor in Rotating Cantilever Beam

### 5.6.3 Blade Strain

Now, the blade elastic strain model will be rigorously derived with all assumptions stated so that the proposed wire sensor network's limitations are clearly

stated. This follows Datta's derivation [96]. Start by considering a generic point P lying on the undeformed elastic axis of the blade. The orientation of a frame consisting of the axes normal to and along principle axes for the cross section at P defines the undeformed coordinate system  $(x,y,z)$ . The blade deforms such that P goes to P'. The orientation of a frame consisting of the axes normal to and along principle axes for the cross section at P' defines the deformed coordinate system  $(\xi, \eta, \zeta)$ . So, these are the distances from the elastic axis.  $u,v,w$  are the translational variables from P to P' and three rotational variables from  $(x,y,x)$  to  $(\xi, \eta, \zeta)$  as well as any out of plane deformations of the cross section (warp). The first main assumption is the blade is an Euler-Bernoulli beam, so the warp is neglected. Also, two of the three angles can now be expressed as derivatives of the deflection variables. So, four variables -  $u,v,w$  and a rotational angle, completely determine the deformed geometry. The rotational angle is the angle of elastic twist,  $\phi$ . Also, because the goal is not to relate the blade deformations to the helicopter body motion, but only to measure blade deformation relative to the blade root, the blade root angle does not matter as it does in Datta's derivation. This is true of the blade rigid twist as well. So, unlike Datta, there are no  $\theta$  terms.

The general non-linear displacement equations are complex. So to simplify, an ordering scheme is used [96]. Terms of order  $\epsilon^2$  are ignored with respect to unity. In this case, the largest term is  $O(\epsilon)$ , so terms of  $O(\epsilon^3)$  and higher are neglected. The equations to second order are (' is  $\frac{\partial}{\partial x}$ ):

Axial Strain:

$$\epsilon_{xx} = u' + \frac{v'^2}{2} + \frac{w'^2}{2} + (\eta^2 + \zeta^2) \frac{\phi'^2}{2} - v''(\eta \cos(\phi) - \zeta \sin(\phi)) - w''(\eta \sin(\phi) + \zeta \cos(\phi)) \quad (5.15)$$

Engineering Shear Strains:

$$\epsilon_{x\eta} = -\zeta\phi' \quad (5.16)$$

$$\epsilon_{x\zeta} = -\eta\phi' \quad (5.17)$$

It is worth noting that:

$$\epsilon_{yy} = 0 \quad (5.18)$$

Eq. 5.15 can be further simplified using the ordering scheme:

$$\begin{aligned} \frac{u}{R} &= O(\epsilon^2) & \frac{v}{R} &= O(\epsilon^2) \\ \frac{w}{R} &= O(\epsilon) & \frac{\eta}{R} &= O(\epsilon) \\ \frac{\zeta}{R} &= O(\epsilon) & \phi &= O(\epsilon) \end{aligned} \quad (5.19)$$

For this analysis, it is assumed that:

$$\frac{1}{R} = O(\epsilon) \quad (5.20)$$

Dividing Eq. 5.15 by  $R^2$  yields:

$$\begin{aligned} \epsilon_{xx} = \frac{u'}{R} \frac{1}{R} + \frac{1}{2} \frac{v'^2}{R^2} + \frac{1}{2} \frac{w'^2}{R^2} + \left( \frac{\eta^2}{R^2} + \frac{\zeta^2}{R^2} \right) \frac{\phi'^2}{2} - \frac{v''}{R} \left( \frac{\eta}{R} \cos(\phi) - \frac{\zeta}{R} \sin(\phi) \right) \\ - \frac{w''}{R} \left( \frac{\eta}{R} \sin(\phi) + \frac{\zeta}{R} \cos(\phi) \right) \end{aligned} \quad (5.21)$$

The extension term,  $u'$ , is  $O(\epsilon^3)$ . This is neglected because of its higher order and for simplification. A wire placed along the neutral axis could be added to measure this. The term,  $\left( \frac{\eta^2}{R^2} + \frac{\zeta^2}{R^2} \right) \frac{\phi'^2}{2}$ , is  $O(\epsilon^4)$  and so is neglected. Finally, the

deflections of the blade are assumed small so that:

$$\frac{1}{2}v'^2 \ll v''\eta \quad (5.22)$$

$$\frac{1}{2}w'^2 \ll w''\zeta \quad (5.23)$$

This assumption will be more valid if  $\eta$  and  $\zeta$  are as large as possible such as the blade LE for  $\eta$  and its maximum thickness for  $\zeta$ . With these assumptions, the final engineering strain equation is:

$$\epsilon_{xx} = -v''\eta - w''\zeta \quad (5.24)$$

Summing the two shear strain equations (Eq. 5.16,Eq. 5.17) yields:

$$\epsilon_{x\eta} + \eta_{x\zeta} = -\phi'(\eta + \zeta) \quad (5.25)$$

#### 5.6.4 Conclusion

This is the model of the blade strains that will be used for the wire sensor network in-flight. It is important to emphasize what is neglected in the model. There is no blade structural properties such as mass or stiffness. The only blade property is the location of the wire sensor from the neutral axis. This can be determined on the benchtop if there is uncertainty about this. The assumptions are as follows:

1. The blade is a slender beam and so Euler-Bernoulli assumptions apply.
2. Blade warping is ignored (E-B).
3. All terms  $O(\epsilon^3)$  and higher are neglected as the lowest order term is  $O(\epsilon)$ .

4. Blade extension is neglected.

5. Deflections are small enough that:

$$\frac{1}{2}v'^2 \ll v''\eta \quad (5.26)$$

$$\frac{1}{2}w'^2 \ll w''\zeta \quad (5.27)$$

Though these assumption do limit the accuracy of the model, it is important to note that if higher accuracy is needed, the extension term,  $u'$ , can be brought back into the equations and measured along the blade neutral axis. Also, accuracy is relative as no other system for in-flight measurement of blade elastic deformations is available.

## 5.7 Model of Rotorcraft Blade Wire Sensor

In this section, the wire sensor theory is applied to the previous sections's blade strains in order to obtain blade deformations, including twist. Elastic twist directly changes the blade AOA (angle-of-attack) driving the aerodynamic force on the blade. Thus, it is more important to measure blade elastic twist than other deflections. Although numerical integration is needed for bending, for elastic twist, the wire sensor directly gives the twist angle without any numerical integration. This means no twist shape function is needed, so the sensor can handle any arbitrary blade moment distribution. To start, it is helpful to think of splitting the blade into two parts: a beam for lead-lag bending ( $v$  deformation) and flap bending ( $w$  deformation) and a rod in torsion for elastic twist.

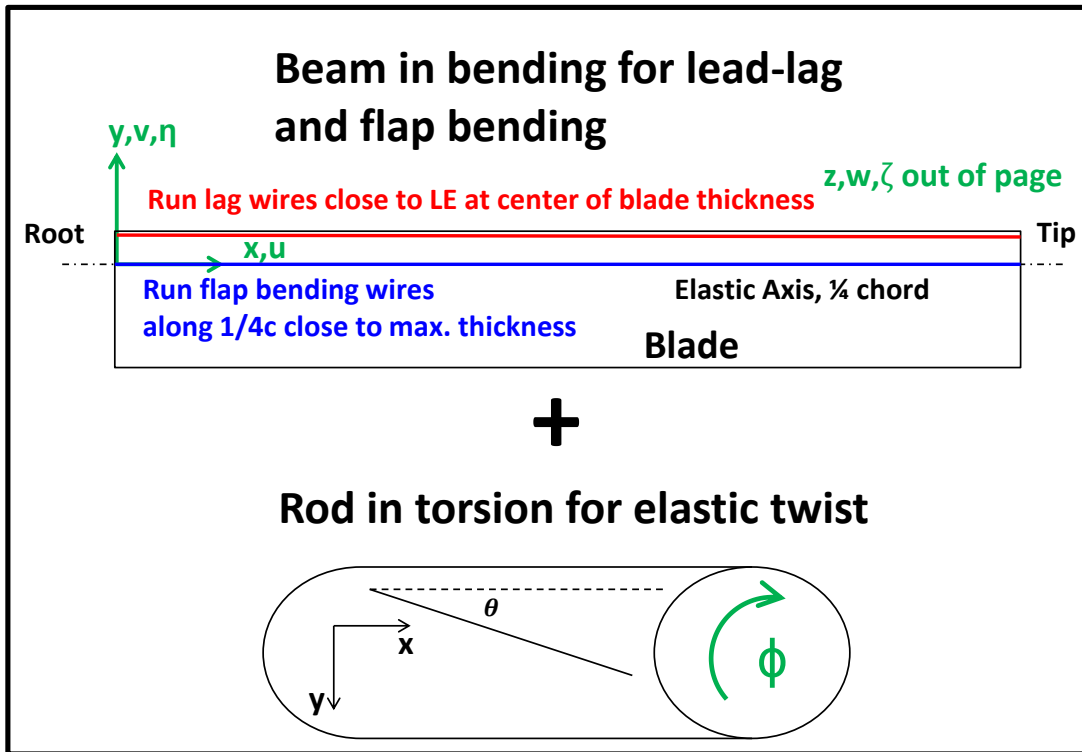


Figure 5.9: Splitting Blade: Beam in Bending + Rod in Torsion

### 5.7.1 Bending

Fig. 5.9 shows the wire concept for measuring blade bending. Lag wires are run along the center of the blade thickness where  $\zeta = 0$ . The flap bending wires are run along the top of the blade spar where the thickness is maximum and  $\eta=0$ . So, this requires the blade elastic axis to be known. This reduces the equations further.

For lead-lag bending:

$$\epsilon_{xx} = -\eta v'' \quad (5.28)$$

For flap bending:

$$\epsilon_{xx} = -\zeta w'' \quad (5.29)$$

Thus, the wires should be positioned in order to maximize  $\eta$  for lead-lag bending and  $\zeta$  for flap bending. So, each finite element will be the same as the example in Section 5.6.2 with 2 wires in each element for 2 unknowns of the element, the slope and displacement at the end of the element. The slope and displacement of the start of each element comes from the previous element. The full finite element matrix equations of the theory applied to a rotorcraft blade will come after the actual network for experimental validation is described.

### 5.7.2 Twist

This is the main contribution of this work. Start with the rod in torsion in Fig. 5.9, where the angle  $\theta$  is relative to the x-y plane. The equation for the shear strain measured by a strain gage at an angle,  $\theta$ , on the rod is:

$$\epsilon_{\theta} = \frac{\epsilon_{xx} + \epsilon_{yy}}{2} + \frac{\epsilon_{xx} - \epsilon_{yy}}{2} \cos(2\theta) + \frac{\gamma_{xy}}{2} \sin(2\theta) \quad (5.30)$$

But for the idealized blade,  $\epsilon_{yy}=0$ , so:

$$\gamma_{xy} = \frac{2\epsilon_{\theta}}{\sin(2\theta)} - \frac{\epsilon_{xx}(1 + \cos(2\theta))}{\sin(2\theta)} \quad (5.31)$$

Then, just as with bending, the shear strain is integrated over an element's span (over  $x$ ). This, along with Eq. 5.25 leads to:

$$\int \gamma_{xy} dx = \int -\phi'(x)(\eta(x) + \zeta(x)) dx = \int \frac{2\epsilon_{\theta}}{\sin(2\theta)} - \frac{\epsilon_{xx}\cos(2\theta)}{\sin(2\theta)} dx \quad (5.32)$$

where  $\phi$ ,  $\eta$  and  $\zeta$  are can vary along the wire length in any arbitrary fashion. Expanding Eq. 5.32, letting:

$$A = \frac{1 + \cos(2\theta)}{\sin(2\theta)} \quad (5.33)$$

$$\int -\phi'(x)(\eta(x) + \zeta(x)) dx = \frac{2}{\sin(2\theta)} \int \epsilon_{\theta} dx + A \int \eta(x)v''(x) dx + A \int \zeta(x)w''(x) dx \quad (5.34)$$

The only unknown term is  $\phi'(x)$ . The wire sensor measurement is:

$$\Delta L = \int \epsilon_{\theta} dx \quad (5.35)$$

The two bending terms can be from bending wires over the same blade spanwise section as the twist sensor. However, if the bending wires do not exactly overlap, this is not a problem. Instead, the blade bending wires can be used to get the distribution of  $v''(x)$  and  $w''(x)$  in the spanwise length of the twist sensor.

A linear distribution for  $\phi'$  within a finite element is chosen, though any distribution can be chosen:

$$\phi'(x) = Cx + D \quad (5.36)$$

Apply boundary conditions for a single element (WS is start of wire element,  $x=0$ ):

$$\phi'(x = 0) = \phi'_{WS} = D \quad (5.37)$$

The terms,

$$\int x(\eta(x) + \zeta(x))dx \quad (5.38)$$

and

$$\int (\eta(x) + \zeta(x))dx \quad (5.39)$$

can be arbitrary and numerical integration can be used over each wire length to get the value for these terms. So, there is just one unknown, C. Plugging Eq. 5.36 into Eq. 5.34 leads to:

$$\begin{aligned} C \int x(\eta(x) + \zeta(x))dx &= \phi'_{WS} \int x(\eta(x) + \zeta(x))dx \\ &- \frac{2}{\sin(2\theta)} \Delta L - A \int (v''(x)\eta(x) + w''(x)\zeta(x))dx \end{aligned} \quad (5.40)$$

Everything is known so C can be solved for. This leaves the twist within the single element as:

$$\phi(x) = \int_{Wire} \phi'(x)dx = \frac{1}{2}Cx^2 + \phi'_{WS}x + \phi_{WS} \quad (5.41)$$

So, now the elastic twist on a rotor blade in flight can be measured. A common misconception is that because of the assumed shape function, this sensor will not do better at measuring elastic blade twist than a single shear strain gage. However, this sensor is similar to having an infinite number of single shear strain gages so that even if the assumed shape function is wrong, the change in elastic twist over the wire sensor length will be accurate.

### 5.7.3 Blade Wire Sensor Network

The final step is to apply the theory to a real rotorcraft blade. Take for instance, the Mach scale rotor blade with TE flaps for primary control. In this section, the physical layout of the blade wire sensor network will be described. Then, the wire material will be discussed.

For lead-lag bending,  $\eta(x)$  should be large to increase the SNR ratio as well as make the assumption Eq. 5.22 more valid. Then,  $\zeta(x)$  should be zero. This is a wire at either the LE or TE. The TE cannot be used because the TE flaps are in the way. So, lead-lag wire sensors should lie at the blade LE.

For flap bending,  $\zeta(x)$  should be large to increase the SNR ratio as well as make the assumption Eq. 5.22 more valid. Then,  $\eta(x)$  should be zero. This is a wire at the blade  $\frac{1}{4}c$  where the blade thickness is at its maximum and presumably where the elastic axis lies.

For the shape of the twist wire, it is useful to derive the equation for the wire sensor measurement from Eq. 5.34 and Eq. 5.35:

$$\Delta L = \int \epsilon_{\theta} dx = \frac{\sin(2\theta)}{2} \left[ \int (-\phi'(x)(\eta(x) + \zeta(x)) - A\eta(x)v''(x) - A\zeta(x)w''(x)) dx \right] \quad (5.42)$$

The integral is carried out over the length of the wire sensor. The sum,  $(\eta(x)+\zeta(x))$ , must not change sign over the wire length. Otherwise the shear strain changes sign and so over the wire length, twist will be canceled out lowering the SNR ratio (Fig. 5.10). This requires the wire to be wholly in quadrant 1 or wholly in quadrant 4. For a blade with TE flaps, quadrant 4 cannot be used. Also, for the best SNR, the sum,  $(\eta(x)+\zeta(x))$ , should be maximized and so should be on the blade skin.

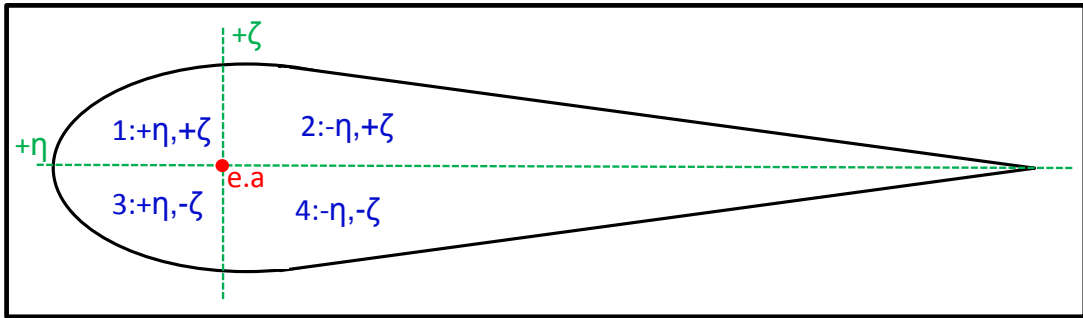


Figure 5.10: Blade Profile Split into Quadrants for Measuring Twist

Ideally, the twist sensor would be sensitive only to twist. To minimize the effect of bending,  $A$  (Eq. 5.33) should be minimized and  $\frac{\sin(2\theta)}{2}$  maximized. Thus,  $\theta$  should be  $45^\circ$ . A straight line cannot be used, because  $\theta$  for the wire sensor would need to be small to fit in quadrant 1 while covering a significant spanwise length of the blade (Fig. 5.11). A sawtooth pattern solves this problem. The angle can be made  $45^\circ$  while the straight sections of the wire do not measure anything according to the assumption that  $\epsilon_{yy}=0$ . However, this assumption does not need to be made. Instead, the straight sections of the sawtooth can have a electrical resistance much lower than the slant sections.

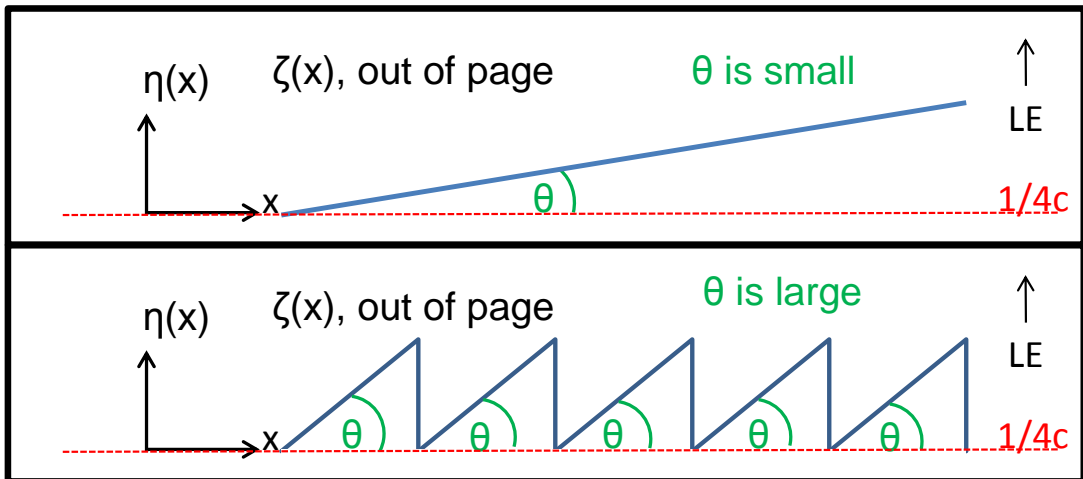


Figure 5.11: Sawtooth Pattern Required for Sufficiently Large Sensor  $\theta$

Table 5.1: Steel vs. Constantan as Wire Sensor

<b>Property</b>	<b>Constantan</b>	<b>Steel</b>
$\rho$ , $\Omega$ -in @ 20°C	1.93x10 <sup>-5</sup>	2.72x10 <sup>-5</sup>
$\alpha$ , Temp. Coeff.	8.00x10 <sup>-6</sup>	17.3x10 <sup>-6</sup>
R/L for 2 mil dia. wire, $\Omega$ /in	6.14	8.65

So, a network of wire sensors to measure blade elastic deformations is described. Wires running along the blade LE measure lead-lag bending. Wires running along the 1/4c, at blade maximum thickness, measure flap bending. A sawtooth pattern running along the blade skin ahead of the 1/4c and always on the upper or lower half of the blade thickness measures elastic twist.

#### 5.7.4 Wire Material

The wire sensor cross-section should be as small as possible so that it can be embedded within the blade structure without interfering with the structure. The wire material should meet several conditions:

1. Sufficient resistance over the wire length to be measurable with a bridge circuit.
2. Ductile so it can strain without permanent deformation or damage.
3. Can be insulated electrically so that it can transfer the strain from the structure to the wire.
4. Low temperature coefficient of resistivity.
5. Sufficient strength for handling.

Steel and Constantan meet these requirements and are compared in Table 5.1.

Although constantan is often chosen for strain gages due to its low  $\alpha$ , steel also has a low  $\alpha$ , yet higher resistivity. Steel also solders more easily. If the resistivity is lower than this, then the cross section area of the wire becomes too small and so the wire becomes fragile. The cross section does not need to be a circle so thin shim stock or deposition could be used for the sensor instead of wire.

### **5.7.5 Conclusion**

The wire sensor theory has been expanded from bending to elastic twist and then applied to a rotorcraft blade. The effect of rotation can be neglected. A sawtooth shape is required for the twist sensor in order to maximize the twist sensor sensitivity to elastic twist. The sensor should stay within a single quadrant of the blade cross section as divided by the elastic axis. Any ductile material with proper resistance can be used for the sensor. Constantan and steel are examined because of their high resistivity. However, a material with less resistivity can be used if the material cross sectional area is smaller than steel and constantan.

## **5.8 Validation of Rotorcraft Blade Wire Sensor**

The concept is validated on the benchtop for a section of a Mach scale rotor blade. The blade is the same as that used for the TE flaps for primary control. So, the concept is validated with a non-uniform composite blade consisting of a spar, foam core and skin. The goal is to validate the twist sensor. Baz and others have proven the wire sensor for bending.

### 5.8.1 Test Description

Two twist sensors are placed in a Mach scale blade. The sensors are placed where the inboard and outboard TE flaps would be located (Fig. 5.12). A common concern with the Mach scale testing with TE flaps for primary control is that the TE flaps cause the blade to twist locally. So, placing sensors at the TE flap spanwise locations could monitor local twist during flap deflection. The blade spanwise locations could monitor local twist during flap deflection. The blade span is 28 in. Each sensor has a spanwise length of 4.59 in.

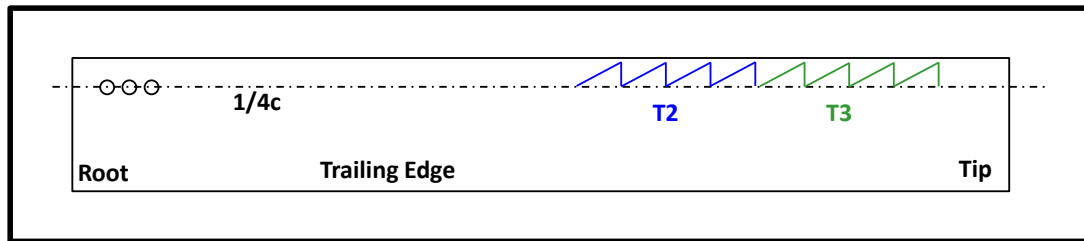


Figure 5.12: Twist Sensors in Mach Scale Blade Skin

The chosen sensor  $\theta$  ( $37^\circ$ ) is less than  $45^\circ$  because the sawtooth pattern is painstaking to make. The blade has two layers of carbon fiber prepreg skin. The wire sensor is between these two layers and so is part of the structure. The wire diameter for the sensor is approximately 5 mils (2 mil dia. steel wire with insulation). So, the wire sensor does not interfere with the blade structure. The sawtooth pattern is made by cutting out a paper pattern and laying it on top of the first skin layer before curing. Then the steel wire is wrapped around the triangle vertices. In order to maintain wire tension, the wire had to be bonded to each triangle vertex before moving the wire to the next vertex (Fig.

Before curing, the skin is soft and so it is very difficult to maintain wire tension. Each end of the sensor is soldered to copper wire leads that go to the bridge circuit to measure the change in resistance.  $\theta$  is  $37^\circ$  so the sensor has 5 slants in order to cover the spanwise distance. The second skin layer is laid on

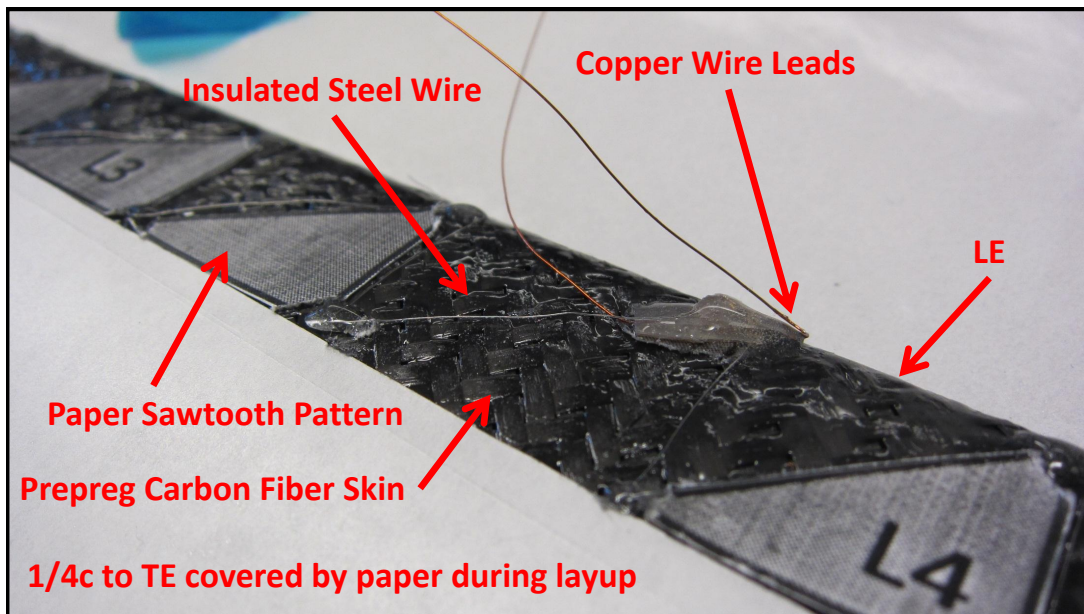


Figure 5.13: Laying Up Sawtooth Pattern - Skin Softness Causes Loss of Wire Tautness

top of the sensor after the paper pattern is removed. Then the blade is cured under pressure.

The wire sensor resistance is not exactly  $350\Omega$  or  $120\Omega$  which are standard Wheatstone bridge resistances. So, bridges were built using 3 resistors of equal value resistance as the sensor wire.

## 5.8.2 Computational Model

### 5.8.2.1 Model Description

In order to address concerns about the twist sensor and the assumptions made for it, a blade under flap bending and torsion loads with the twist sensor described in the previous section is modeled computationally. Just one spanwise section is examined. Lead-lag is neglected as the lead-lag stiffness is high and so the deformation is small for this blade. The blade section is modeled by prescribing

any arbitrary  $w''(x)$  and  $\phi'(x)$  along the elastic axis in response to any arbitrary load.

Then, numerical integration ( $10^5$  elements) is used to calculate the resultant  $w'(x)$ ,  $w(x)$ ,  $\phi(x)$  and the wire sensor measurement as described by Eq. 5.42. It is assumed that a 2 wire single bending element sensor over the same span as the twist wire sensor gives  $w$  and  $w'$  exactly at the element endpoint. Eq. 5.41 describes the elastic twist in the blade section where  $C$  is:

$$C = \frac{-\frac{2}{\sin(2\theta)}\Delta L - A \int w''(x)\zeta(x)dx}{\int x(\eta(x) + \zeta(x))dx} \quad (5.43)$$

from Eq. 5.40 when lead-lag bending is neglected and  $\phi'_{WS}=0$ . The prescribed  $w''$  and  $\phi'$  are shown in Fig. 5.14, along with the  $w',w$  and  $\phi$  resulting from these. The bending and twist loads have two components: a linear function of span and a sinusoidal function of span. The case to be studied has an elastic twist of  $2.56^\circ$  and elastic bending deflection of 0.91 in. over the span, or  $w/R = 20\%$ . Both of these values would be very large on the rotor blade in flight.

### 5.8.2.2 Model Results

Fig. 5.15 shows the blade bending. The chosen shape function for bending does not match the actual curve. Everything in this section refers to computational results, so the actual curve is the numerical integration of the bending second derivative.

However, the twist sensor still yields the correct change in elastic twist over the blade section (Fig. 5.16). The chosen shape function for twist also does not match the actual curve.

So, for arbitrary loading, the single elastic twist sensor yields the actual twist

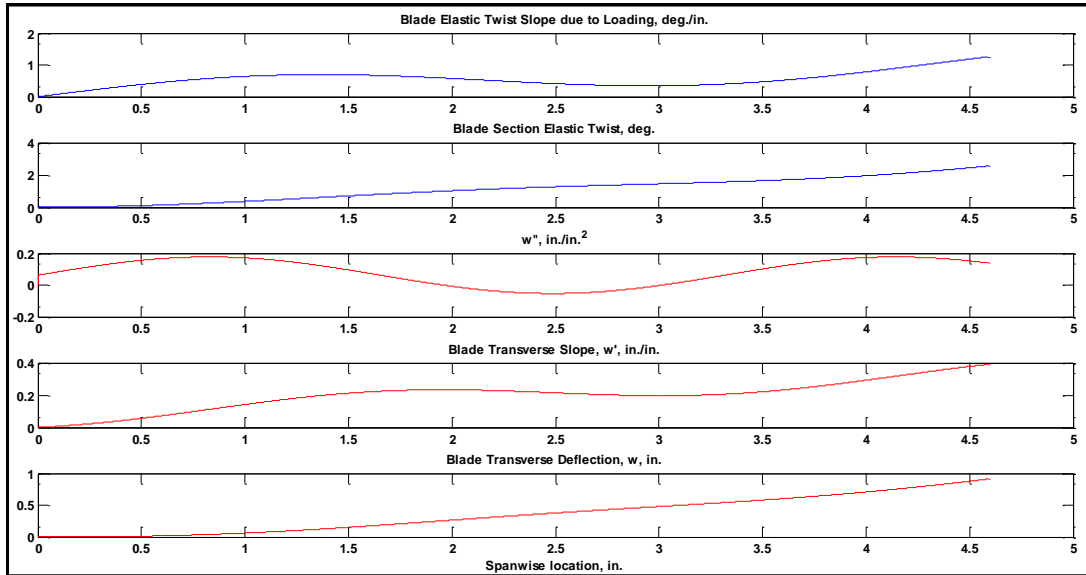


Figure 5.14: Blade Section Twist and Bending With Arbitrary Loading

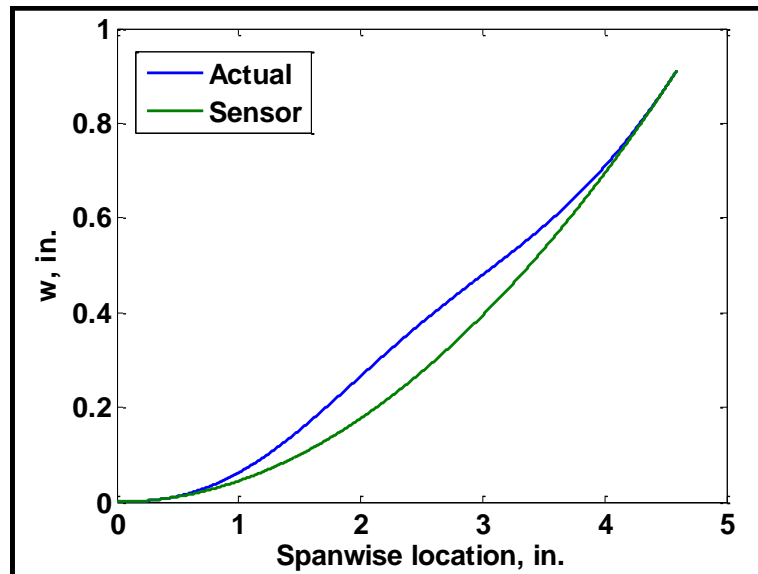


Figure 5.15: Blade Section Bending: Actual vs. Sensor With Arbitrary Loading

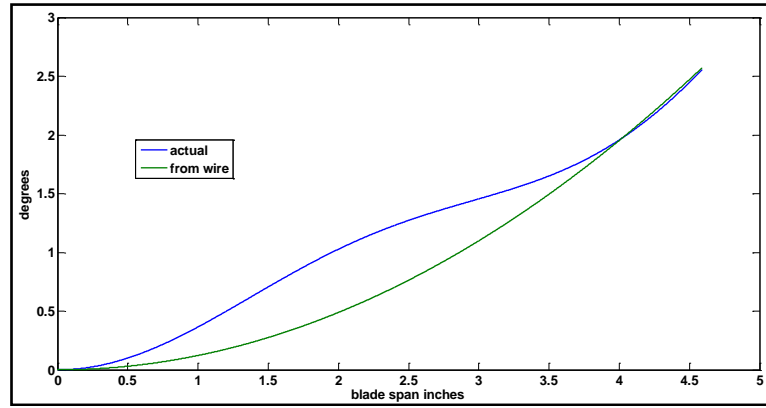


Figure 5.16: Blade Section Twist: Actual vs. Sensor With Arbitrary Loading angle precisely. However, for a real sensor, noise will be present. Also, the blade structure is complex - local discontinuities exist due to poor bonds in composites or microcracks. So, Gaussian zero-mean noise and local discontinuities are added to the prescribed  $w''$  and  $\phi'$ . Local discontinuities are added through the use of impulses as seen in Fig. 5.17. The noise and discontinuities are larger than would be expected on a real blade and sensor.

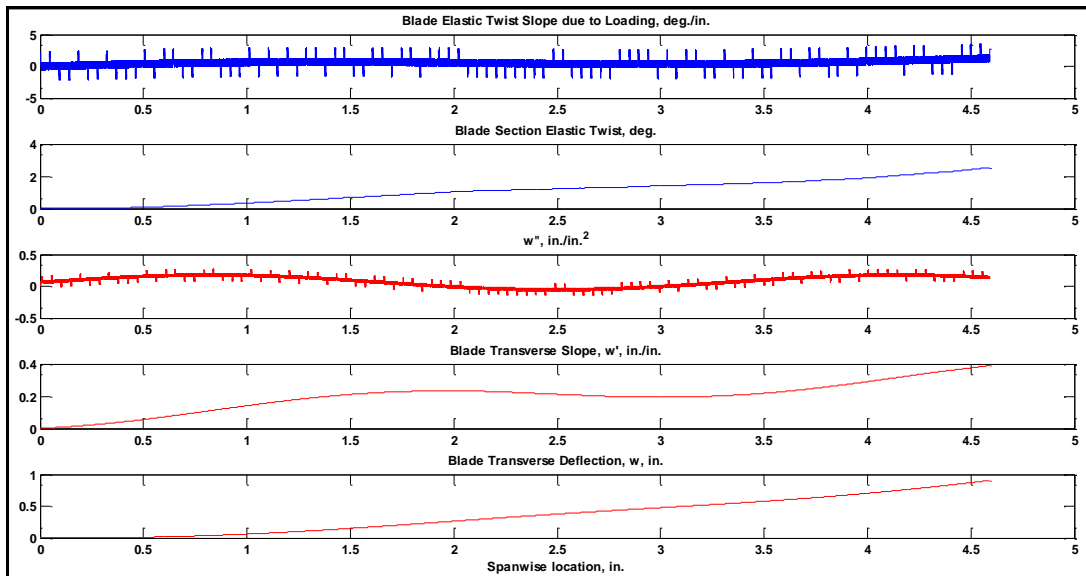


Figure 5.17: Blade Section Twist and Bending With Arbitrary Loading, Noise, Local Discontinuities

Fig. 5.18 shows the bending deflection again. The lines are about the same as without noise and local discontinuities due to double integration.

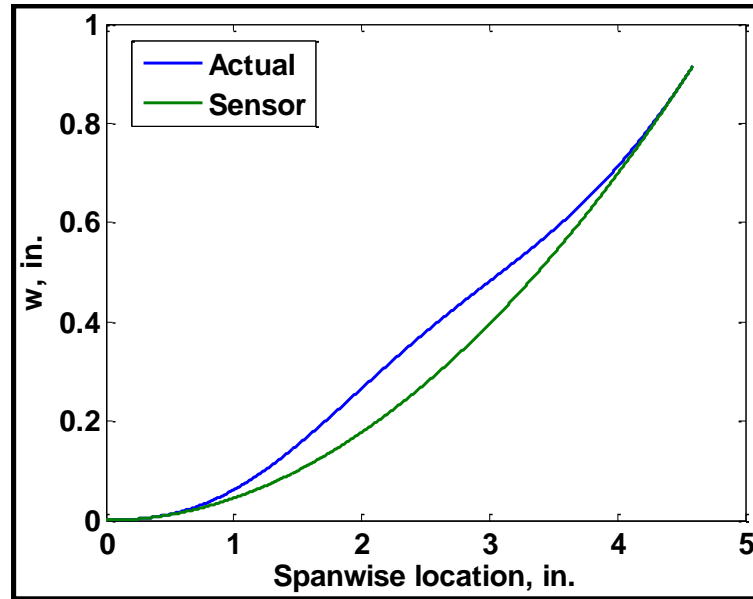


Figure 5.18: Blade Section Bending: Actual vs. Sensor With Arbitrary Loading, Noise, Local Discontinuities

Fig. 5.19 shows the elastic twist deflection again. Again, the sensor measurement deviates from the actual over the spans of the sensor due to the shape function, but the twist at the end of the sensor exactly matches the actual. It is obvious from Fig. 5.17, that a single point sensor would yield no useful information about blade twist or bending and even many sensors would have a large uncertainty. Yet, the single element twist sensor yields exactly the change in elastic twist angle over the spanwise section. If accuracy is needed at other points along the span, additional wire sensors can be added.

### 5.8.2.3 Model Conclusions

A computational model is used to examine the wire sensor concept for measuring blade elastic twist over a spanwise section of a Mach scale rotor. The elastic twist

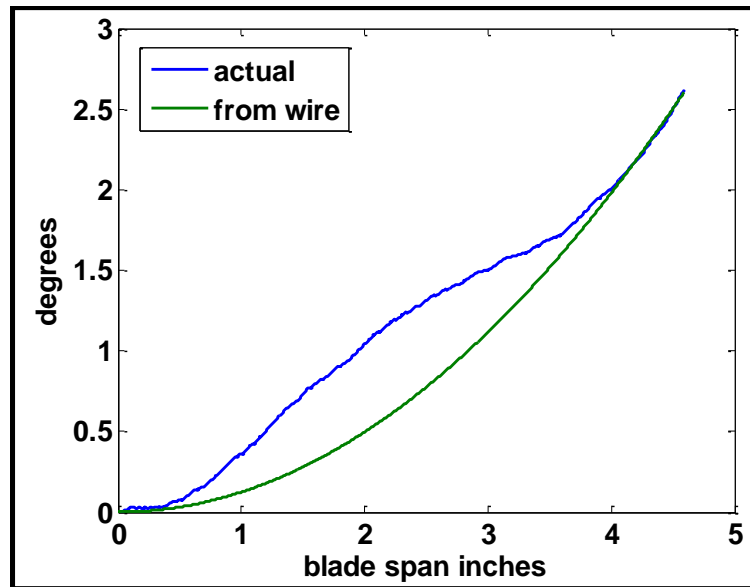


Figure 5.19: Blade Section Twist: Actual vs. Sensor With Arbitrary Loading, Noise, Local Discontinuities

angle and bending deflection are both large - the  $2.5^\circ$  twist angle is for only a portion of the blade and the bending deflection is 20% of span. The following points are demonstrated:

1. The elastic twist shape function does not need to match the actual blade deflections in order to measure precisely the change in elastic twist deflection over the sensor.
2. The bending shape function does not need to match the actual blade deflections in order to measure exactly the change in elastic twist deflection over the sensor.
3. Large bending or twist deflections are not a problem.
4. The sensor is not affected by noise or local structural discontinuities.

### 5.8.3 Single Point Validation

One of the twist sensors (T2) embedded in the Mach scale blade (Fig. 5.12) was validated on the benchtop. The blade root was cantilevered while the tip was constrained in bending by a radial bearing, so that only blade twisting was allowed. The blade tip twist angle was measured by a potentiometer (Fig. 5.20).

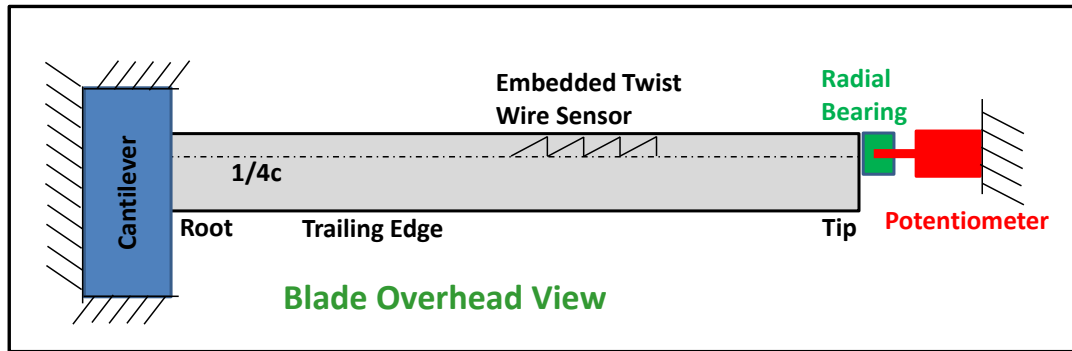


Figure 5.20: Single Point Experimental Setup

The blade is uniform, so the twist was assumed to be linear from the blade root to the tip. So, the elastic twist over the sensor section was:

$$\theta_{T2} = \theta_{Tip} \frac{T2Span}{BladeSpan} \quad (5.44)$$

The first step is to calibrate the sensor. This is done by twisting the blade tip by hand. The sensor output through the bridge circuit can be plotted against the elastic twist angle. The equation describing the twist measurement (if there is no bending) is:

$$-\frac{\sin(2\theta)}{2} C \int x(\eta(x) + \zeta(x)) dx = \Delta L \propto \Delta R \propto \Delta V \quad (5.45)$$

where R is the initial resistance of the wire (130) and V is the bridge output voltage (5V excitation). Fig. 5.21 shows the calibration curve. From Eq. 5.40,

the relationship should be linear. The calibration factor includes the electrical bridge circuit and the shape of the twist sensor. For this test, bending is neglected.

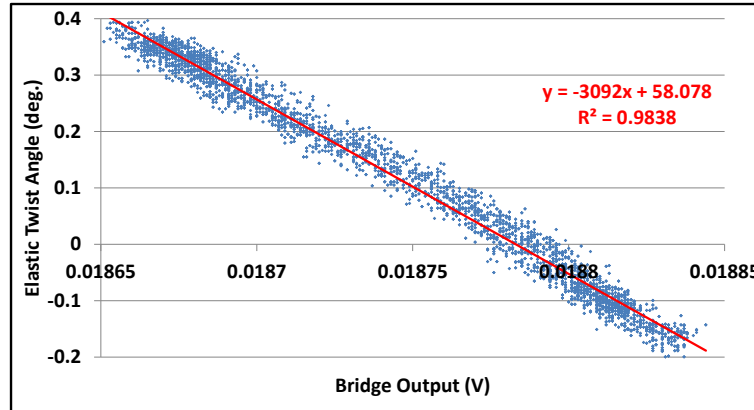


Figure 5.21: Calibration Curve for Single Twist Sensor

The relationship is linear, but noisy, due to poor quality resistors completing the bridge circuit. Better resistors for the bridge circuitry could lower the sensor noise. This calibration is then used to measure the blade elastic twist over the spanwise section covered by the twist sensor and compared to the potentiometer measurement (Fig. 5.22). The sensor is shown to work quite well.

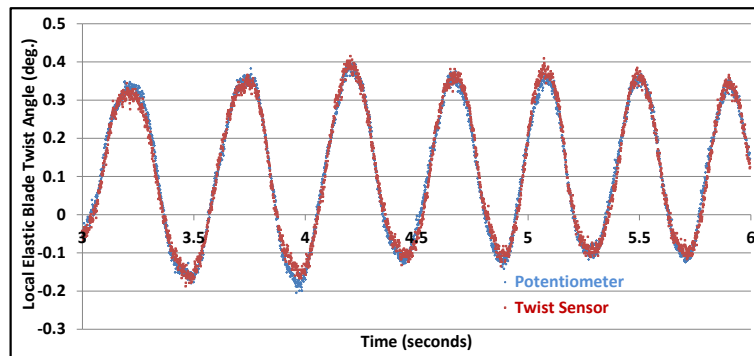


Figure 5.22: Comparison of Single Twist Sensor to Actual

A torsion impulse is also applied and when the blade has a small twisting angle, the wire sensor is compared to the actual angle in Fig. 5.23. Even for

very small twist angles, the sensor performs well. Like a strain gage, the zero has to be reset before using the sensor, but the calibration factor did not change over different testing days.

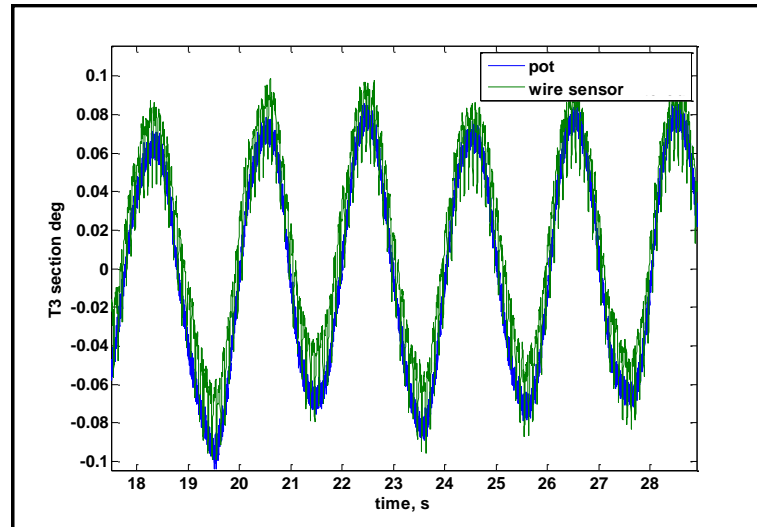


Figure 5.23: Comparison of Single Twist Sensor to Actual for Small Angles

#### 5.8.4 Motion Capture Camera Validation

A motion capture camera system is also used to measure blade elastic deflection to evaluate the sensor performance. Unlike the potentiometer, this can measure the blade twist at many points along the blade. So, the change in elastic twist over the sensor spanwise section can be directly measured. It was determined experimentally that the motion capture system has a resolution of  $0.125^\circ$ . For a tip load, the twist is found to be linear over the span. With these tests, a DC drift was observed. This is because the wire sensor is slipping in the structure. This is most likely because of the difficulty in making the sawtooth shape out of the wire. This problem can be resolved. The DC drift required an AC filter to be applied to the sensor measurement. For a small angle,  $\pm 0.15^\circ$  elastic twist

oscillation over the twist sensor, the twist sensor matches the motion capture (Vicon system) angle well (Fig. 5.24).

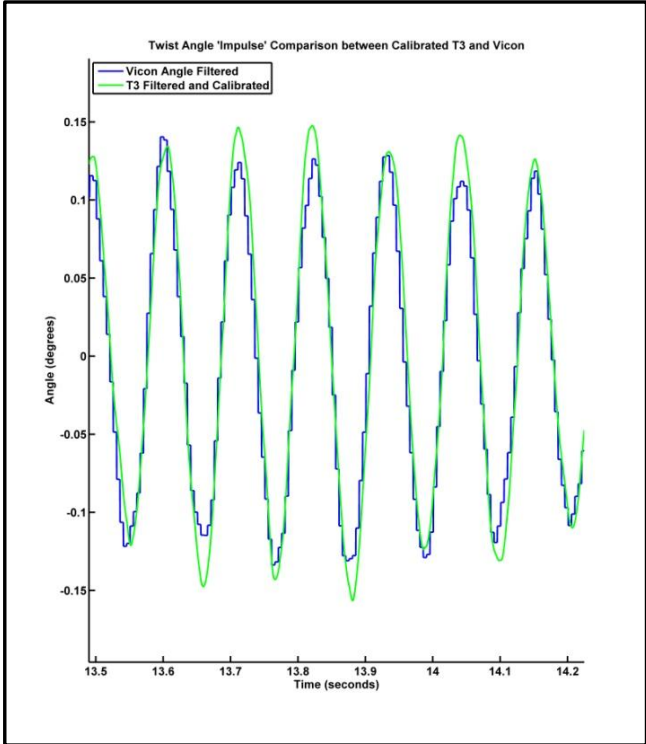


Figure 5.24: Single Twist Sensor for Small Angles with Motion Capture System

## 5.9 Conclusions and Future Work

A system for measuring rotorcraft blade elastic deformations (flap bending, lead-lag bending, elastic twist) in-flight has been proposed. The formulation has been derived with the assumptions clearly stated. The theory builds on Baz’s distributed wire sensor work, expanding it into measuring the elastic twist. It is analogous to placing an infinite number of strain gages on the blade. The change in elastic twist over the sensor length can be measured without assuming a shape for the twist distribution. The sensor has no bandwidth limitations, a

high signal to noise ratio, negligible weight, negligible power requirements and can be easily embedded in the blade structure. The twist sensor is a resistive wire in a sawtooth pattern. The sensor is proven in a computational model and in a Mach scale rotor blade on the benchtop. The sensor can measure large and very small elastic twist angles exactly. Large noise and local structural discontinuities do not effect the sensor due to the sensor integrating the local strains.

For future work, several issues should be resolved. High quality resistors should be used in the bridge circuit to lower sensor noise. A new way of embedding the sensor in the blade is needed. This could be done by milling the sawtooth pattern before embedding it into the blade. This sawtooth pattern would not have the problem with maintaining tension during blade layup that this present setup had using steel wires. Circuit printing methods could also be used. The sawtooth pattern could be deposited on the blade surface. The main difficulty is proving the system during rotation. An independent method for measuring blade elastic deformations during blade rotation is needed. One of the methods discussed in this chapter's introduction would need to be applied.

## Chapter 6

# Conclusions and Recommendations for Future Work

### 6.1 Summary

While the elimination of the swashplate has held great promise for vertical flight for several decades, it is only in more recent years that it has become a realistic goal. This is due to the maturation of smart actuation systems that allow for a lightweight, compact actuator with sufficient control authority to fit inside the blade profile to drive trailing edge flaps. Primary rotor control through trailing edge flaps allows for the elimination of the hydraulics (reduced maintenance, lower empty weight), lower profile drag due to the elimination of the swashplate, improved safety due to multiple actuators and multifunctional capability to simultaneously target noise reduction, increased performance, reduced vibration and blade tracking. Piezoelectric actuators provide not only the compactness necessary for on blade actuators, but also the bandwidth to meet all these targets, including primary control. Analysis showed the viability of the swashplateless concept with trailing edge flaps for primary control, but it has

not yet been demonstrated experimentally.

In this research, primary control of a Mach-scale rotor driven by trailing edge flaps actuated with piezobenders is demonstrated. A piezobender with sufficient actuation authority for primary control is designed and tested on the benchtop. The piezobender uses the new commercial piezoceramic, PZT-5K4, a soft material with high  $d_{31}$ . Each flap is driven by a 12 layer tapered PZT-5K4 bender, where each layer is 10 mils thick. The bender length is 1.38 in. and a 1.0 in. width with an additional 0.24 in. length to achieve proper cantilever support for the bender. The equivalent tip bending stiffness is 0.325 lb/mil with a stroke of 19.6 mils HPP producing an energy output of 62.4 mil-lb. The weight is 15.1 g, so the work density is 5.02 lb-ft/slug. The performance of piezobenders under very high electric fields is examined next.

Each Mach scale rotor blade has 2 flaps, one spanning from 61%R to 75%R and a second spanning from 75%R to 89%R, each with a chord of 26%c. The blade is an untwisted NACA0012 airfoil with a radius of 32.75 in. and chord of 3.15 in. The hoverstand hub is modified in order to reduce the blade torsional stiffness. The rigid pitch links are replaced with linear springs and blade root pitching motion is measured using Hall sensors. This setup is shown to have negligible blade pitch friction while providing the desired torsional stiffness. At 900 RPM, on the hoverstand, greater than 12° HPP is possible at 15Hz, which is well below the flap or bender natural frequency. With the blade natural torsional frequency reduced to 1.5/rev, primary control of the rotor system is demonstrated at 900 RPM through measurements of the blade root pitching angle and the hub forces and moments. Blade pitching of 7° HPP at resonance for a torsional frequency of 1.47/rev is achieved. At resonance, the flap authority is  $\pm 100\%$  thrust at 15 lbs. mean thrust.

Finally, a sensor is proposed to allow blade elastic twist to be measured in flight. This would assist in the development of a swashplateless rotor system by permitting control of a soft-in-torsion blade structure. The theory of the wire sensor is derived and then a demonstration of the wire measuring twist and flap bending is carried out on the benchtop. The wire sensor network is embedded in a Mach scale rotor blade and the twist angle of the blade is accurately measured. The sensor would be of value in gathering in-flight blade elastic deflections for any rotorcraft.

## 6.2 Full-scale Application

This work can be extended to driving a trailing edge flap at the full scale. The piezobender has a work density similar to the SMART actuator system. This is even though the present bender utilizes the smaller  $d_{31}$  effect instead of the  $d_{33}$  effect. If a piezobender can be developed, which utilizes the  $d_{33}$  effect (131% more than  $d_{31}$ ), then the bender's work density could increase by a factor of 5. The piezobender would have the same electrical efficiency as the stack actuator (see 6.4.1). The rod-cusp can efficiently convert the actuator motion into flap motion without the many losses of the X-frame actuator that is required to amplify the stroke of a stack actuator. The bender does not need any stroke amplification system. The drawback in the rod-cusp arrangement is the gap losses, which would be proportionally much smaller at the full size scale than Mach-scale. The key concern would be the survivability of the piezobender.

## 6.3 Key Conclusions

The principal conclusions from the present work are summarized here:

### 6.3.1 Piezobenders

Piezobenders utilizing the  $d_{31}$  effect can drive a Mach-scale trailing edge flap with a size sufficient for primary control.

1. Soft piezoelectric materials, such as M1876 and PZT-5K4, offer greater strain than hard materials, such as PZT-5H2, for the same electric field. This leads to greater piezobender stroke for the same driving voltage.
2. No database exists for piezoceramic maximum strain ranges which are important for determining the maximum stroke of an actuator. The given piezoelectric coefficients are valid at only small electric fields. A database should be developed for the maximum electric field, the depoling field and the strain range and power draw at the maximum field strength.
3. While two-component, solvent-thinned, epoxy-phenolic adhesives work well for bonding together layers of PZT-5H2 plates with nickel electrodes to form multimorphs, the soft materials with gold electrodes require methacrylate esters with anaerobic cures. Unlike epoxy-phenolic adhesives, which require elevated temperature curing ( $\geq 100^\circ\text{C}$  for 4 hours), the methacrylate esters do not, though the bonding process is accelerated and improved by moderate heat ( $93^\circ\text{C}$  for 1 hour).
4. Film adhesives are found that can used to cure at a temperature less than  $100^\circ\text{C}$  in order to secure the piezobender into the blade. This means the

low Curie temperature of the soft materials ( $125^{\circ}\text{C}$  for PZT-5K4) is not a barrier.

5. The PZT-5K4 piezobender performance at high electric fields ( $-3.54\text{kV/cm}+10.63\text{kV/cm}$ ) is examined. At this electric field, the material strain is  $0.092\%$  and if the field is increased to ( $-3.54\text{kV/cm}+17.72\text{kV/cm}$ ) the strain is  $0.104\%$ .
6. The bender stiffness is shown to be independent of electric field.
7. A new, unexpected phenomenon of piezobender relaxation is documented. The piezobender loses much of its initial DC stroke over time ( $\geq 50\%$  over 10 seconds) at this high electric field.
8. Piezobenders perform well with high local pressures. Large clamping pressures provide a good cantilever for the piezobender without causing any damage to it. A slotted steel rod directly in contact with the bender tip ensures that the force from the flap is transferred to the bender. This has been demonstrated at  $50\text{Hz}$  for an extended time without damage to the bender. The stiff support and slotted steel rod eliminate performance losses due to compliance between force transfer points.
9. A 12-layer tapered piezobender fitting inside the Mach-scale blade profile is designed and built. It has a work density of  $5.02\text{ lb-ft/slug}$  which compares favorably to the 2X-Frame SMART full-scale actuator with a work density of  $5.68\text{ lb-ft/slug}$ . Neither of these values accounts for the efficiency of converting this actuator output to flap motion.

### 6.3.2 Mach Scale Swashplateless Rotor with Trailing Edge Flaps

A Mach scale rotor with trailing edge flaps actuated with a piezobender is designed and tested in the vacuum chamber and on the hoverstand. On the hoverstand, primary control of the 2-bladed rotor system through the trailing edge flaps is demonstrated at 900 RPM (2400 RPM is Mach-scale speed).

1. For piezobenders to actuate Mach-scale trailing edge flaps, the flaps must be supported by both radial bearings and thrust bearings, where the radial bearings do not take any thrust load. Otherwise, friction will limit the flap deflection.
2. The rod-cusp mechanism converts piezobender tip motion to flap rotational motion efficiently, if the flap support points have sufficient stiffness.
3. At half the maximum driving voltage,  $13^\circ$  HPP for the flap is obtained at 38.3 Hz for 1300 RPM in the vacuum chamber demonstrating the setup's low friction.
4. At 900 RPM on the hoverstand,  $14^\circ$  HPP for the flap is obtained at 15 Hz for a flap panning 75%R to 89%R (14% span) and 26.5% chord. The flap has mass balancing in order to lower the inertial load and overhang to lower the aerodynamic moment.
5. The hoverstand hub is modified by replacing the rigid pitch links with soft pitch links such that the blade torsional frequency of  $\leq 2.0/\text{rev}$  can be obtained. All ceramic ball bearings allow blade pitching without friction. This is proven by matching the measured blade rotating torsional frequency with the predicted value.

6. The flap effectiveness (blade pitching/flap deflection) matches what is predicted by a simple aerodynamic model. However, the flaps are ineffective at small angles, perhaps due to separated flow at 900 RPM.
7. Primary control through the trailing edge flaps (swashplateless) is demonstrated. Blade pitching of  $6.9^\circ$  HPP is obtained at a frequency of 22 Hz at 900 RPM and  $2.7^\circ$  HPP at 15 Hz with a torsional frequency of 1.47/rev. Thrust authority of  $\pm 100\%$  at 15 lbs. mean thrust is obtained.

### 6.3.3 Blade Wire Sensor Network

A swashplateless rotor system could be better controlled if the blade elastic twist angle was known in-flight. A sensor to measure this is proposed. The theory undergirding it is derived and then, the sensor is demonstrated in a Mach-scale rotor blade on the benchtop using a motion capture system.

1. Starting with a rotor blade idealized as a Euler-Bernoulli beam undergoing lead-lag and flap bending and elastic twist, the wire sensor constitutive equations are derived with very few assumptions. The theory shows how to construct a sensor network to measure blade flap bending, lead-lag bending and twist deformations. The theory requires shape functions for the blade deformations to be assumed. The sensor physically integrates the local strain over a spanwise portion of the blade. This filters out noise and local strain phenomenon and yields the global effect of the integrated local strains.
2. A blade with wire sensor network is modeled computationally. The blade is modeled as a Euler-Bernoulli beam undergoing lead-lag and flap bending

and elastic twist without any simplifying assumptions. The model shows that the sensor can give the blade elastic twist over any arbitrary span of the blade, regardless of zero-mean noise in the sensor or extremely large local strain phenomenon.

3. A Mach scale rotor blade with a wire sensor network for blade twisting and flap bending is constructed. The sensor is calibrated and validated using a motion capture system.
4. The wire sensor network holds promise for full size rotorcraft blade applications as well as scaled rotors. It can work in-flight, has negligible weight and negligible power requirement.

## 6.4 Recommendations for Future Work

Mach-scale rotor testing is difficult due to the high CF environment at the design tip speed, but the difficulties have been overcome. The author sees no reason why testing could not continue with the Mach scale setup at the design rotational speed. The demonstration of a Mach-scale swashplateless rotor with trailing edge flaps actuated with piezobenders in the wind tunnel appears feasible.

### 6.4.1 $d_{33}$ Piezobender

The main drawback to a piezobender, as opposed to a piezostack, is the large difference between the  $d_{31}$  effect and the  $d_{33}$  effect. However, in theory it appears possible to make a  $d_{33}$  piezobender. The bender would have the same multilayer tapered design as used in this work. However, each layer would be wired differently. Instead of the piezoceramic layer having a sheet electrode on

the top and bottom, interdigitated electrodes (IDE) would be used to produce an electric field transverse to the layer thickness (Fig. 6.1).

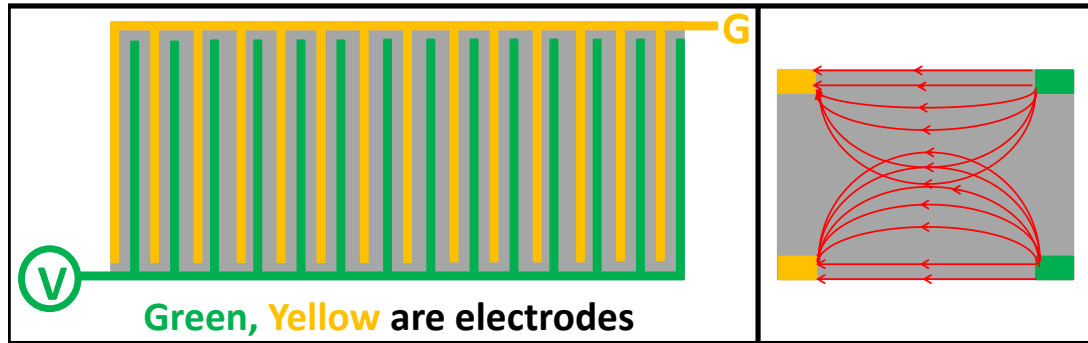


Figure 6.1: a) Top view of piezoplate with interdigitated electrodes b) Electric field lines between IDEs

The material is poled using these electrodes so that the 3 direction is transverse to the thickness. The electric field is not uniform and so some of the piezoceramic volume is a dead zone. This is mostly the area underneath the electrode arms. The electrode arms' width and separation must be optimized in order to keep the driving voltage low while minimizing the dead zone. Thinner piezoceramic layers minimize the driving voltage, as well as the dead zone, by making the electric field more uniform [103].

Other concerns are the life of the actuator and bonding layers together. Most papers focus on a unimorph, but for a multimorph, many piezolayers with IDEs must be bonded together. To avoid shorting between the electrode arms, a non-conductive adhesive must be used. Also, there is a transition zone around the electrodes with strong field concentrations that can lead to failures. Fig. 6.2 shows the field inside the piezoceramic layer with homogeneous zone, the inactive zone and transition zone with field concentrations [104].

The manufacturing process for laying down electrodes is constantly improving due to the enormous effort placed on the miniaturization of electronics. This

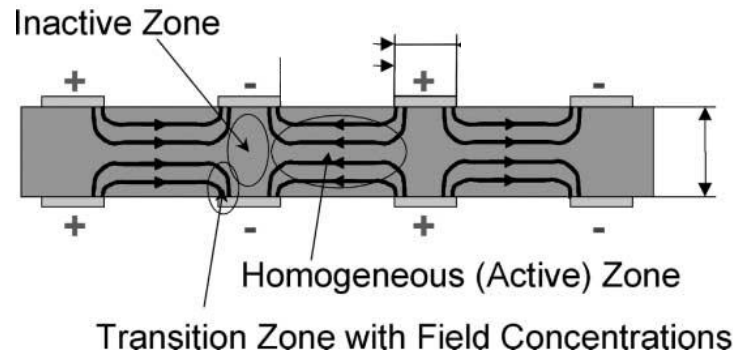


Figure 6.2: Electrical field zones in piezoceramic layer with IDEs

means that possible electrode widths are decreasing, which decreases the size of the inactive zone and the field concentration zone. IDE optimization has also been simplistic with a focus on just electrode width and spacing. As seen in Fig. 6.2, the electrodes are always in line. If they were staggered, then the inactive zone could be reduced. More complex electrodes such as a sawtooth pattern or something other than a straight line could be used to cancel out the concentrations. The models for determining the electrode pattern are quite complex, but to take full advantage of this work, different electrode patterns should be considered with the goal of reducing the inactive zones and lowering the field concentrations.

So, if this project's 12-layer bender is constructed as a  $d_{33}$  bender, then for the same weight and power consumption, the bender stroke would be approximately doubled, while the stiffness remained unchanged. So, the bender actuation authority would double. The piezobender would also be of interest for the full size as like piezostacks, it utilizes  $d_{33}$ .

## 6.4.2 Present Setup Improvements

Whether the  $d_{33}$  bender is developed or not, the present Mach-scale setup can be used for significantly more hoverstand testing culminating in wind tunnel testing. The author suggests several small improvements to the present setup as well as testing goals.

1. Flap Mean: The flap mean or neutral angle is sensitive to the bender steel rod location. If it is off from the expected location by a few mils, the mean flap angle can be off by  $10^\circ$  or more. This can be solved by making the actuator with its clamps a subassembly (instead of the bottom clamp being a part of the flap anchor). The location of this subassembly can be adjusted relative to the anchor to change the flap mean and the flap hinge. Fig. 6.3 shows the idea. For the present setup, the bottom clamp of the actuator is part of the anchor. To allow for height of the actuator relative to the cusp to be adjusted, so that the flap mean can be adjusted, the actuator is bonded into its top and bottom clamps to form a sub-assembly. Slots are added to the anchor that this subassembly is secured to. So, the bender rod height can be adjusted to change the flap neutral angle. This also allows the flap hinge to be set exactly, so that the flap stiffness matches the actuator stiffness (impedance matching). For testing this has the added benefit that if any actuator fails, it can be quickly replaced.
2. Flap phasing: The flaps need to be phased with the rotor blade azimuth using closed loop control.
3. Actuator Power: It is of great interest to estimate the power required by the piezobenders to drive the TE flaps. The voltage is known, but the

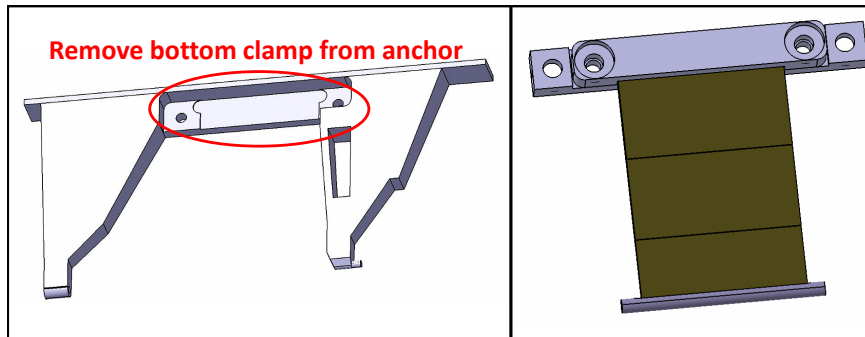


Figure 6.3: Modification to allow for flap mean and hinge adjustment for primary control implementation

current is not available. The current is difficult to measure, because the measurement needs to be made on the high side where the common mode voltage can be in excess of 300V. Microchips are available that can handle very high common-mode voltages in order to measure the current across a small value resistor.

4. Outer Loop: With the present flap controller for flap mean, amplitude and phase relative to the other flaps as the inner loop, an outer loop for the soft pitch link (blade pitch phase, mean and amplitude) should be added.
5. Full speed demonstration: 4 blades can be constructed, so that primary control can be demonstrated on the hoverstand first at 900 RPM and then at increasing rotor speeds until the Mach scale of 2400 RPM is reached.
6. Develop and implement closed loop trim control of the rotor blade.
7. Wind Tunnel Tests: Trim rotor system to high advance ratios. Demonstrate maneuvering authority (measurement of hub forces and moments) over range of advance ratios. Examine the rotor drag performance and compare to the blade trimmed with rigid pitch links and the flaps locked

in place, so that have performance comparison between swashplateless and conventional rotor.

## Bibliography

- [1] Sonneborn, W. "Vision 2025 for Rotorcraft". AIAA/ICAS International Air and Space Symposium and Exposition: The Next 100 Years, Dayton, OH, July 2003.
- [2] Wood, E.R., Powers, R.W., Cline, J.H. and Hammond, C.E. "On Developing and Flight Testing a Higher Harmonic Control System". Journal of the American Helicopter Society, Vol. 30, (1), January 1985, pp. 3-20.
- [3] Jacklin, S.A., Blaas, A., Teven, D. and Kube, R., "Reduction of Helicopter BVI Noise, Vibration, and Power Consumption through Individual Blade Control", American Helicopter Society 51st Annual Forum Proceedings, Fort Worth, TX, May 1995.
- [4] Cheng, R. and Celi, R., "Optimum Two-Per-Revolution Inputs for Improved Rotor Performance", Journal of Aircraft, Vol. 42, No. 6, November-December 2005, pp. 1409-1417.
- [5] Kessler, C., "Active Rotor Control for Helicopter - Motivation and Survey on Higher Harmonic Control", Proceedings of the 36th European Rotorcraft Forum, September 2010. <http://www.springerlink.com/content/55hq04528wu3jr70/fulltext.pdf>
- [6] Kessler, C., "Individual Blade Control and Swashplateless Rotor Designs". Proceedings of the 36th European Rotorcraft Forum, September 2010.
- [7] Prouty, R., and Curtiss Jr., H.C., "Helicopter Control Systems: A History", *Journal of Guidance, Control and Dynamics*, Vol. 26, No. 1, January-February 2003.
- [8] Hobbs, J. *Bristol Helicopters: A Tribute to Raoul Hafner*, Frenchay Publications, Bristol, UK, 1st Edition, 1984.
- [9] Johnson, W. *Helicopter Theory*, Dover Publications, Inc., New York, 1994.

- [10] Carlson, R., "Helicopter Performance - Transportation's Latest Chromosome: The 21st annual Alexander A. Nikolsky Lecture", *Journal of the American Helicopter Society*, 47(1):3-17, January 2002.
- [11] Leishman, J., *Principles of Helicopter Aerodynamics*, Cambridge University Press, Cambridge, UK, 1984.
- [12] Haber, A., Jacklin, S. and deSimone, G., "Development, Manufacturing and Component Testing of an Individual Blade Control System for a UH-60 Helicopter Rotor", American Helicopter Society Aerodynamics, Acoustics and Test and Evaluation Technical Specialists Meeting, San Francisco, CA, January 2002. [http://rotorcraft.arc.nasa.gov/Publications/files/Haber\\_AHS02.pdf](http://rotorcraft.arc.nasa.gov/Publications/files/Haber_AHS02.pdf)
- [13] Norman, Thomas R. and et. al., "Full-Scale Wind Tunnel Test of a UH-60 Individual Blade Control System for Performance Improvement and Vibration, Loads, and Noise Control.", American Helicopter Society 65th Annual Forum Proceedings, Grapevine, TX, May 2009. [http://rotorcraft.arc.nasa.gov/publications/files/Norman\\_09AHS\\_IBC\\_Final\\_eva.pdf](http://rotorcraft.arc.nasa.gov/publications/files/Norman_09AHS_IBC_Final_eva.pdf)
- [14] Kuefmann, P., Bartels, R., Kessler, C. and van der Wall, B.G., "On the Design and Development of a Multiple-Swashplate Control System for the Realization of Individual Blade Control (IBC) for Helicopters", American Helicopter Society 67th Annual Forum, Virginia Beach, VA, May 2011.
- [15] Chen, P. and Chopra, I., "Wind Tunnel Test of a Smart Rotor Model with individual Blade Twist Control", *Journal of Intelligent Material Systems and Structures*, 8(5):414-425, May 1997.
- [16] Wilkie, W., Wilbur, M., Mirick, P., Cesnik, C. and Shin, S., "Aeroelastic Analysis of the NASA/Army/MIT Active Twist Rotor", American Helicopter Society 55th Annual Forum Proceedings, Montreal, Canada, May 1999.
- [17] Wilbur, M., Mirick, P., Yeager, W., Langston, C., Cesnik, C. and Shin, S., "Vibratory Loads Reduction Testing of the NASA/Army/MIT Active Twist Rotor", American Helicopter Society 57th Annual Forum Proceedings, Washington, D.C., May 2001.
- [18] Shin S., Cesnik, C. and Hall, S., "Closed-Loop Control Test of the NASA/Army/MIT Active Twist Rotor For Vibration Reduction", *Journal of the American Helicopter Society*, 50(2):178-194, April 2005.
- [19] Ormiston, R., "Aeroelastic Considerations for Rotorcraft Primary Control with On-Blade Elevons", American Helicopter Society 57th Annual Forum Proceedings, Washington, DC, May 2001.

- [20] Bir, G., Chopra, I. and Nguyen, K., "Development of UMARC (University of Maryland Advanced Rotorcraft Code)", 46th American Helicopter Society Annual Forum, Washington, D.C., May 1990.
- [21] Shen, J., Chopra, I. and Johnson, W., "Performance of Swashplateless Ultralight Helicopter Rotor with Trailing-Edge Flaps for Primary Control", American Helicopter Society 59th Annual Forum, Phoenix, AZ, May 2003.
- [22] Shen, J. and Chopra, I., "Swashplateless Helicopter Rotor with Trailing-Edge Flaps", *Journal of Aircraft*, Vol. 41, No.2 March-April 2004, pp. 208-214.
- [23] Datta, A. and Chopra, I. "Validation of Structural and Aerodynamic Modeling Using UH-60 Flight Test Data", American Helicopter Society 59th Annual Forum Proceedings, Phoenix, AZ, May 2003.
- [24] Shinoda, P., Yeo, H. and Norman, T., "Rotor Performance of a UH-60 Rotor System in the NASA Ames 80 by 120 Foot Wind Tunnel", American Helicopter Society 58th Annual Forum, Montreal, Canada, June 2002. [http://rotorcraft.arc.nasa.gov/publications/files/Shinoda\\_AHSF02.pdf](http://rotorcraft.arc.nasa.gov/publications/files/Shinoda_AHSF02.pdf)
- [25] Falls, J. "Design and Performance Prediction of Swashplateless Helicopter Rotor with Trailing Edge Flaps and Tabs", Ph.D. Dissertation in Aerospace Engineering, University of Maryland, 2010. [http://drum.lib.umd.edu/bitstream/1903/10420/1/Falls\\_umd\\_0117E11267.pdf](http://drum.lib.umd.edu/bitstream/1903/10420/1/Falls_umd_0117E11267.pdf)
- [26] Shen, J., Yang, M. and Chopra, I. "Swashplateless Helicopter Rotor System with Active Trailing-Edge flaps for Primary and Vibration Controls". 45th AIAA/ASME/ASCE/AHS/ASC Structures, Structural Dynamics and Material Conference, Palm Springs, FL, April 2004.
- [27] Kaman, C.H. Aircraft of rotary wing type. U.S. Patent Office, May 1948. Patent No. 2,455,866.
- [28] Roccanella, B. and Wei, F., "Wind Tunnel Model Testing of the Improved K-MAX Servo-Flap Blade Section". American Helicopter Society 57th Annual Forum, Washington, D.C., May 2001.
- [29] Wei, F.S., "Design of an integrated servo-flap main rotor", American Helicopter Society 59th Annual Forum, Phoenix, AZ, May 2003.
- [30] Wei, F.S., "Advanced servo flap rotor using variable blade index angle control", 38th AIAA/ASME/ASCE/AHS/ASC Structures, Structural Dynamics and Materials Conference, pp. 876-884, Kissimmee, FL, April 1997. AIAA.

- [31] Hunt, G.K., "Similarity Requirements for Aeroelastic Models of Helicopter Rotors", Aeronautical Research Council Current Papers, C.P. No. 1245, Library Royal Aircraft Establishment, Bedford, 1973. <http://naca.central.cranfield.ac.uk/reports/arc/cp/1245.pdf>
- [32] Friedmann, P.P., "Aeroelastic Scaling for Rotary-Wing Aircraft with Applications". *Journal of Fluids and Structures*, Issue 19, 2004, pp. 653-650. [http://ac.els-cdn.com/S0889974604000519/1-s2.0-S0889974604000519-main.pdf?\\_tid=1d937f92-066c-11e2-a2e3-00000aab0f6cac&nat=1348507399\\_082c5e89c284a6cf176ce8a201e6370](http://ac.els-cdn.com/S0889974604000519/1-s2.0-S0889974604000519-main.pdf?_tid=1d937f92-066c-11e2-a2e3-00000aab0f6cac&nat=1348507399_082c5e89c284a6cf176ce8a201e6370)
- [33] Chopra, I., "Review of State of Art of Smart Structures and Integrated Systems", *AIAA Journal*, Vol. 40, No. 11, November 2002, pp. 2145-2187.
- [34] Giurgiutiu, V., "Review of Smart-Materials Actuation Solutions for Aeroelastic and Vibration Control", *Journal of Intelligent Material Systems and Structures*, 2000 11:525. <http://jim.sagepub.com/content/11/7/525>
- [35] Sirohi, J. and Chopra, I., "Fundamental Behavior of Piezoceramic Sheet Actuators", *Journal of Intelligent Material Systems and Structures*, Vol. 11, January 2000, pp. 47-61.
- [36] Lee, T. and Chopra, I., "Design Issues of a High-Stroke, On-Blade Piezostack Actuator for a Helicopter Rotor with Trailing Edge Flaps", *Journal of Intelligent Material Systems and Structures*, Vol. 11, May 2000, pp. 328-342.
- [37] Lee, T., Design of High Displacement Smart Trailing Edge Flap Actuator Incorporating Dual-Stage Mechanical Stroke Amplifiers for Rotors, Ph.D. Dissertation in Aerospace Engineering, University of Maryland, 1999.
- [38] Prechtl, E. and Hall, S., "Design of a High Efficiency, Large Stroke, Electromechanical Actuator", *Smart Materials Structures*, Vol. 8, 1999, pp 13-30.
- [39] Straub, F., "A feasibility study of using smart materials for rotor control", *Smart Materials and Structures*, vol. 5, 1996, pp. 1-10. [http://iopscience.iop.org/0964-1726/5/1/002/pdf/0964-1726\\_5\\_1\\_002.pdf](http://iopscience.iop.org/0964-1726/5/1/002/pdf/0964-1726_5_1_002.pdf)
- [40] Straub, F, et. al., "Smart Material-Actuated Rotor Technology - SMART". *Journal of Intelligent Material Systems and Structures*, vol. 15, no. 4, 1996. pp. 249-260. <http://jim.sagepub.com/content/15/4/249>
- [41] Straub, F.K., Ngo, H.T., Anand, V. and Domzalski, D.B. "Development of a Piezoelectric Actuator For Trailing Edge Flap Control of Full Scale Rotor

- Blades”, *Smart Materials and Structures*, vol. 10, no. 1, 2001, pp. 25-34.  
[http://iopscience.iop.org/0964-1726/10/1/303/pdf/0964-1726\\_10\\_1\\_303.pdf](http://iopscience.iop.org/0964-1726/10/1/303/pdf/0964-1726_10_1_303.pdf)
- [42] Straub, F., et. al., ”Development and whirl tower test of the SMART active flap rotor”, SPIE International Symposium on Smart Structures and Materials, San Diego, CA, March 14-18, 2004.
- [43] Straub, F., et. al., ”Wind Tunnel Testing of the SMART Active Flap Rotor”, American Helicopter Society 65th Annual Forum and Technology Display, Grapevine, TX, May 2009.
- [44] Straub, F., Anand, Va., Birchette, T. and Lau, B., ”SMART Rotor Development and Wind Tunnel Test”, 35th European Rotorcraft Forum, Hamburg, Germany, Sept. 2009.  
<http://halfdome.arc.nasa.gov/Publications/files/straub2009783.pdf>
- [45] Dieterich, O., Enenkl, B. and Roth, D., ”Trailing Edge Flaps for Active Rotor Control Aeroelastic Characteristics of the ADASYS Rotor System”, American Helicopter Society 62nd Annual Forum, Phoenix, AZ, May 2006.
- [46] Saito, S., et. al., ”Overview of the Novel Intelligent JAXA Active Rotor Program”, Heli Japan 2010, AHS International Meeting on Advanced Rotorcraft Technology and Safety Operations, Ohmiya, Japan, November 2010.  
[http://ntrs.nasa.gov/archive/nasa/casi.ntrs.nasa.gov/20110011793\\_2011012290.pdf](http://ntrs.nasa.gov/archive/nasa/casi.ntrs.nasa.gov/20110011793_2011012290.pdf)
- [47] Spangler Jr., R., ”Piezoelectric Actuators for Helicopter Rotor Control”, Masters of Science Thesis, MIT, February 1989.  
<http://hdl.handle.net/1721.1/14462>
- [48] Spangler, R. and Hall, S., ”Piezoelectric Actuators for Helicopter Rotor Control”, Proceedings 33rd Structures, Structural Dynamics and Materials Conference, Long Beach, CA, 1990.
- [49] Hall, S. and Prechtel, E., ”Development of a Piezoelectric Servoflap for Helicopter Rotor Control”, *Smart Materials and Structures*, (6):26-34, 1996.
- [50] Prechtel, E., ”Development of a Piezoelectric Servo-Flap Actuator for Helicopter Rotor Control”, Masters of Science Thesis, MIT, May 1994.  
[http://dspace.mit.edu/bitstream/handle/1721.1/35912/prechtel\\_mthesis.pdf?sequence=1](http://dspace.mit.edu/bitstream/handle/1721.1/35912/prechtel_mthesis.pdf?sequence=1)
- [51] Fulton, M. and Ormiston, R., ”Hover Testing of a Small-Scale Rotor with On-Blade Elevons”, *Journal of the American Helicopter Society*, 46(2):96-106, April 2001.

- [52] Roget, B. and Chopra, I., "Wind-Tunnel Testing of Rotor with Individually Controlled Trailing-Edge Flaps for Vibration Reduction", *Journal of Aircraft*, Vol. 45, No. 3, May-June 2008. <http://arc.aiaa.org/doi/pdf/10.2514/1.28455>
- [53] Roget, B. "Individual Blade Control for Vibration Reduction of a Helicopter with Dissimilar Blades", Ph.D. Dissertation in Aerospace Engineering, University of Maryland, 2004. <http://drum.lib.umd.edu/bitstream/1903/1996/1/umi-umd-1950.pdf>
- [54] Falls, J., Datta, A. and Chopra, I., "Integrated Trailing-Edge Flaps and Servotabs for Helicopter Primary Control", *Journal of the American Helicopter Society*, Vol. 55, 032005, 2010.
- [55] Falls, J. and Chopra, I., "Piezobimorph Actuated Servotab for Controlling a Trailing Edge Flap", 46th AIAA/ASME/ASCE/AHS/ASC Structures, Structural Dynamics and Materials Conference, Austin, TX, April 2005.
- [56] Lorber, P. and et. al., "Whirl and Wind Tunnel Testing of the Sikorsky Active Flap Demonstration Rotor", American Helicopter Society 67th Annual Forum Proceedings, Virginia Beach, VA, May 2011.
- [57] Saxena, A. and Chopra, I., "Development and Testing of a Swashplateless Rotor with Compact Brushless Motor Actuated Flaps for Primary Control". American Helicopter Society 67th Annual Forum Proceedings, Virginia Beach, VA, May 2011.
- [58] Saxena, A. and Chopra, I., "Hover Testing of a Swashplateless Rotor with Compact Brushless Motor Actuated Flaps for Primary Control", American Helicopter Society 68th Annual Forum, Forth Worth, TX, May 2012.
- [59] Wood, B., Kothera, C. and Wereley, N., "Wind Tunnel Testing of a Helicopter Rotor Trailing Edge Flap Actuated via Pneumatic Artificial Muscles", *Journal of Intelligent Material Systems and Structures*, Vol. 22, September 2011, pp. 1513-1528. <http://jim.sagepub.com/content/22/13/1513>
- [60] Huber, J.E., Fleck, N.A. and Ashby, M.F., "The Selection of Mechanical Actuators Based on Performance Indices", *Proceedings: Mathematical, Physical and Engineering Sciences*, Vol. 453, No. 1965, Oct 1997, pp. 2185-2205. <http://www.jstor.org/stable/53045>
- [61] Woods, B., "Pneumatic Artificial Muscle Driven Trailing Edge Flaps for Active Rotors". Ph.D. Dissertation in Aerospace Engineering, University of Maryland, 2012. [http://drum.lib.umd.edu/bitstream/1903/12537/1/Woods\\_umd\\_0117E12910.pdf](http://drum.lib.umd.edu/bitstream/1903/12537/1/Woods_umd_0117E12910.pdf)

- [62] Woods, B., Gentry, M., Kothera, C. and Wereley, N., "Fatigue Life Testing of Swaged Pneumatic Artificial Muscles as Actuators for Aerospace Applications", *Journal of Intelligent Material Systems and Structures*, February 2012, vol. 23, no. 3, pp. 327-343.
- [63] Samak, D.K. and Chopra, I. "Design of High Force, High Displacement Actuators for Helicopter Rotors", *Smart Structures and Intelligent Systems: Proceedings of the Conference, Orlando, FL, Feb. 1994*, pp. 86-98.
- [64] Walz, C. and Chopra, I., "Design and Testing of a Helicopter Rotor Model with Smart Trailing Edge Flaps", *AIAA/ASME Adaptive Structures Forum, Hilton Head, SC, Apr. 1994*, pp. 309-319.
- [65] Ben-Zeev, O. and Chopra, I., "Advances in the Development of an Intelligent Helicopter Rotor Employing Smart Trailing Edge Flaps", *Smart Materials and Structures*, Vol. 5, (1), Feb. 1996, pp. 11-25.
- [66] Sirohi, J. and Chopra, I., "Fundamental Behaviour of Piezoceramic Sheet Actuators", *Journal of Intelligent Material Systems and Structures*, Vol. 11, January 2000, pp. 47-61.  
<http://jim.sagepub.com/content/11/1/47.full.pdf>
- [67] Allen, K., "Development of a Mach-scale Swashplateless Rotor with Integrated Flaps for Primary Control", *AIAA Region I-MA Student Conference, May 2007*.
- [68] Web Reference: [http://www.piceramic.com/piezo\\_materials1.php](http://www.piceramic.com/piezo_materials1.php)
- [69] Chopra, I., Course Notes: University of Maryland, Aerospace Engineering Department, Smart Structures: Piezos.
- [70] Web Reference: <http://www.datasheetcatalog.org/datasheet/vishay/bond610.pdf>
- [71] Web Reference: <http://tds.loctite.com/tds5/docs/680-EN.pdf>
- [72] Chaplya, P. and Carman, G., "Dielectric and Piezoelectric Response of Lead Zirconate-Lead Titanate at High Electric and Mechanical Loads in Terms of non-180° Domain Wall Motion", *Journal of Applied Physics*, Vol. 90, No. 10, November 2001, pp. 5278-5286.
- [73] Uchino, K., "Material Issues in Design and Performance of Piezoelectric Actuators: An Overview", *Acta Metallurgica*, Vol. 46, No. 11, 1998, pp. 3745-3753.

- [74] Jung, H., Shim, J.Y. and Gweon, D., "Tracking Control of Piezoelectric Actuators", *Nanotechnology: Institute of Physics Publishing*, Vol. 12, 2001, pp. 14-20.
- [75] Park, S.E. and Shrout, T., "Ultrahigh Strain and Piezoelectric Behavior in Relaxor Based Ferroelectric Single Crystals", *Journal of Applied Physics*, vol. 82, no. 4, 1997, pp. 1804-1811.
- [76] Randall, C., et. al., "High Strain Piezoelectric Multilayer Actuators - A Material Science and Engineering Challenge", *Journal of Electroceramics*, vol. 14. 2005, pp. 177-191.
- [77] Koratkar, N.A., and Chopra, I., "Development of a Mach-scaled Model with Piezoelectric Bender Actuated Trailing-Edge Flaps for Helicopter Individual Blade Control (IBC)", *AIAA Journal*, Vol. 38, No. 7, 2000, pp. 1113-1124.
- [78] Sirohi, J., Allen, K. and Chopra I., "Development of Mach-Scale Swashplateless Rotor with Embedded Trailing-Edge Flaps", 33rd European Rotorcraft Forum, Kazan, Russia, September 2007.
- [79] Bao, J., Allen, K., and Chopra, I., "Design and Test of a Mach-Scale Swashplateless Rotor Using Smart Trailing-edge Flaps", Proceedings of the American Helicopter Society 62nd Annual Forum, Phoenix, AZ, May 9-11, 2006.
- [80] Web Reference: [http://www.cemselectorguide.com/pdf/FM300\\_81211.pdf](http://www.cemselectorguide.com/pdf/FM300_81211.pdf)
- [81] Jose, A. "Investigation into the Aerodynamics of Swashplateless Rotors using CFD-CSD Analysis", Ph.D. Dissertation in Aerospace Engineering, University of Maryland, 2012. <http://hdl.handle.net/1903/12995>
- [82] Jose, A., Mishra, A. and Baeder, J., "An Investigation into the Aerodynamics of Trailing Edge Flaps with Overhang and Gap", AHS Specialist's Conference on Aeromechanics, San Francisco, Jan. 2008.
- [83] Abbot, I. and von Doenhoff, A., *Theory of Wing Sections: Including a Summary of Airfoil Data*, Courier Dover Publications, 1959, pp. 190.
- [84] Koratkar, N. "Smart Helicopter Rotor with Piezoelectric Bender Actuated Trailing-Edge Flaps", Ph.D. Dissertation in Aerospace Engineering, University of Maryland, 2000.
- [85] Paturski, K., *Handbook of the Moiré Fringe Technique*, Elsevier Science Publishers, 1993.

- [86] Pirodda, L., "Shadow and Projection Moiré Fringe Techniques for Absolute or Relative Mapping of Surface Shapes", *Optical Engineering*, vol. 21, no. 4, July/August 1982, pp. 640-649.
- [87] Indebetouw, G. and Czarnek, R. *Selected Papers on Optical Moiré and Applications* SPIE Milestone Series, Vol. MS 64, 1992.
- [88] Fleming, G. and Gorton, S., "Measurement of Rotorcraft blade Deformation using Projection Moiré Interferometry", Proceedings SPIE 3411: Third International Conference on Vibration Measurements by Laser Techniques, Advances and Applications, June 1998.
- [89] Pryputniewicz, E., Fleming, G. and Pryputniewicz, R., "Experimental Characterization of Vibrations of a NASA Active Twist Rotor Blade", Web Reference: <http://sem-proceedings.com/22i/sem.org-IMAC-XXII-Conf-s23p07-Experimental-Characterization-Vibrations-NASA-Active-Twist-Rotor-Blade.pdf>
- [90] Fleming, G., Soto, H. and South, B., "Projection Moiré Interferometry for Rotorcraft Applications: Deformation Measurements of Active Twist Rotor Blades", American Helicopter Society 58th Annual Forum, Montreal, Canada, June 2002.
- [91] Olson, L., Abrego, A., Barrows, D. and Burner, A., "Blade Deflection Measurements of a Full-Scale UH-60A Rotor System", American Helicopter Society Aeromechanics Specialist' Conference'', San Francisco, CA, January 2010.
- [92] Sirohi, J. and Lawson, M., "Measurement of Helicopter Rotor Blade Deformation using Digital Image Correlation", *Optical Engineering*, Vol. 51(4), April 2012.
- [93] Baz, A. and Poh, S., "A New Class of Distributed Sensors", *ASME Journal of Vibration and Acoustics*, Vol.119, No. 4, 1997, pp. 582-590.
- [94] Baz, A. Poh, S. and Gilheany, J., "A Multi-Mode Distributed Sensor for Vibrating Beam", *Journal of Sound and Vibration*, Vol. 165, No. 3, 1993, pp. 481-495.
- [95] Akl, W., Poh, S. and A. Baz. "Wireless and Distributed Sensing of the Shape of Morphing Structures", *Journal of Sensor and actuators A: Physical*, Vol. 14, 2007, pp. 94-102.
- [96] Datta, A. "Fundamental Understanding, Prediction and Validation of Rotor Vibratory Loads in Steady Level Flight", Ph.D. Dissertation in Aerospace Engineering, University of Maryland, 2004. <http://drum.lib.umd.edu/bitstream/1903/1900/1/umi-umd-1880.pdf>

- [97] Abhishek, A. "Analysis, Validation, Prediction And Fundamental Understanding Of Rotor Blade Loads In An Unsteady Maneuver", Ph.D. Dissertation in Aerospace Engineering, University of Maryland, 2010. <http://drum.lib.umd.edu/handle/1903/11177>
- [98] Hodges, D. and Dowell, E., "Nonlinear Equations of Motion for the Elastic Bending and Torsion of Twisted Nonuniform Rotor Blades", NASA TN D7818, December 1974.
- [99] Ormiston, R., Hodges, D. and Peters, D., "On the Nonlinear Deformation Geometry of Euler-Bernoulli Beams", NASA Technical Paper 1566, 1980.
- [100] Kaza, K. and Kvaternik, R., "Nonlinear Aeroelastic Equations for Combined Flapwise Bending, Chordwise Bending, Torsion, and Extension of Twisted Nonuniform Rotor Blades in Forward Flight", NASA TM 74059, August 1977.
- [101] Ganguli, R. and Chopra, I., "Aeroelastic Optimization of an Advanced Geometry Helicopter Rotor", *Journal of the American Helicopter Society*, Vol. 41, No. 1, January 1996, pp. 18-28.
- [102] Baz, A. and Poh, S., "Distributed Deflection Sensing of Rotating Beams", SPIE Smart Structures and Intelligent Systems, Vol. 1917, 1993, pp. 390-406.
- [103] Nguyen, N., Yoon, B., Park, K. and Yoon, K. "Analytical Model and Optimal Design of a  $d_{33}$ -Mode Active Layer for the Lightweight Unimorph Piezo-Composite Actuator", *Journal of Electroceramics*, Vol. 26, 2011, pp. 175-184. <https://springerlink3.metapress.com/content/dw15nu5704611748/fulltext.pdf>
- [104] Beckert, W. and Kreher, W., "Modelling Piezoelectric Modules with Interdigitated Electrode Structures", *Computational Materials Science*, Vol. 26, 2003, pp. 36-45. <http://144.206.159.178/FT/204/78956/1334252.pdf>